TURBULENT MIXING LAYER EXPERIMENT IN SUPERSONIC FLOW

Thesis by
Hideo Ikawa

In Partial Fulfillment of the Requirements
For the Degree of
Doctor of Philosophy

California Institute of Technology
Pasadena, California
1973
(Submitted May 4, 1973)

ACKNOWLEDGMENTS

I wish to express my sincere appreciation to Professor Toshi Kubota who, throughout the course of my graduate education, provided the encouragement, inspiration and continued guidance so essential for the successful completion of the research project.

I also wish to extend my gratitude to the members of the GALCIT faculty, staff and fellow students for their advice and support in progress of the research. The author is especially grateful to Professors Wilhelm Behrens, Edward E. Zukoski and Anatol Roshko for their interest and invaluable contributions in the present effort; to Dr. Donald J. Collins for his advice and assistance in preparation of the research project; to Mr. Dale Berg for proof reading of the manuscript; to Messrs. S. Roman and P. Baloga for their assistance and guidance in conducting the wind tunnel tests; to Messrs. G. Carlson, E. Dahl and members of the Aeronautics machine shop for their suggestions and skillful construction of experimental equipment; to Mrs. B. Wood and Mrs. J. Colbert for preparation of the figures; and special thanks to Mrs. Virginia Conner for her patience and expert typing of the thesis.

I wish to thank the California Institute of Technology who, through the graduate appointments, provided the financial assistance throughout my graduate studies; and the U. S. Army Research Office and the Advanced Research Projects Agency, Contract No. DA-31-124-ARO (D)-33 for sponsoring the present project.

This thesis is dedicated to my wife, Yoshiko, whose devotion and encouragement throughout the difficult years and whose assistance in the preparation of this manuscript made the completion of the present task possible.

ABSTRACT

A supersonic, two-dimensional, turbulent free mixing layer was experimentally investigated in the GALCIT Supersonic wind tunnel to clarify the Mach number dependence of this flow field. The tests were conducted with a nominal Mach number of 2.47 with an ambient stagnation condition. Self similarities of the mean and turbulent flow fields were established.

The mean and fluctuating flow measurements were made. In addition, the actual entrainment rate of the turbulent free mixing layer through the low speed interface was also measured and it was verified that this quantity equals the growth rate of momentum thickness. The spreading rate, the entrainment rate and the maximum shear stress were appreciably smaller than the respective incompressible values. Velocity profile scaled to an incompressible form by a linear transformation of the lateral coordinate. The maximum streamwise velocity fluctuation was approximately 1/3 of the incompressible value. The flow field of turbulent free mixing layer was found to be highly dependent upon the supersonic compressibility effect.

TABLE OF CONTENTS

Table of Contents (Continued)

Table of Contents (Continued)

PART TITLE PAGE NO.

Table of Contents (Continued)

List of Tables

LIST OF FIGURES

List of Figures (Continued)

List of Figures (Continued)

List of Figures (Continued)

List of Figures (Continued)

LIST OF SYMBOLS

A	area of porous plate (inch^2)
$A_{11}(\tau)$	autocorrelation function
a	$k_w/[k_o(L/D)^2]$
a_1	$1 + \frac{\gamma-1}{2} M^2$
b	TFML width (inch); or $Nu_o - i^2 r_r \alpha_r/\pi k_o$
B1, B2, B3, B4	logarithmic partial derivatives (see Eq. B. 14)
BW	bandwidth of Tektronix 1L5 Spectrum Analyzer (Hz)
C	coefficient of sensitivity coefficients
$C_{AB}(\tau)$	correlation functions (Eq. II. 2)
C_w	specific heat of hot-wire
D	hot-wire diameter (cm)
e'	hot-wire fluctuation voltage (mv)
E_{tc}	hot-wire thermocouple output ($e'^2 \approx K_{tc}E_{tc}$) (Eq. B.11)
$\overline{E}$	$E_{tc}(x)/E_{tc}(0)$
f	frequency (Hz)
$F_{11}(\omega)$	spectra function, $\int_0^\infty F_{11} d\omega = 1.0$
$f_A(\tau)$, $f_B(t-\tau)$	time dependent input signal to be correlated (Eq. II. 2)
g	frequency and wire aspect ratio dependent parameter $\tanh\sqrt{\beta}/\sqrt{\beta}$
G_o	zero frequency gain of amplifier
$G^*(f)$	frequency response of amplifier
h	step height behind upstream block (inch)
i	hot-wire overheat current (ma)
k	$\partial R/\partial(i^2R)$ (Eq. B. 1)
K	wire property $\rho_w C_w D^2/4k_o$

List of Symbols (Continued)

k_o	thermal conductivity of air at stagnation temperature (watt/cm^{o}K)
k_w	thermal conductivity of wire (watt/cm^{o}K)
k_s	constant $S_\rho = k_s S_u$
K_{tc}	calibration constant of thermocouple output (mv^2/mv)
L	hot-wire length (inch)
L_x, L_y, L_z	spatial integral scale of streamwise turbulent component measured in x, y, z separation $\int R_x dx$
M	Mach number
M_A	compensating amplifier time constant (μsec)
M_t	hot-wire thermal lag wire time constant (μsec)
m	$d\ell n\,\mu_o/d\ell n\,T_o$
$\dot{m}_{ACT}$	actually injected mass flux through porous plate
$\dot{m}'$	mass flux fluctuation
n	$d\ell n\,k_o/d\ell n\,T_o$
Nu	Nusselt number
p	pressure (mm Hg)
p_o	stagnation pressure (mm Hg)
p_{p_L}	plenum chamber pressure (mm Hg)
$\overline{q'^2}$	$\overline{u'^2 + v'^2 + w'^2}$
r	S_u/S_{T_o} or $S_{\dot{m}}/S_{T_o}$
R	hot-wire resistance (ohm)
r_r	reference resistance per length of hot-wire (ohm/cm)
R_{e_o}	Reynolds number, $\rho U D/\mu_o$

List of Symbols (Continued)

R_{e_θ}	Reynolds number based on momentum thickness $\rho U \theta / \mu_o$
R_{ij}	normalized correlation functions $\begin{pmatrix} \text{i flow direction} \\ \text{j separation direction} \end{pmatrix}$
$R_{\overline{\dot{m}'T_o'}}$, $R_{\overline{u'T'}}$	correlation coefficients
$S_u, S_\rho, S_{T_o}, S_{\dot{m}}$	hot-wire sensitivity coefficients (Eq. B. 14)
T	actual computation period of temporal correlation
T	temperature (^oK or ^oR)
T_{sup}	hot-wire support temperature
T_r	reference temperature of hot-wire
$\mathcal{J}$	temporal integral scale $\int R_\tau \, d\tau$
U	free stream velocity
u, v, w	velocity components
x, y, z	axial, lateral, spanwise coordinate
α	$[1 + \frac{\gamma-1}{2} M^2 (1 + \overline{q'^2})]^{-1}$
α	b/a, hot-wire parameter of finite length and overheat
α_r	thermal-resistivity of hot-wire ($^oK^{-1}$)
β	$(\gamma-1)M^2\alpha$; or $\alpha\sqrt{1 + (\bar{\omega}/b)^2}$
γ	ratio of specific heat; or intermittency factor
θ	momentum thickness $\int_{-\infty}^{\infty} \frac{\rho u}{\rho_e u_e} (1 - \frac{u}{u_e}) dy$; or Mach wave angle (deg.)
λ_e	entrainment rate $= \rho_w v_w / \rho_e u_e = \dot{m}_{ACT} / \rho_e u_e A$
η	recovery factor; or normalized lateral coordinate ($\sigma y/x$)

List of Symbols (Continued)

ψ	stream function
ψ_N	hot-wire end loss correction parameter
κ	floor to ceiling ratio ($\kappa = 420$) of amplifier response
σ	spreading parameter ($\sigma y/x$)
σ_θ	spreading parameter ($\sigma_\theta \, d\theta/dx$)
σ_m	spreading parameter ($\sigma_m y/\theta$)
ρ	density of fluid
$\rho_w C_w$	heat content of wire $\left(\frac{\text{watt sec}}{\text{cm}^3 \, {}^o\text{K}}\right)$
$\rho_w v_w$	entrained mass
τ	shear stress; or delay time of temporal correlation function, or $(T-T_{aw})/T_{aw}$
ω	angular frequency, $2\pi f$

Superscripts

$(\ )'$	fluctuation quantity
$\overline{(\ )'^2}$	mean squared fluctuation quantity
$(\tilde{\ })'^2$	normalized mean squared quantity; $\tilde{g}'^2(f) = \dfrac{\overline{g'^2}}{\int \overline{g'^2} \, df}$
$(\tilde{\ })'$	RMS fluctuation normalized with local mean quantity $\tilde{g}' = \sqrt{\overline{g'^2}}/g_L$
$(\ )^*$	dividing streamline coordinate

Subscripts

A	amplifier dependent
awm	hot-wire measured quantities at $i = 0$
e	edge condition of TFML

List of Symbols (Continued)

eff E	effective quantity measured from virtual origin
f	frequency dependent $g_f = g(f)$
i	ideal fluctuation; or incompressible flow condition
L	local flow properties
m	measured quantity
o	stagnation flow properties
s	static flow quantities
w	hot-wire; or wall condition

Definitions

F-T-F	boundary layer trip with fine grain sandpaper (carborandum C-320)
R-T-F	boundary layer trip with rough grain sandpaper (aluminum oxide EC #30)
operating condition I	p_o = 730 mm Hg, R-T-F
operating condition II	p_o = 610 mm Hg, F-T-F
SB	contoured streamline block
TBL	turbulent boundary layer
TFML	turbulent free mixing layer
TWML	turbulent wall (forced) mixing layer

I. INTRODUCTION

In the past two and a half decades, some experimental and theoretical studies of compressible (supersonic) turbulent free mixing layers have appeared. Experimental investigations were confined to determine the mean velocity profiles and the rates of growth of the free mixing layer by direct Pitot pressure measurements (Maydew and Reed(1) and Johannesen(2)) or density distributions by interferometer (Gooderum, et al(3) and Bershader and Pai(4)) in the mixing zone of jet issuing from an axisymmetric or a rectangular nozzle into a quiescent air. The surveys were made in the mixing region from the nozzle exit to some distance downstream where the axisymmetric effect is not yet significant. Two dimensionality of the mixing layer is usually assumed in the region where the width of the mixing layer is small compared with a radius of jet.

Indirect investigations of supersonic mixing layer associated with base pressure studies(5-8) were also conducted in the wind tunnel. A mixing region is formed to separate the external and internal flow fields. Wind tunnel experiment is complicated by the expansion of supersonic flow at a corner of the rearward facing step creating a low-pressure base flow region. Termination of the dividing streamline at the wall feeds the recirculation flow upstream in the inner base region and hence the mixing profile does not form a pattern of classical turbulent mixing layer but it is accompanied by a reverse flow profile. Detailed investigations of this type of flow with various corner conditions were made by Hama.(8)

Entrainment of mass into the axisymmetric mixing region behind a cone was investigated by Hill and Nicholson.(9) The entrained air was introduced into the base region of the cone through the perforated axisymmetric tube supporting the model. However, no Pitot pressure survey was made to confirm the growing rate of mixing layer predicted by the entrainment measurements. One interesting aspect of the mixing layer behind a cone is that the entrainment takes place in the inner side of axisymmetric flow in contrast to the axisymmetric jet, in which the entrainment occurs outside. This difference is reflected in the difference of mixing layer growth rate; spreading is greater for the mixing layer behind a cone than the mixing layer produced by a jet.

It appears that only two wind tunnel tests by Roshko and Thomke(10) and Sirieix and Solignac(11) were carried out to investigate the mean flow field of the two dimensional supersonic turbulent free mixing layer. The former investigators measured the actual entrained mass by the specially constructed bleed system and compared it with the growth rate of momentum thickness obtained from the Pitot pressure survey. However, the number of Pitot pressure surveys were limited and no definite quantitative comparison between the measured entrainment and the growth rate of momentum thickness was attained. Evolution of velocity profiles from the boundary layer to the mixing layer were obtained by the latter investigators using the Pitot pressure survey. The velocity profiles below $u/u_e = 0.10$ were not investigated in detail so the existence of reverse flow region cannot be completely discarded.

Theoretical determination of the spreading rate and velocity profile were made by several investigators.(12-16) The general consensus based on experimental observations is that the mixing layer growth rate decreases with increasing Mach number. The velocity profile can be represented by the modified error function(17, 18) or the velocity profile in a low-speed mixing layer measured, for example, by Liepmann and Laufer,(19) with suitable normalization of lateral coordinate with linear scaling parameter ($\eta = \sigma y/x$). Since the density varies appreciably across the mixing layer at supersonic speeds, relating the spreading parameter (σ) to the ratio of densities at slow stream and fast stream sides (ρ_o/ρ_e) was a very attractive idea and many attempts were made to that effect. However, Brown and Roshko(20) showed that the effect of density ratio alone cannot explain the behavior of the supersonic free mixing layer. For example, the subsonic two-dimensional mixing layer experiments simulating a density ratio equivalent to the M = 5.5 flow showed a little change in the spreading rate when compared with the incompressible, uniform density data of Liepmann and Laufer (approximately 70~80%). However, the supersonic, adiabatic mixing layer experiments conducted at M = 4.0 showed a considerable reduction, i.e. the spreading rate was approximately 33% of incompressible value.

A supersonic experiment in which massive blowing of air or foreign gas into the fully developed turbulent boundary layer flowing over a flat porous plate was performed by Fernandez and Zukoski.(21) In their experiment the injection rate was increased to such an extent that the boundary layer was blown off the wall and the shear stress at the wall was considered negligibly small. The momentum of injectant was still small compared to the freestream momentum and hence the governing equations were reduced to a form identical to that of the free mixing layer. With zero pressure gradient, a self-similar flow field (linear with respect to axial distance) was achieved in which the momentum thickness growth rate equals the entrainment rate of the free mixing layer. Comprehensive surveys of the flow profile evolution from boundary layer to the mixing layer with increasing injection rates were performed. The results were quite different from the previous investigations, especially in two respects: (1) A mass-injection rate (λ_e) equivalent to the entrainment rate of incompressible mixing layer ($\lambda_e \cong 0.035$) was required to create a mixing layer type of flow; and (2) the velocity profiles could be reduced to incompressible form with application of the Howarth-Dorodnitsyn coordinate transformation. Fernandez and Zukoski successfully demonstrated that the results with different blowing rates matched favorably with the incompressible flow data of McQuaid(23) for the corresponding blowing rate. If we consider blown-off boundary layer as a free shear layer, their data indicate that the spreading rate of the supersonic mixing layer remained constant under the transformed coordinate and was independent of Mach numbers. Since the lateral coordinate in compressible flow is stretched in the low density region by the integral transformation, the foregoing results imply that the actual spreading rate of the turbulent wall mixing layer is greater than that of incompressible flow. This interpretation was also made by Brown and Roshko.(20)

The apparent contradiction between findings of Fernandez and Zukoski(21) and others led to the present wind tunnel experiments. The half nozzle section with rearward facing step replaced the customary full nozzle configuration. The bottom wall behind a rearward facing step was replaced with a 2.0 in. x 8.0 in. porous plate of 10 micron-porosity. With this setup, air or other gases can be injected into the base region so that precise matching of the base pressure and freestream can be accomplished and the mixing layer can be brought out straight with minimum interference to the external flow. The classical turbulent mixing layer can be simulated under the controlled supersonic environment. This unique setup serves a double purpose: (1) Pressurization of the base region to create a non-reversed flow mixing layer; and (2) it permits actual measurements of the entrained mass. Continuous, closed cycle operation of the wind tunnel with controlled environment allowed a detailed survey of mean flow properties to be conducted.

Since the self-similar turbulent mixing layer is a conical flow and no length parameter enters into the problem, the turbulent free mixing layer flow should be an independent of step heights. Step heights come into the laboratory problem in a region where interaction of mixing layer and the bottom wall occurs. It was found that the proper setting of injection rate and the proper tailoring of the interaction region eliminated the wall effect. A self-similar flow was established in a large portion of the test section and the uniform pressure field extended far beyond the termination point of injection.

Testing under controlled environment, the mass injection must match the entrained mass of mixing layer. Therefore, the present configuration offers a precise measurement of entrainment rate of turbulent free mixing layer which can be checked against the value computed from the velocity profile. Under the perfectly matched condition, the growth rate of momentum thickness and the measured entrainment rate agreed ($d\theta/dx = \lambda_e$).

Since very little is known on the turbulence structure of the supersonic mixing layer, it was decided to conduct the detailed fluctuation surveys of air to air mixing rather than performing a mean-flow investigation of air and foreign gas mixing. The hot-wire technique developed for the supersonic turbulent field was extended to cover the entire mixing layer including the subsonic region. Fluctuation intensities and power spectral density distributions of streamwise mass flux, total temperature, velocity and static temperature (density) fluctuations were surveyed. Qualitative autocorrelations and crosscorrelations were also investigated to obtain data on the turbulence field structure. Unfortunately, the smallness of the test section and the complexity of the hot-wire technique did not permit the construction of a usable X-wire probe and hence the Reynolds stress distribution computed from the mean flow profiles could not be related to the direct measurements of the turbulent field. Although the extent of the turbulent investigation was restricted to the measurements of streamwise components of turbulence velocity and was far less extensive than the investigations accomplished in the incompressible flow, some insights into the turbulent structure of the supersonic mixing layer were gained to further the understanding of this flow field.

II. DESCRIPTION OF EXPERIMENTS

II. 1. Tunnel and Model Description

The experiments were conducted in the Leg 1 Supersonic Wind Tunnel of the Graduate Aeronautical Laboratories, California Institute of Technology (GALCIT). The tunnel test section is 2 inches deep, 2.5 inches wide and 18.25 inches long. The half nozzle configuration was constructed by replacing the upper nozzle block with a 10 inch long flat block made of brass. The nominal operational Mach number is 2.47 ± 0.02 and most of the tests were conducted with a stagnation pressure of 735 mm Hg (± 5 mm Hg) and stagnation temperature of 27°C (± 3°C). The tunnel is operated in closed mode and the air is cycled through the dryer to remove its moisture (see Oliver(24)). Proper utilization of the dryer (heating and cooling cycle of activated alumina between each test) results in very dry air with the average dewpoint reading of as low as -10°F (lowest recording was -35°F), considerably better than the one Gran(25) has observed. Under this operating condition, the Mach number determined by the combination of freestream stagnation pressure, Pitot pressure and static pressure is accurate to ± 0.01.

During the initial phase of hot-wire surveys, frequent breakage of hot-wire was experienced. The cause of breakage has been traced to the flow of microscopic particles introduced in the tunnel circulating system by the trial run of newly constructed Leg 2 Supersonic Tunnel. To capture these particles, layers of filter paper were installed in two sections of upstream settling chamber, which dropped the operating total pressures to 610 mm Hg. The boundary layer on the half nozzle block was tripped just upstream of the throat with a strip of fine grain (Carborandum C-320) and rough grain (aluminum oxide EC # 30) sandpapers. During the course of hot-wire surveys with p_o = 610 mm Hg, it was found that a strip of fine grain sandpaper (operating condition II) did not effectively trip the flow to produce a fully developed turbulent boundary layer. All hot-wire measurements were, therefore, repeated with an operating condition I (p_o = 735 mm Hg. with rough trip). The turbulent boundary layer thickness of about 0.12 ~ 0.14 inch with associated momentum thickness of approximately 0.01 inch was obtained just upstream of the rearward facing step.

The downstream block of a plenum chamber and porous plate, through which air can be injected, was placed in recessed positions behind the rearward facing step of the upstream block. Supplemental pieces such as a streamlined block installed behind a porous plate and full length fences installed at both sides of the porous plate were required to establish the interference free flowfield. Each model block was equipped with a series of static pressure taps to monitor the flowfield conditions during the test. Pertinent dimensions of each model and the locations of pressure taps are illustrated in Figure II.1a to II.1c. These static pressures are monitored on a bank of mercury manometers. The responses of manometers are accurate within ± .5mm Hg. with a reading error of ± .20 mm Hg. Also the selected pressure taps are monitored by a Statham pressure transducer simultaneously with Pitot pressure trace. The downstream block is designed to be placed at two recessed positions, i.e., 1.0 inch and 0.5 inch from the top surface of the upstream block. One fence, made of a 0.25 inch thick clear plexiglass, filled the gap to the window. Its upper surface is made flush with the surface of the upstream block so that no flow interference is produced when the mixing layer is brought out straight. The opposite fence is made of stainless steel plate and equipped with a series of 40 pressure taps in 1 inch increments. A gap between the fence and window is filled with epoxy to remove the low pressure region as much as possible.

Advantage of the present setup is that an investigation of truly two-dimensional supersonic turbulent free mixing layer under the controlled environment can be made possible with a proper mass injection. Slightly overblown and underblown cases can be investigated, but some effect of undesirable pressure gradient will be introduced so these unmatched cases were not pursued in detail. The disadvantage of using the half nozzle configuration is that the vertical working section of the freestream has been reduced by half, which may introduce more complicated wave interactions.

Details of the porous plate characteristics and construction of the plenum chamber are given in Appendix A-1. In the present experiment, detailed surveys of mean flow with pressure measurements and fluctuation field with hot-wire measurements were made with air injection. The injected air is supplied from the house air with 90 psig back pressure. In order to maintain the supply pressure at a constant value, double filters and double regulators were installed before the flow-meter. Double flow-meter system (Fig. II. 2) has been set up but a Meriam Laminar Flow-Meter (calibration accuracy of ± 0.5% of all range) was used for the primary measurements. The differential pressure reading across the flow-meter was monitored by the silicone oil micromanometer, and the supply pressure by a Wallace & Tiernan 15 psig pressure gauge, which allows the pressure reading of 0.05 psig.

The metering valve (Vacco Valve Company) was installed in the circuit so that very fine adjustment of injectant is made possible with a good repeatability. The flow rate is also monitored by the model plenum pressure which is displayed on the mercury manometer board. The entrainment, (λ_e), is computed by first determining the mass flow per unit area by dividing the total injection mass flow by the plate area and normalizing it by the freestream mass flux.

$$\lambda_e = \rho_w V_w / \rho_e u_e = \dot{m}_{act} / (\rho_e u_e A) \quad . \qquad \text{(II. 1)}$$

The computed λ_e based on measured injection rate and measured freestream mass flux is expected to be accurate within ± 5% including the flow-meter inaccuracies.

In order to establish the temperature equilibrium in the test section, the tunnel is usually operated for at least 1/2 hour before any measurements are taken. The assumption of uniform total temperature across an entire test section is found to be very good as the total temperature surveys across the mixing layer made at a few longitudinal stations show the deviation of ±2% of the total mean temperature. The energy flux across the mixing layer is integrated to zero which confirms the existence of adiabatic flow. Temperatures of the injectant air and the primary flow were monitored by the iron-constantan thermocouples and found within a few degrees of each other.

II. 2. Instrumentation

II. 2. 1. Pitot Probe and Static Pressure Probe

The Pitot probes and static pressure probes used in the experiments are shown in Fig. II. 3. The Pitot probe tips were fabricated from 0.065 inch O.D. stainless steel tubing with a tip flattened and filed to 0.005 inch by 0.08 inch and an opening of approximately 0.003 inch. The Pitot tube tip was pitched up at an angle of about 10° to the freestream direction in order to minimize the angle-of-attack effect within the mixing layer. Fernandez(22) showed that the flattened tip Pitot tube is insensitive to angle-of-attack variation of $\pm 10^\circ$ for subsonic and supersonic flow. The probe holder was made with 0.25 inch O.D. stainless steel tubing with 0.098 inch internal diameter. For convenience, a holder tip with a leakproof and quick change capability was designed and carefully fabricated with special threading.

The static pressure probes were fabricated from 0.032 inch O.D. stainless tubing. The tip is sealed and sharpened to a conical shape with an $8^\circ \sim 10^\circ$ semi-vertex angle. Four holes of 0.007 inch diameter were drilled 90° apart at about 12 probe-diameters behind the shoulder of conical tip in the region where the pressure recovers to local flow condition. The holes are aligned with vertical and horizontal directions. This arrangement was found to be least sensitive to the angle-of-attack effect, and the pressure deviation of less than 2% is measured in the angle-of-attack range of $\pm 5^{\circ}$. The calibration made in M = 2.5 freestream flow is given in Fig. II.3 with the probe drawings. However, no reliable calibration technique is available for the static pressure probe response in the rapidly changing shear flow, especially in the type of supersonic shear layer of the present investigation in which maximum velocity gradient occurs near the sonic point. Therefore, it is felt that the static pressure measured by the fence tap is taken more reliably.

The Pitot pressure and static pressure were measured using a Statham pressure transducer (PA-208TC-10-350, 0-10 psia). The vertical position of probe is measured to the accuracy of 0.002 inch by a 40-turn Helipot (Model E) directly coupled to the vertical traverse. In order to eliminate the position error produced by the mechanical backlash, the measurement is always taken in one direction from the freestream into the mixing layer. Since the air loading on the probe shifts the vertical position slightly, zero setting is always established at X = 0, Y = 0 position after the tunnel is started and expected to be accurate within ± 0.005 inch. The relative position of X and Y is accurate to 0.002 inch of mean position (occasional probe tip vibration appears). The pressures versus probe position were plotted on a Moseley X-Y recorder.

During the Pitot and static pressure measurements, a selected fence tap pressure is also measured by a Statham pressure transducer (PA-208 TC-5-350, 0-5 psia) with respect to probe position. The flow disturbances created by the probe can be detected by this method.

In the low velocity region of turbulent mixing layer, the differential pressure between probe and fence tap is measured by the Statham differential pressure transducer (PM6TX ± 5-350, ± 5 psid) to increase the resolution of measurements.

II. 2. 2. Hot-wire Instrumentation

II. 2. 2. 1. Fluctuation Measurements

The hot-wire probe[*] used in the present experiment is shown in Figure II. 4. The hot-wire needles are made by a size 30 mill nickel wire and the needles and probe support are held together by a heat-resistant ceramic compound (Saureisen #7). However, the poor bonding of needle to the support was found to cause a tip vibration and the wire strain gauging (see Figure II. 4). Note the noise in high frequency components of spectra . Mixing of Saureisen #7 and Ceramic Glaze HT[**] (approximately equal amounts) by trial and error has produced the excellent bonding between needles and support. The needle tips are sharpened to a wedge shape(tip thickness of less than 0.003 inch) to minimize the flow interference. Platinum-10% Rhodium wire (manufactured by the Sigmund Cohn Corporation) of 0.00005 inch diameter is etched in a concentrated nitric acid. The etched wire is gold plated to the probe tip using the liquid bright gold #7621 (Englehardt Industry) and heated to about 1200°F in a small oven for a few

---

[*] Author is indebted to Dr. R. L. Gran of TRW for supplying a valuable hot-wire technique, which was originally designed and developed by Dr. A. Demetriades of Aeronutronics, Philco-Ford, and for the use of his equipment to fabricate the hot-wire probe which made this portion of the investigation very successful.

[**] Obtained from Ceramics class of Pasadena City College.

minutes. About ten coatings are applied to insure good bonding. The length to diameter ratios of wire (L/D) are 120 ~ 160 and the probes are calibrated ($\alpha_r = 1.25 \sim 1.35 \times 10^{-3}/^{o}K$, $R = R_r \cdot [1 + \alpha_r (T-T_r)]$ and R_r is a function of length). These wires will burn out at midpoint with applied electric current of about 12 ma. The highest current used in the test is limited to 8.0 ma in the turbulent flow.

The electronic instrumentation consisted of a Shapiro-Edward constant current hot-wire anemometer set and has been described by Behrens(26) and recently calibrated by Gran.(25) Auxiliary equipment used in conjunction with the hot-wire set include a Tektronix Oscilloscope Type 547 (dual trace) and/or Type 549 (storage), a Tektronix Spectrum Analyzer Plug-in Type 1L5, a Hewlett-Packard Wave Analyzer Model 310A, a Princeton Applied Research Correlation Function Computer Model 101A,* a Signal Analysis Industry Corporation Correlation and Probability Analyzer Model SAI 43A, a Philco-Ford Intermittency Meter, a Monsanto Frequency Counter Model 100B, a Beckman Amplifier (Fitgo Model RP-1B) and a Cimron Digital Voltmeter Model 6653A.

The mean hot-wire voltage and the applied wire current were measured by an external circuit of Shapiro-Edward set constructed by Gran(25) and the outputs were read on a Cimron digital voltmeter. The distribution of mean square fluctuation voltage were measured by feeding the fluctuating signal to a built-in thermocouple circuit of

---

* The author is indebted to Dr. R. Batt of TRW for making the PAR Model 101A Correlation Function Computer available for the present research.

the Shapiro-Edward Hot-wire set and its outputs (E_{tc}) were amplified by a Beckman Amplifier before being plotted on the Moseley X-Y recorder. The power-spectral density distributions were taken with a Tektronix spectrum analyzer operating in manual sweep mode to obtain the maximum response in all resolution settings.
The results were verified by the Hewlett-Packard wave analyzer. Auto and crosscorrelation measurements were made with a PAR correlator and later repeated with a SAICOR correlator. Two sets of Shapiro-Edward hot-wire anemometers were used for the cross-correlation measurements.

It must be noted that the mean square fluctuation and correlation measurements are uncorrected for the amplifier frequency response. The amplifier frequency response is flat up to 100 KHz and down to half power at 320 KHz (Gran(25)). Since most of the turbulent energy is concentrated between 25 KHz to 100 KHz, the error introduced in the E_{tc} and the correlation measurements should not be too serious. Proper setting of the compensating amplifier (M_A) is also difficult in the turbulence measurements. Prior knowledge of thermal response time constant (M_t) of hot-wire to local turbulent flow for each wire used is low and the actual measurements of M_t in highly turbulent flow is very difficult. A suggested scheme is to set the M_A at freestream and hold it constant during the survey. The correction is then applied during the data reduction, which is valid if the turbulence contributions come mostly from the high frequency domain where $(2\pi f\, M_A)^2 >> 1$ and $(2\pi f\, M_t)^2 >> 1$. However, this condition fails to be satisfied in some area of the mixing layer with freestream M_A setting, especially in the low speed region. In this region, proper setting of $M_A \cong M_t$ is essential for E_{tc} and correlation surveys. Next to the ideal approach is to obtain an initial survey of M_t distribution and use these data as a reference to the subsequent surveys. This approach is reasonable because most wires are constructed almost identically to each other and hence the error in measurements is minimized (Appendix B-2).

The quantitative data of fluctuation fields were, therefore, obtained by the power spectral density distribution measurements. Although this technique is tedious and time consuming, the approach is well warranted, because the data can be fully corrected for the amplifier frequency response and wire-time constant. At least six or more measurements of power spectral distribution with low ($i \cong 2.0$ ma) to high ($i \cong 8.5$ ma) overheats were made at a given point of mixing layer to obtain an accurate mode-separation of fluctuating quantities.

II. 2. 2. 2. Correlation Measurements

Autocorrelations and crosscorrelation functions of the turbulent shear flow were obtained by means of a PAR 101A correlator. The measurements were taken in real time as the experiment was conducted. The correlator essentially consists of four main computational circuits: 1) time delaying function, 2) multiplier, 3) integrator, and 4) averager. Single input of fluctuating voltage from a hot-wire is used for the autocorrelation measurements, and the correlation function of time dependent function $f_A(t)$ and delayed signal $f_A(t-\tau)$ is computed. Crosscorrelation measurement requires an input of two time dependent signals measured by two different probes. One of the signals is delayed before the two signals are correlated. The mathematical relation of the correlation function is:

$$C_{AB}(\tau) = \lim_{T \to \infty} \frac{1}{2T} \int_{-T}^{T} f_A(t)\, f_B(t-\tau) dt \qquad (II.2)$$

where $C_{AB}(\tau)$ = correlation function computed.

$f_A(t)$, $f_B(t-\tau)$ = input signal.

T = actual period of computation.

τ = time delaying parameter

when $A = B$, autocorrelation is computed; $A \neq B$, crosscorrelation is computed.

Correlation measurements were made with a best estimated time constant setting for the local flowfield. From the spectral measurements, the frequency response of turbulence is known and hence bandpassed filters of amplifier were set accordingly to reject the undesirable amplifier noise, etc. Since the flow properties remained constant along the u/u_e line, longitudinal and spanwise crosscorrelation surveys were less troublesome. However, lateral crosscorrelation survey requires a penetration of different levels of the flowfield. Consequently changes in sensitivity, frequency response and time constant of the wire resulted, but no correction was made during the survey. However, indirect correction is applied in data reduction.

Crosscorrelation of narrow band passed-signal was obtained by placing two independent HP-310A wave analyzers between the respective hot-wire sets and correlator. The same center frequency to be measured was set on both wave analyzers. The matching of the two was accomplished by monitoring the center frequency on a Monsanto 100B digital frequency counter.

III. EXPERIMENTAL TECHNIQUE AND DIFFICULTIES

III. 1. Preliminary Mean Flow Measurements of TFML with h = 1.0 inch and h = 0.50 inch

Preliminary investigations of the supersonic turbulent free mixing layer behind a rearward-facing step were conducted to delineate the nature of the flow field. The porous bottom wall in which air is injected was initially positioned at two heights of 1.0 or 0.50 inch below the surface of the upstream block.

With h = 1.0 inch, the injection rate (λ_e) of 0.01 was required to bring the mixing layer straight out. The static pressure distribution (Fig. III.1) just downstream of the step was nearly constant up to x = 5.0 and followed by a negative pressure gradient resulting in about 20% pressure drop at the end of the injection plate. The static pressure measurements taken with the static-pressure probe, the fence taps and the lowest Pitot pressure were found uniform within ± 2% of each other. The flow is remarkably self-similar in the region of constant pressure and the virtual origin can be traced back to 2.5 inches upstream of the step. The growth rate of momentum thickness ($d\theta/dx$) computed from the velocity profile is 0.007, less than the actual injection rate.

With the bottom wall repositioned at h = 0.5 inch, the actual injection of $\lambda_e = 0.0068$ was required to establish the self-similar flow in the same region. In this case, positive pressure gradient was noted beyond x = 4.0. The velocity distribution and $d\theta/dx$ were almost identical with the h = 1.0 case, indicating that the turbulent free mixing layer is independent of the step heights in the uniform pressure region. It appeared also that there exists a proper height in which the injection rate and growing rate of momentum thickness can be matched (i.e., $\lambda_e = d\theta/dx$ for $dp/dx = 0$).

The difference between λ_e and $d\theta/dx$ observed in the preliminary tests can be explained in the following way. For the $h = 1.0$ case, the lower boundary of the mixing layer intersects the wall at a point beyond the end of the porous plate creating a cavity (mass deficit) between the mixing layer and the wall. To fill the cavity with fluid, the streamlines in the mixing layer are bent downward and negative pressure gradient is created. As a result, axial flow is induced, which accounts for the unmatched value between λ_e and $d\theta/dx$.

Now for the $h = .50$ case, the ideal mixing layer intersects the lower wall on the blowing region. Since the fluid is injected uniformly along the porous plate, excess mass not required by the ideal mixing layer is blown into the layer beyond the intersection, causing a compression. The positive pressure gradient induces reverse axial flow and the actual injection of slightly less than the ideal entrainment was required. These observations suggest that the ideal condition may be established by tailoring the wall shape beyond the termination of injection. This modification will be discussed in Section III. 2. 2.

Important finding of the preliminary test was that the entrainment of supersonic TFML in the nearly constant pressure mixing region is much lower than the subsonic mixing layer of Liepmann and Laufer.(19) Present results show the strong compressibility effect of supersonic flow, also observed by other investigators. However, these results were contradicted by the finding of strong-blowing experiments along a flat, porous surface carried out by Fernandez(22) in the same GALCIT Supersonic Wind Tunnel. This contradiction led to the detailed and more refined experiments of this thesis.

III. 2. Experimental Difficulties

During the calibration of porous plate and during the preliminary and major phases of experiments, numerous types of flow interference have been noted. In some cases, major modification of models and wind tunnel traversing mechanisms, etc., were required.

Out of many problems encountered, five major modifications which have had the impact on the improvement of flow field will be discussed briefly in Appendix A for future reference. These are: 1) Porous plate characteristics; 2) Elimination of pressure gradient by the simulated streamline block downstream of the injection region; 3) Elimination of shock wave-mixing layer interference produced by the vertical traversing mechanism; 4) Effect of finite turbulent boundary layer upstream of a rearward facing step; and 5) The possible secondary flow produced by the finite length fences.

IV. DATA REDUCTION

IV. 1. Pressure Data

Local mean Mach number was computed from the measured Pitot and static pressures by applying a Rayleigh Pitot formula. Corrections for Pitot probe angle of attack and local turbulence were not included in this reduction, because the error introduced from these effects is probably as large as that from Reynolds number effects and calibration limits on the pressure transducer. The Reynolds number correction developed by Ramaswamy,(27) applied when the mean hot-wire data were reduced, showed a negligible effect on the corrected profile and the difference was found to be smaller than the raw data fluctuation. Velocity, density and temperature profiles were computed from Mach number distribution by assuming that the mean total temperature is constant throughout the mixing layer, which was confirmed by hot-wire measurements.

Once the entire flow profiles were determined, all integral properties such as a momentum thickness (θ), vertical velocity and shear distribution can be computed. Interpolation was carried out to determine a location and properties of the dividing streamline by applying a momentum balance. Since the initial boundary layer is non-negligible, initial momentum thickness must be accounted for in the calculation of momentum balance. Vertical velocity and shear computations (Fernandez(22)) were simplified and hence the results are valid only in the self-similar flow regime.

$$\theta = \int_{-\infty}^{\infty} \frac{\rho u}{\rho_e u_e}\left(1 - \frac{u}{u_e}\right) dy \qquad \text{Momentum Thickness.} \qquad (IV.1)$$

$$\theta - \theta_o = \int_o^x \lambda_e \, dx' = \left(\int_{-\infty}^{y^*} \frac{\rho u}{\rho_e u_e} dy'\right)_x \qquad y^* \text{ - Lateral Coordinate of Dividing Streamline.} \qquad (IV.2)$$

$$\lambda_e = \frac{\rho_w v_w}{\rho_e u_e} = \frac{d\theta}{dx} \qquad \text{Entrainment Rate for } \frac{dp}{dx} = 0. \qquad (IV.3)$$

$$\frac{v}{u}(y) = \lambda_e \left[\frac{\rho_e u_e}{\rho u} - \frac{\rho_e u_e}{\rho u} \int_0^{y/\theta} \frac{\rho u}{\rho_e u_e} d(y'/\theta) + y/\theta\right] \qquad \text{Vertical Velocity Profile.} \qquad (IV.4)$$

$$\frac{\tau(y)}{\rho_e u_e^2} = \lambda_e \left\{\frac{u}{u_e} - \frac{u}{u_e} \int_0^{y/\theta} \frac{\rho u}{\rho_e u_e} d(y'/\theta) + \int_0^{y/\theta} \frac{\rho u^2}{\rho_e u_e^2} d(y'/\theta)\right\} \qquad \text{Shear Profile.} \qquad (IV.5)$$

Streamline patterns are determined by the integration of continuity equation. Self similarity is established by linear curve fitting of axial distributions of constant u/u_e and linear growth of momentum thickness. The convergent point of these determines the virtual origin of turbulent free mixing layer. Another confirmation of similarity is that the velocity profiles collapsed to a single curve when lateral coordinates are normalized by the local momentum thickness.

IV.2. Hot-Wire Data Reduction

Quantitative descriptions of mean and fluctuating flow field of hot-wire measurements were determined in accordance with methods developed by Kovasznay,(28) Morkovin,(29) Kistler,(30) Laufer(31) and Behrens.(32) Behrens' method takes account of the frequency-dependent heat loss correction from the wire to the supports which is applied to the finite length wire. The excessive heat loss at both ends influences the temperature loading on short aspect ratio wire, resulting in a non-uniform temperature response along the wire. Therefore, it is desirable to use a probe with relatively long aspect ratio or a probe with thermally shielded supports to minimize the end heat conduction. However, the structure failure of long wire in highly turbulent flow forced us to use the wire with $120 \leq L/D \leq 200$.

The mean flow reduction of hot-wire data, including the end loss correction, is given by Behrens(33) and a condensed version by Gran(25) and its iteration scheme is given by Ramaswamy.(27) Since the reliable Pitot and static pressure profiles are available, the first method described by Ramaswamy is followed and thus the pressure data supplement the hot-wire data reduction. Smallness of the hot-wire probe prevented the direct measurements of support temperature (T_{sup}); therefore, an uncertainty is introduced in the estimation of support temperature. The reduced data showed that $(T_{sup}-T_s)/(T_o-T_s) = 0.9$ is a reasonable assumption. Wire diameter (D) and resistance per inch (r_r) are based on the manufacturer's specification. The thermal coefficient of wire resistivity (α_r) was obtained for each wire mounted on the probe. α_r consistently ranges between 1.25 to $1.35 \times 10^{-3}/^{o}K$, which is lower than the value quoted for platinum - 10% rhodium ($\alpha_r = 1.66 \times 10^{-3}$) wire alone, and the difference is perhaps attributed to the construction of the probe. The starting shock of wind tunnel passing over the hot-wire slightly affects the reference resistance (R_r) of the initially calibrated wire in the still air. Since the Mach number and the total temperature in the freestream are known within 1 to 2% of mean values, sets of hot-wire data are always taken in this region, and then the value of the reference wire resistance is corrected during the data reduction to match the freestream total temperature. This correction is usually less than 1% of the initial R_r. Resistances versus applied currents were taken before and after the operation and variation of adiabatic resistance of more than 2% is discarded, because it is usually associated with a wire damage. The mean total temperature and the Nusselt number profiles are computed from the measured mean resistances of wire taken with respect to the applied current. Brief descriptions of the reduction technique are presented in Appendix B-1.

As pointed out by Behrens,(32) the end-loss corrections depend on the frequency of the fluctuation. At low frequencies the temperature over the whole length is affected by the heat-conduction to the support as in the steady case. At high frequencies, however, the conduction effect is confined in a small region near the support, and under typical conditions in supersonic turbulent flow the hot-wire may be considered to be of infinite length as far as fluctuations are concerned. The end-loss corrections of fluctuating quantities are, therefore, made through the sensitivity coefficients of wire which are computed from the measured mean flow values (Appendix B-4). Also, it was found that the foregoing assumptions are valid in the low speed turbulent flow of the present investigation and the discrepancy introduced is less than 10% of the root-mean-square values of the integrated turbulent quantities.

The relationship between the fluctuating voltage response of real hot-wire to "ideal" hot-wire which also includes the proper transfer functions of instruments is given in Appendix B-3. The power spectral density distribution and its integrated mean square voltage are fully corrected for these instrument responses. The mean square voltage measured through the thermocouple (E_{tc}) are uncorrected for the amplifier frequency and compensator responses. However, E_{tc} data are corrected approximately if the measurements were taken in the turbulence field dominated by the high frequency components. (See Appendix B-3).

Once the fluctuating voltages of "ideal" hot-wire and the corresponding sensitivity coefficients were computed, the mass flux and total temperature fluctuations can be separated by the application of mode diagram technique developed for the supersonic turbulence. In the present investigation, the survey was made in the entire Mach number range from freestream supersonic to zero flow. Therefore, some of the simplifying assumptions used in the supersonic flow become invalid in low speed flow regime. (1) Correction of fluctuating voltage output by simple ratio of $(M_t/M_A)^2$ fails; (2) hence fluctuation measurement by thermocouple (E_{tc}) produces a large error unless the M_A is set very close to M_t; and (3) the sensitivity coefficients of velocity, density and mass flux are not identical but can be approximately related by $S_\rho \cong k_s S_u$ where k_s is a function of Mach number and Reynolds number (Appendix B-4). Technique and approximations required to extend the mode diagram method into the subsonic region of turbulent mixing layer are given in Appendix B-5.

Separation of velocity and density fluctuations requires further assumptions (Appendix B-6). Freestream turbulence is assumed to be produced by the plane wave acoustic radiation from the turbulent boundary layer or mixing layer. Velocity and pressure fluctuations are computed by assuming a vorticity mode of fluctuation is negligible and the isentropic process is considered. In the case of turbulent mixing layer, a vorticity and an entropy mode of fluctuations dominate the flow field and a pressure fluctuation is assumed negligible compared with the other two modes. This assumption does not preclude that the pressure fluctuation is entirely insignificant. Therefore, at the edges of the mixing layer, where velocity and static temperature fluctuations reduced to the same level as the pressure fluctuations, the aforementioned assumption is violated. Based on the foregoing assumptions, the turbulence spectra and turbulence profiles across the mixing layer are computed.

IV. 3. Correlation Measurements

Only qualitative autocorrelation and crosscorrelation surveys of freestream and mixing layer turbulence were made. Autocorrelation measures the coherence time of the original signal being investigated, which can be a simple or complex periodic wave or randomly varying noise. By studying the wave shape and decaying characteristic of autocorrelation functions, one can extract information regarding the type of time dependent signal to be observed. Another useful application is to extract and identify the foreign signals overriding on the basic signal, which has been used to identify the effect of boundary layer instability. Autocorrelation function is maximum and related to the total power of a signal when the delay time is zero. Thus, $C_{AA}(0)$ is proportional to the thermocouple data (E_{tc}). Autocorrelation function presented herein has been normalized with respect to the maximum power output.

$$R_{AA}(\tau) = \frac{C_{AA}(\tau)}{C_{AA}(0)} \qquad \text{(IV. 6)}$$

Crosscorrelation function measures the degree of conformity of two signals being sampled simultaneously. It is a very useful tool in the turbulence investigation; for example, space-time conformity of the turbulent field, instantaneous space correlation of the two signals and convection velocity of the turbulent field can be determined. Crosscorrelation function has been normalized with respect to a square root of autocorrelation function of the respective probe with zero time delay. An example is shown for a longitudinal crosscorrelation function.

$$R_{12}(\Delta x, 0, 0; \Delta\tau) = \frac{C_{12}(\Delta x, 0, 0; \Delta\tau)}{\{C_{11}(0, 0)C_{22}(\Delta x, 0)\}^{\frac{1}{2}}} \qquad \text{(IV. 7)}$$

However, measurements of autocorrelation functions at different levels of shear layer were sometimes not obtained. In such cases, the correction described in Appendix B-7 has been applied.

V. DATA PRESENTATION

V.1. Freestream Turbulence

The contribution of freestream turbulence to the investigating flow field is always asked in the turbulence experiments. A thorough investigation of freestream turbulence was made with the hot-wire including the spectral analysis and the correlation measurements. The full accounts of this investigation are presented in Appendix C. Only the main features of freestream turbulence are summarized herein.

The longitudinal gradients of unresolved freestream turbulent energy distributions were obtained through the built-in thermocouple (E_{tc}). The freestream E_{tc} gradients induced by the upstream boundary layer ($x \leq 0$), the downstream boundary layer on a flat plate filler with initial mismatch at $x = 0$ and the turbulent mixing layer are found to be $d\overline{E}/dx = 0.14$/inch, 0.6/inch and 1.4/inch, respectively. $\overline{E}$ is the freestream E_{tc} distributions normalized with the freestream E_{tc} induced by the undisturbed boundary layer at $x = 0$. It has been observed by Laufer,(31) Liepmann,(34) Kovasznay,(28) and others that the freestream turbulence in the supersonic wind tunnel is produced by the radiation of acoustic energy from the turbulent boundary layer or from the free mixing layer. Since the turbulent scale of mixing layer is considerably larger than the bounded shear flow due to the entrainment of fluid from both sides, it is expected that the acoustic radiation field is enhanced, which is qualitatively verified.

Power spectral density distributions showed the rapid development of low frequency components of turbulence with the downstream stations. It also showed that a significant level of energy contributions are produced by the relatively high frequency components of turbulent mixing layer travelling with a subsonic speed relative to the freestream flow. This implies that the process of interaction between the moving wall and the supersonic flow alone cannot explain the radiation phenomenon. Therefore, it appears that the acoustic generating source is imbedded in the turbulent mixing layer.

The velocity and the pressure fluctuations of freestream can be computed from the measured data, if one assumes the plane-wave acoustic radiation. In the self similar flow regime, the measured pressure fluctuation is approximately 0.4 ~ 0.5% of dynamic pressure and has remained relatively constant with longitudinal and lateral variations of positions. Laufer(31) observed that the pressure fluctuations produced by the uncorrelated signals of four walls contribute to the measured freestream value. Therefore, the actual radiation of pressure fluctuation from the turbulent mixing layer is expected to be less than the measured value. The velocity fluctuations varied from 0.5% at the mid-test section to 0.75% near the outer edge of the mixing layer. The upstream freestream velocity and pressure fluctuations are considerably smaller, 0.2% and 0.1%, respectively.

Appearance and disappearance of the wave in the freestream with a variation of total pressures were also detected by the spectra and the autocorrelation measurements. The interpretation of this phenomenon will be discussed fully in Section V.4.

V.2. Self Similar, Supersonic Turbulent Free Mixing Layer (TFML)

Investigations of self similar, supersonic turbulent free mixing layer have been conducted for the mean flow field and the fluctuating turbulent flow field.

V.2.1. Mean Flow Field

Mean flow field surveys were made with conventional Pitot pressure measurements and hot-wire used as a resistance thermometer to determine the total temperature.

V.2.1.1. Pressure Survey

Detailed Pitot pressure surveys have been conducted in the region of the test section from one inch upstream of the rearward facing step to 9.75 inches downstream of the step ($-1.0 \leq X \leq 9.75$).

V.2.1.1.1. Free Stream Properties

The typical static pressure and the edge Mach number (free stream outside of turbulent free mixing layer) distributions are shown in Fig. V.1. Aside from the interference region of the starting mixing layer, both pressure and Mach number distributions become uniform beyond $X \leq 2.75$. Repeatability of the tests is within ± 2% of the static pressure setting but uniformity of the flow per test is very good. These conditions with minimum disturbance in the free stream outside of the TFML are achieved by proper injection of air through the porous plate in the subsonic entrained region as discussed in Section III.

V.2.1.1.2. Velocity Distributions and Streamline Pattern

The evolution of velocity profiles from the upstream boundary layer to the fully developed mixing layer obtained with operating condition I is shown in Fig. V.2. Nearly identical velocity distributions were obtained with operating condition II, indicating that a small variation in the turbulence level appears to influence the mean flow properties very little. The longitudinal distributions of constant velocities are given in Fig. V. 3. Lines of constant velocity are straight and converge to a point 2. 5 inches upstream of the step, indicating that the mean flow quantities of turbulent free mixing layer have reached the similar flow condition beyond $X \geqslant 2.75$ ($\sim 275\ \theta_o$). The spreading rate (dY/dX) defined between the velocity ratios of .10 and . 90 ($0.10 \leq u/u_e \leq 0.90$) for this experiment is approximately $dY/dX \sim 0.064$ and considerably less than the subsonic data of Liepmann and Laufer, which is approximately $dY/dX \sim 0.16$. Based on this, the spreading parameter of $27 \leq \sigma \leq 29$ is obtained, which agrees reasonably well with the extrapolated data given by Maydew and Reed.(1)

Although the injection is terminated at X = 8. 00, the measurement taken at X = 8. 75 above the streamline block is in excellent agreement with the upstream flow, indicating the effectiveness of simulation of injected streamline by the contoured solid block. The effectiveness of the streamline block is more dramatically demonstrated in the next figure (Fig. V. 4) showing the streamline pattern determined by the integration of the continuity equation. Note the measured streamline patterns smoothly follow the streamline block and no appreciable deviation of pattern is observed. The dividing streamline, $\psi = 0$, is determined by the mass balance of linearly distributed injected air, and lies slightly below the sonic Mach number ($0.92 \leq M \leq 0.98$). However, the dividing streamline defined by the momentum balance shows the value very close to M = 1.0, which is shown as black circle and linear beyond X ≥ 2.75.

V.2.1.1.3. Dividing Streamline

More detailed descriptions of the dividing streamline are shown in Fig. V.5. The lateral position, velocity and Mach number distributions along the dividing streamline determined by the mass balance of actually injected air are shown with the triangle data points. Circle data points represent the properties along the dividing streamline determined by the momentum balance computed from the measured flow profiles.

$$\int_{-\infty}^{y^*} \frac{\rho u}{\rho_e u_e} dy = \int_{-\infty}^{\infty} \frac{\rho u}{\rho_e u_e} \left(1 - \frac{u}{u_e}\right) dy - \theta_o \qquad \text{(V-1)}$$

where θ_o is the initial momentum thickness of the boundary layer near X = 0.

The circle data points are observed to be more consistently distributed and approach a constant value more rapidly. The Mach number along the dividing streamline is approximately unity.

Two possible causes, inaccuracy in the velocity measurement in the low-speed region and excess entrainment in starting mixing layer, may have contributed to the observed discrepancies. Definition of tail end of the velocity profile is very critical especially in the thinner mixing layer region. In the low velocity side of TFML, 1% error in Pitot pressure measurement contributes approximately 5% u_e difference in velocity ratio. 0.1% error in Pitot pressure (~ 0.05 mm Hg) contributes almost 2.5% u_e difference in velocity ratio. The error in this area is cancelled in the momentum balance (i.e., $\int_{-\infty} \frac{\rho u}{\rho_e u_e}\left(1-\frac{u}{u_e}\right)dy \sim \int_{-\infty} \frac{\rho u}{\rho_e u_e}\,dy;\ u/u_e << 1$). On the other hand, the noticeable discrepancies of data determined by the mass balance are produced by a combined effect of a uniform distribution assumption of injected air and the slight error introduced in the integration of low speed mass. Detailed investigation of low speed region indicates that no noticeable reverse flow is detected (see Appendix D-1).

V.2.1.1.4. Momentum Thickness Gradient Vs. Entrained Mass

Momentum thickness (θ) and measured entrained mass distributions are presented in Fig. V.6. The entrainment rate is assumed to be uniformly distributed. Note the measured injected mass remains constant beyond X = 8.0 due to the termination of physical injection. The gradients of measured entrained mass and momentum distributions are reasonably compared within the experimental accuracy of measurements. For the operating condition I, the measured entrainment rates are $\lambda_e \cong 0.0074$. The slope of momentum thickness distribution is approximately $0.0071 \leq d\theta/dx \leq 0.0075$, depending upon how the straight line is fitted through data. The zero momentum thickness is traced to approximately 2.5 inches upstream of the step which is determined by the linear extrapolation of data. In fact, the convergent point agrees with the virtual origin of TFML obtained by the velocity distribution. Linear growth of momentum thickness assures the satisfaction of another necessary condition of self similar TFML. Off-center measurements, taken along 60% of tunnel semi-span from the centerline, also showed good agreement with the centerline value, indicating the existence of reasonably good two-dimensional flow.

Qualitatively similar results are obtained for the operating condition II.

Note the growth rate of momentum thickness is considerably smaller than the subsonic data of $d\theta/dx = 0.035$ and the supersonic forced mixing layer experiment of Fernandez(22) which gives $d\theta/dx = 0.029$. The comparison will be made in Section V.2.1.4.

V.2.1.1.5. Normalized Velocity Profiles

The velocity profiles over the range of X from 3.75 ~ 7.75 are normalized with momentum thickness of respective stations. All profiles referenced to the dividing streamline taken at $M = 1.0$ collapsed to a single profile (Fig. V. 7) as expected from the previous observations. Little difference between the profiles obtained with two types of boundary layer trippings, F-T-F and R-T-F, operated with $p_o = 735$ mm Hg condition is observed. The profile at $X = 9.75$ measured above the streamline block has been normalized with the effective momentum thickness, i.e., the linear extrapolation of θ distribution of Fig. V.6 to simulate the extension of TFML. In this normalization, the high speed portion of TFML matches identically with other profiles, whereas the flow near the solid block began to deform to boundary layer flow. Non-dimensionalized velocity gradient is also shown in the same figure.

With the assumption of constant static pressure and total temperature profiles across the TFML, density and shear stress distributions were computed and are shown in Fig. V.8 with Mach number profile. Note that more than 80% of the density change occurs in the supersonic side of the TFML above the dividing streamline, and less than 20% of the density gradient occurs below the dividing streamline. This ratio is expected to increase as the Mach number flow increases. This offers a partial explanation of the difference in growth rate of TFML observed with the binary mixing of subsonic flow simulating the same density ratio as supersonic flow. A controlling parameter is not only the density ratio of fast and slow speed sides of TFML but the shape of the density profile. This discussion will be taken up in more detail in the section of scaling of TFML.

V.2.1.1.6. Shear Stress Distribution

Shear stress distributions were computed by the integration of the momentum equation. For the similar TFML, Fernandez(22) shows that if $\lambda_e = \frac{d\theta}{dx}$, then the shear stress normalized with λ_e can be written as

$$\frac{\tau}{\lambda_e \rho_e u_e^2} = \frac{u}{u_e}\left(1 - \int_{-\infty}^{\tilde{y}/\theta} \frac{\rho u}{\rho_e u_e}\, d(y/\theta)\right) + \int_{-\infty}^{\tilde{y}/\theta} \frac{\rho u^2}{\rho_e u_e^2}\, d(y/\theta). \quad \text{(V.2)}$$

The computed shear stress distribution is given in Fig. V.9. The peak occurs slightly above the dividing streamline, where local $u/u_e \sim 0.64$. For the truly asymptotic turbulent mixing layer, the locations of maximum shear stress and dividing streamline should coincide. The discrepancy may be attributed to the presence of finite initial boundary layer. The peak value $(\tau_{max}/\lambda_e \rho_e u_e^2)$ is approximately 0.385 and is constant with axial distance. The constancy of peak value with X also satisfies another self similarity condition of two-dimensional TFML. This value is slightly higher than the incompressible value of Liepmann and Laufer(19) $(\tau_{max}/\lambda_e \rho_e u_e^2 \simeq 0.34)$.

However, $\lambda_e(M)$ decreases with an increasing Mach number, so $\tau_{max}/\rho_e u_e^2$ decreases with increasing Mach number.

The turbulent shear stress without viscous contribution in the supersonic shear flow consists of two correlations of fluctuating quantities, i.e., $\tau = - \rho \overline{u'v'} - u \overline{\rho'v'}$. With the assumptions of $p' << u'$, T' in the turbulent shear flow and the fluctuations of scalar quantities (T_o', T', ρ') are insensitive to the hot-wire orientations, it was found that $\overline{\rho'v'} = (\gamma-1)M^2 \overline{u'v'}$ and hence this term is negligible if Mach number is small. However, in the supersonic portion of the shear layer, $\overline{\rho'v'}$ becomes comparable to $\overline{u'v'}$. Unfortunately, the measurements with hot-wire to obtain $\overline{\rho'v'}$ and $\overline{u'v'}$ separately were unsuccessful.

The eddy viscosity, the turbulence production term and the flow angle distribution with u/u_e are shown in Fig. V.10. The normalized eddy viscosity is smaller than the incompressible value and the peak appears in the supersonic side of the layer. The production term is maximized near or slightly above the dividing streamline. The minimum flow angle of 0.4 degree is attained near $u/u_e \sim 0.60$. The flow angle greater than 12 degrees occurs in the region where $u/u_e \leqslant 0.05$.

V.2.1.1.7. Static Pressure Profiles

Static pressure profiles were measured with static pressure probe and fence taps (Fig. V.11). In order to obtain the high resolution, a Statham differential pressure transducer was used to monitor the pressure between the static p-probe and the reference fence taps distributed along Y = -0.5 stations. Nonuniformity of up to 3% of static pressure produced by the free stream wave interactions were detected, but the pressure deviation of this magnitude in the free stream edge does not contribute to serious error.

An interaction of wave emanating from the p-probe and the mixing layer produces a false pressure profile, which must be corrected. The interaction pattern is shown in the sketch in Fig. V.11. At some distance away from the effective edge of the mixing layer the pressure ports first sense the reflection of compression waves from the mixing layer. As the p-probe moves toward the mixing layer, the bulge of interaction shifts upstream such that the expansion waves pass through the p-ports to give the negative pressure dip. The pressure recovers as the second compression waves strike the p-ports and continue until the p-probe is completely immersed in the mixing layer.

The general shape of the pressure profile is a gradual decrease of pressure as the center core of TFML is approached. It appears that the minimum pressure of 1 ~ 2% below the mean static pressure is attained near the dividing streamline and recovers as the opposite edge is reached. This trend is also observed by Maydew and Reed.(1) A static pressure probe is very sensitive to the flow angle and also has not been calibrated in the shear flow (especially in the supersonic shear layer), and it is not certain that the observed phenomenon is actually a real one. The static pressure readings from the fence taps distributed along Y = -.06, -.20, -.35, -.50

and -.85 show relatively constant distributions when the interference free TFML is created (i.e., reposition of the p-probe far downstream away from the testing region).

It must be noted also that the slight interference from the probe still exists even after the vertical traverse has been relocated. Monitoring of the pressure from the single fence tap (usually $Y = -.50$ tap) with respect to the probe position indicates the slight variation (± .5%) of pressure across the entire mixing layer which occurs as a function of probe position.

V.2.1.2. Total Temperature

By using the hot-wire as a resistance thermometer combined with the Pitot pressure measurements, mean total temperature (T_o) distribution was obtained. Total temperature distribution normalized with edge T_o, ($T_o/T_{o_e} - 1$), is shown in Fig. V.12. A peak value of approximately 2% above T_{o_e} is observed at the turbulent edge of the TFML where highly intermittent flow is expected ($Y/\theta \sim 3.6$). Then it decreases to approximately 2% below T_{o_e} near the dividing streamline and recovers to the freestream value at the opposite edge of TFML. The data taken with operating condition I show a slight anomaly in the lower velocity region.

Total temperature flux distribution shows approximately equal positive and negative areas so that the integration across the TFML gives zero net energy flow. The results confirm the validity of the assumption of constant total temperature distribution. Difference in the velocity profiles obtained by use of constant and measured total temperature is found to be small.

V.2.1.3. Scaling of Supersonic TFML

Fernandez$^{(22)}$ suggested that when the supersonic turbulent mixing layer is compared with the subsonic data, the integral transformation of Howarth-Dorodnitsyn type ($\bar{y} = \int \frac{\rho}{\rho_e} dy$) should be used to transform the lateral coordinate. Similar transformation was applied to compare the velocity profile of current experiments with subsonic data, namely, the velocity profile of Liepmann and Laufer$^{(19)}$ (Fig. V.13). Both data have been matched at a common point of $u/u_e = 0.5$. The transformed supersonic profile is stretched more in the high speed side and contracted in the low speed side compared to the low-speed profile.

It is concluded that although the Howarth-Dorodnitsyn transformation is valid in application on compressible boundary layer flow, it is not the proper transformation for the free mixing layer flow. When the Y-coordinate of the present profile has been reduced by a constant factor, excellent matching of supersonic and subsonic profiles is observed, except near both ends of the profile. The linear scaling suggests the existence of the universal TFML velocity profile in the physical coordinate. Of course, this observation must be substantiated by further experiments in the higher Mach number. This observation also confirms the validity of linear scaling parameters used by the previous investigators of this type of flow.

Scaling of supersonic TFML is examined by many investigators, Korst and Tripp,$^{(15)}$ Alber,$^{(16)}$ Fernandez,$^{(22)}$ Roshko and

Thomke$^{(10)}$ and others, in an attempt to connect this parameter with physically measurable properties such as density ratio, Mach number, etc.

Previous investigators have shown that a reasonable dependence of the spreading rate of supersonic TFML on the density ratio across the layer was obtained, although the exact nature of the relation is not firmly established. Brown and Roshko$^{(20)}$ found in the experiment of heterogeneous gas (binary-incompressible) mixing that the spreading parameter, σ did not vary with ρ_1/ρ_2 as much as supersonic flow did with the same density ratio. They concluded that the observed variation in σ in supersonic flow must have come from the compressibility, mainly from non-negligible $\frac{\partial \overline{p}}{\partial y}$ and $\frac{\partial \overline{p'v'}}{\partial y}$. For the supersonic TFML, the spreading rate can be reasonably approximated (10% of actual spreading) with density ratio as shown in Appendix D.2.

V.2.1.4. Comparison of Supersonic TFML and Turbulent Wall Mixing Layer

Uniform injection of mass (X-distribution) into turbulent boundary layer (TBL) creates a flow pattern which deviates from the TBL profile. Supersonic experiments of this type have been carried out by Fernandez,$^{(22)}$ who found that a flow field similar to TFML type ($dp/dx = 0$) can be created when the uniform injection rate approaches $\lambda_e = .035$, the value comparable to the incompressible TFML case. Scaling of velocity profiles with Howarth-Dorodnitsyn transformation ($\overline{y} = \int \frac{\rho}{\rho_e} dy$) shows that the supersonic velocity profiles with various blowing rates were reduced in scale to match the respective subsonic velocity profiles of various blowing rates. $\lambda_e = 0.029$ data matched fairly well with Liepmann and Laufer's incompressible TFML data. It was concluded that the entrainment rate, $\lambda_e = (d\theta/dx)$, of the supersonic TFML is given also by $\lambda_e = 0.035$ and thus the growth rate of momentum thickness in the similar-flow TFML is independent of Mach number. (θ is invariant under Howarth-Dorodnitsyn transformation).

However, other investigators,(1-4, 9-11) of supersonic TFML found the Mach number dependence in the growth rate. Present experimental results have confirmed the entrainment dependence with Mach number of supersonic TFML. Since both experiments were done (i.e., Fernandez and the present) in the same two-dimensional supersonic tunnel, the conditions existing in both tests are identical, i.e., Mach number, upstream boundary layer, etc. Then, why are the two different results obtained as to the growth rate of supersonic TFML? We must note that Fernandez' experiments required mass injection into the turbulent boundary layer from the bottom wall to create the TML. Thus, this problem should be defined as "turbulent wall mixing layer (TWML)" or "forced mixing layer."

As discussed before, the growth rate of TFML is Mach number dependent and the velocity profile in the physical coordinate appears invariant except by the linear scaling of Y-coordinate. The flow is conical as predicted and the virtual origin can be determined by linear fitting of velocity profile distribution as observed.

However, TWML is Mach number independent and the scaling of profile conforms to the integral transformation of Howarth-Dorodnitsyn. Careful investigation of Fernandez' data revealed that TWML can be divided into two distinct regions, i.e., above and below the dividing streamline (η^*) which was determined by actual mass balance of injected air. The external flow field above η^* is almost invariant in velocity profile as the injection rates were varied (Y coordinate normalized with X_E of upper layer) as shown in Fig. V.14. It appears that the external pattern (supersonic portion) is identical to the similar TFML. The flow pattern below the η^* varies with the injection rates. The stretching of lateral coordinate below the dividing streamline by forced entrainment appears to be cancelled by the contraction of Y-coordinate by the H-D transformation. This behavior suggests the valid application of H-D transformation to the TWML flow.

Collins has also conducted a forced mixing layer flow experiment using the 20° ramp model of Fernandez. His data* taken with and without the downstream block are also shown in Fig. V.16 and compared with the present data. In order to achieve a straight mixing layer with zero pressure gradient, the injection rate of $\lambda_e = 0.0176$ is needed for a model with streamline block (SB). Without the streamline block, uniform pressure distribution cannot be achieved so that no truly similar flow exists. The data taken at $X = 2.00$ (middle of injection region) show qualitatively identical results as for TWML, except that the tail of velocity profile is stretched

---

* These unpublished data were made available by the courtesy of D. J. Collins of JPL.

with almost constant low velocity to the surface of the injection plate to accomodate for the forced entrainment. External profile above the breaking point is identical with the present TFML data. Integration of mass confirms that the difference in mass flow between TWML and TFML can be accounted for in the tail profile. Although the momentum gradient and entrainment rate cannot be balanced for the flow with pressure gradient, entrained mass must define the dividing streamline. Note that this flow with large injection rate of $\lambda_e = 0.0262$ also shows the modification of profile only below the sonic point.

So far no turbulent mixing layer with forced entrainment large enough to alter the flow pattern in the supersonic side of the velocity profile has been observed. It is uncertain at this moment that the dividing streamline always remains on or below the sonic point or if the profile of the supersonic side of the TFML will ever be altered appreciably.

V. 2. 1. 5. Investigation of Mach Number Dependence of TFML

Available experimental data were investigated in order to assess quantitatively the effect of Mach number dependence of two-dimensional TFML properties. The maximum shear stress and growth rate of momentum thickness decreases sharply with increasing Mach number as shown in Fig. V. 15. Dividing streamline Mach number and spreading rate parameter, σ_m, are also shown and the detailed discussion is given in Appendix D. 3.

V. 2. 2. Turbulent Field

In this section turbulent field of TFML is investigated. As will be seen in this section, the criteria for similarity of fully developed TFML becomes very stringent. It appears from the current investigation that at least the following three conditions must be met before the turbulent mixing layer (subsonic or supersonic) is declared as the fully developed asymptotic form: 1) Linear dependence of spreading rate with longitudinal distance, X, including the normalization of turbulent spectra; 2) Turbulent spectra of broad band character with no peak signal which implies the existence of no well-organized large scale wave-like motion; and 3) Constancy of total energy level independent of longitudinal distance.

Hot-wire measurements with thermo-couple (E_{tc}), turbulent spectra and auto-cross correlations were made and the results are discussed in the following subsections. Because of limited dimension of the test section, installation of X-wire was not possible and hence no $\overline{u'v'}$ and $\overline{\rho'v'}$ correlations were obtained. An attempt was made with a single slanted wire but alignment of two orientations of wire with flow field was uncertain and undesirable cross coupling of terms appeared, and this task was abandoned.

V.2.2.1. Turbulent Energy Profile (E_{tc})

Hot-wire fluctuation voltage processed through the built-in thermocouple of the Shapiro-Edwards Hot-Wire Anemometer represents the mean square voltage resulting from unknown combination of fluctuations in the compressible turbulent flow.

In order to deduce the different mode of flucutation components, a series of E_{tc} profiles with several overheat parameters was obtained. Typical profiles of low, medium and high overheats are shown in Fig. V.16. These profiles were obtained with the amplifier time constant (M_A) of compensator adjusted for the free stream condition ($M_t \cong 50$ μ sec) and held constant across a shear layer. Investigation of turbulent spectra in the middle to low velocity region revealed that the above technique introduces substantial error in the quantitative data reduction of TFML, which is associated with a large region of low velocity field. Nevertheless, this technique provides the information as to the qualitative changes taking place within the TFML. The bell shaped energy distribution with a peak appearing near the maximum mean mass flux gradient is observed with low current (overheat parameter is function of current) setting, i = 2.4 ma. Amplifier gain was increased to obtain more meaningful data in low signal region.

No qualitative change was observed on i = 4.0 ma. data, except the increase in amplitude. But with the highest current setting, i = 6.0 ma., the profile began to develop a noticeable change below the first peak. Since the wire with high overheat responds to the mass flux fluctuation, this development away from the region of maximum mean mass flux gradient corresponds to the increase in the contribution from velocity fluctuation. Also a plateau appears in the low-speed region, which was found later as the static temperature fluctuation. **Note** the 3 decibel change in gain represents approximately twice the amplitude scale of the previous setting. That means that the ratio of the peak amplitude of i = 6.0 ma. and i = 2.4 ma. settings is approximately 17:2.5.

Comparison of the resolved spectra of mass flux and total temperature fluctuation with two fluctuating voltage spectra are shown in Fig. V.17 to demonstrate the hot-wire response to the flow. Low overheat ($\Delta R/R_{aw} \sim 4\%$) spectra agree reasonably well to the total temperature fluctuation spectra. $\widetilde{e'^2}(f)$ is the fluctuating voltage normalized by the integrated quantity. When the wire current was increased to the level corresponding to $\Delta R/R_{aw} \sim 30\%$, the unresolved spectra matches better with the mass flux fluctuation spectra. With higher overheat better matching will be attained, but excessive overheating will weaken the wire in highly turbulent flow such that $\Delta R/R_{aw} \sim 25\%$ is the recommended limiting test condition in the high Mach number regime. $\Delta R/R_{aw} \geqslant 40\%$ has been attained in the low speed side of TFML without breaking the wire.

V. 2. 2. 2. Turbulent Spectra

Turbulent spectrum analyses in the turbulent free mixing layer were conducted in accordance with the methodology described in Sect. II. 2. 2. Quantitative data were obtained by the method described in Sect. IV. 2. Unsteady mass flux (see Appendix B. 5 for more precise definition of this quantity) and total temperature spectra were obtained by well-established curve fitting technique. The sensitivity coefficients of hot-wire response equation were assumed independent of the frequency and determined only by the mean flow field (see Appendix B. 4).

V. 2. 2. 2. 1. Unsteady Mass Flux Spectra

Unsteady mass flux spectra taken in several lateral stations of TFML are presented in Fig. V. 18. The abscissa and ordinate of spectra are the dimensionless frequency $f\theta/u_L$ and the normalized intensity $u_L \; g(f)/\theta \int_0^\infty g \, df$. Under these normalizations, the maximum amplitude occurs near $f\theta/u_L \sim 10^{-2}$. The data taken in the mid subsonic and supersonic domain of TFML appear to collapse reasonably into a single curve. Disagreement is noted in the low frequency component of spectra taken at $Y/\theta = 3.36$. Three more spectra taken below $Y/\theta = 5.25$ collapsed into reasonable agreement.

Since the major variation of mean mass flux occurs in the supersonic region of TFML, it is anticipated that the proper normalization parameter is a mass flux ratio instead of the velocity alone. Excellent agreement of spectra taken in the Mach number range of 1.99 to 0.66 under this normalization is shown in Fig. V.18b. The distribution of integrated quantities is given in Fig. V.25. Under the new normalization, the peak intensity occurs at $(f\theta/u_e)(\rho_e u_e/\rho u) \sim 2 \times 10^{-2}$ and the intensity is flat below this point.

V.2.2.2.2. Unsteady Total Temperature Spectra

Unsteady total temperature spectra normalized with momentum thickness and local mean velocity are shown in Fig. V.19. Spectra of all Mach number range collapse into a single curve within reasonable scatters. Since the variation of total temperature is practically nil (approximately ± 2%), within the TFML, it is anticipated that normalization with the convective field is a reasonable one. The spectra is much broader than the mass flux fluctuation and the peak intensity points have shifted to approximately $f\theta/u_L \sim 5 \times 10^{-2}$ and appear flat below that point. Very low-speed region shows further shift of peak value to $f\theta/u_L \sim 10^{-1}$, but in this region, the amplifier response of signal to noise ratio has deteriorated and also the low frequency domain was measured. The results are less accurate than the ones obtained in the intense turbulent region.

V. 2.2.2.3. Unsteady Streamwise Velocity Spectra

Unsteady streamwise velocity spectra normalized with θ/u_L are shown in Fig. V.20. Reasonable agreement among the data taken within the Mach number range from 1.99 to 0.66 is obtained. The peak intensity occurs near $f\theta/u_L \sim 2 \times 10^{-2}$ and appears to flatten out below this point. A relatively large portion of the spectra are distributed proportional to f^{-1}. Hinze(37) has shown for the incompressible shear layer with high mean vorticity distributions (i.e. $\partial u/\partial y$), the large velocity gradient not only serves as a constant source of turbulent energy, but it also interferes with the turbulence. Spectra of the frequency range in which the violent interaction occurs between two motions were shown to be distributed proportional to -1 power of frequency. From the observation, the foregoing argument also appears to be valid for the supersonic TFML. Spectral distribution of the small scale eddies is proportional to -5/3 power.

V. 2. 2. 2. 4. Unsteady Static Temperature Spectra

Unsteady static temperature spectra normalized with θ/u_L do not fall into a single curve, which implies that this is not a proper parameter for normalizing the unsteady temperature field. Data are shown in Fig. V. 21a. The spectra collapses to a single curve, as shown in Fig. V.21b, if the parameter is normalized with the local mean temperature field $\left(\text{i.e.,}\ \frac{\overline{T'^2}}{\int \overline{T'^2}\, df}\ \frac{u_e}{\theta}\ \frac{T}{T_e}\ \text{vs.}\ \frac{f\theta}{u_e}\ \frac{T_e}{T}\right)$.

The peak intensity appears to occur at new non-dimensional frequency of 10^{-2} and is flat below this point.

V. 2. 2. 2. 5. Comparison of Turbulent Spectra

Direct comparison of spectra of mass-flux, total temperature, streamwise velocity and static temperature fluctuation fields appear to show each has its independent turbulent structure. For example, recall the unsteady mass flux and total temperature spectra taken at X = 4.75, Y = 0.0 shown in Fig. V.17. Since θ/u_L is constant for a given position in the TFML, this figure shows the direct comparison of two fluctuation quantities in the frequency domain. Intensity of mass flux fluctuation is greater than the unsteady total temperature. However, the spectra of the latter is much broader than the former, implying that more energy is distributed in a higher frequency domain and has a slower decaying structure. The energy level of the former is concentrated in a low frequency domain and is followed with a rapid decay of energy field in high frequency components. Similar trend is observed in the streamwise velocity and the static temperature fluctuation spectra. At a first glance, these spectra indicate no resemblance to each other.

However, the investigation of Sect. V.2.2.2.1 to V.2.2.2.4 has revealed that the proper normalization parameters of the turbulent spectra are the respective mean flow quantities. Under these normalization parameters, very interesting and perhaps most useful facts of supersonic TFML were found. Spectra of all fluctuating quantities (i.e., Fig. V.18b, V.20 and V.21b) collapse into a single curve when they are overlaid on top of each other. The differences among these curves are indistinguishable within the data scatters and show very good correlation to each other, at least in the region where local Mach number is mid subsonic to supersonic (Fig. V.22a).

Total temperature fluctuation spectra, however, does not fall into this category of data because the mean quantity is practically constant across the TFML and independent of shear flow distribution. Therefore, the fact that this spectra does not comply with the above rule is understandable. However, the nature of the log-log plot is that it does not alter the shape of the spectra if the change in its magnitude is dependent only on the multiplicative constant. The adjustment of the coordinate to compare the qualitative nature of the spectra is possible. Overlap of Fig. V.19 onto Fig. V.22a also shows the excellent agreement of the qualitative shape of the spectra. This finding is important because the spectra of the entire supersonic TFML (or at least the spectra in the mid subsonic to supersonic region of TFML) can be found by knowledge of the mean flow profile and at least one of the spectra measurement at any one point in the TFML. Because the hot-wire operating with high overheat parameter ($\Delta R/R_{aw} \sim 40\%$) of constant current hot-wire anemometer responds to unsteady mass flow, then the measurement of this fluctuating spectra can supply the necessary information without the quantitative data reduction.

Turbulence spectra of subsonic (incompressible), two-dimensional, self-preserving turbulent mixing layer of two stream flow have been reported by Spencer and Jones(38) and Yule.(39) Spectra from both investigators show the qualitative agreement including the slight overshoot at peak intensity point and flat distribution below the frequency where the peak intensity occurs.

The present investigation of supersonic TFML may show some overshoot of spectra, but they are not as pronounced as the subsonic ones and data scatter does not warrant the same conclusion to be drawn. The abscissa of the velocity fluctuation spectra is renormalized with the width (b) of the mixing layer determined by the slope intercept method suggested by Batt, et al.(40) The new scale is shown below Fig. V. 22a. The incompressible spectra of Batt, et al falls into the present data when the ordinate is properly normalized to the common scale. Excellent agreement of the low frequency range of spectra is observed and the falloff point begins at the Strouhal number of unity ($2\pi fb/u_L = 1.0$). The f^{-1} range of supersonic spectra is larger than the incompressible one. The high frequency components of incompressible data fall off with -2 power, whereas the spectra of the present investigation decreases with -5/3 power.

Further investigation of the present experiment leads one to suspect that the pronounced spectra peak observed in the faster stream side of the subsonic TML might be caused by the flow disturbance fed in from the upstream boundary layer or transitional mixing layer. The quantitatively reduced spectra of streamwise velocity, static temperature and mass flux fluctuation obtained by the operation condition II ($p_o = 610$ mm Hg, $R_{e_\theta} \sim 2000$, F-T-F) show a peculiar peak. This peak becomes less pronounced as the low speed side of TFML is surveyed. This spectrum plotted in the log-log scale shows the qualitative characteristic observed in the subsonic velocity spectrum (see Fig. V. 22b). Furthermore, this anomalous peak vanishes as higher operating Reynolds number or coarse boundary layer trip is used. The disturbance may be Reynolds number dependent, except that this phenomenon does not appear to be the inherent characteristic of fully developed turbulent mixing layer. Therefore, the results of the current investigation reveal that the turbulent spectrum of the entire TFML is similar and without the pronounced peak, not as shown by other investigators. This implies that the structure of fully developed TFML consists of a randomly fluctuating and disorganized field with no large scale wave motion in a preferred frequency range. However, Brown and Roshko$^{(20)}$ have shown the existence of such motion visually in the subsonic binary mixing layer experiment to disprove the extension of the foregoing argument to the incompressible mixing layer. Batt, et al$^{(40)}$ have shown the vanishing trend of the overshoot of spectra with the increasing operating velocity of two-dimensional TFML in subsonic flow. Because of the poor resolution of the existing spark Schlieren ($\Delta t \sim 2\mu$ sec. produces flow motion of approximately .04 in.) and the existence of low density flow below the dividing streamline, the flow is visible only in the supersonic side of TFML. However, it is expected that the presence of large scale motion should be visually detected, if it is present. Unfortunately, no organized motion was visually observed with the present experiment.

V.2.2.3. Self Similarity

Self similarity of supersonic TFML in turbulence level was checked by conducting the turbulent spectra surveys at X = 3.75, 4.75 and 6.75 along the two constant u/u_e lines ($u/u_e \sim 0.91$ and 0.58) with the operating condition I. Frequency and spectra intensity are normalized by respective integrated quantities and u_L/θ such that $\int_0^\infty F\, d(\frac{f\theta}{u_L}) = 1$ as before. Since the surveys were made along the constant u/u_e, the independent variable is the momentum thickness, θ, which is a linear function of X_E measured from the virtual origin of TFML.

The spectra of mass flux, total temperature and their correlation coefficients; the spectra of streamwise velocity, static temperature and their correlation coefficients for the constant u/u_e taken along the vicinity of the dividing streamline are given in Fig. V.23a to V.23f. Reasonable agreement of data from widely separated longitudinal stations ($X/\theta_o \sim 375, 475, 675$) are encouraging. If the turbulent field of TFML has reached a similar flow condition, it is expected the integral scale of turbulence is also a linear function of longitudinal distance. Then one can conclude that the integral scale, L_x, is proportional to the momentum thickness of TFML. In fact, the behavior of spectra collapsing to a single curve with respect to the normalizing parameter, θ, supports the foregoing argument that the growth of the turbulent field is linear with X_E.

Data of correlation coefficients, $R_{\overline{\dot{m}'T_o'}}$ and $R_{\overline{u'T'}}$, are more widely scattered than the other spectral distributions, but nevertheless, the qualitative behavior of these quantities are well matched. $R_{\overline{\dot{m}'T_o'}}$ obtained at the $u/u_e \sim 0.91$ of TFML (Fig. V.23d) shows the moderate correlation of the large scale components of mass-flux and total temperature but small scale components ($f\theta/u_L \gtrsim 10^{-1}$) appear to be uncorrelated or slightly anti-correlated. $R_{\overline{u'T'}}$ (Fig. V.23e) shows a trend completely reversed from the trend of $R_{\overline{\dot{m}'T'}}$, i.e., the energy carrying low frequency components are highly anti-correlated but high frequency components are correlated. Correlation of high frequency components of u' and T' suggests that the transformation of kinetic energy to heat takes place by the small scale eddies. The hypothesis that small scale eddies are responsible for the final decay of turbulence and the production of heat is qualitatively observed. Anticorrelation of u' and T' in low frequency components means the positive correlation of ρ' and u' of large scale eddies. $R_{\overline{\dot{m}'T'_o}}$ measurements taken at the center of TFML ($u/u_e \sim .58$) show the direct correlation with constant value throughout the frequency domain. $R_{\overline{u'T'}}$, however, follows exactly the same trend of the former position (Fig. V.23c and f).

It appears that so far every requirement of self-similarity has been met. However, a single uncertainty which seemed to negate the self similar criteria crept up such that it cast a shadow of doubt as to the existence of truly fully developed TFML even in this experiment. The uncertainty was that the total fluctuation energy level measured in the TFML kept increasing with the longitudinal distance. However, the observed discrepancy was found to be produced by the instrumentation response and the corrected value showed the constant turbulence intensity (see Appendix D.4).

This finding is very encouraging because all necessary and sufficient conditions for the existence of fully developed TFML have been met by the present investigation. Asymptotic form of turbulent mixing layer requires a considerably long developing distance. In the case with fully developed turbulent mixing layer without any upstream disturbances, the similar TFML appears to be developed in $400\ \theta_o$ downstream of the step. However, a much greater distance is required with some upstream disturbances and laminar boundary layer for the starting condition.

V.2.2.4. Turbulent Intensities

V.2.2.4.1. Fluctuation Mode Diagram

Quantitative data of turbulent flow properties in the core of TFML have been reduced by the application of the method described in Sect. IV. Typical mode diagrams of fluctuations taken under the operating condition I are shown in Fig. V.24. The mode diagrams have been constructed by least square curve fitting of the data compiled from several tests to the equation of hyperbola. Data points include the properly corrected E_{tc} data and integrated data of spectral density distributions.

Scattering of data is inevitable in this type of experiment, thus the confidence level of the computed data is reduced when it is compared with the mean flow measurements. However, ensemble of many data points establishes a certain trend of physical measurements associated with the flow field of realizable turbulence. Recall that the linearity of fluctuation mode diagrams has been observed in measurements of freestream turbulence (Fig. C.5). In the core of TFML, vorticity and temperature fluctuation are believed to dominate and it is expected that the curve is no longer linear and correlation of the mass flux and total temperature fluctuation ($R_{\overline{\dot{m}'T_o'}}$) will no longer remain at -1.0. Kistler(30) has observed that $R_{\overline{\dot{m}'T_o'}}$ will shift from high negative (~ -1.0) to positive correlation as supersonic turbulent boundary layer is traversed from the outer edge. In fact, the appearance of vertex of hyperbola in the region of positive overheat parameter ($r = S_u/S_{T_o}$) indicates the shifting of the correlation as one moves from the high speed outer flow to the low speed inner core of the TFML.

V.2.2.4.2. Mass Flux Fluctuation

The mass flux fluctuation profile of supersonic TFML is shown in Fig. V.25a. The solid lines represent the E_{tc} measurement taken with a time constant of the compensating amplifier set at the value correct in the freestream ($M_A = 50\ \mu$ sec). The dashed lines represent the measurements taken with the matched time constants of the local flow field (see Appendix D-5 for the mismatched error). Individually plotted data points represent the results reduced from the integrated spectral measurements. Points shown as large circles or large triangles represent the averaged value of all available data as shown in the typical fluctuation mode diagram. Reasonable agreement with data points and dashed lines is encouraging.

Mean mass flux distribution is also shown in the same figure. Since most of the mass flux change is taking place in the supersonic flow regime above the dividing streamline, the peaks appearing in that side of the flow are expected. The peak fluctuation appears near $Y/\theta = 2.0$ and occurs just below the maximum gradient of the mean mass flux distribution. The peak fluctuation level is somewhere between 8 and 10% of the mean value.

V.2.2.4.3. Total Temperature Fluctuation

Total temperature fluctuation distribution is shown in Fig. V.25b. Note that the solid and dashed lines are very close as expected from the previous discussion. A peak fluctuation level of 6% of the mean total temperature exists near the point where maximum gradient of mean total temperature occurred (i.e., switching point of total temperature).

V.2.2.4.4. Streamwise Velocity Fluctuation

Streamwise velocity fluctuation in the core of TFML has been computed and is shown in Fig. V.25c. Negligible pressure fluctuation is assumed as discussed in the data reduction section. The discrepancies between solid and dashed lines reappear for the reason given in the mass flux fluctuation section. Integrated power spectra and dashed line curve show reasonable agreement. In the core of the mixing layer, the transformation equations of $\overline{u'^2}$ and $\overline{T'^2}$ based on $\overline{\dot{m}'^2}$ and $\overline{T_o'^2}$ are shown as (see Appendix B.6)

$$\begin{pmatrix} \overline{u'^2} \\ \overline{T'^2} \\ \overline{u'T'} \end{pmatrix} = \frac{1}{(\alpha+k_S\beta)^2} \begin{bmatrix} \alpha^2 & k_S^2 & 2k_S\alpha \\ \beta^2 & 1 & -2\beta \\ -\alpha\beta & k_S & (\alpha-k_S\beta) \end{bmatrix} \begin{pmatrix} \overline{\dot{m}'^2} \\ \overline{T_o'^2} \\ \overline{\dot{m}'T_o'} \end{pmatrix} \qquad (V.9)$$

where the correlation coefficients are defined as

$$R_{\overline{\dot{m}'T_o'}} = \frac{\overline{\dot{m}'T_o'}}{\sqrt{\overline{\dot{m}'^2}}\sqrt{\overline{T_o'^2}}} \quad \text{and} \quad R_{\overline{u'T'}} = \frac{\overline{u'T'}}{\sqrt{\overline{u'^2}}\,\sqrt{\overline{T'^2}}}$$

Note that the velocity fluctuation is affected substantially by total temperature fluctuation in supersonic region where k_S is near unity. In the slow speed region mass flux contribution is seen to predominate. Peak streamwise velocity fluctuation based on local mean value $(\sqrt{\overline{u'^2}}/u_L)$ is approximately 8 ~ 9% and occurs just above the dividing streamline. Absolute maximum fluctuation of approximately 5 to 6% of freestream velocity, $(\sqrt{\overline{u'^2}}/u_e)$ occurs near $Y/\theta \cong 1.5$.

The similar measurements of incompressible, two-stream mixing layer of air made by Spencer and Jones(38) show a peak

$\sqrt{\overline{u'^2}}/\Delta U$ of 18 ~ 20% and peaks near zero streamline. In their experiment ΔU is the velocity difference of two streams, and as U_2 approaches 0, the above definition becomes precisely the same as $\sqrt{\overline{u'^2}}/u_e$ of the present experiment. Subsonic data of Wygnanski and Fiedler(42) indicate peak fluctuations of 17.5%. Results of Liepmann and Laufer(19) of incompressible TFML also show substantially higher fluctuation intensities ($\sqrt{\overline{u'^2}}/u_e \sim 16\%$). The basic qualitative difference between subsonic and supersonic flow is also noted. Since Liepmann and Laufer's data have been plotted with respect to Y/θ, matching of their coordinate and the present one will be accomplished by matching the mean velocity profile. Comparison of the two data are shown in Fig. V.26a. Note that the data taken in the supersonic flow shows the bell shape profile with respect to $Y/\theta = 0$, but subsonic data peaks at the lower speed side if the fluctuation quantity was normalized with the local velocity. If the fluctuation velocity field is normalized with respect to the freestream velocity, both curves become bell shaped, except for the shift in the point of peak values (Fig. V.26b).

Based on this comparison, the intensity of RMS velocity fluctuation of supersonic TFML is approximately 1/3 of subsonic TFML. This finding may be the partial explanation for the reduction of the TFML growth rate. It is expected that general relationahip between the remaining fluctuation velocity components in the supersonic TFML should not be greatly different from that observed in the subsonic TFML. Then it is safe to conclude that the relative kinetic energy of velocity fluctuation is also considerably lower. One must be cautioned that assumption of $\overline{p'^2} << \overline{u'^2}$ and $\overline{T'2}$ may become invalid in both edges of TFML where the magnitudes of $\overline{u'^2}$ and $\overline{T'^2}$ become small. However, fluctuation intensity in the core of TFML is expected to be accurate within ± 15%.

V.2.2.4.5. Static Temperature Fluctuation

By inspection of the transformation equation, static temperature fluctuation is seen to be highly dependent on the total temperature fluctuation. Contribution from the mass flux fluctuation is strongly felt in the supersonic region (β^2 dependence) and negligible in the subsonic side. The static temperature fluctuation is found to be considerably higher than expected as shown in Fig. V.25d. The peak temperature fluctuation of approximately 8.5% based on local static temperature, $\sqrt{\overline{T'^2}}/T_L$, is noted in the region of maximum temperature gradient. Note that the second plateau which was observed in the E_{tc} profile below $Y/\theta \cong -4.0$ (Fig. V.16) with high overheat is observed in the temperature fluctuation. The observed phenomenon may be produced by the interaction of two fluids with slightly mismatched temperature or from the possibility of Prandtl number not equal to one ($Pr \neq 1$).

The stagnation temperatures of primary flow and injected air have been monitored by iron-constantan thermocouples and found to be within 2° F. However, the Brown potentiometer pyrometer (Model #156 X 15p) is rated for an accuracy of ± 4° F. Since the mean static temperature was reduced from the Pitot pressure data with an assumption of constant static pressure across the TFML, the mean temperature of a few percent mismatch will not be detected. However, total temperature profile taken with the operating condition I shows slight data anomaly in the low speed region where entrainment of injected air occurs (see Fig. V.12). Under the assumption of negligible pressure fluctuations, the temperature fluctuation is precisely a negative of density fluctuation ($\frac{T'}{T} = -\frac{\rho'}{\rho}$), but RMS fluctuations of density and temperature are the same ($\sqrt{\overline{T'^2}}/T = \sqrt{\overline{\rho'^2}}/\rho$).

V.2.2.4.6. Correlation Coefficients $R_{\overline{\dot{m}'T_o'}}$ and $R_{\overline{u'T'}}$

The correlation coefficient of mass-flux and total-temperature fluctuations is initially highly anti-correlated (i.e., $R_{\overline{\dot{m}'T_o'}} < -0.7$ in the freestream edge of TFML). There is a trend approaching to zero correlation as the dividing streamline is approached and becoming positive as the streamline is crossed (Fig. V.27). Kistler(30) observed a similar phenomenon in supersonic turbulent boundary layer. Although a considerable scattering of data is observed, the general trend indicates that the switching point may coincide with that for the mean total temperature distribution.

The correlation coefficient of streamwise velocity and static temperature ($R_{\overline{u'T'}}$) almost follows the trend of $R_{\overline{\dot{m}'T_o'}}$. Observation of the transformation equation shows that $R_{\overline{u'T'}}$ takes the sign of $R_{\overline{\dot{m}'T_o'}}$ where $\alpha - \beta k_s$ becomes positive (if $k_s = 1$, $M \leq 1.58$) and the negative contribution from the mass flux fluctuation becomes negligible as Mach number decreases (i.e., β approaches zero). In the turbulent boundary layer survey made by Kistler, $R_{\overline{u'T'}}$ remained anticorrelated throughout the layer. This is possible because the local mean flow remains supersonic in case β does not become small and the negative contribution from mass flux fluctuation offsets the contribution from $R_{\overline{\dot{m}'T_o'}}$ even if it becomes positive.

V.2.2.5. Autocorrelation and Space-Time Crosscorrelation in TFML

Qualitative analysis of autocorrelation and crosscorrelation made in the TFML will be presented herein. The measurements are taken in accordance with the methodology described in Sect. II.2.2. Initial investigations were conducted with the operating condition II and the qualitative results were verified later under the operating condition I. Autocorrelation measurements were taken in several lateral positions in TFML at X = 6.75. In order to check the self-similarity of the turbulent scale, the measurements were also taken at longitudinal stations along the line where maximum fluctuation signals were detected (Y = 0.12). To establish a meaningful trend of data with variation of longitudinal or lateral stations, most of the comparison investigations were conducted the same day with the same probe when possible in order to avoid introducing the additional uncertainties in the measurements (i.e., variation in the operating condition, probe sensitivity, etc.).

V.2.2.5.1. Autocorrelation

Unresolved autocorrelations at three overheat parameters ($\Delta R/R_{aw} \sim 25\%$, 15%, 2%) are shown in Fig. V.28a. The ordinate has been normalized with respect to the value of autocorrelation measurements taken with zero delay time ($A_{11}(0)$). The delay time has been normalized with respect to the effective longitudinal stations measured from the virtual origin of TFML. Since the TFML grows linearly from the virtual origin, this normalization is proportional to the normalization with respect to the local width (b) of the TFML. Non-dimensionalized delay time is obtained by an introduction of free-stream velocity ($\Delta\tau\, u_e/X_E$). Data at five stations extending from X = 3.75 to X = 7.75 collapsed into reasonably good single curves for each respective overheat parameter. This implies that the turbulent structures of TFML of the present investigation have reached the self-similar flow. The decay of the correlation functions with increasing delay time is markedly different with different overheat parameter. Although this observation implies that the separation of fluctuation into different modes is desirable to delineate the structure of the turbulent field, qualitative conclusions can be drawn from these unresolved autocorrelation functions by an application of the knowledge gained from the study of turbulent spectra.

Recall that a hot-wire operating at low overheat responds to the total temperature fluctuation and a hot-wire operating with very high overheat parameter ($\Delta R/R_{aw} \sim 40\%$) responds to mass flux fluctuation. The data of the lowest overheat show the fastest decay and the general trend is slower decay of autocorrelation functions with increasing overheat. Thus it is safe to say that the coherence time of total temperature fluctuation is shorter than the one of mass fluctuation. In fact, this trend reaffirms the findings from the spectra measurements. The mathematical relation between autocorrelation function and power spectrum is a pair of Fourier transforms

$$F_{11}(\omega) = \frac{1}{2\pi}\int_{-\infty}^{\infty} A_{11}(\tau)\cos\omega\tau\, d\tau \text{ and } A_{11}(\tau) = \int_{-\infty}^{\infty} F_{11}(\omega)\cos\omega\tau\, d\omega \qquad (V.10)$$

where $F_{11}(\omega)$ is the power spectrum, $A_{11}(\tau) = \lim_{T\to\infty} \frac{1}{2T} \int_{-T}^{T} f_1(t)f_1(t-\tau)dt$ is an autocorrelation function and ω is angular frequency. The larger coherence time implies that the scale of the fluctuating field is larger and it takes more time to pass through the point of measurements. In spectral evaluation, this implies that the peak amplitude shifts to a lower frequency as the turbulent field of larger extent exists. That is, the energy containing frequency is inversely proportional to the correlation time. Observation of measured data confirms the above argument. For example, the autocorrelation measurements taken at three lateral stations are shown in Fig. 28b. The most rapid decay of autocorrelation function is noted in the data taken at $Y/\theta = 3.3$ where the maximum turbulence signal was detected and power spectra extended to 300 KHz. The qualitative trend of slower decay with decrease in Y/θ was observed. The slowest decay was noted at $Y/\theta = -1.82$ where the low frequency turbulent components predominate.

V.2.2.5.2. Crosscorrelation with Longitudinal (X) Displacement

Crosscorrelation functions of axial components of flow are made by two hot-wire probes placed in tandem along the constant u/u_e field. Since the growth rate of TFML is linear and the flow properties are equivalent along rays from the virtual origin (conical flow), the moving probe must be shifted in Y-axis as well as in X-axis to remain along the constant velocity field. This was assured by maintaining the mean voltage output of moving hot-wire at a constant level.(31) Because the hot-wire sensitivity is dependent upon the mean flow field (Mach number, Reynolds number, Nusselt number), the constancy of mean voltage output of hot-wire means constant flow field. In order to avoid the wake interference of each other, probes were installed so that leesides of the probes faced each other. Also, the moving probe (M-probe) was initially displaced in the Y-direction by approximately 0.01 inch to avoid probe contact produced by occasional vibration. The stationary probe (S-probe) was positioned at X = 4.75 for operating condition II and at X = 6.75 for operating condition I and the M-probe was traversed fore and aft of the S-probe.

The definition of convection velocity adopted by Wills(44) and Wilmarth(45) is given as $u_c = \partial x/\partial \tau$ at the point where $(\partial R/\partial x)_{\tau = \text{const.}} = 0$. This point can be determined by finding the tangency of cross-correlation function and the contour of the envelope. Typical space-time correlation taken at $Y/\theta = 3.3$ is shown in the lower part of Fig. V.29. Normally, the mapping of space-time crosscorrelation of this figure is sufficient to determine the convection velocity. The spatial correlation is determined by plotting the crosscorrelation function at zero time-delay with respect to the longitudinal separation distance. The discrepancy of peak amplitude noted at the zero Δx separation is attributed to the initial Δy separation required to avoid the probe interference (Fig. V.29).

The contour map of space-time correlation is shown in Fig. V.30. This contour map is produced from Fig. V.29 by plotting constant correlation contour in the Δx-τ plane. Fitting a curve through points where the least change in correlation occurs with respect to Δx gives the $u_c/u_e \cong 0.795$. The most uncertain part of the present investigation lies in the accurate determination of the initial separation, thus it is unwise to force the curve to go through the origin. The relative separation from any known point is accurate to 0.002 inch, and hence confidence level outside of the initial point is rather high.

The convection velocities within the entire lateral profile of TFML have been obtained by the method of Fig. V.29 (tangency). The results compared with the mean velocity are shown in Fig. V.31a. It appears that the convection velocity of the energy carrying turbulent field lags behind the mean flow velocity in the supersonic region and leads it in the subsonic region. Within the experimental scatter, the convection velocity determined by the operating conditions I and II have produced almost identical results. The subsonic data obtained by Wills(44) in axisymmetric jet mixing layer are also shown and agree approximately with the present results. Bradshaw(41) obtained the same results as Wills. Subsonic 2-D mixing layer results obtained by Wygnanski and Fiedler(42) show consistently lower convection velocity throughout the TFML.

Convection velocities of selected frequency components of turbulence at $u/u_e \cong .90$ (maximum turbulence signal), $u/u_e \cong .61$ (near the dividing streamline) and $u/u_e \sim .25$ are obtained by application of two Hewlett-Packard wave analyzers and the results are presented in Fig. V.31b. At point A ($u/u_e \cong .90$), the convection velocities of large scale turbulence are found lower and monotonically increasing with frequency. The mean convection velocity at this lateral position is approximately 0.80 u_e, indicating that the energy carrying turbulent components are concentrated near the frequency domain of 25K to 100 KHz. The unresolved power spectrum in this frequency domain appears to be proportional to f^{-1}. At point B ($u/u_e \cong .61$), all frequency components of turbulence are convecting with uniform speed. Convection velocities of the turbulence components below the dividing streamline decrease with frequency. Note that large scale turbulence of TFML appears to be convecting with relatively constant speed across the layer. This observation suggests that the small scale turbulence adjusts to the local environment faster than the large scale eddies, and it supports the following interpretation of TFML.

The present and Wills' results indicate that the switching point of the relative velocity occurs very close to the dividing streamline of TFML. In fact, this result suggests that the turbulence is created in the vicinity of the dividing streamline by maximum shear stress and maximum velocity gradient. Recall that the production rate, $\tau \frac{\partial u}{\partial y}$, determined from the mean flow values maximized at $u/u_e \cong 0.55 \sim 0.60$ (Fig. V.10), which also supports the foregoing argument. Since the outer flow is moving at a higher speed, entrainment of faster flow accelerates the newly created turbulence field as it grows, but every frequency component of turbulence does not fully attain the local velocity for the reason given in the foregoing paragraph. Below the dividing streamline, newly created turbulence imparts its momentum and drags along the originally stationary fluid. Thus, it is expected that the turbulent field will propagate faster than the mean fluid. Additional supporting evidence of the foregoing argument is given in Appendix D.6.

Space-time crosscorrelation measurements were made with an intermediate overheat so that the hot-wire sensed the coupled fluctuations. Then a question was raised as to what mode of fluctuation quantity propagates with the measured convection velocity. To investigate this, space-time crosscorrelation measurements at several overheats were made at a given separation distance. Within the accuracy of measurements, no appreciable shift in time delay was noted for all overheat ranges, which implied all fluctuating quantities were propagating in one blob.

V. 2. 2. 5. 3. Comparison of Autocorrelation and Crosscorrelation Function

The condition which must be satisfied to justify the Taylor's hypothesis(46) is that transformation of autocorrelation function into space-correlation and vice versa by means of convection velocity, such as $u_c = \Delta x / \Delta \tau$, is valid (see Appendix D. 7).

Comparison of autocorrelation and space correlation functions taken at two lateral stations along $u_L / u_e = 0.90$ and 0.59 are shown in Fig. V. 32. Separation distance of the space correlation function was transformed to time delay by the local convection velocity. Although the Taylor's hypothesis is expected to fail in the turbulent mixing layer flow because it is non-homogeneous, (Wygnanski-Fiedler(42)), agreements between both correlation functions were surprisingly good. Noted discrepancies near the zero Δx separation were produced by an initial Δy separation of two probes. The apparent validity of Taylor's hypothesis in the present investigation was attributed to 1) existence of small fluctuating velocity field ($\sqrt{\overline{u'^2}} / u_L < 10\%$, Sect. V. 2. 2. 4);

and 2) convection of quasi-frozen turbulent pattern (see Sect. V.2.2.5.6). Usefulness of Taylor's hypothesis was that the axial spatial correlation measurements could be simplified by the autocorrelation measurements, using modern equipment, in the TFML where small scale turbulence exists. Since the direct measurements of space correlation required unavoidable Δy separation, the accuracy of the data in the initial separation was greatly improved by autocorrelation measurements. Within tolerable data scatter, sufficient proof was presented to validate Taylor's hypothesis even in the free shear flow.

V.2.2.5.4. Crosscorrelation with Lateral (Δy) Displacement

The lateral scale of turbulence can be determined by the crosscorrelation measurements of streamwise flow components taken with lateral displacement. The difficulty encountered in this type of measurement was that the sensitivity of wire response with a constant current setting varied as different lateral positions of the flow field were surveyed. Corrections were made in data reduction (see Sect. IV.3).

The foregoing measurements were made with operating condition I at X = 6.75. The M-probe was traversed above and below the S-probe positioned at $Y/\theta = 3.6$ and $Y/\theta = 0.64$. The typical correlograms plotted with peak correlation as a common reference point are shown in Fig. V.33a. The S-probe has always been delayed and hence the measurements in both directions were referenced with respect to the S-probe. The measurements showed that the relative position of the turbulent field in the fast stream side leads and the slow stream side lags with respect to the reference point in the flow, which conforms with the previous observation (see Appendix D.8).

Considering the X-station in which the S-probe is positioned as a reference plane, the lead or the lag time of the maximum correlation of the streamwise component measured with respect to the lateral separation represents the relative position of the convecting turbulence field (Δy vs. Δx). The arrival time of the maximum correlation normalized with an effective X-distance and a convection velocity of the reference point is shown in Fig. V.33b. The normalized negative delayed time can be considered as the downstream Δx position ($\Delta x/X_E = -\Delta\tau\, u_c/X_E$). It must be cautioned that the Δy vs. $\Delta\tau$ does not represent the lateral component of velocity (i.e., $v_c \neq \Delta y/\Delta\tau$).

The lateral spatial correlation of unresolved turbulence taken above and below the reference points are shown in Fig. V.34. The peaks of autocorrelation functions at different lateral positions of mixing layer and the corrected spatial correlation of corresponding points are also shown. The correlation functions above and below $Y/\theta = 3.6$ appear to be symmetric and uncorrelated in the normalized lateral dimension of 0.02 ($\Delta Y/X_E \cong 0.02$). Asymmetric correlation functions are noted in the data taken at $Y/\theta = 0.64$. The difference may be attributed to the unmatched time constant of wire as it traversed into the TFML where low frequency contributions became large. Comparison of the correlation functions of operating conditions I and II shows the latter case has a slightly broader decaying trend which may be due to the presence of large scale motion (Fig. 34a).

V. 2. 2. 5. 5. Crosscorrelation with Spanwise (ΔZ) Displacement

Similarly, crosscorrelation in spanwise displacement was obtained with S-probe stationed at the centerline of the tunnel at X=6.75, $Y/\theta = 3.2$. Two wires were arranged in vertical position normal to stream so that initial ΔZ separation could be set as small as possible.

Unresolved space-time correlation and normalized space correlation taken at zero time delay are presented in Fig. V. 35. The delay-time at the peak correlation function did not shift with ΔZ, as shown in the figure, implying that the turbulent flow field is perfectly two-dimensional. Additional confirmation of two-dimensionality was observed in the distribution of correlogram, i. e., the crosscorrelation functions of the spanwise separations were enveloped within the skirt of autocorrelation function and very little distortion of the flow pattern is observed. Additional correlograms were taken with fore and aft separations ($\Delta x = \pm 0.15$ inch) of the center probe with respect to the spanwise swept probe and the delayed and advanced time corresponding to the peak correlations remain constant within the experimental scatter. Once again the space-correlation function obtained with the operating condition II shows the slower decay indicating the existence of larger scale motion. Two-dimensionality is expected, because no mean flow gradient should exist in the spanwise direction.

V. 2. 2. 5. 6. Moving Frame Correlations

The moving frame autocorrelation function characterizes the evolution of turbulence as convected in the streamwise direction. The slow decay of the moving frame autocorrelation with increasing time delay implies a slowly changing pattern of turbulence as it moves downstream and hence the assumption of a frozen pattern passing at a stationary point becomes nearly correct. This function can be constructed by forming an envelope of space-time correlation functions as observed in Fig. V.29. The decay of the moving frame correlation indicates that the turbulence pattern is not frozen in the mixing layer. However, the ratio of integral time scales between the moving frame and a single point autocorrelation is large ($\mathcal{J}_{mf}/\mathcal{J}_{sp} \cong 10$). Hence the convection of quasi-frozen pattern is a reasonable assumption, and reflects the validity of Taylor's hypothesis.

The integral length scale in the moving frame is determined from a moving frame spatial correlation. This function is constructed by forming an envelope of space-time correlation functions plotted against Δx at constant $\Delta\tau$. The moving-frame spatial correlation functions are shown in Fig. V.36 along with the fixed-frame functions taken at $Y/\theta = 3.3$ (near the maximum fluctuation signal) and $Y/\theta = 0.28$ (near the dividing streamline). Slight anomalies near the small Δx separation are probably caused by the interaction of shock emanating from the forward probe. This phenomenon was also observed by Demetriades.$^{(47)}$ The moving frame integral scale is larger at $Y/\theta = 3.3$ than the value taken at $Y/\theta = 0.28$. Considering the relative change in the wire sensitivity at different points within the mixing layer, it appears that uniform evolution of turbulence exists across the mixing layer. However, a definitive conclusion cannot be drawn from the present investigation. Comparison of the integral scales between the stationary and moving frame correlations are also shown in the same figure. The method described by Demetriades$^{(47)}$ and actual integration of correlations between $0.1 \leq R_o(\Delta x) \leq 1.0$ show almost identical results. The ratios of moving frame to stationary integral scale (L_o/L_s) vary from 5.1 to 8.0 indicating the relatively slow growth of turbulence and support the quasi-frozen turbulent spot assumptions.

Incidentally, the integral scales determined from the correlation function and from the power spectral density distribution agree within 20% of each other.

V. 2. 2. 5. 7. Integral Scale Comparison

Relative scales of streamwise components of turbulent field in three axes can be observed in Fig. V. 37. Integral scale of space-correlation defines the dimension of large scale eddies. Within the experimental data scatter, the longitudinal and lateral scales of turbulence appear to be identical ($L_x \cong .0056\ X_E$, $L_y \cong .0051\ X_E$). This may imply that the scale of turbulence structure is proportional to the width of the mixing layer. The spanwise scale is larger than the other scales ($L_Z \cong .0094\ X_E$).

V. 2. 3. Intermittency Factor (γ)

Intermittency factors across the turbulent mixing layer were obtained by passing a hot-wire signal through a Philco-Ford Intermittency meter. In order to detect a large scale motion, band-passed turbulent signals of 100 Hz to 40 KHz were surveyed. The triggering level of the signal was set so the peak value of γ within a shear layer was near unity. One difficulty encountered here was the variation of hot-wire sensitivity across the layer for a given setting of hot-wire current. However, no correction was applied during the survey. It must be cautioned that the investigation establishes only the qualitative nature of intermittency.

In order to distinguish the different modes of fluctuation fields the surveys were conducted with a moderately high (i = 6 ma) overheat and a low (i = 2.3 ma) overheat to detect mass flux fluctuation and total temperature spottiness. Traces of intermittency factor (γ) distributions across the shear layer are presented in Fig. V.38. A survey with the higher overheat representing the combined response of mass flux and total temperature fluctuations shows that a very sharp demarcation exists between the turbulent and potential fields. This phenomenon was found to occur in the velocity ratio (u/u_e) range of 0.95 to 1.0. Since very little change in wire sensitivity occurred in this region, the uncorrected data are reliable. Relatively flat γ-distribution was noted for values of Y/θ between 4 and 0. Below $Y/\theta = 0$ ($M = 1.0$), gradual decaying of the γ-distribution accompanied by a secondary hump, which was also observed in the E_{tc} profile, occurred. The observation also implies that the turbulent edge consists of the small scale eddies. In contrast, the mixing process below the dividing streamline appeared to be extending into the entire lower subsonic layer. The skewness of the γ-profile of this magnitude was not observed in the incompressible turbulent mixing layer of Wygnanski and Fiedler,(42) which is superimposed on the same figure as $\gamma(u/u_e)$.

The second hump observed in the γ and E_{tc} profiles must be associated with a mass flux fluctuation because it vanished with lower overheats ($i \leq 4.0$ ma). The γ-distribution of total temperature spottiness measured by the low overheat showed a relatively gradual variation with a peak appearing at $Y/\theta \cong 2.0$. This distribution also showed that the fully turbulent field was confined in the supersonic side of the mixing layer. The difference between the two profiles obtained at the different overheat currents, therefore, can be interpreted as being the contribution from the mass flux, and the correlation $\overline{\dot{m}'T_o'}$. The observed phenomena, confinement of turbulence in the layer above the dividing streamline and greater intermittency zone below the dividing streamline, appear to be some of the distinguishing features of the supersonic mixing layer. Distributions of actual fluctuation signals and probability density are given in Appendix D.9.

V. 3. Development of Supersonic TFML with Finite Turbulent Boundary Layer Upstream of the Step

With the presence of the finite turbulent boundary layer (TBL) upstream of the corner of the rearward facing step, the flow must travel some distance downstream before it develops into a self-similar turbulent free mixing layer (TFML). Thus a virtual origin of similar TFML can usually be traced back upstream of the physical origin. Analysis of mixing layer with initial boundary layer made by Chapman and Korst(12) and Nash(14) did not show the evolution of mixing layer development. Baum(49) and Denison and Baum(50) solved the problem of compressible laminar free shear layer with finite initial thickness of laminar boundary layer. They have demonstrated the evolution of free shear layer from a Blasius boundary layer profile at separation to a Chapman's free mixing layer profile far downstream. Qualitatively, their results show the similar trend of development as observed in the present investigation.

It was quoted that the flow must travel at least 450 θ_o to 1000 θ_o downstream of the corner to have fully developed TFML (see Appendix A. 4). In the present investigation, careful Pitot pressure and hot-wire E_{tc} surveys were made in the starting region. The initial thickness of turbulent boundary layer is approximately 0. 14 inch (based on $u/u_e = 0.99$) and the corresponding momentum thickness is 0. 010 inch. It has been observed that self-similar mean flow was developed beyond $X = 2.75$ ($X/\theta_o = 275$).

At $X = 0$, no-slip condition of the boundary layer at the wall is removed and the outer moving fluid interacts with the stationary inner fluid by a mixing process. Momentum is transported by turbulence from boundary layer to stagnant fluid, which is set into motion. The entrainment of inner fluid at the lower boundary begins to take place and the free mixing layer grows from inside whereas the external portion of flow profile is virtually unaffected and retains the boundary layer form. This phenomenon is caused by the nature of supersonic flow that any disturbance created in the downstream does not propagate upstream of the Mach wedge or Mach cone. In the velocity profile (Fig. V. 39), the development of the inner mixing layer propagating into the original boundary layer profile is indeed observed. The profile of the boundary layer is slowly eaten away from the low speed side and the mixing layer profile is formed below the dividing streamline. At $X = 2.00$, it has developed into the full TFML form. Hot-wire E_{tc} output shows the development of the turbulence field

(Fig. V. 40). Basic turbulence energy profile of turbulent boundary layer is observed in the data taken at X = -1.0. Note that secondary turbulence layer has started from the interface of the moving and stationary fluids and its maximum energy level rapidly increases beyond the boundary layer one. Growth rate of the inner layer is much faster than the one of the later stage when the self similar mixing layer flow is established. The energy spectrum distributions were taken at the peak of E_{tc} profiles. The frequency was normalized with the local velocity and the width of the inner layer determined by the slope intercept method. The peaks of energy carrying spectra are observed at the non-dimensionalized frequency ($2\pi b_i f/u_L$) of unity.

V. 4. Reynolds Number Dependence of TFML

When hot-wire surveys were made with an operating condition II, a peculiar peaking of signal near frequency of 5 KHz appeared in the turbulence spectra taken in the TFML. The cause of this peculiarity was speculated in Sect. V. 1. 3., but the real cause was finally traced down to the one of the upstream conditions, laminar-turbulent transitional boundary layer instability or some Reynolds number dependent disturbance in the boundary layer.

The response of turbulence spectra measured in the free mixing layer to the total pressure variation was investigated. Since all other operating conditions remained unchanged, the total pressure variation implied the direct Reynolds number variation. The unresolved turbulent energy spectra were normalized with the integrated quantity and with the non-dimensionalized effective X-distance which is referenced to X = 4.75 value (i.e., the data taken at X = 4.75

correspond to the spectra displayed in the physical frequency domain). Spectra were taken at several X-stations along the line of constant mean voltage output of hot-wire. The input current to the hot-wire was maintained constant at i = 4.8 ma., but it must be cautioned that the sensitivity coefficients of wire response varied with p_o. Therefore, the comparison of integrated voltages between different cases is not recommended.

The boundary layer of the first three cases (p_o = 500, 610, 900 mm Hg) was tripped with a strip of fine grain sandpaper. The spectra taken with p_o = 500 mm Hg are shown in Fig. V.41a. The spectra are accompanied by pronounced peaking near f = 5 KHz (peak shift is due to X-normalization), which signifies the passage of high energy carrying organized eddies in the preferred frequency range. No significant development of medium to small scale turbulence is noted (oddly, it follows the $f^{-5/3}$ law immediately following the peak). Approximately 80% of the total energy is carried in the frequency domain of less than 100 KHz. But more than 20% of energy is contained in the frequency domain of below 10 KHz. The integration of power spectra was taken in accordance with Appendix D.7 and shows the decreasing trend with X. The energy profile shows that the boundary layer is transitional with high intensity signal existing near the wall which is similar to the ones observed by Laufer and Vrebalovich.(43) The presence of large scale periodic motion was detected by autocorrelation measurements as shown in Fig. 42.

The spectra taken with p_o = 610 mm Hg are shown in Fig. V. 41b. Peaking of spectra near 6 KHz persists but a considerable development of higher frequency energy carrying components is also observed. This observation implies that this flow condition is the followup stage of previous flow field. The agreement of the data of X = 4.75 and beyond is excellent which indicates the linear dependence of high frequency turbulence on the axial growth rate. Approximately 50% of energy is contained in the high frequency components above 100 KHz. The passage of large scale wave-like motion, which is less pronounced in intensity as compared to the previous condition, was also detected (Fig. 42). The integrated intensities were found relatively constant with X.

When the total pressure was increased to p_o = 900 mm Hg, the observed peculiar peak vanished completely and the broad band spectra of turbulence was obtained (Fig. V.41c). To operate the present wind tunnel at high stagnation pressure, the dryer section must be bypassed and the amount of oil impingement on the hot-wire becomes severe. In view of operational handicap, the data showed reasonable agreement. High frequency components of this spectra distribution was identical to the spectra taken with p_o = 610 mm Hg.

Prolonged use of filters in the upstream settling chamber fortunately cleaned the tunnel circulating system and the removal of filters restored the normal operation of the wind tunnel with ambient stagnation condition without breaking the wire. The boundary layer trip was also changed to a strip of coarse grain sandpaper. With these combined operating conditions (operating condition I), the peaking signal was eliminated and the entire spectra were found to be identical with the data taken with p_o = 900 mm Hg. Self-similarity of the turbulence field was evident in these measurements.

The spectral development of turbulence with Reynolds number represents the different sequential developing stages of the turbulent mixing layer. Criteria for the fully developed self-similar TFML are defined as the existence of 1) turbulent spectra of broad band character with no discrete peak, and it can be normalized with X_E ; and 2) constancy of total integrated energy level with X so that equilibrium flow is established.

VI. CONCLUSIONS AND RECOMMENDATIONS

VI. 1. Conclusions

(1) Self-similarity of the two-dimensional, supersonic turbulent free mixing layer has been established. The mean flow field with a linear growth of TFML is observed at $X \geqslant 275\ \theta_o$ and the virtual origin of conical flow is located at approximately $250\ \theta_o$ upstream of the step. Self-similarity of the turbulent field is assured at $X \geqslant 375\ \theta_o$, provided the upstream boundary layer is fully turbulent.

(2) Compressibility effect (supersonic-adiabatic flow) reduces the spreading rate, the entrainment rate and the maximum shear stress of TFML. The quantitative data comparisons of compressible-incompressible TFML are shown in Table 1.

(3) Entrainment rate matches with momentum thickness growth rate ($\lambda_e = d\theta/dx$).

(4) Maximum shear stress is independent of the axial station.

(5) Velocity profiles are reduced to an incompressible form by a linear transformation of the lateral coordinate by a constant scaling parameter, σ. σ varies with Mach number. This observation suggests that a universal velocity profile of the TFML in the physical coordinates may exist. Forced entrainment by the mass injection into the boundary layer appears to alter the profile only in the subsonic region of the mixing layer.

(6) Power spectral density distributions taken at several axial stations along the ray of the constant flow field collapse to a single curve by θ or X_E normalization. The integrated intensities are found to be constant along the ray of the flow field.

(7) Energy carrying spectral components of velocity fluctuation exist near the Strouhal number ($2\pi fb/u_L$) of unity, and they match the incompressible data. A relatively large region where the spectral function varies as f^{-1} exists in the present experiment.

(8) Spectral peaks observed near the Strouhal number of unity appear and disappear with Reynolds number or with different boundary layer trips. This implies that the fully developed TFML consists of the randomly fluctuating fields without the large organized motion of a preferred frequency. This interpretation is based on the present supersonic TFML investigation and it may not necessarily be applicable to the incompressible TFML.

(9) Maximum intensities of different turbulence modes occur near the maximum gradients of the respective mean flow properties which exist in the supersonic side of the TFML. The combined intensities of all fluctuating modes are large but a considerable amount of the energy appears to be dissipated into the thermal energy as observed in the temperature fluctuation profile. Therefore, the vorticity mode of fluctuation which mainly contributes to the growing of the turbulent field is left with relatively low kinetic energy. The maximum streamwise velocity fluctuation of $M_e = 2.47$ flow is approximately 1/3 of the incompressible value.

(10) Convection velocity of turbulence above the dividing streamline lags behind the mean velocity and below the dividing streamline leads the mean velocity. The two velocity fields are identical in the vicinity of the dividing streamline, where the turbulence production is maximized. Small scale turbulences appear to adjust quickly to

the new local environments but the large scale eddies throughout the layer appear to be convecting with the velocity which exists at the dividing streamline.

(11) Taylor's hypothesis appears to be valid.

(12) Two-dimensionality of turbulent front is observed by the spanwise cross correlation measurements.

VI. 2. Recommendations for Future Work

(1) The possible existence of a universal velocity profile should be verified by a higher Mach number TFML experiment using the present technique. The proposed Mach number should be greater than 5.0 ($M_e \geq 5.0$) to observe a meaningful comparison of data.

(2) A high resolution instantaneous visualization technique should be developed to observe the turbulent motion of supersonic TFML, especially the existence of large organized eddies detected in the incompressible TFML.

(3) A two-stream mixing of supersonic and subsonic layer flow should be conducted to determine whether or not the extension of incompressible scaling law to this type of flow is valid.

Table 1: Comparison Between Incompressible and Supersonic Two-Dimensional Turbulent Free Mixing Layer Properties

	Incompressible (Liepmann & Laufer)	Supersonic (M = 2.47) (Present Investigations)
dy/dx $(.10 \leq u/u_e \leq .90)$	~ 0.16	~ 0.064
$d\theta/dx = \lambda_e$	0.035	0.0073
σ	12	27 ~ 29
$\tau_{max}/\lambda_e \rho_e u_e^2$	.34	.385
$\tau_{max}/\rho_e u_e^2$	.012	.0028
ρ_w/ρ_e	1.0	.45
$\left(\sqrt{\overline{u'^2}}/u_e\right)_{max}$	.16 ~ .18	.05 ~ .06

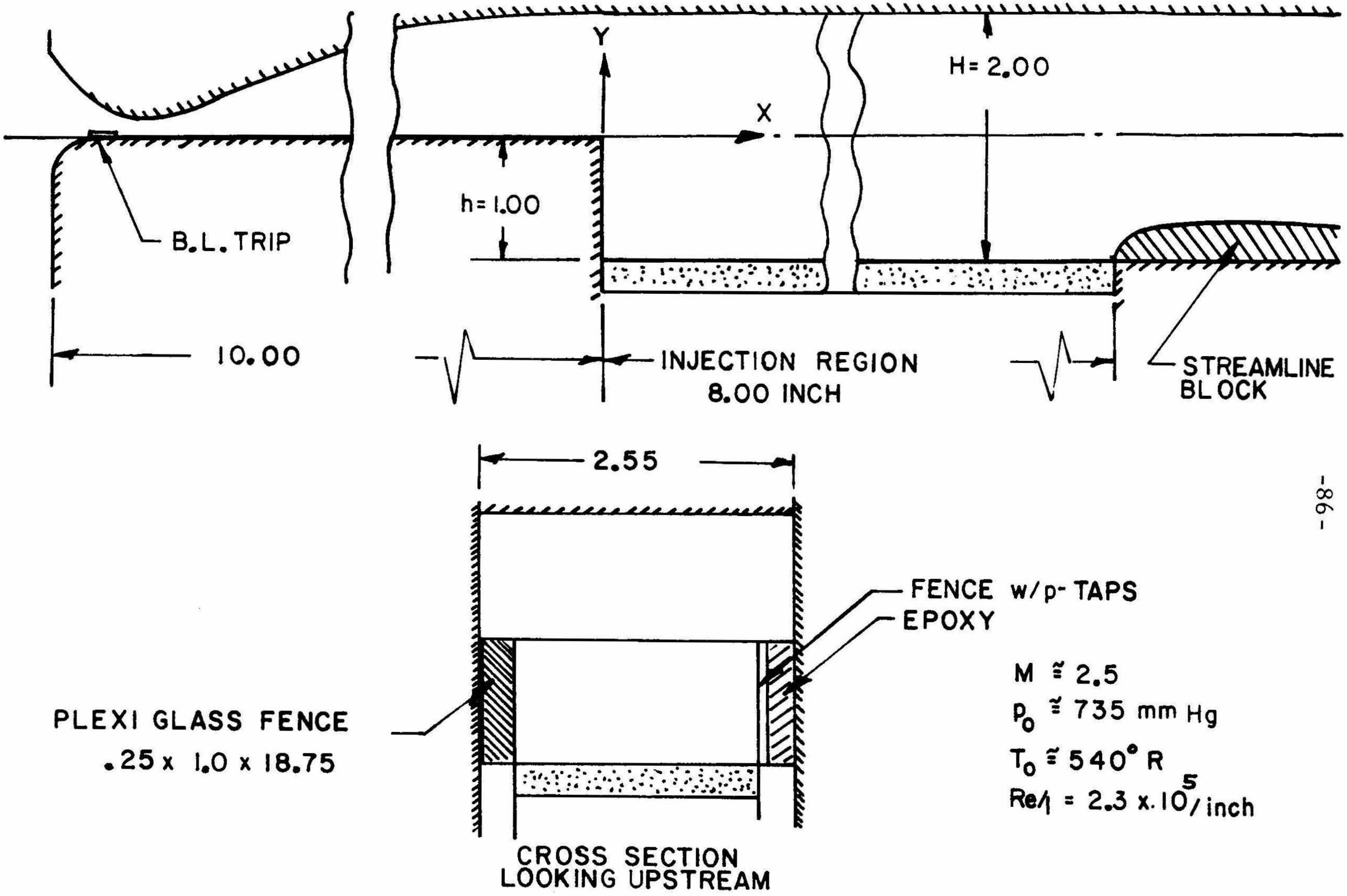

FIG. II. 1a TEST SECTION CONFIGURATION

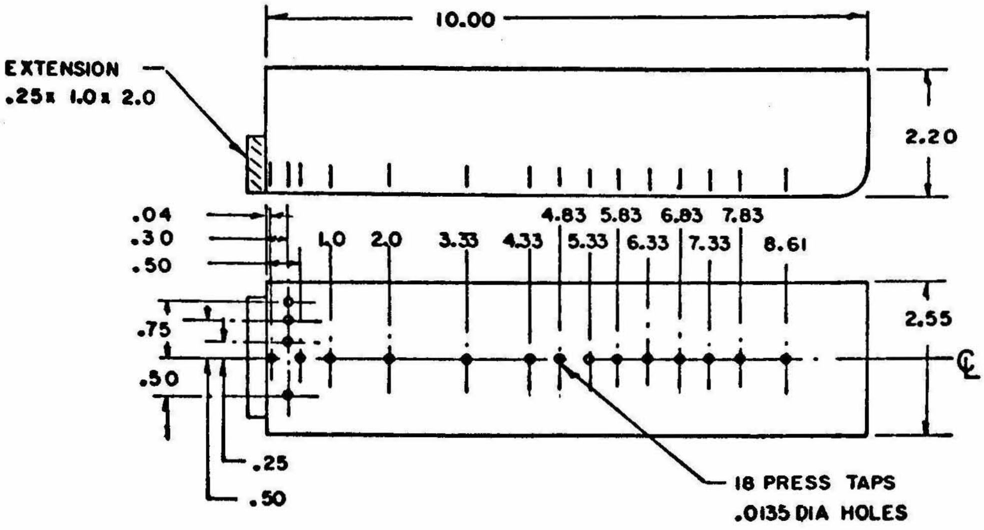

UPSTREAM BLOCK WITH PRESSURE TAPS

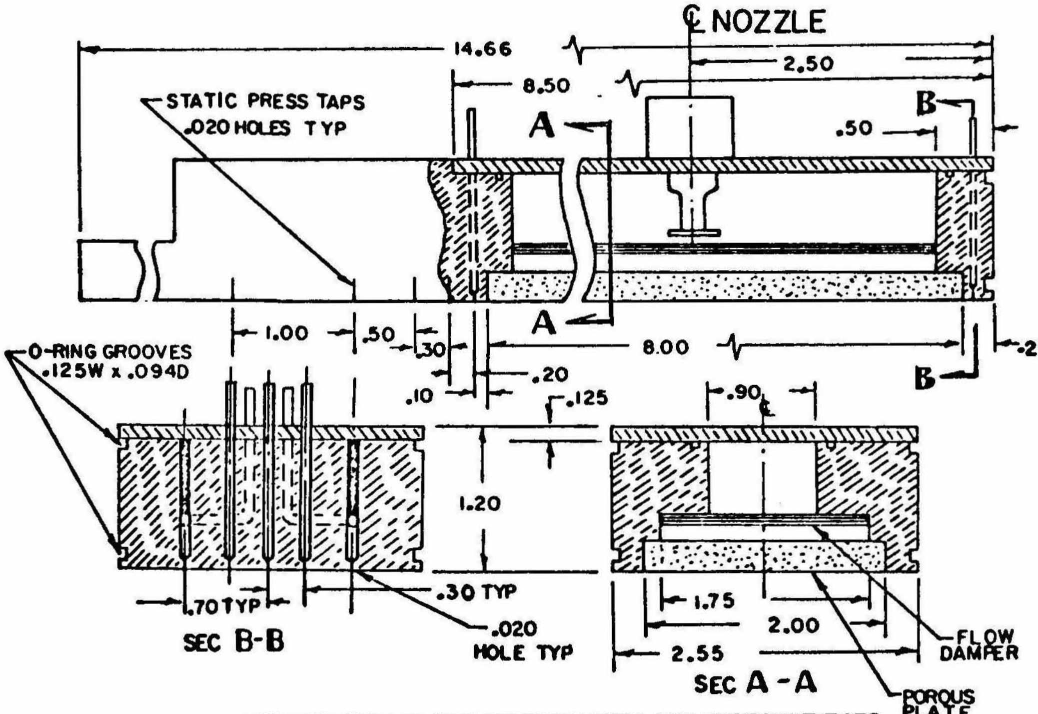

DOWNSTREAM BLOCK WITH PLENUM AND PRESSURE TAPS

FIG. II. 1b MODEL CONFIGURATIONS

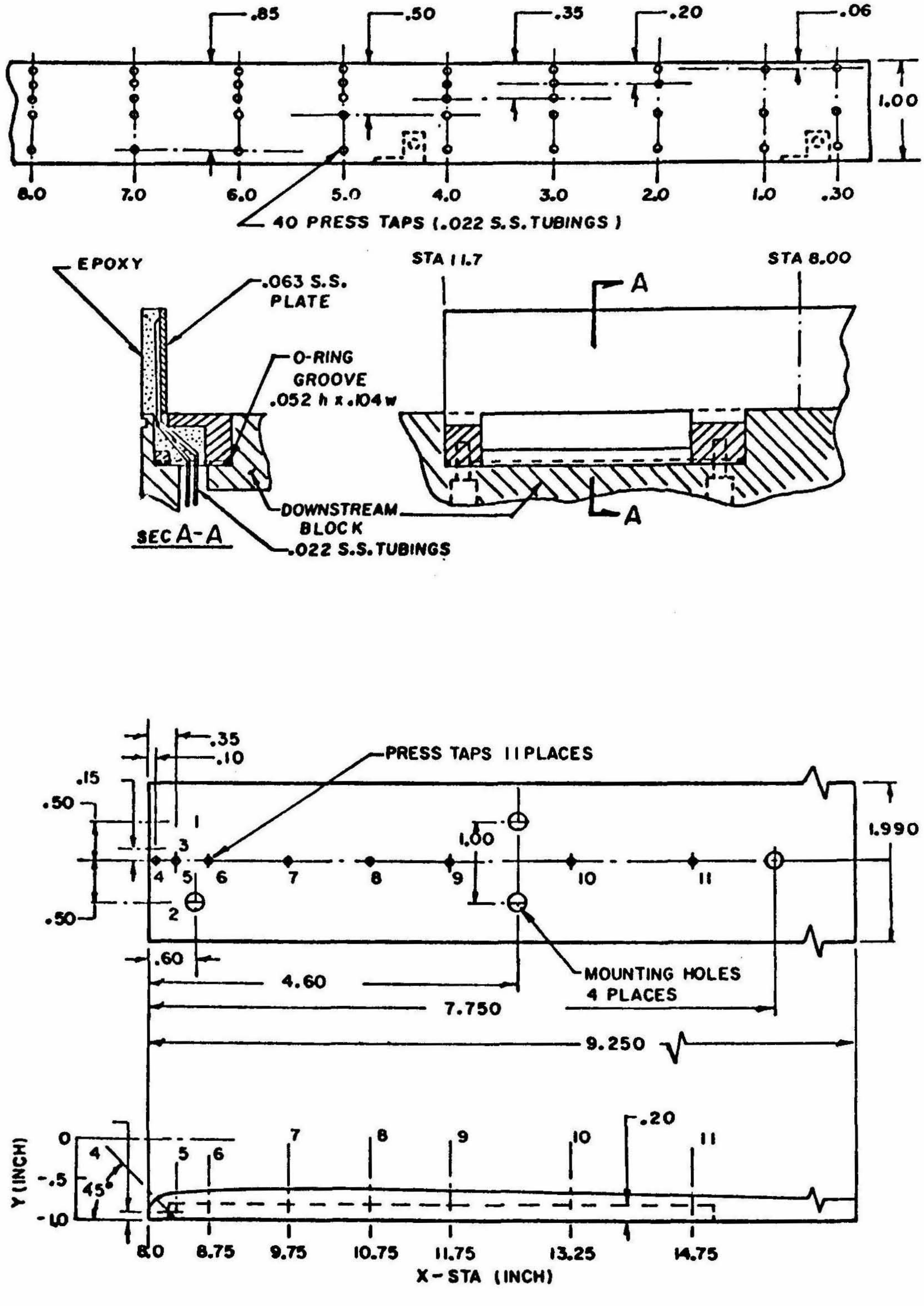

STREAMLINE BLOCK FOR $\lambda_e = .0072$

FIG. II. 1c MODEL CONFIGURATIONS

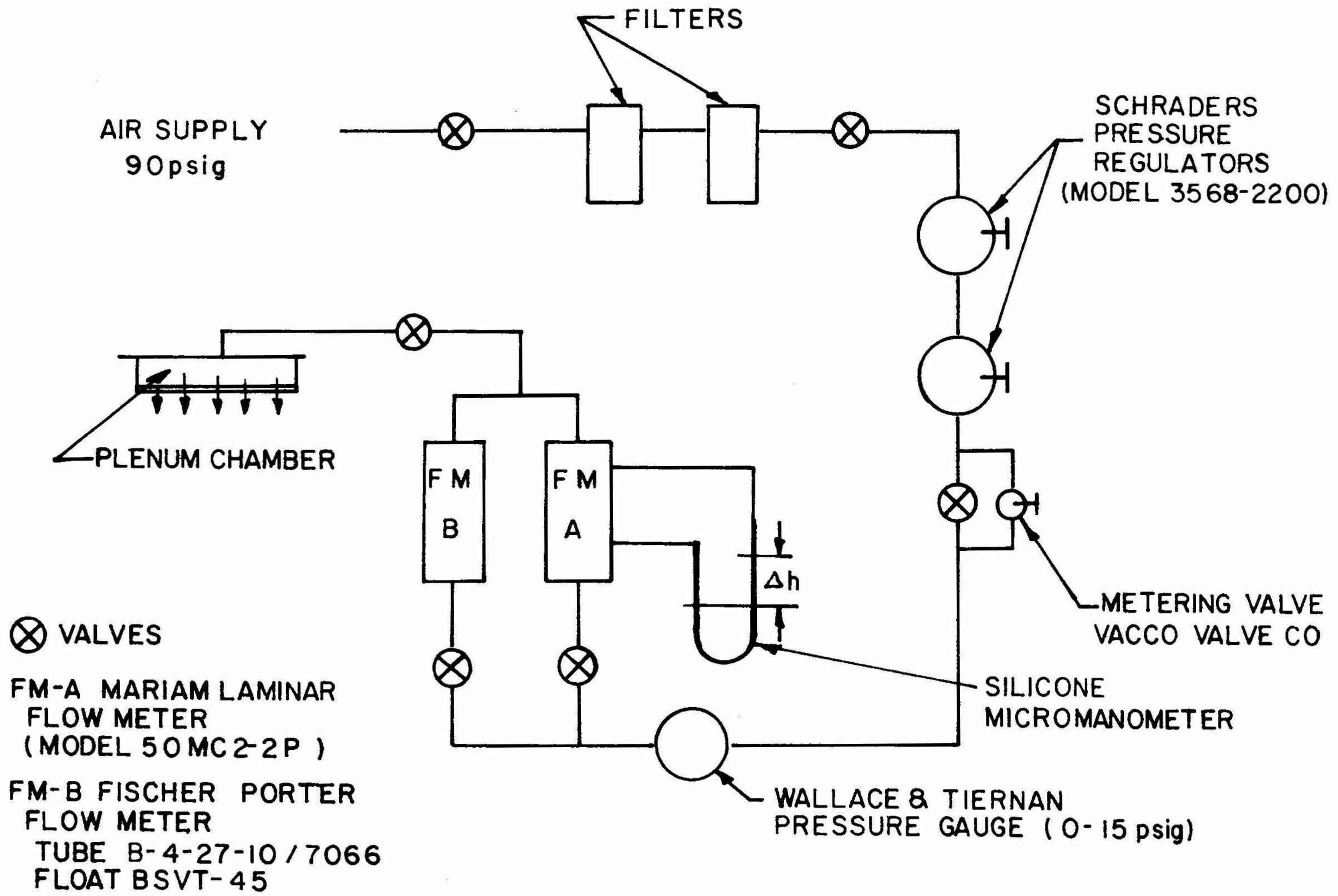

FIG. II. 2 SCHEMATIC OF INJECTION FLOW SYSTEM

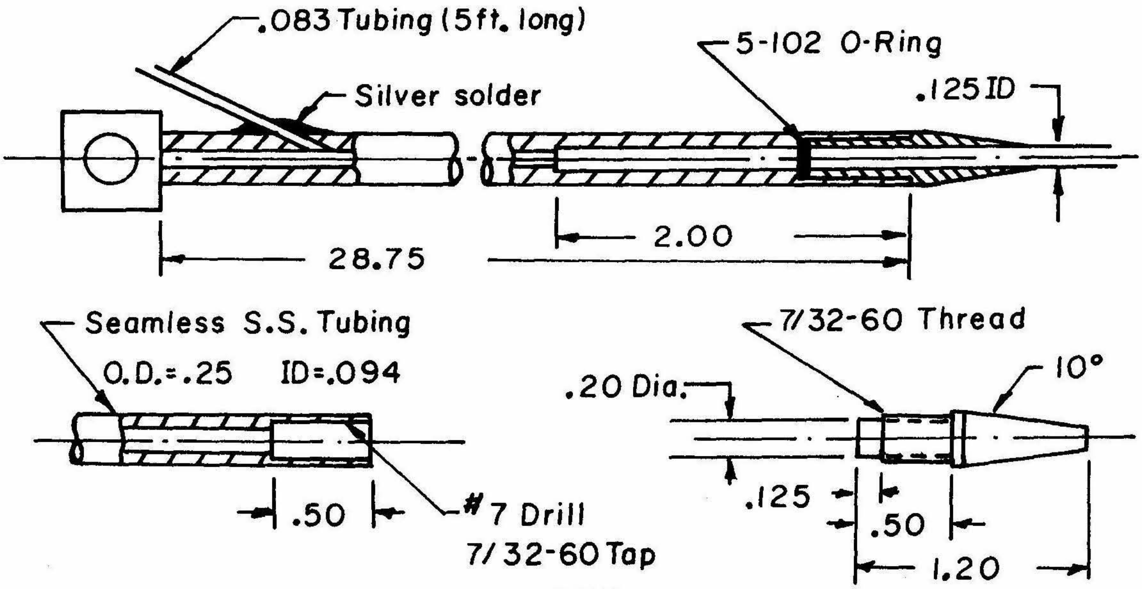

PROBE HOLDER

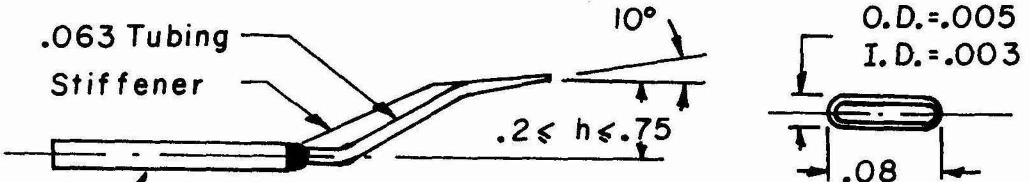

PITOT PROBE

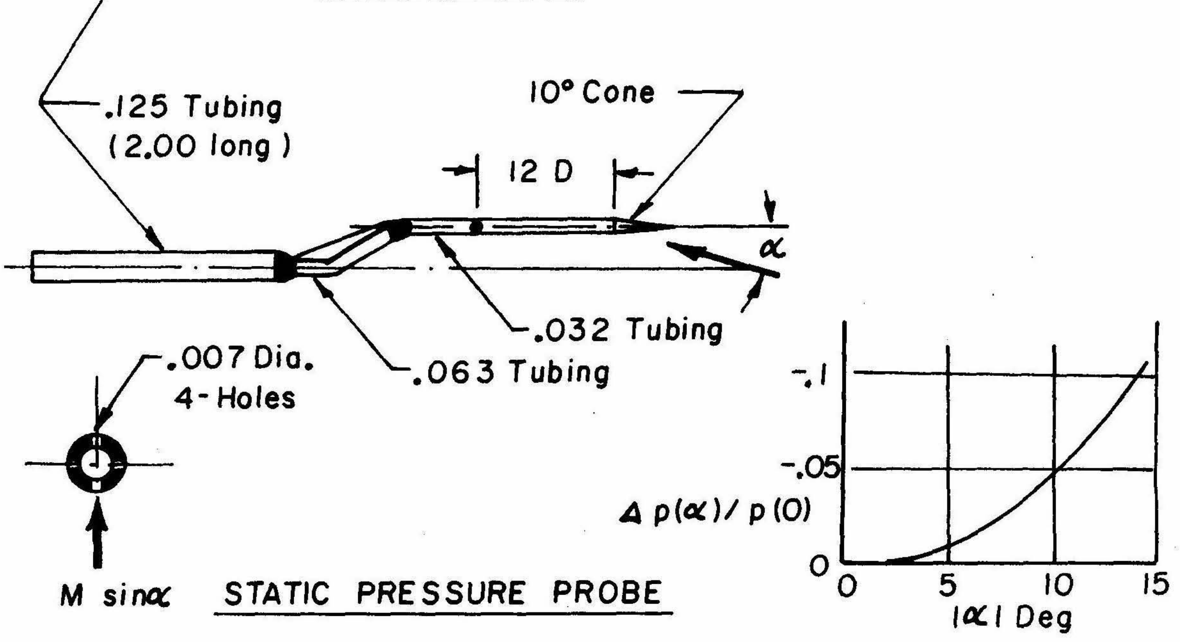

STATIC PRESSURE PROBE

FIG. II. 3 PRESSURE PROBES

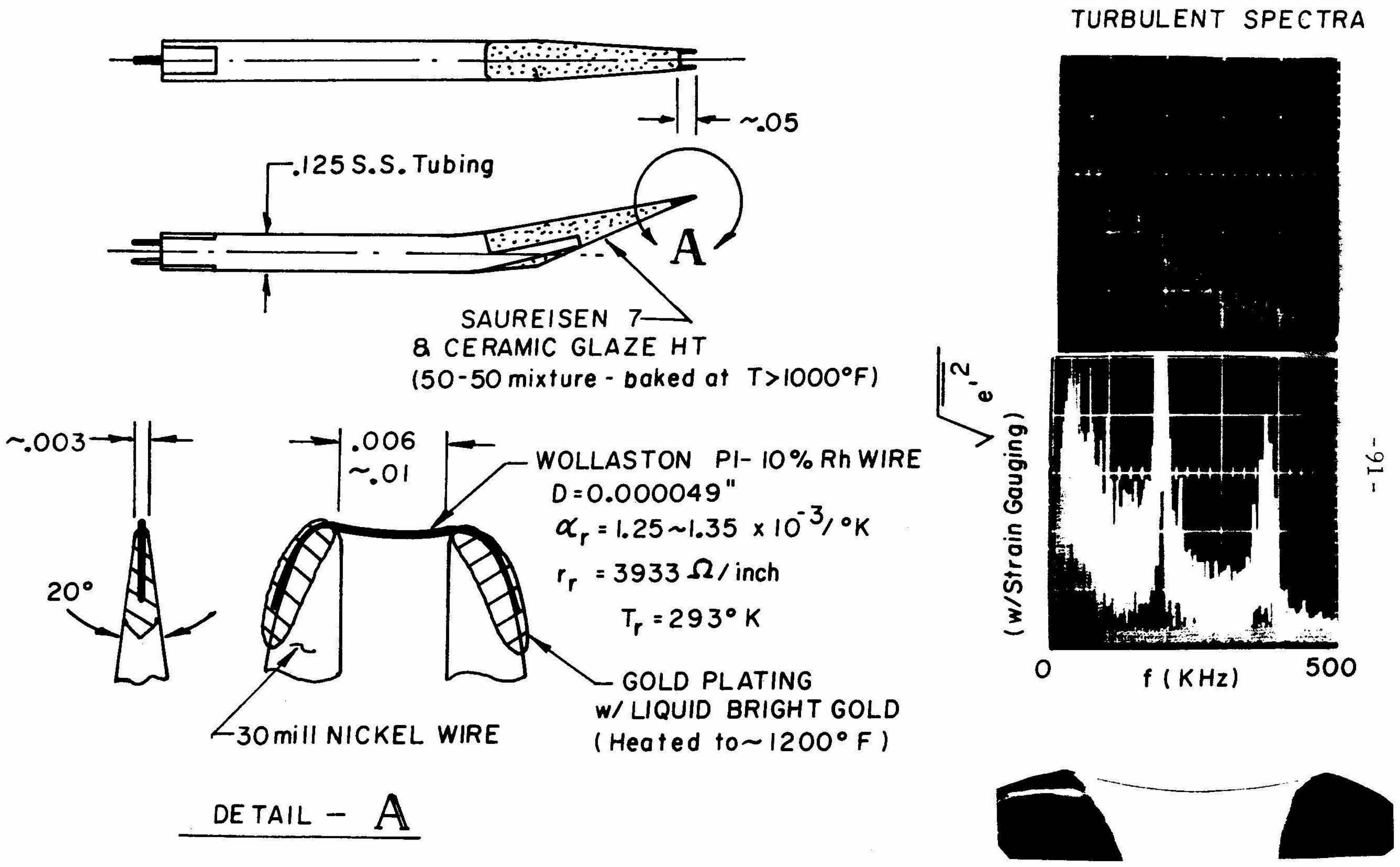

FIG.II.4 HOT-WIRE PROBE

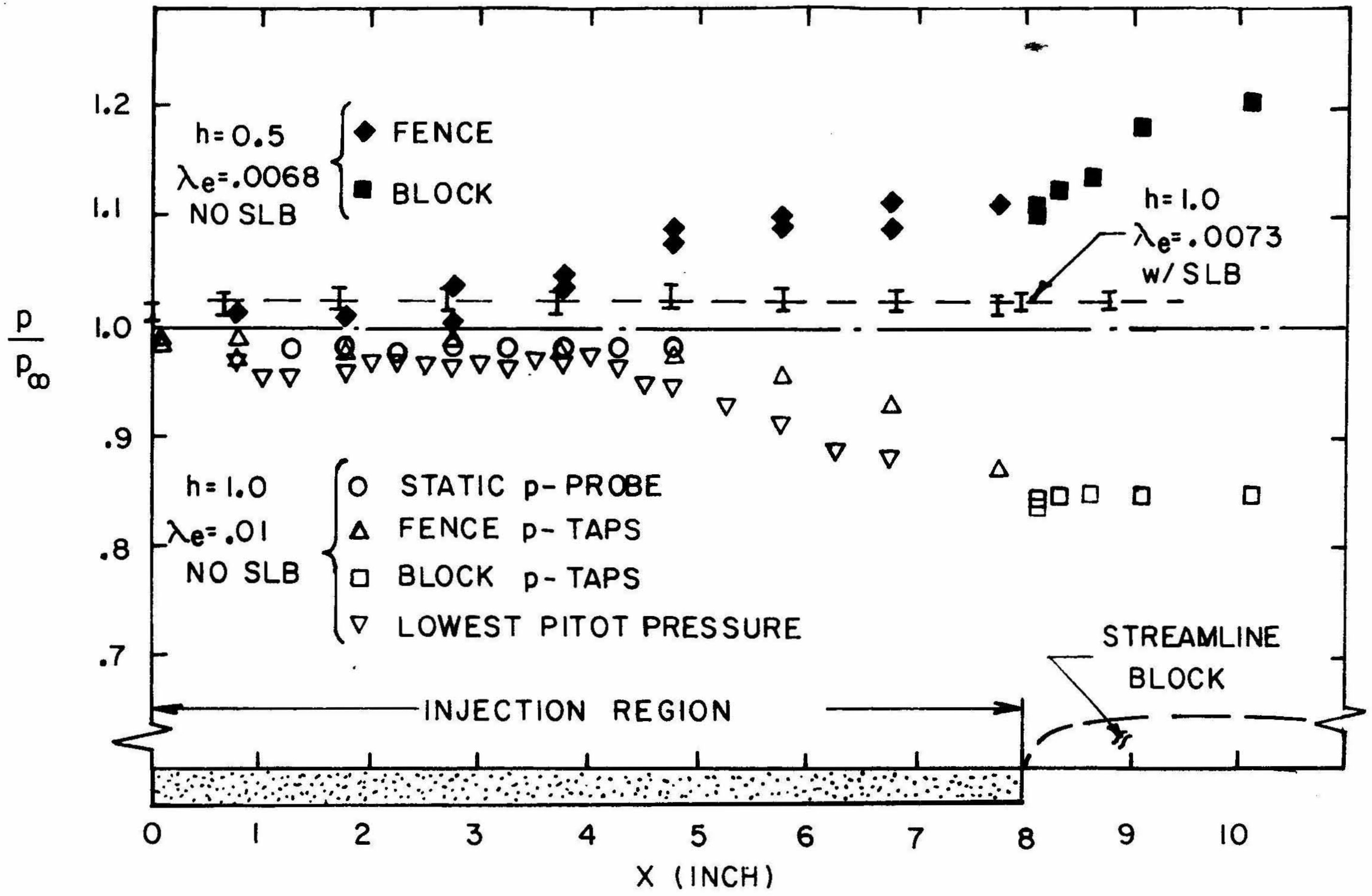

FIG.III.1 STATIC PRESSURE DISTRIBUTION

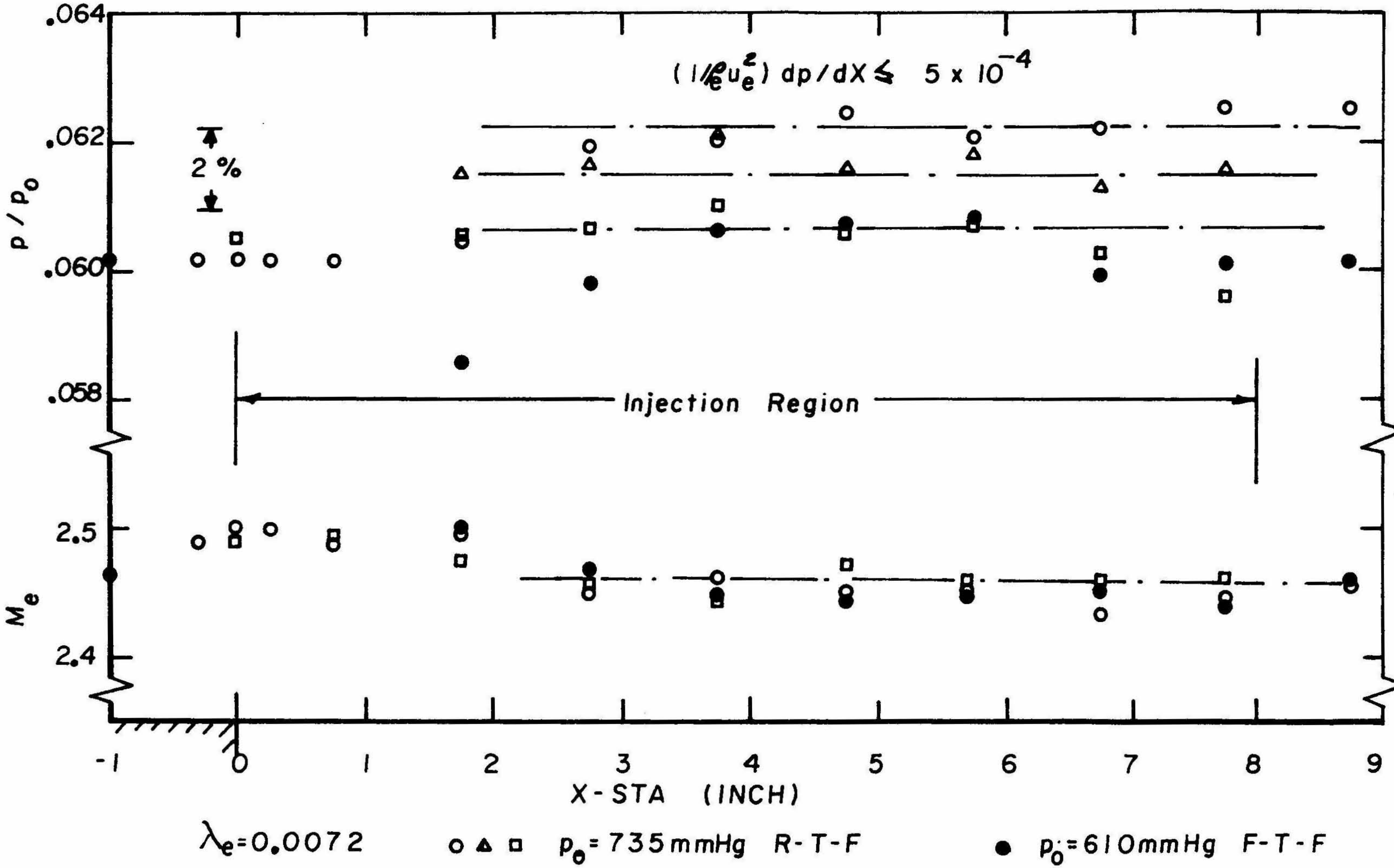

FIG. V.1 TFML-EDGE MACH NUMBER AND STATIC PRESSURE DISTRIBUTIONS

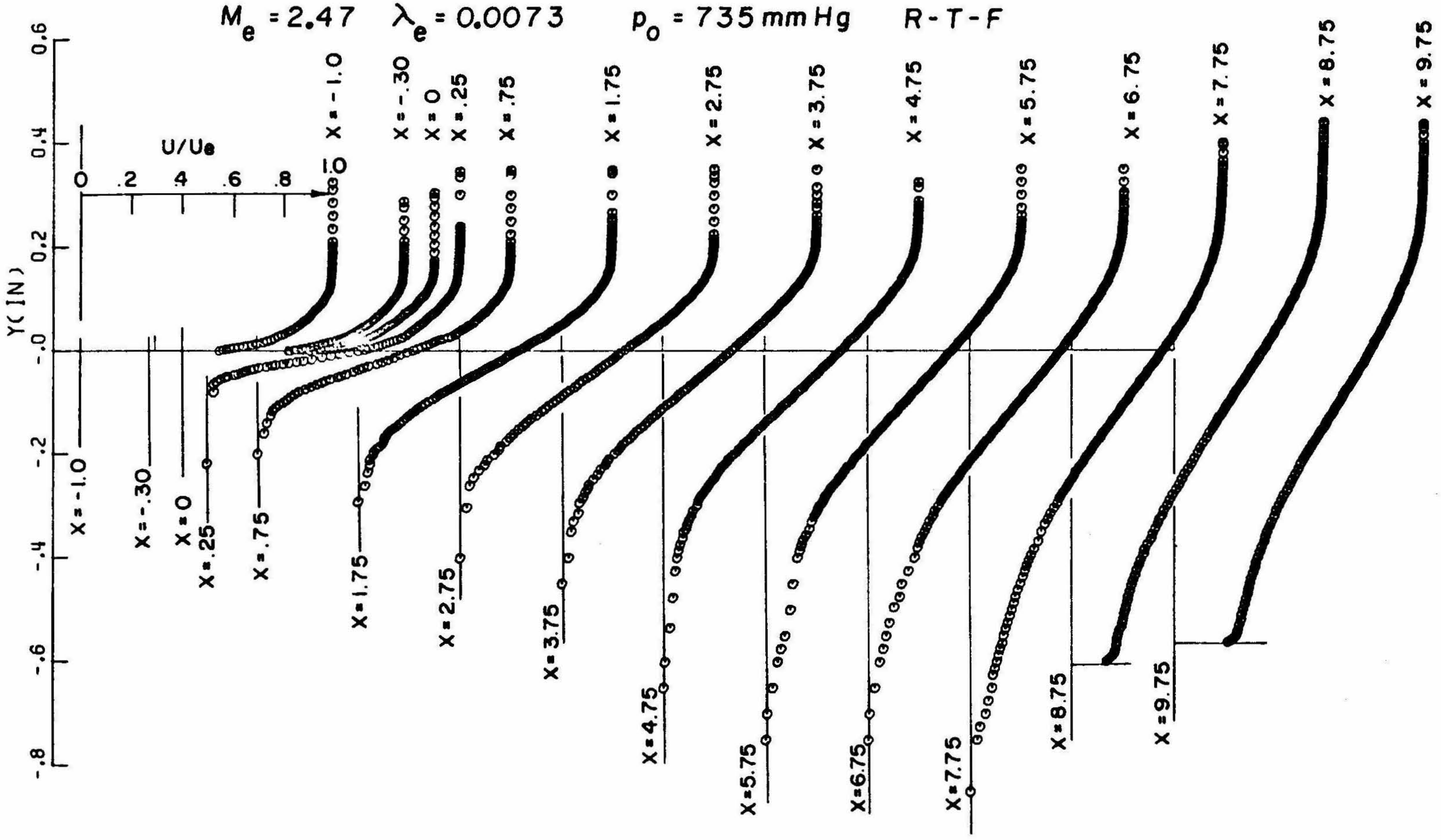

FIG. V.2 EVOLUTION OF VELOCITY PROFILES

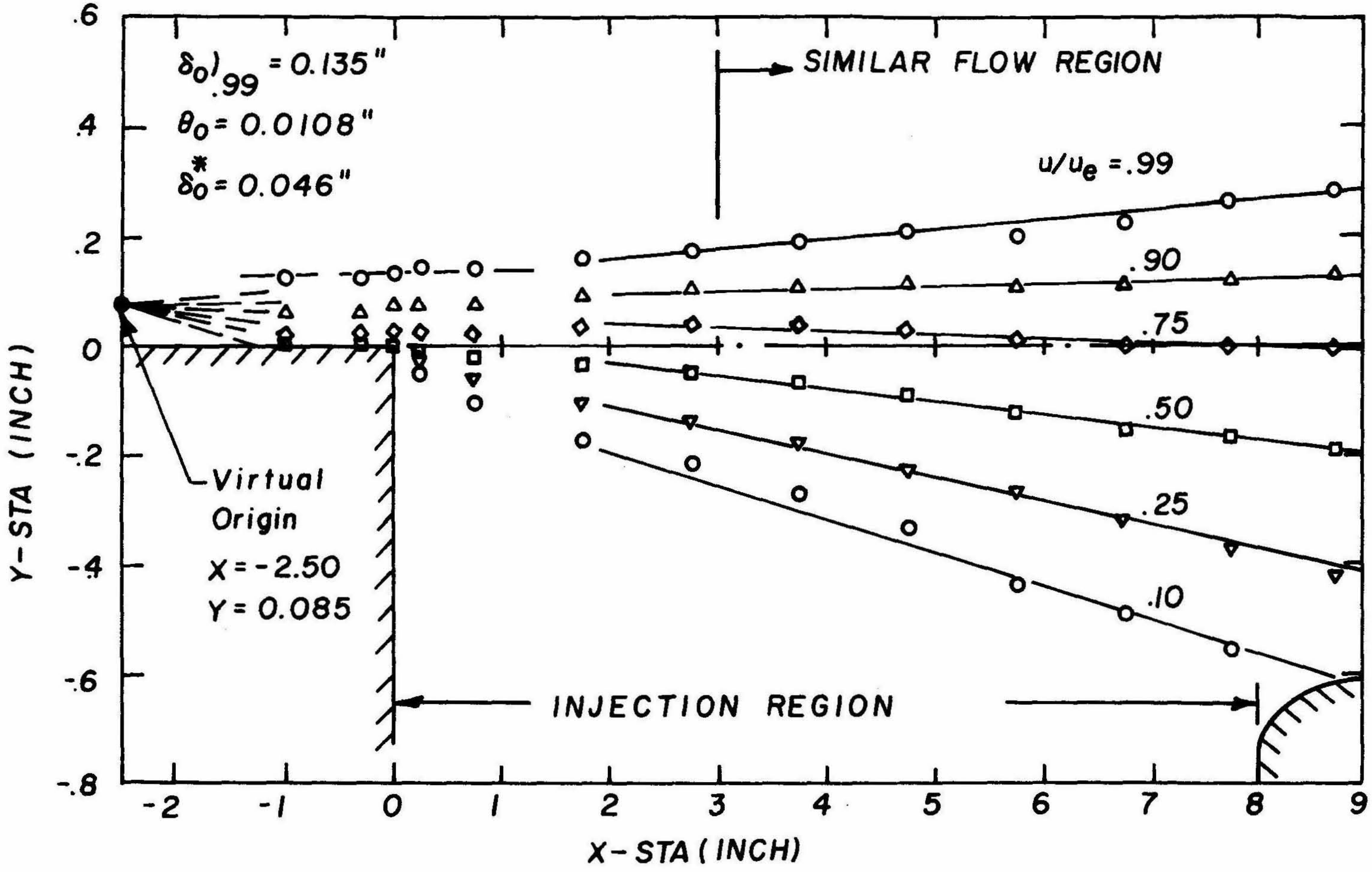

$M_e \cong 2.46$ $\lambda_e \cong 0.0073$ $p_o = 735$ mm Hg R-T-F

$dY/dX \cong .064$ for $M_e \cong 2.46$; $dY/dX \cong 0.16$ for $M = 0$ (Ref. 19): $.10 \leq u/u_e \leq .90$

FIG. V.3 TFML LONGITUDINAL VELOCITY DISTRIBUTIONS

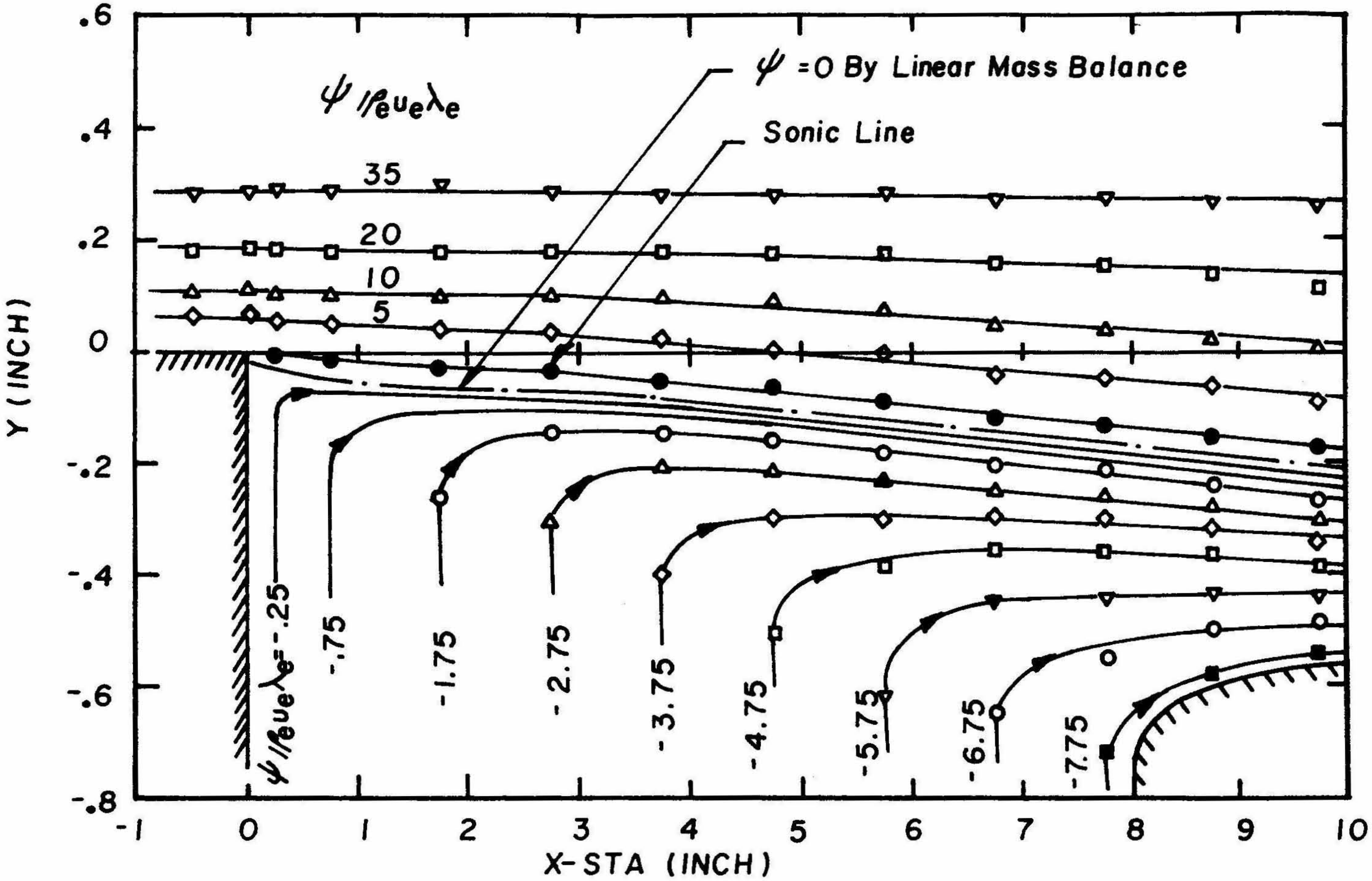

$M_e \cong 2.46$ $\lambda_e \cong 0.0073$ $p_o = 735$ mmHg R-T-F

FIG. V.4 TFML STREAMLINE PATTERNS

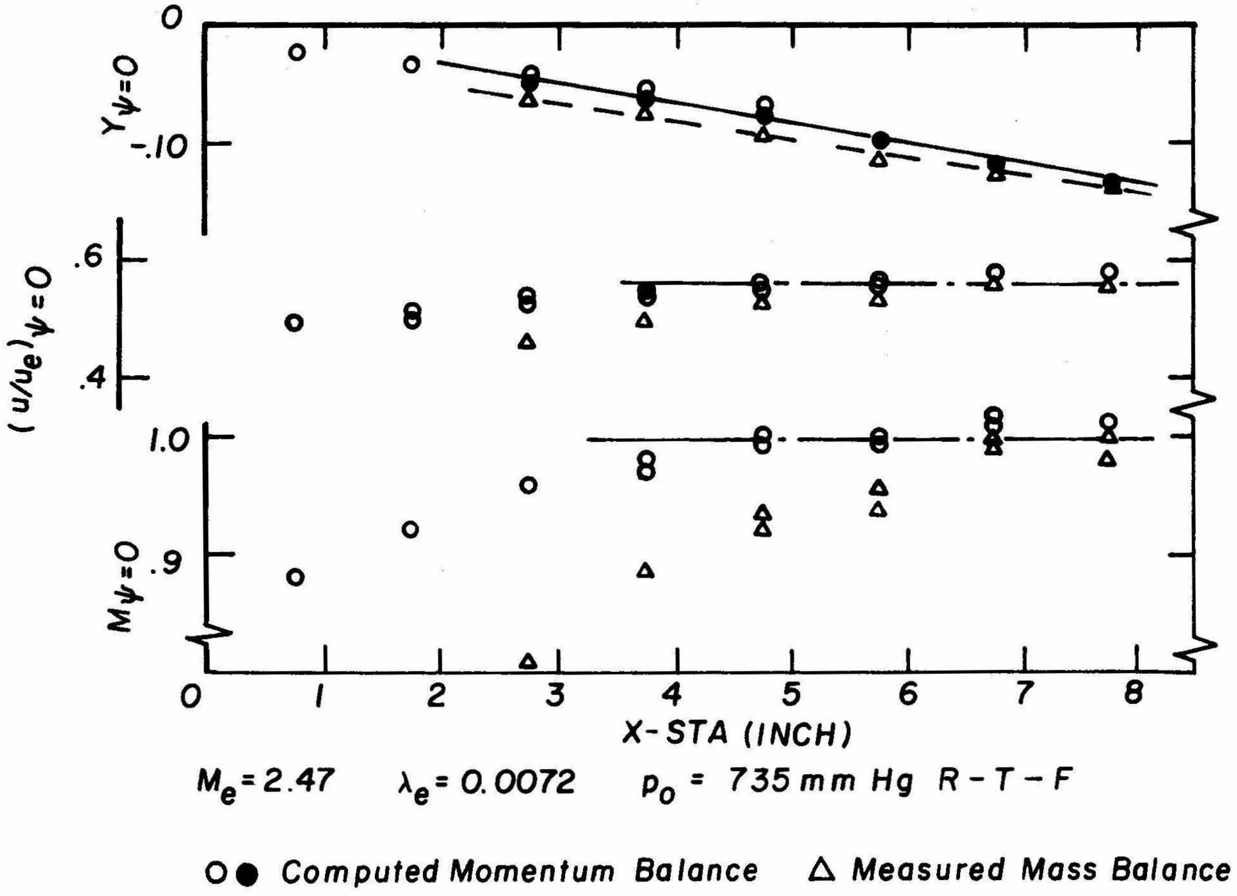

FIG. V.5 TFML DIVIDING STREAMLINE PROPERTIES

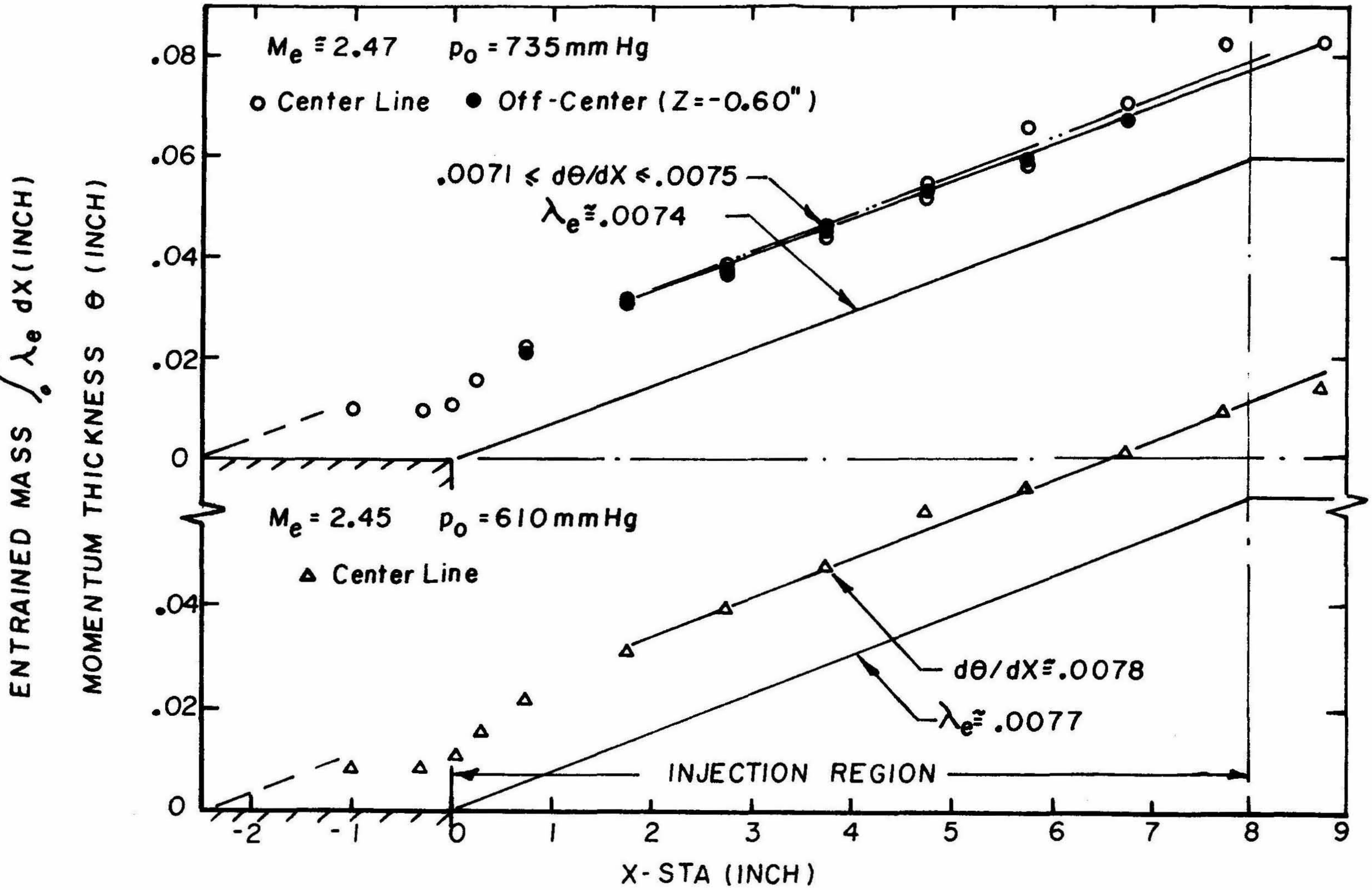

FIG. V.6 TFML-COMPARISON OF MOMENTUM THICKNESS DISTRIBUTIONS Vs. ENTRAINED MASS DISTRIBUTIONS

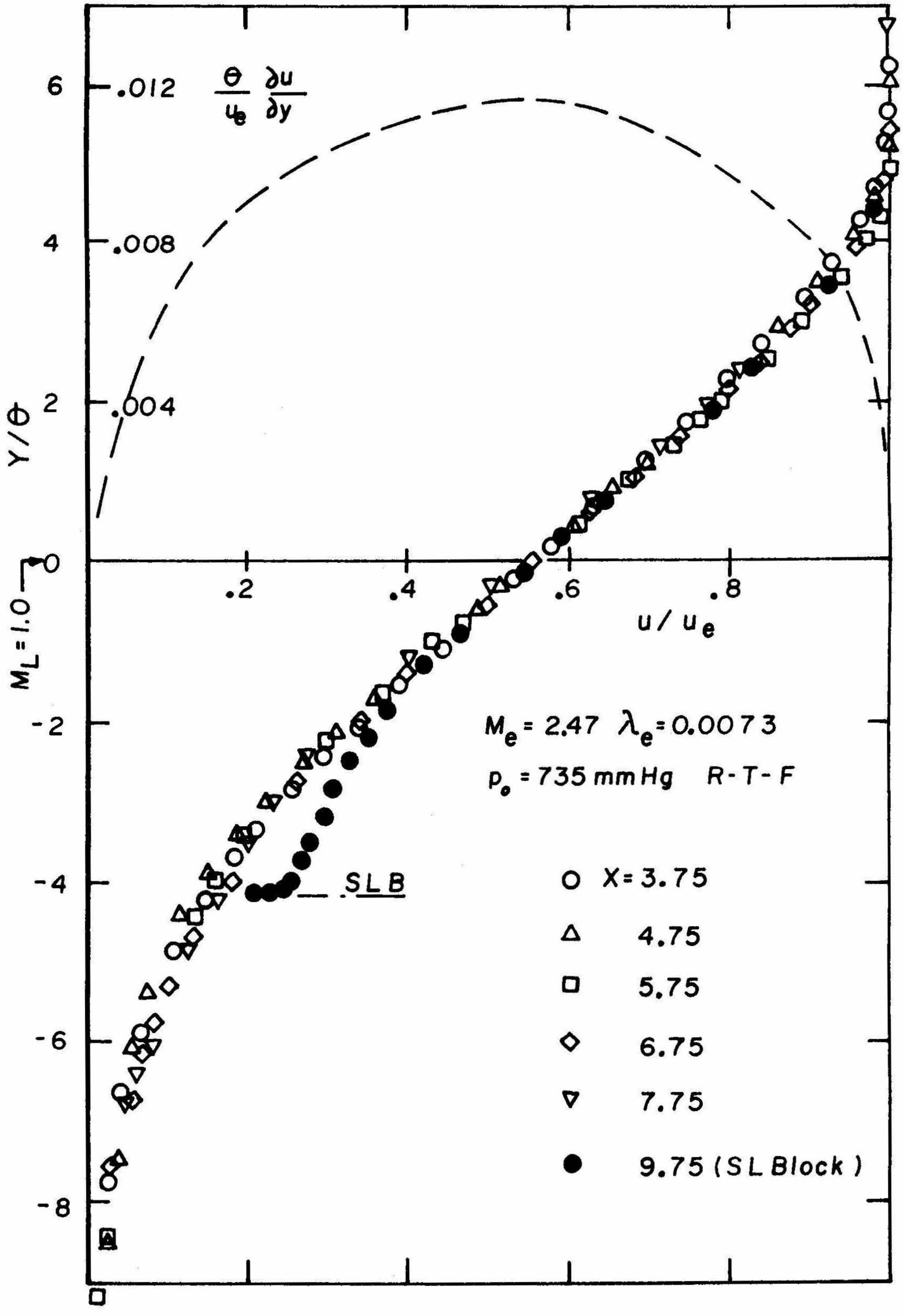

FIG. V.7 TFML VELOCITY AND VELOCITY GRADIENT PROFILES

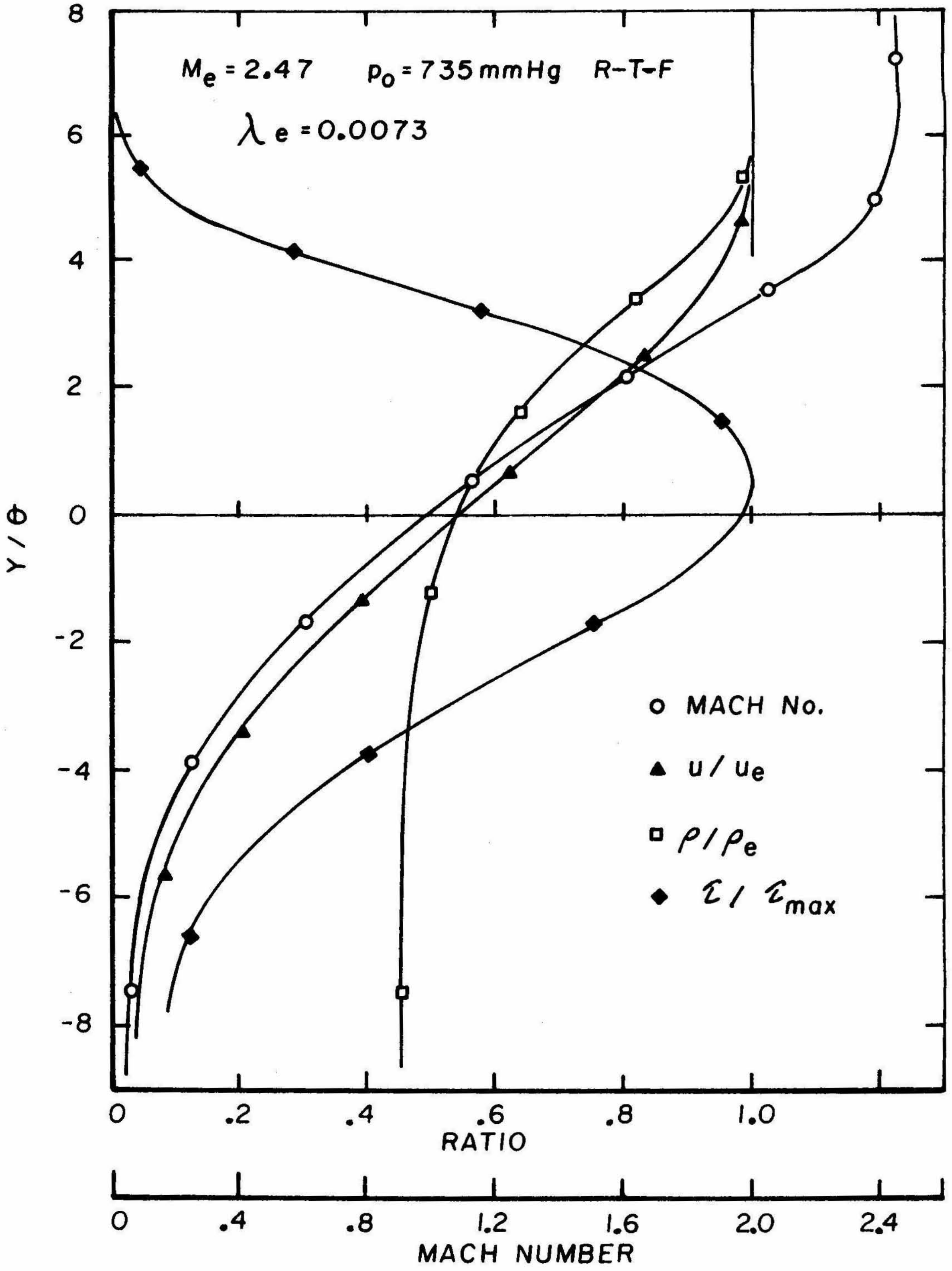

FIG. V.8 TFML MEAN FLOW PROPERTY PROFILES

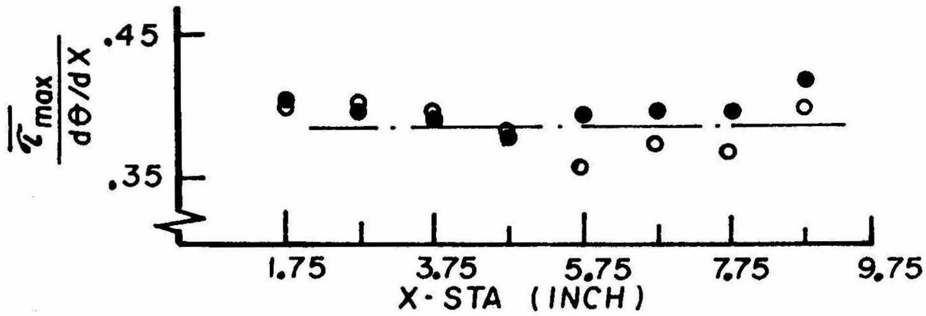

Normalized Max. Shear Distribution

○ p_0 = 735mmHg R-T-F ● p_0 = 610mmHg F-Tr-F

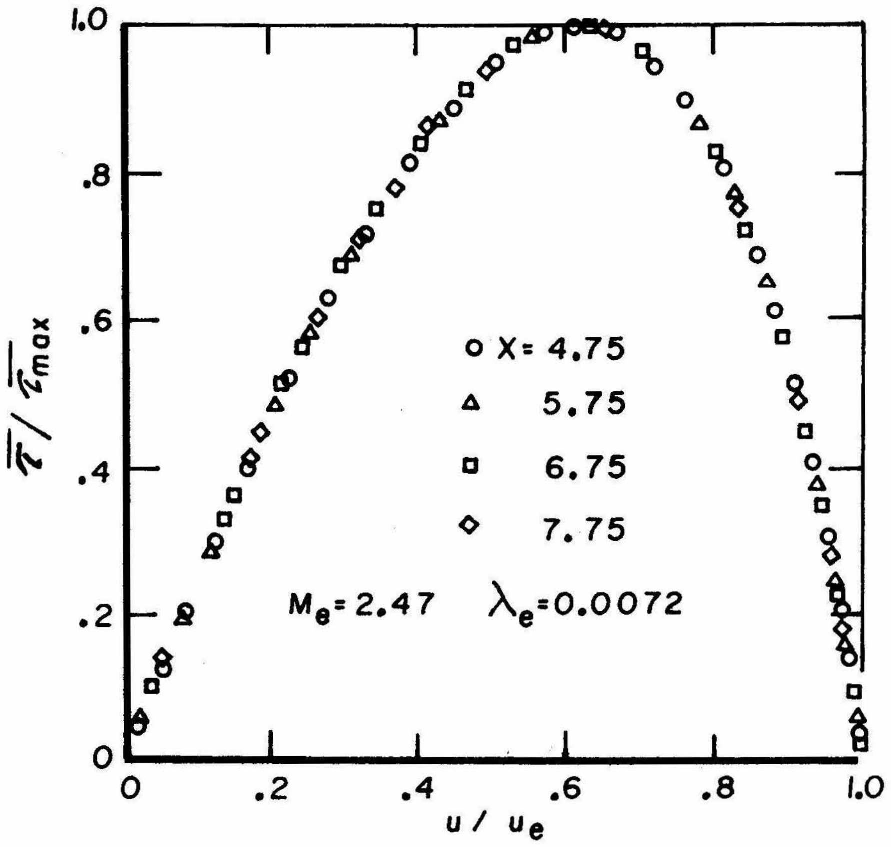

$$\overline{\tau} = \tau/\rho_e u_e^2$$

$\overline{\tau}_{max}/(d\theta/dX)$ = 0.385 (Present)

0.34 (M=0, LIEPMANN & LAUFER)

FIG. V.9 TFML-SHEAR STRESS PROFILES

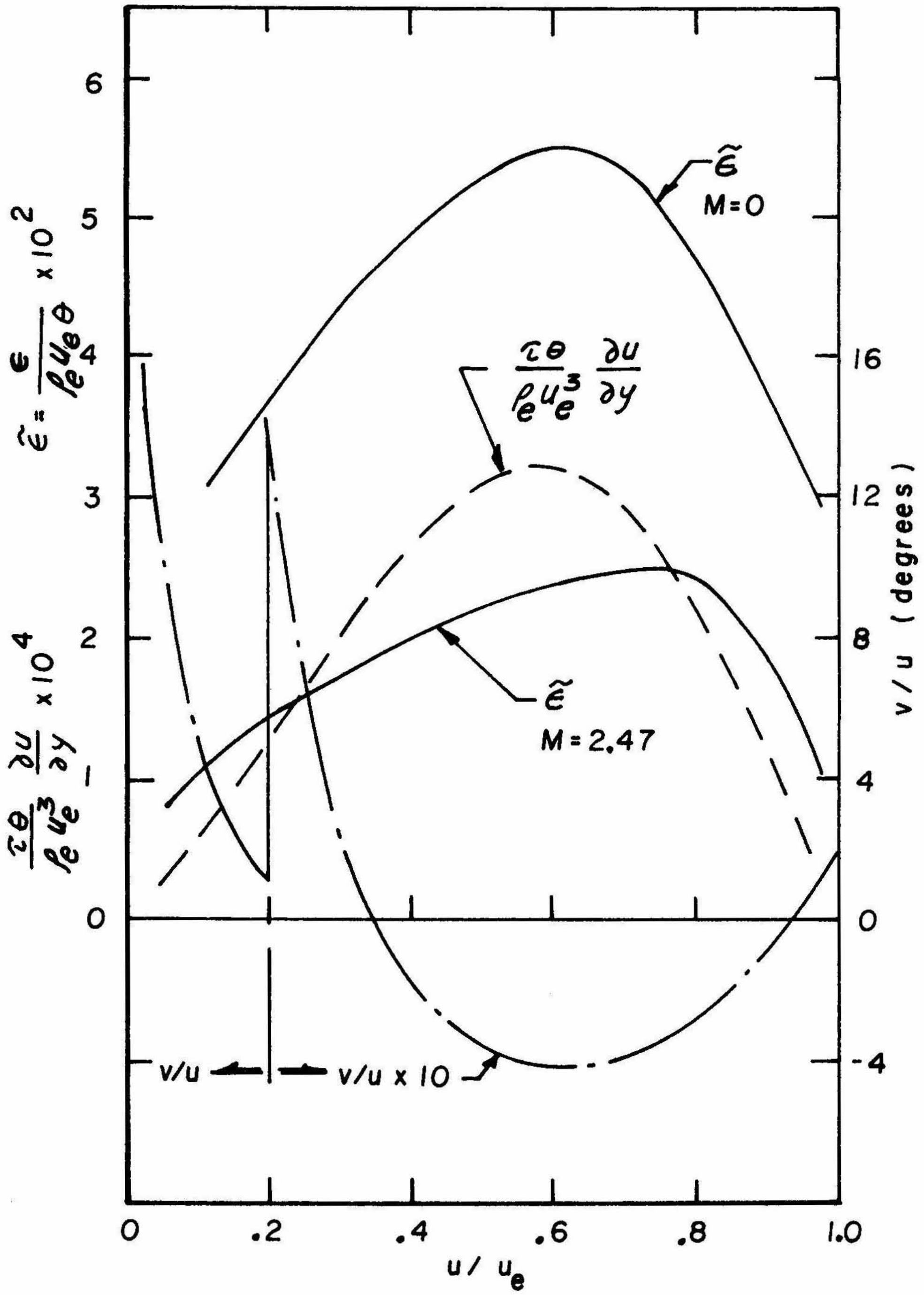

FIG. V10 TFML EDDY VISCOSITY, PRODUCTION TERM, FLOW ANGLE

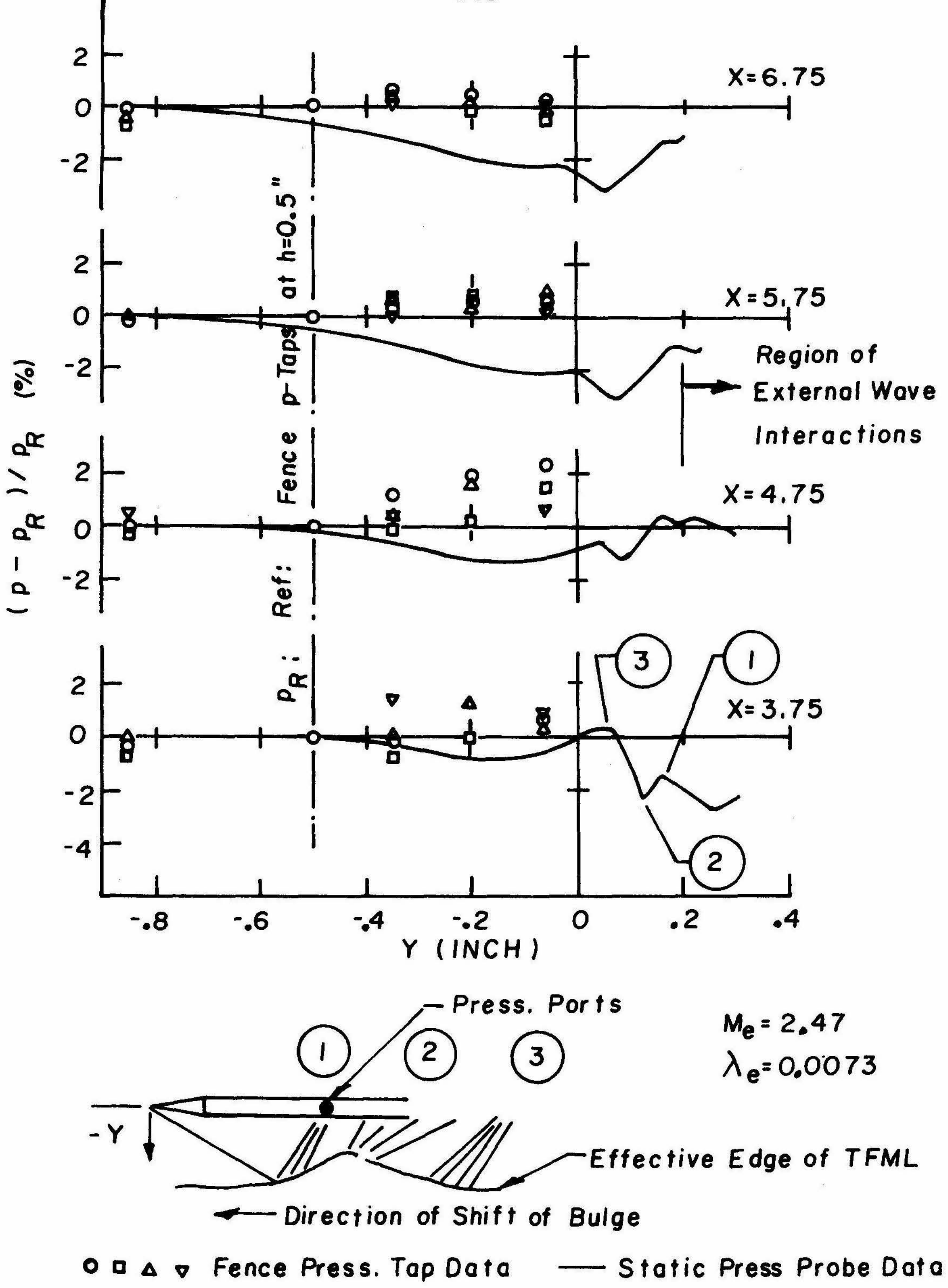

FIG. V. 11 TFML-DIFFERENTIAL STATIC PRESSURE PROFILES

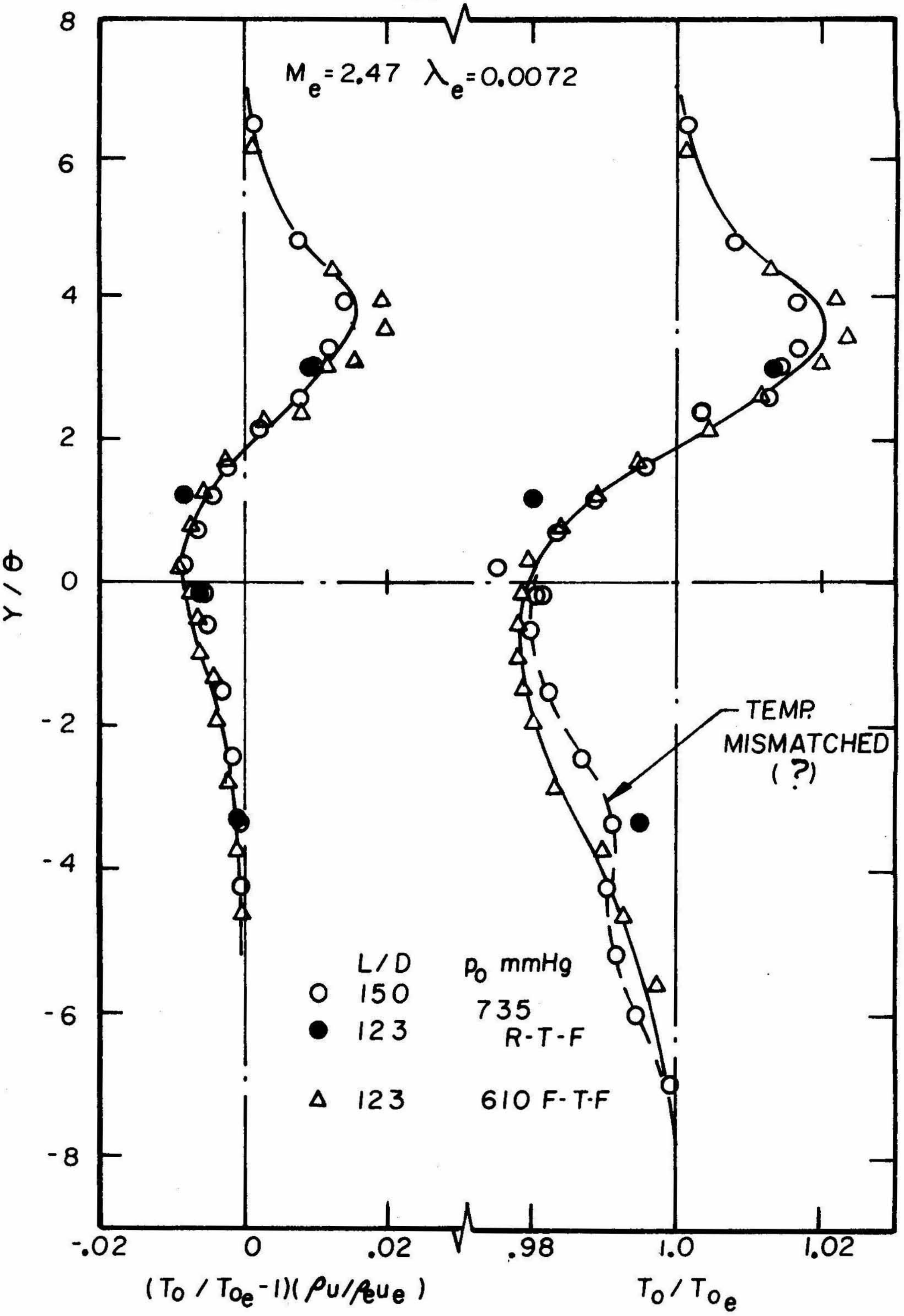

FIG. V.12 TOTAL TEMPERATURE AND TOTAL TEMPERATURE FLUX PROFILES

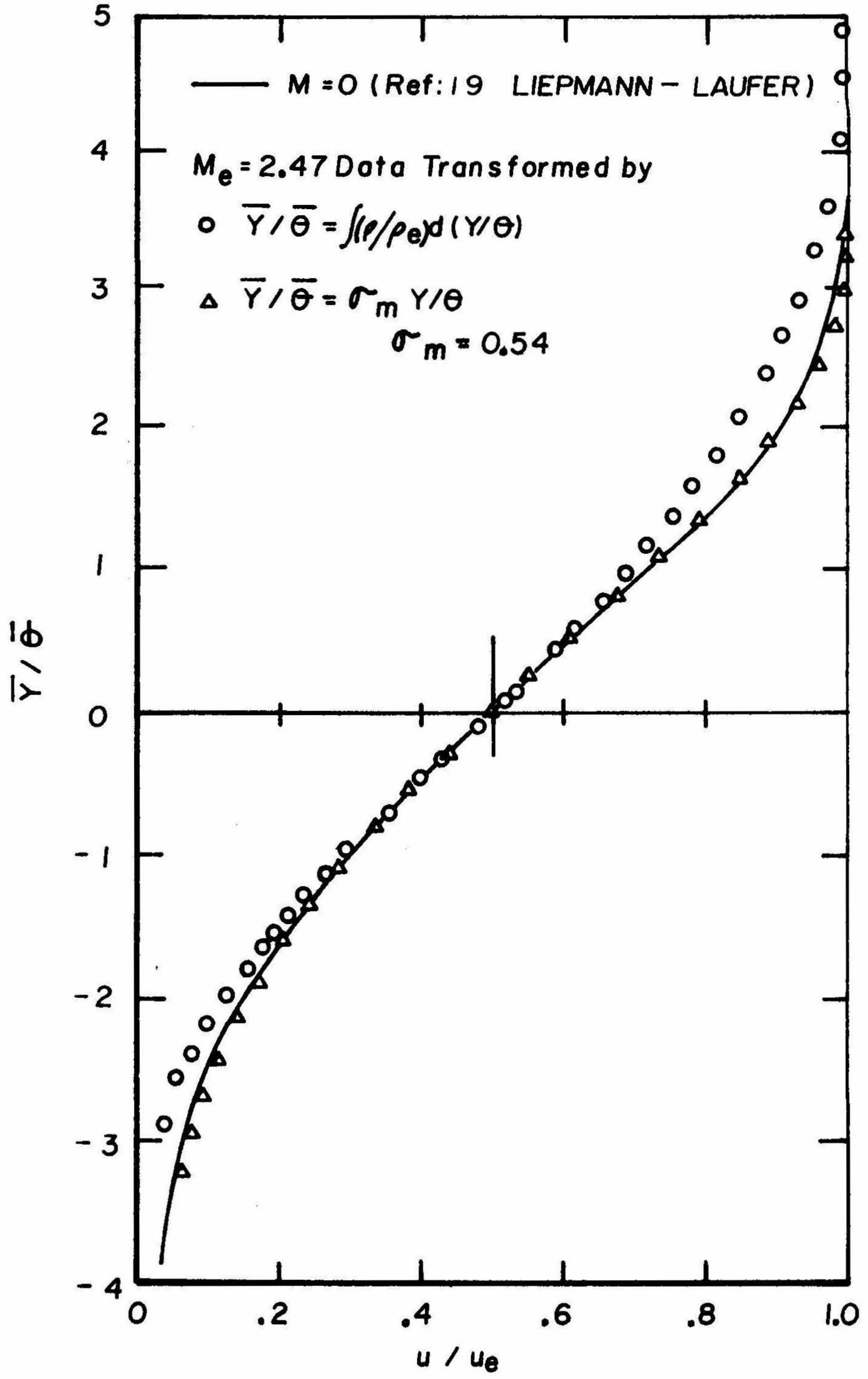

FIG. V.13 COMPARISON OF TFML VELOCITY PROFILES -- LINEAR AND INTEGRAL SCALING OF SUPERSONIC DATA

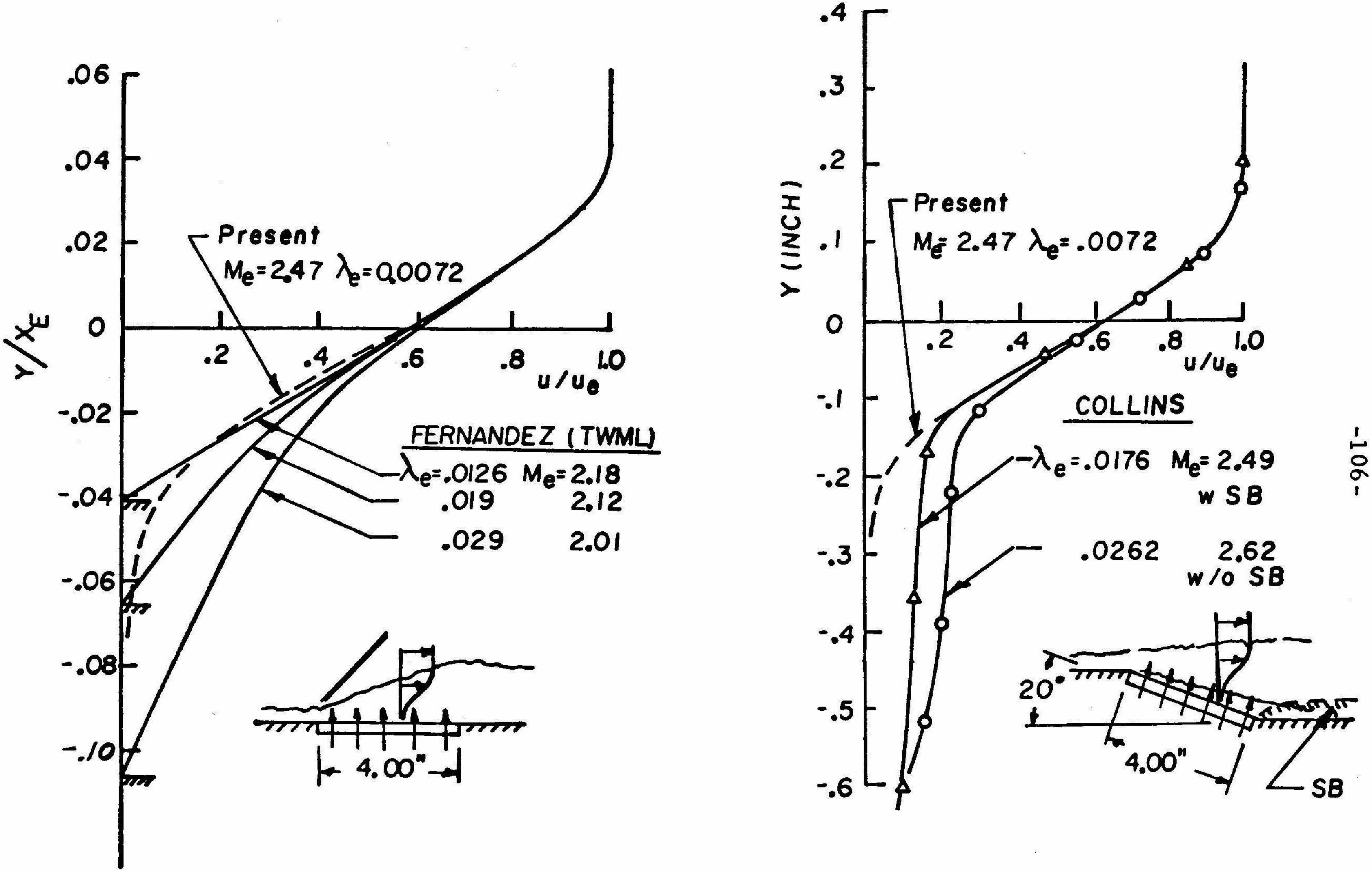

FIG. V.14 COMPARISONS OF VELOCITY PROFILES WITH VARIABLE MASS INJECTION RATES THROUGH FLAT PLATE MODEL AND 20° RAMP MODEL

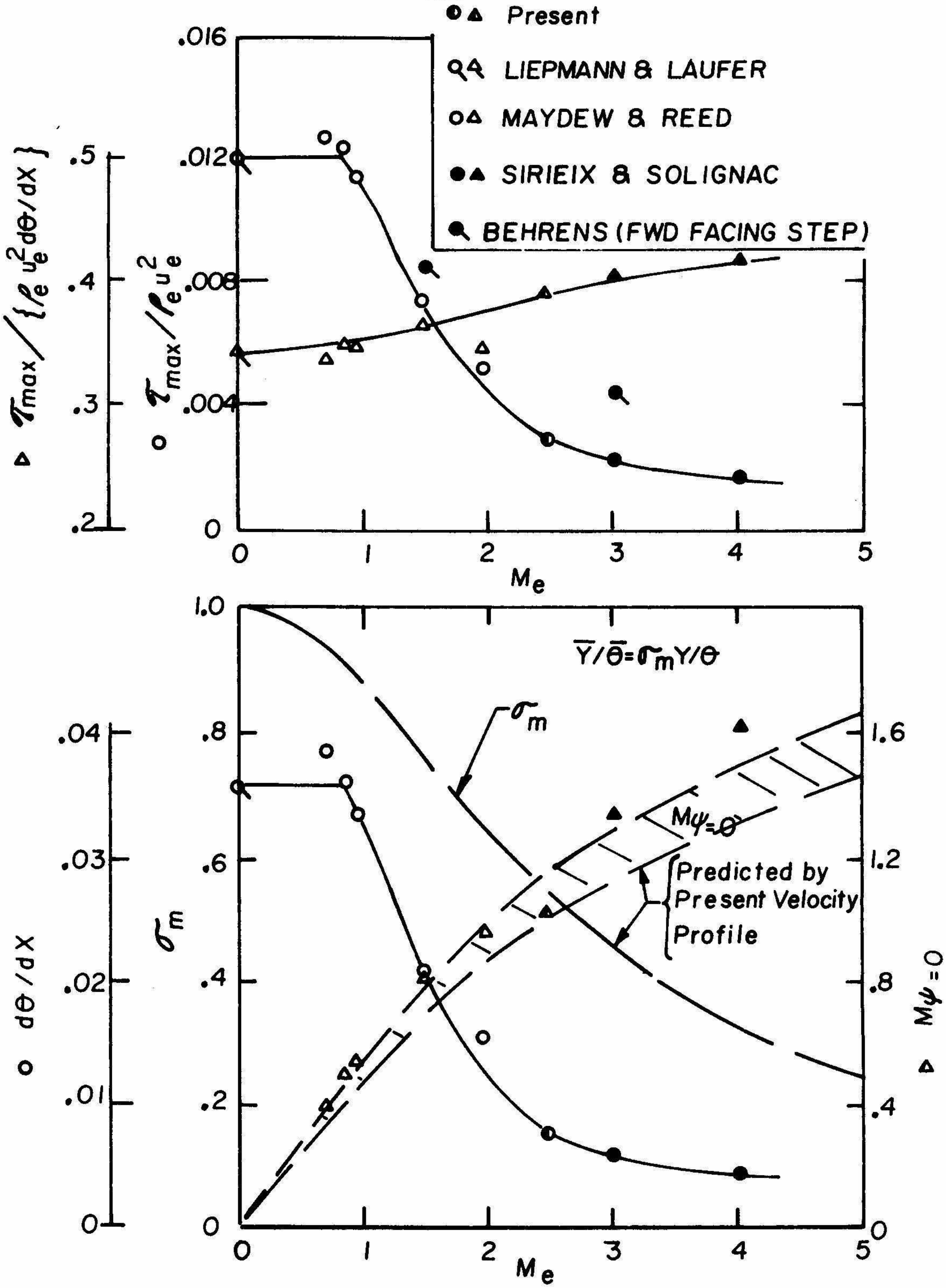

FIG. V. 15 TFML-VARIATIONS OF MAXIMUM SHEAR, MOM. THICK. GROWTH RATE, LINEAR SCALING PARAMETER AND DIVIDING STREAMLINE MACH NUMBER WRT EDGE MACH NUMBER

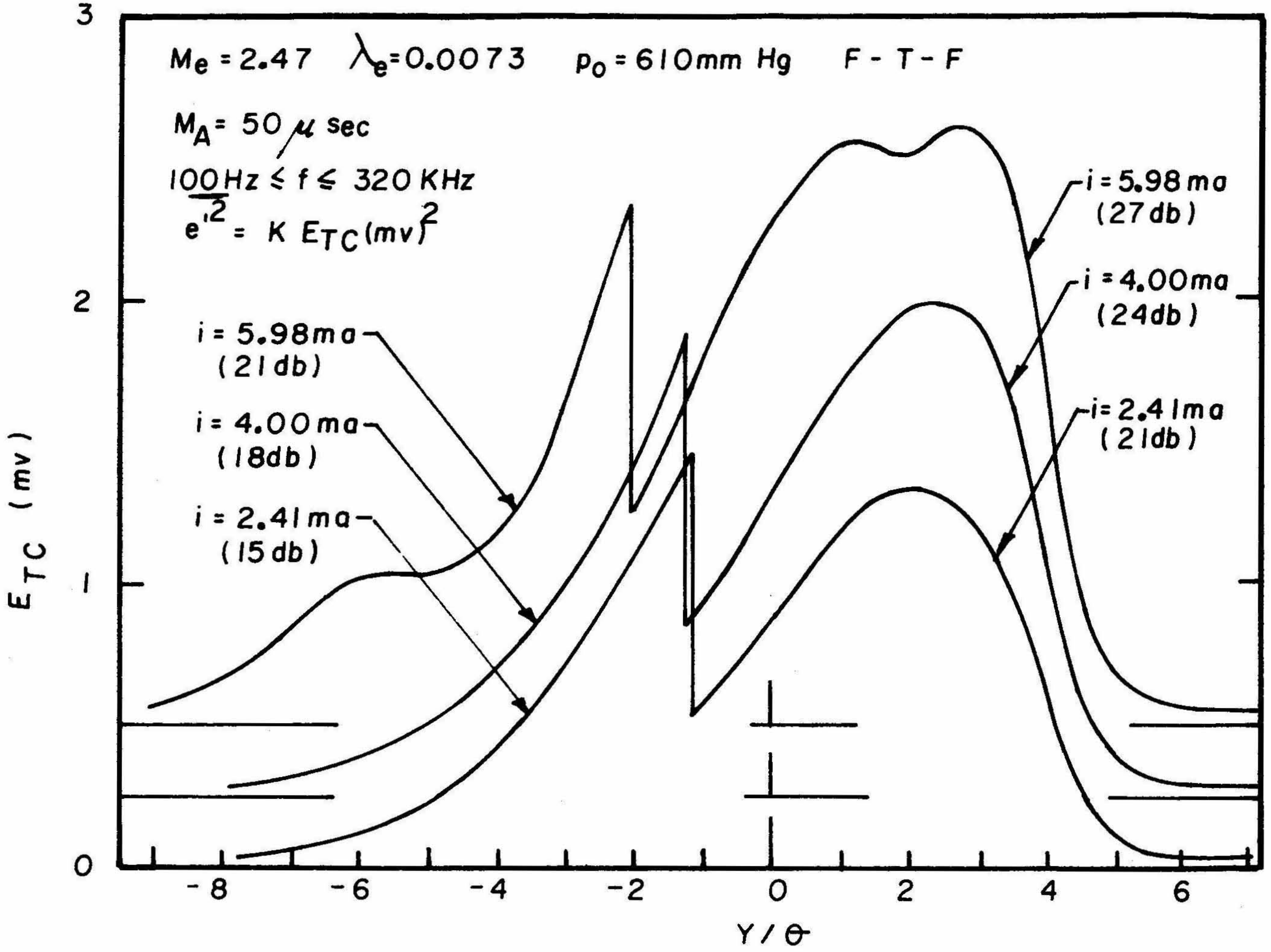

FIG. V.16 TURBULENT SIGNAL PROFILE MEASURED BY HOT-WIRE THERMOCOUPLE (E_{Tc})

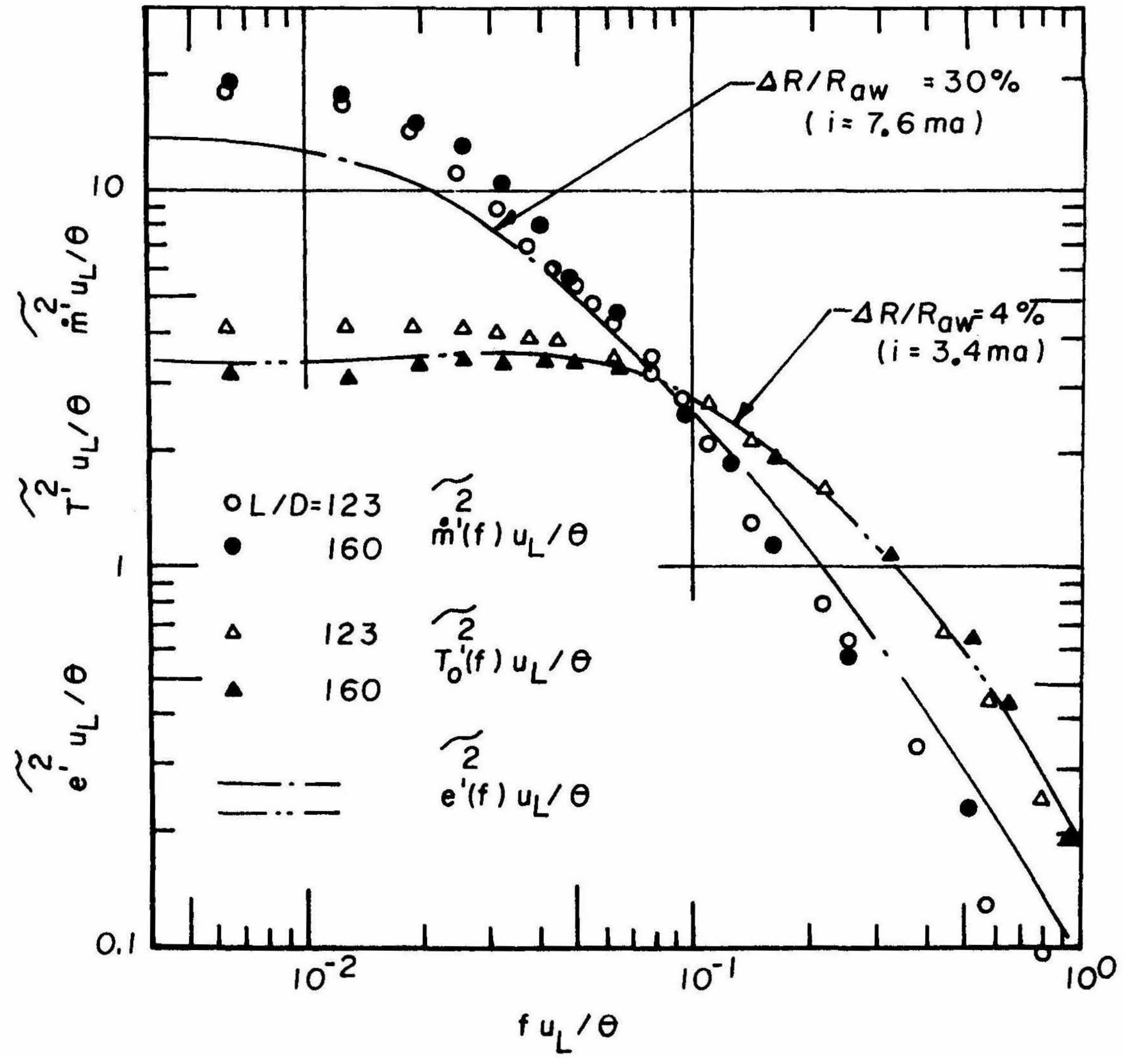

$X = 4.75$ $Y = 0.0$ $M_L = 1.334$

$M_e = 2.47$ $\lambda_e = 0.0073$ $p_0 = 735\,\text{mmHg}$ R-T-F

FIG. V.17 SPECTRA COMPARISON OF RESOLVED TURBULENT QUANTITIES AND RAW FLUCTUATION VOLTAGES

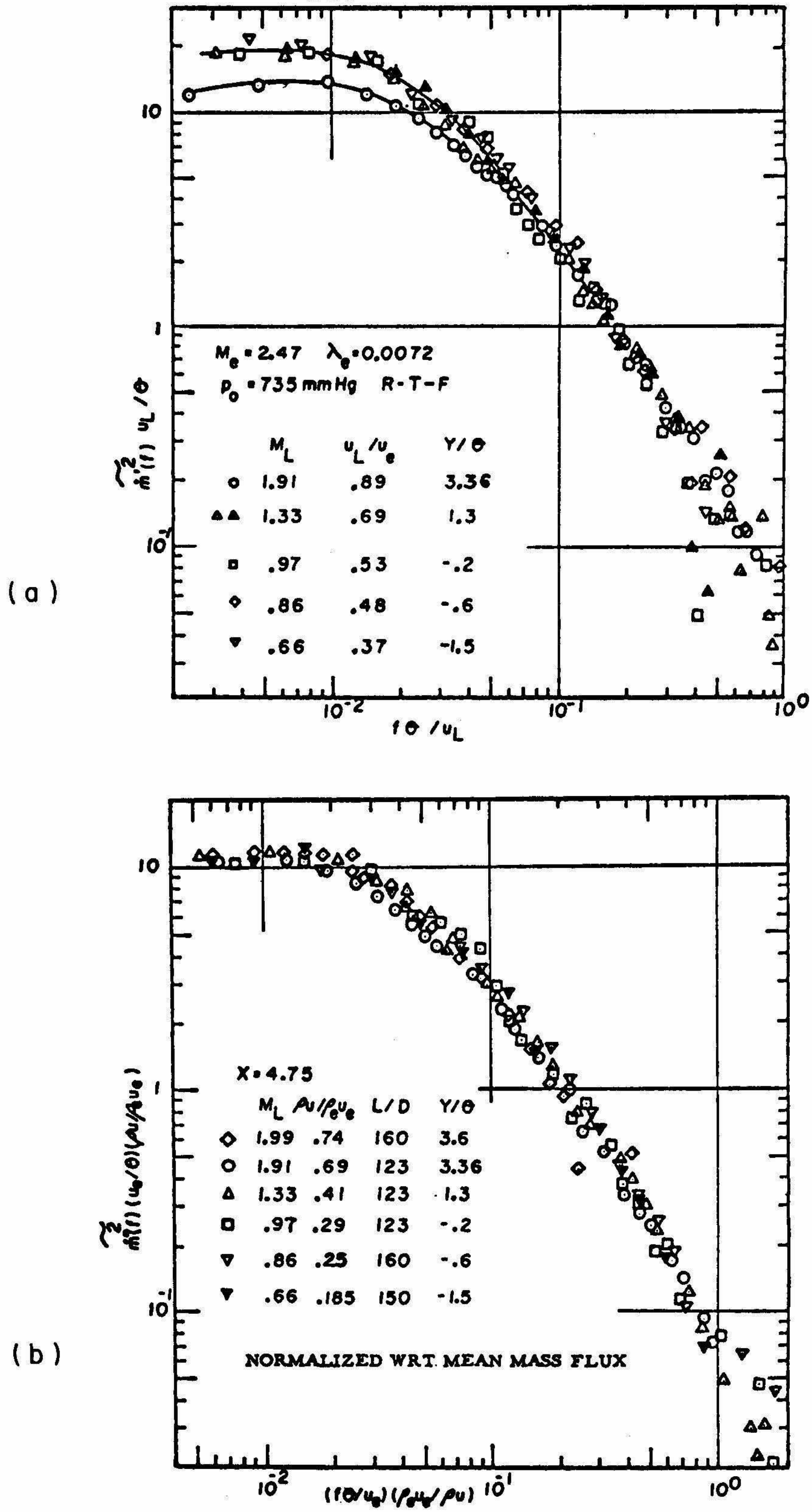

FIG. V.18 TFML MASS FLUX FLUCTUATION SPECTRA

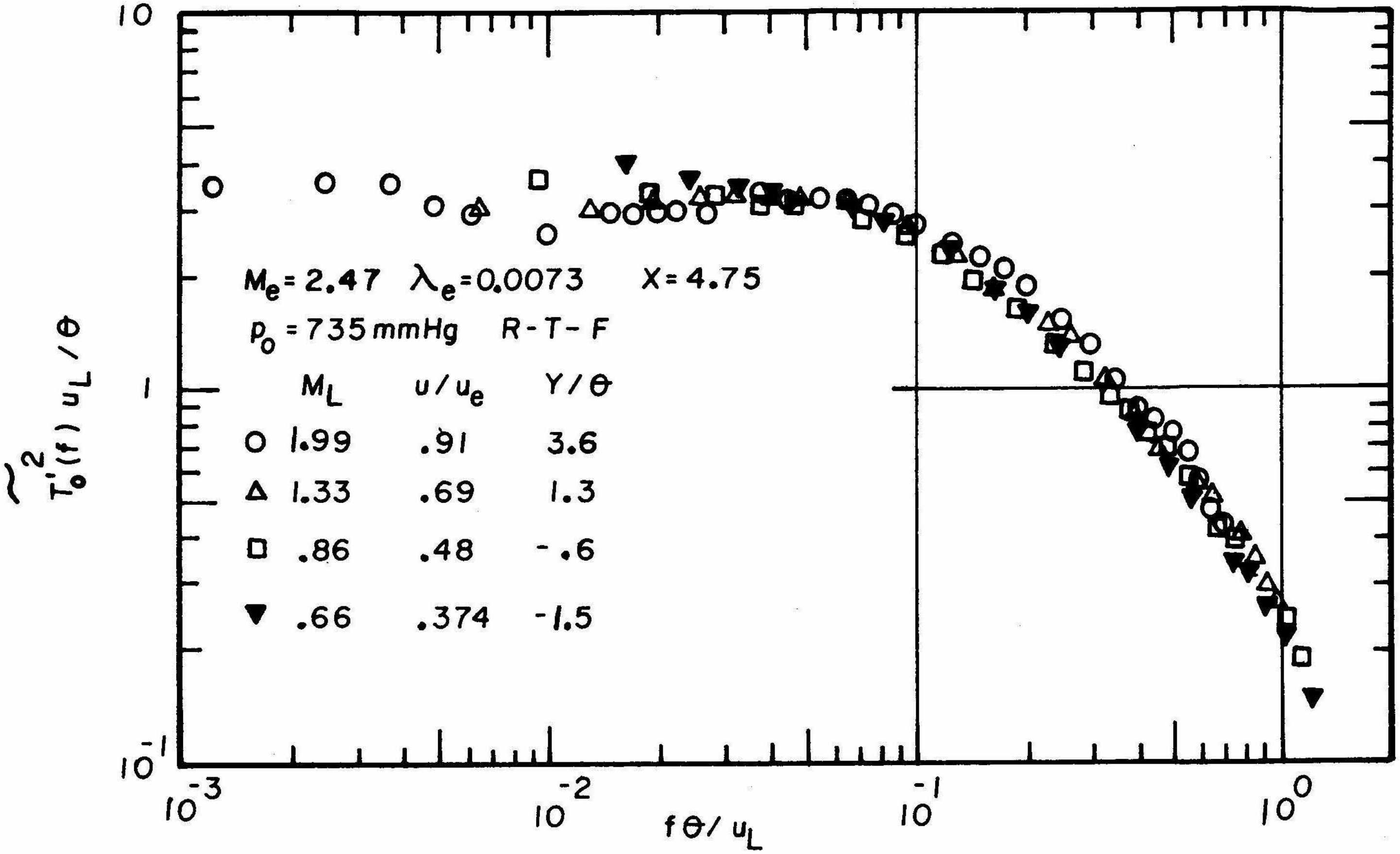

FIG. V.19 TFML - TOTAL TEMPERATURE FLUCTUATION SPECTRA

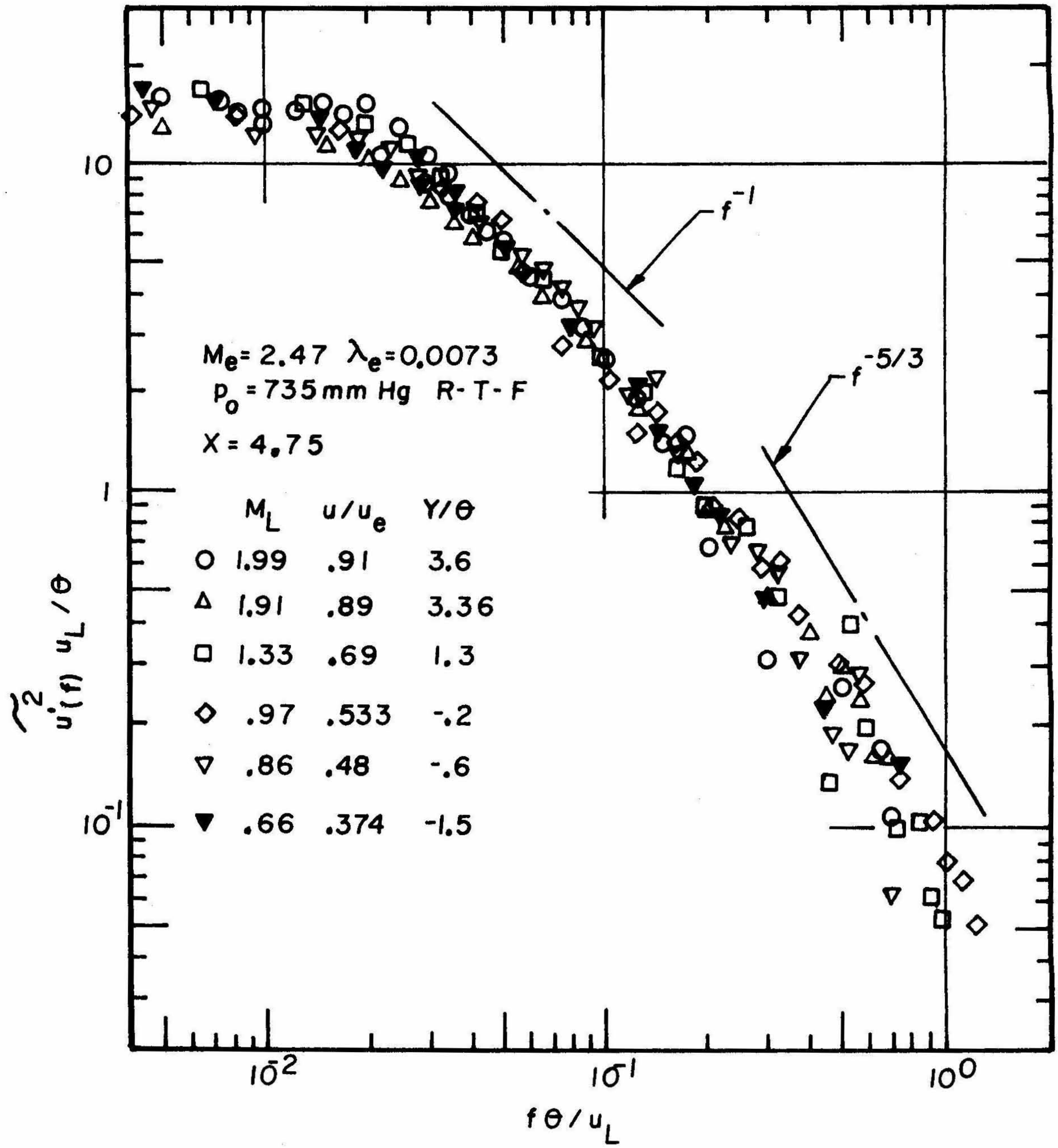

FIG. V. 20 TFML STREAMWISE VELOCITY FLUCTUATIONSPECTRA

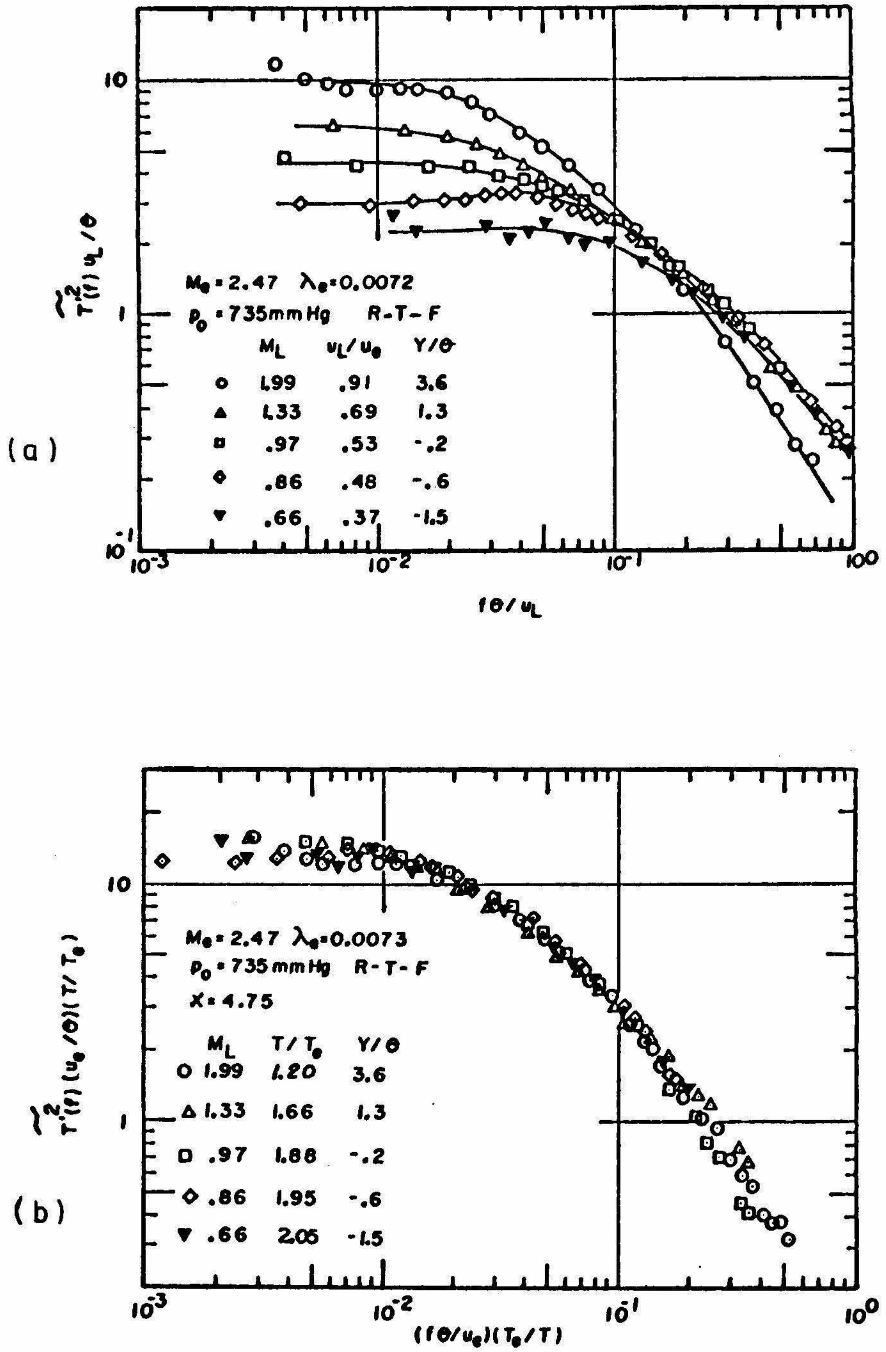

NORMALIZED WRT MEAN TEMPERATURE

FIG. V.21 TFML-STATIC TEMPERATURE FLUCTUATION SPECTRA

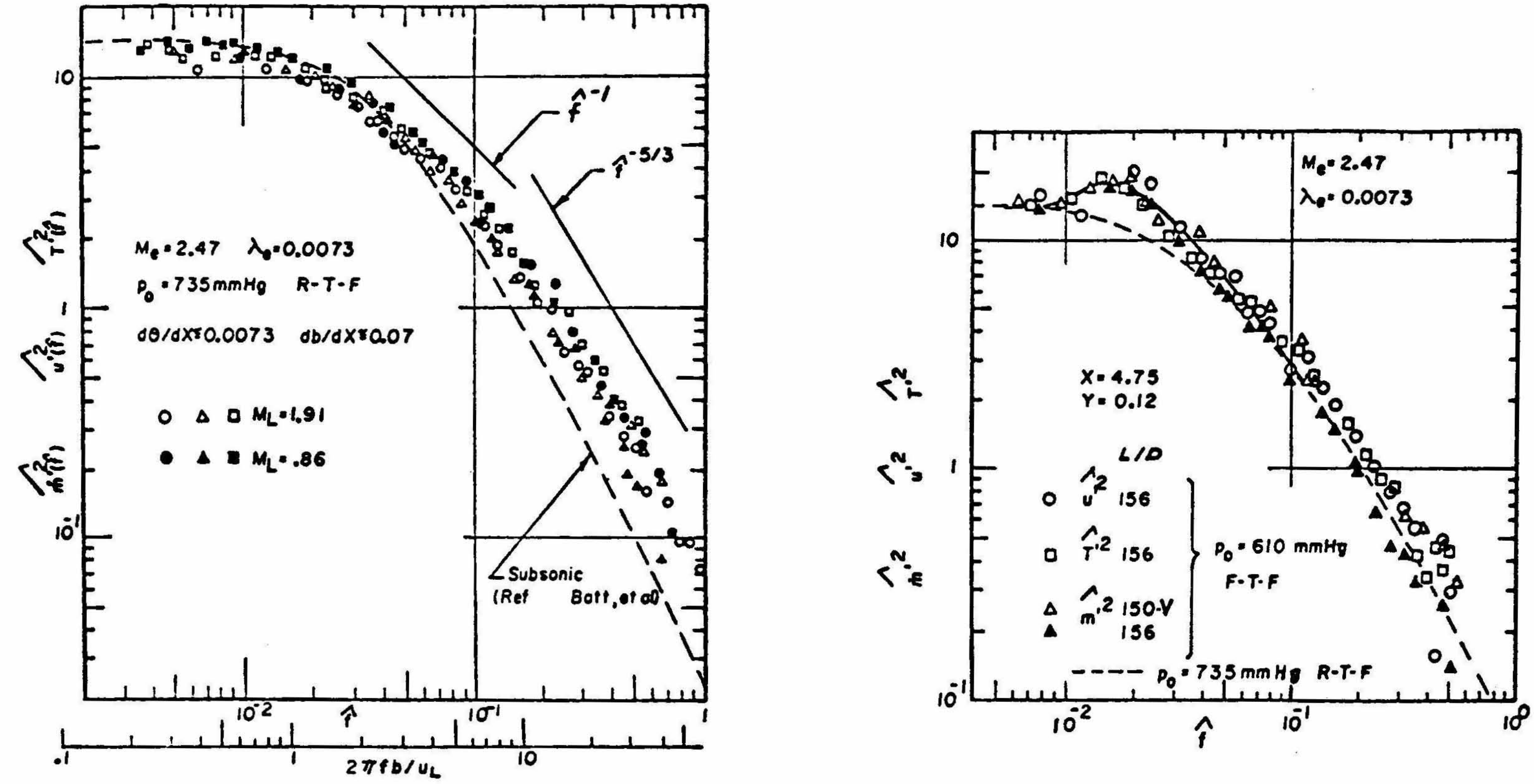

(a)

○ $\hat{\overline{\dot m'^2}}(\hat f) = (\overline{\dot m'^2}(f)\, u_e/\theta)(\rho u/\rho_e u_e)$ vs $(f\theta/u_e)(\rho_e u_e/\rho u)$

△ $\hat{\overline{u'^2}}(\hat f) = (\overline{u'^2}(f)\, u_e/\theta)(u/u_e)$ vs $(f\theta/u_e)(u_e/u)$

□ $\hat{\overline{T'^2}}(\hat f) = (\overline{T'^2}(f)\, u_e/\theta)(T/T_e)$ vs $(f\theta/u_e)(T_e/T)$

(b) EFFECT OF TURBULENT BOUNDARY LAYER INSTABILITY

FIG. V.22 COMPARISON OF TURBULENT SPECTRA NORMALIZED WITH RESPECTIVE MEAN FLOW QUANTITIES

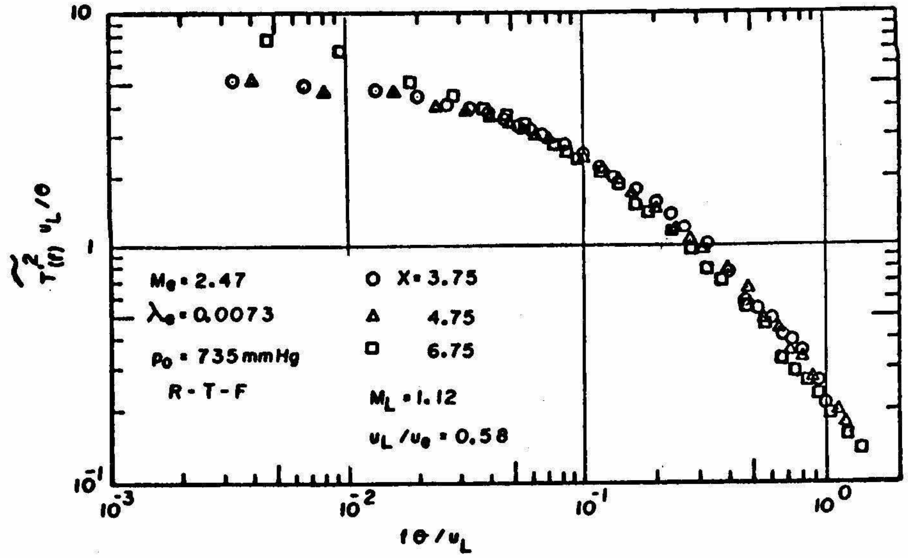

(b) SIMILAR FLOW - TFML STATIC TEMPERATURE FLUCTUATION SPECTRA

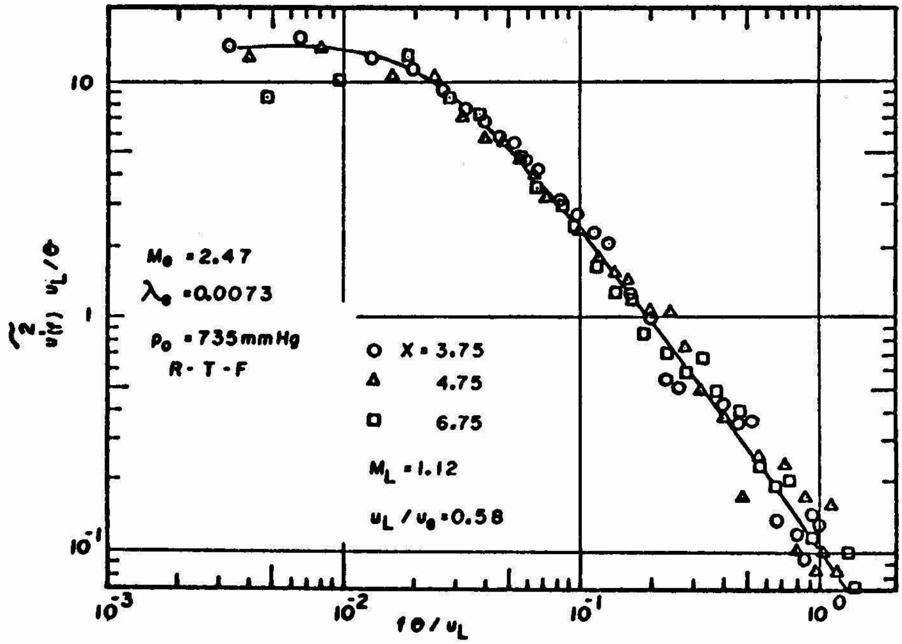

(a) SIMILAR FLOW - TFML STREAMWISE VELOCITY FLUCTUATION SPECTRA

FIG. V.23 SIMILAR FLOW SPECTRA

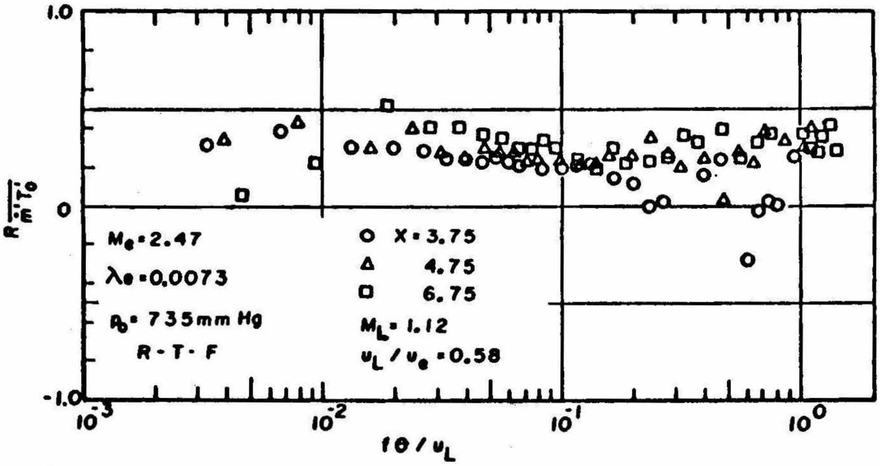

(c) SIMILAR FLOW - TFML CORRELATION COEFFICIENTS OF MASS FLUX - TOTAL TEMPERATURE FLUCTUATIONS

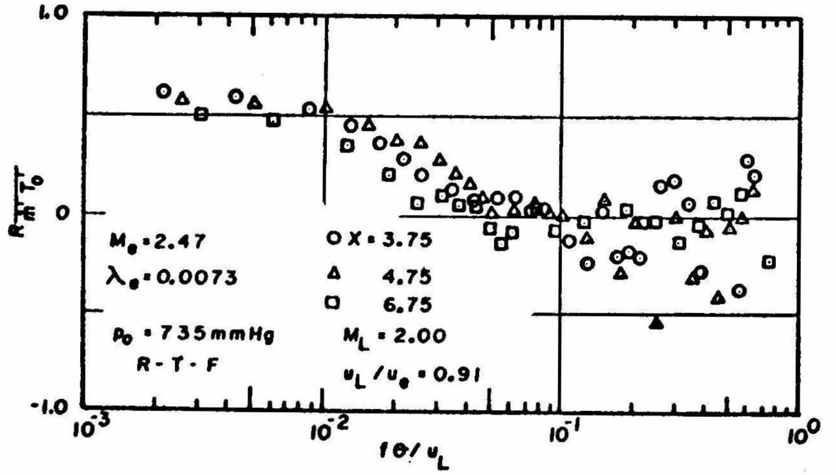

(d) SIMILAR FLOW - TFML CORRELATION COEFFICIENT OF MASS FLUX - TOTAL TEMPERATURE FLUCTUATION

FIG. V.23 SIMILAR FLOW CORRELATION COEFFICIENTS

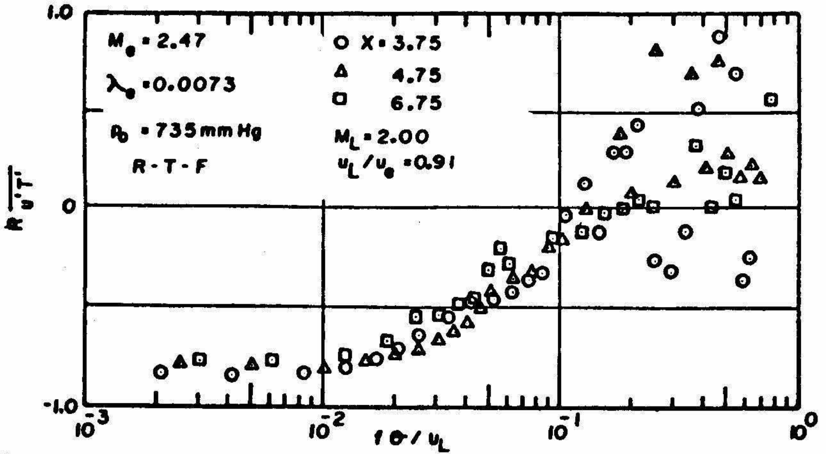

(e) SIMILAR FLOW - CORRELATION COEFFICIENTS OF STREAMWISE VELOCITY - STATIC TEMPERATURE FLUCTUATIONS

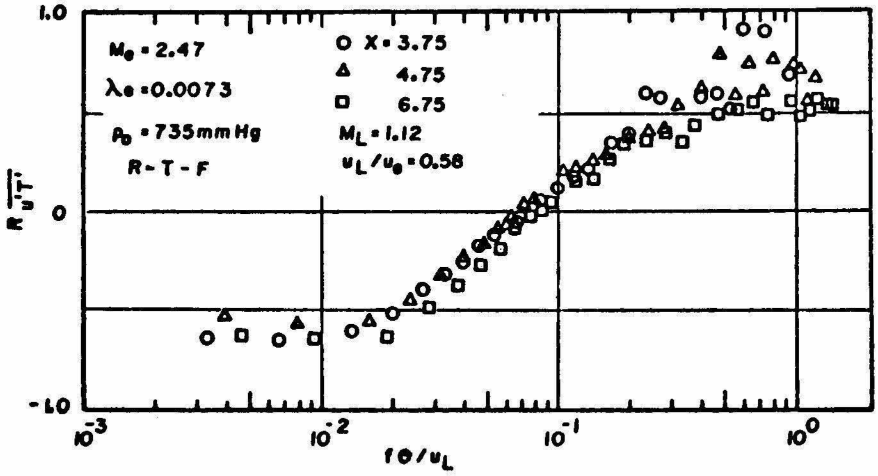

(f) SIMILAR FLOW - TFML CORRELATION COEFFICIENTS OF STREAMWISE VELOCITY - STATIC TEMPERATURE FLUCTUATION

FIG. V.23 SIMILAR FLOW CORRELATION COEFFICIENTS

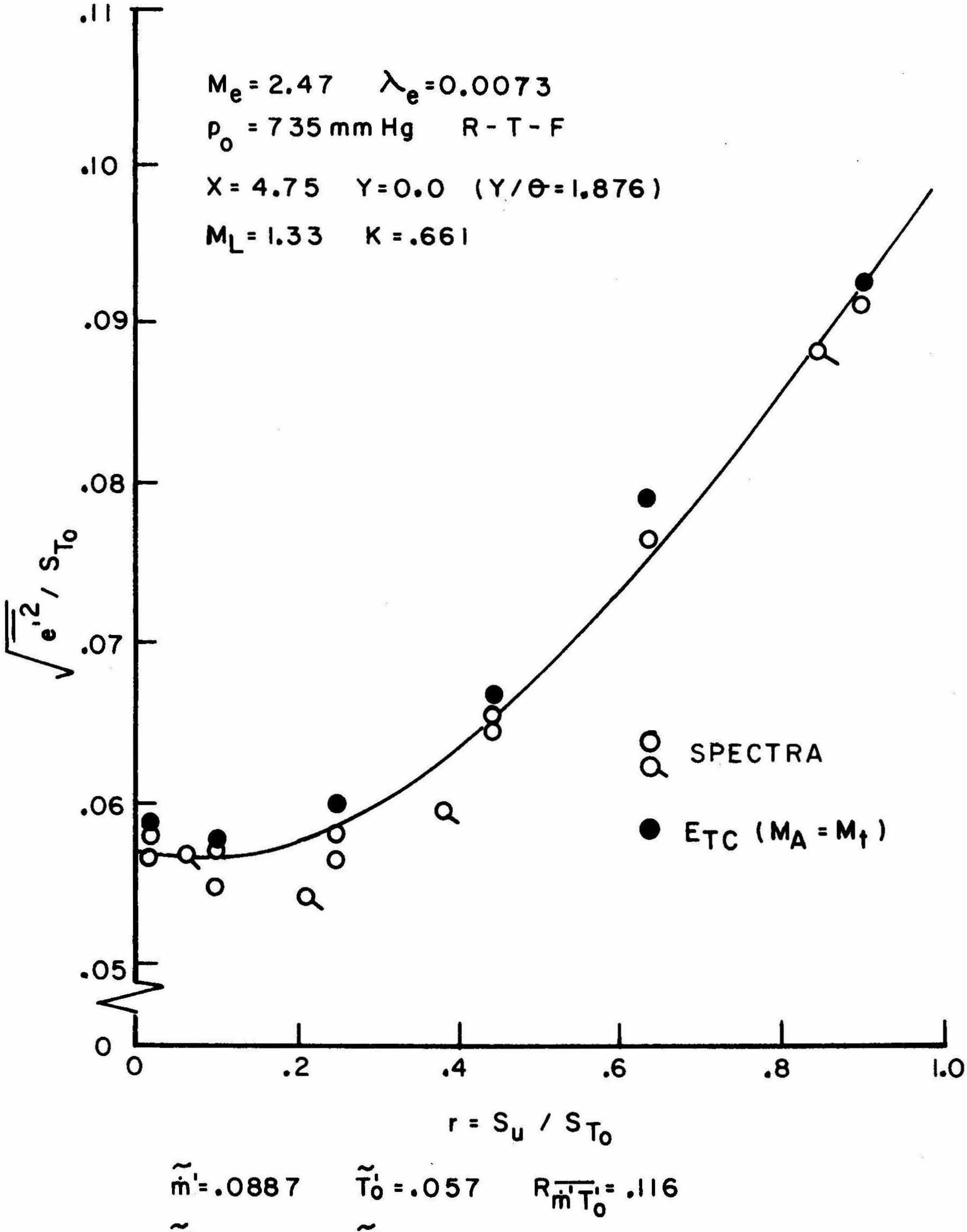

FIG. V. 24 TFML FLUCTUATION MODE DIAGRAM

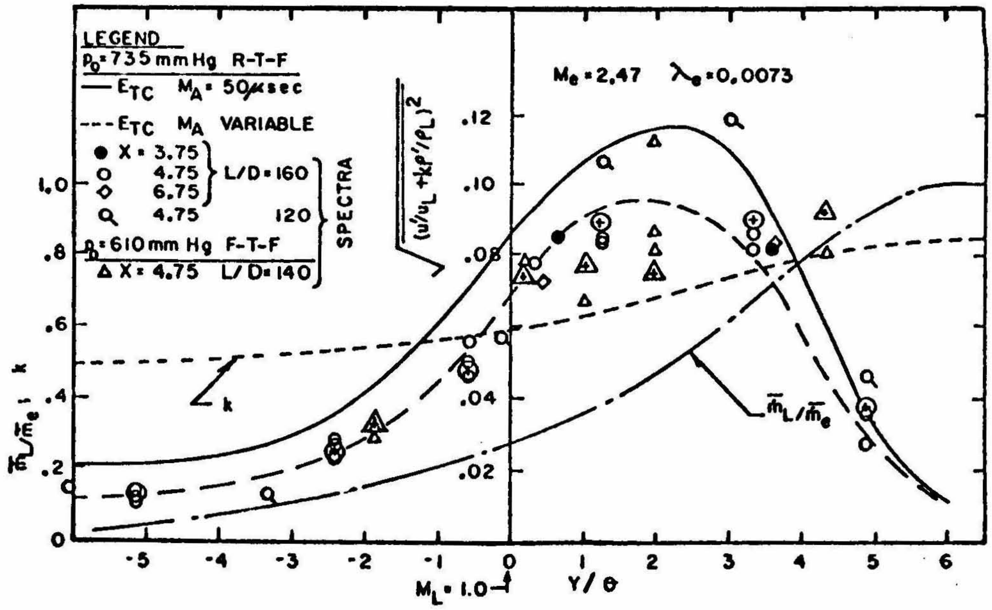

(a) MASS-FLUX FLUCTUATION PROFILE

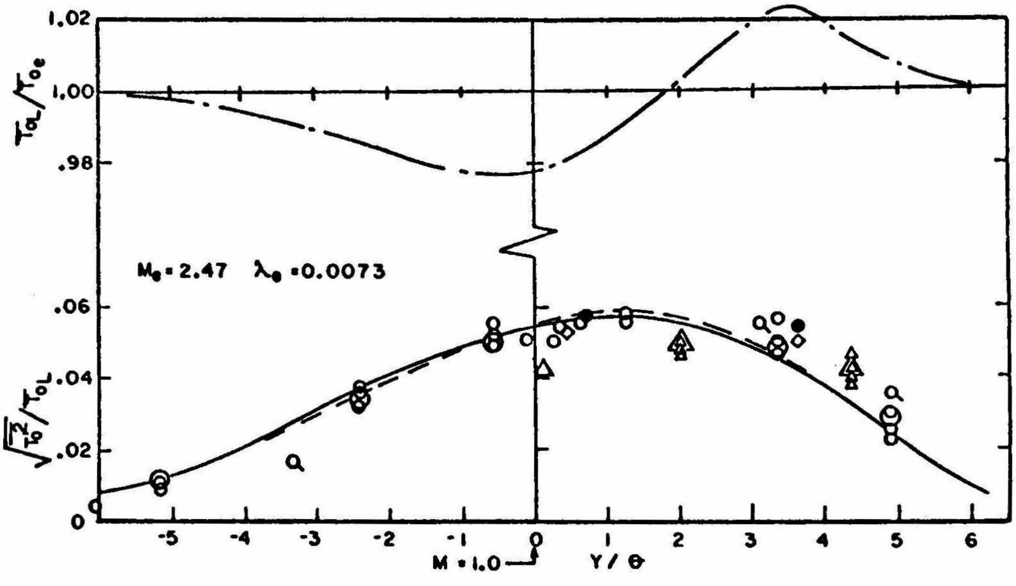

(b) TOTAL TEMPERATURE FLUCTUATION PROFILE

FIG. V.25 TURBULENCE PROFILES

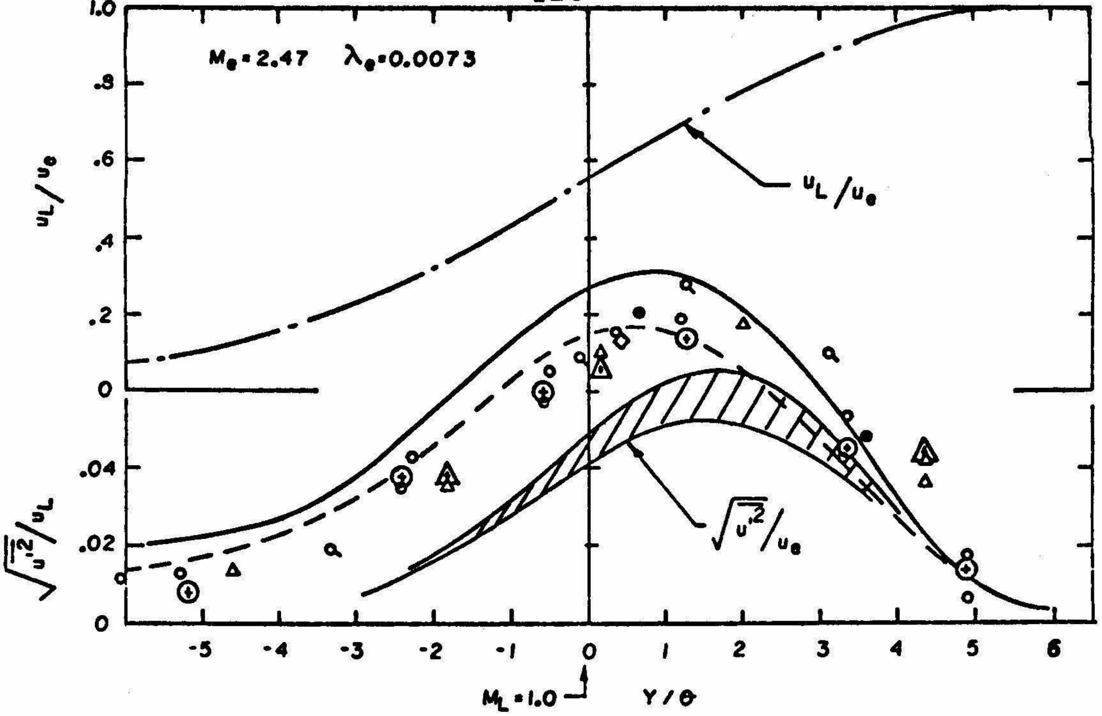

(c) VELOCITY FLUCTUATION PROFILE

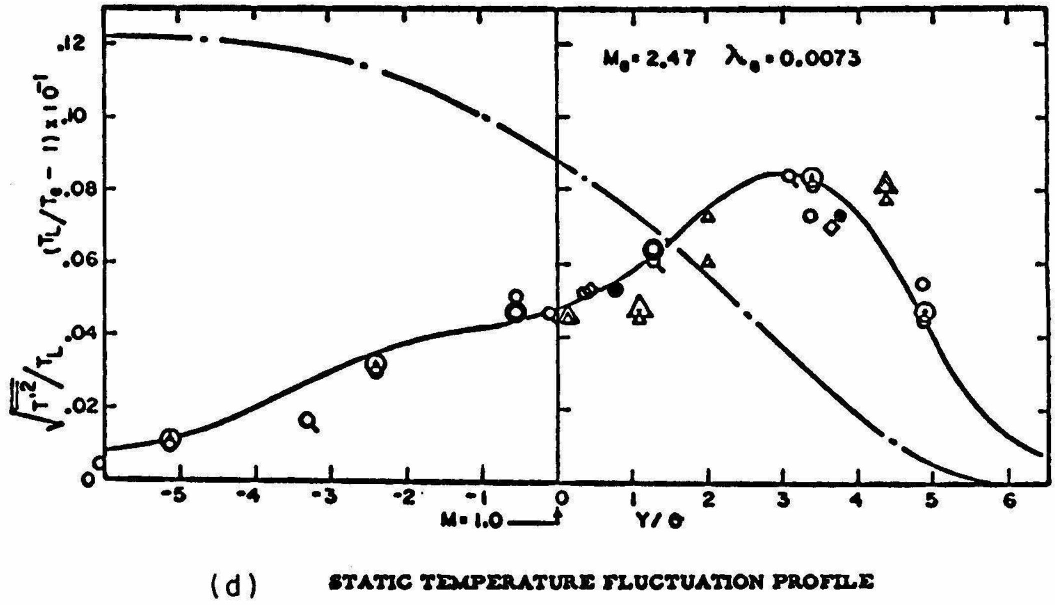

(d) STATIC TEMPERATURE FLUCTUATION PROFILE

FIG. V.25 TURBULENCE PROFILES

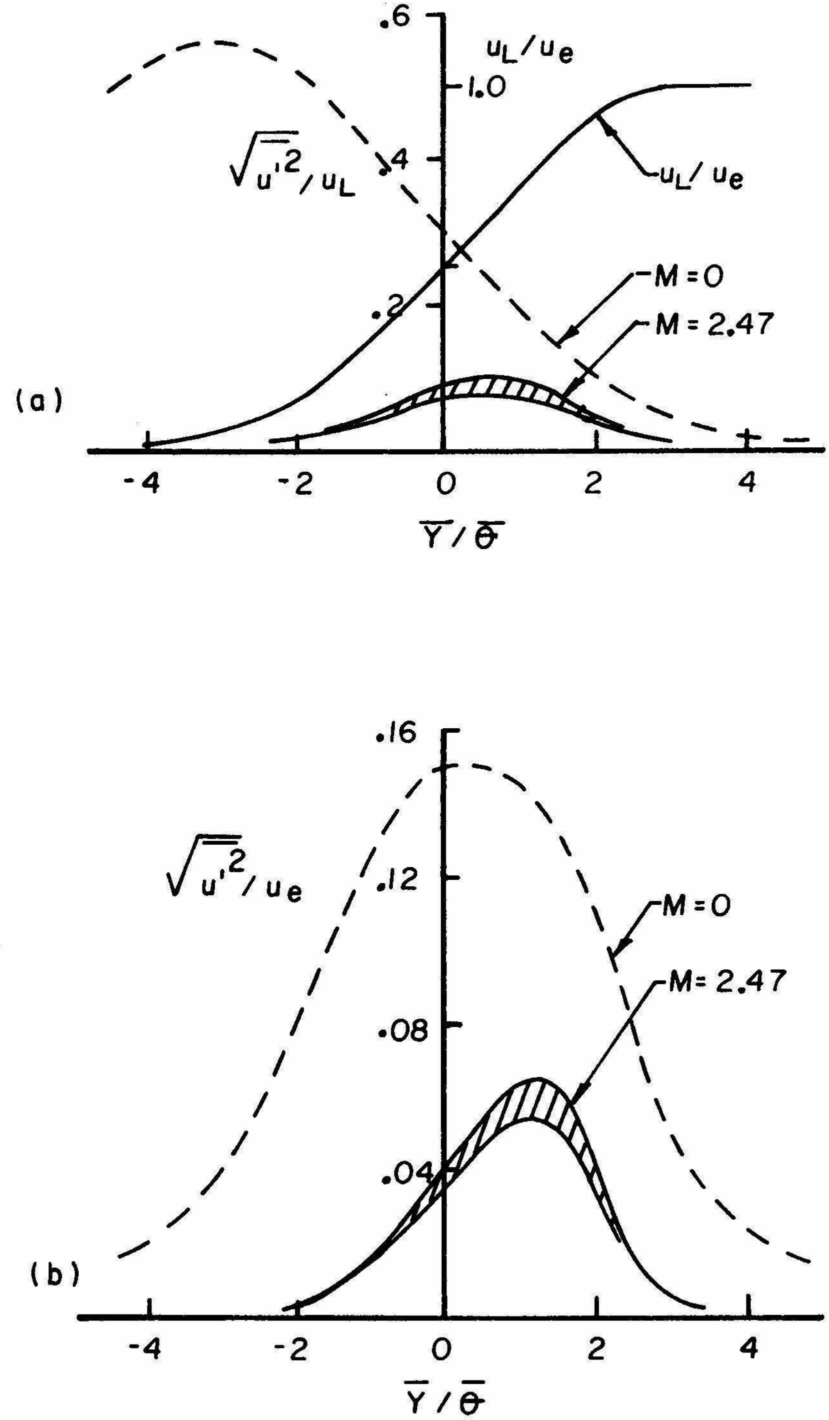

FIG. V.26 COMPARISON OF STREAMWISE VELOCITY FLUCTUATION WITH SUBSONIC DATA (LIEPMANN AND LAUFER)

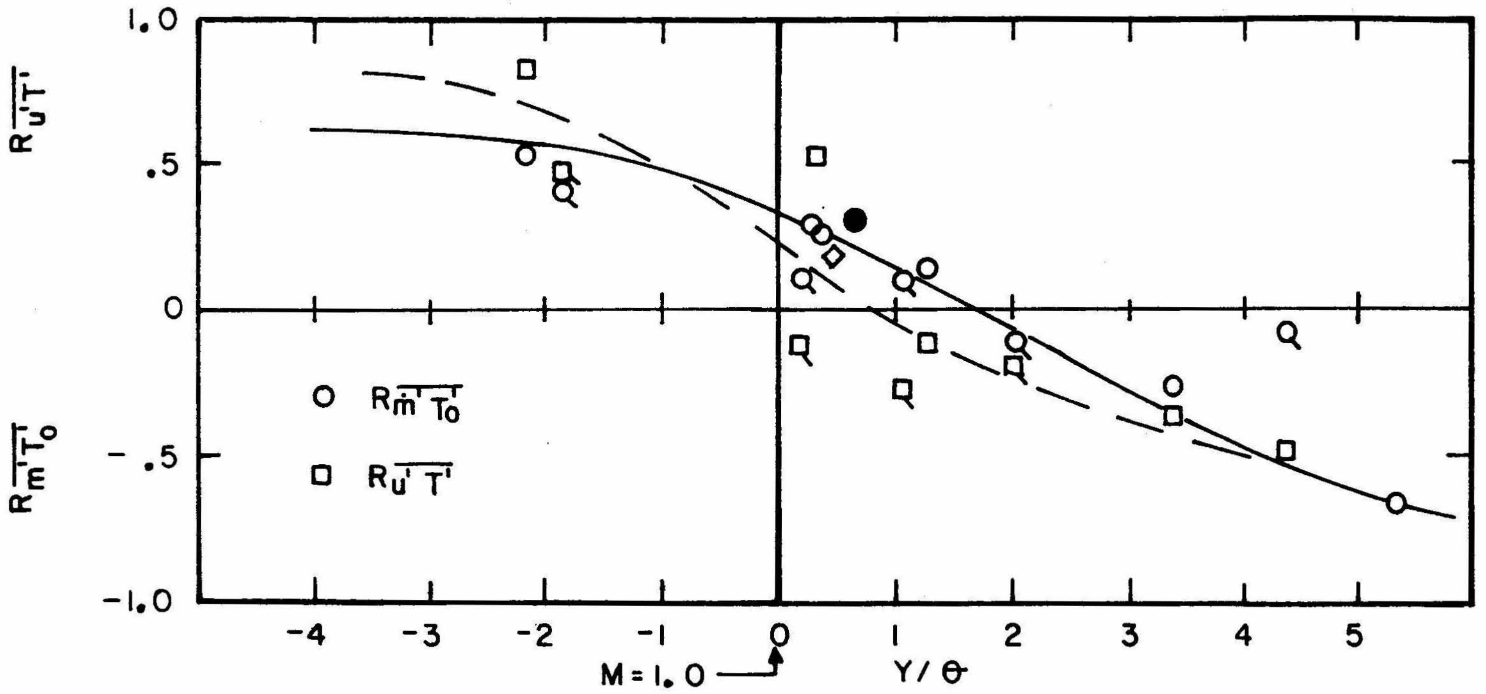

$M_e = 2.47$ $\lambda_e = 0.0073$

FLAGGED $p_o = 610$ mm Hg : UNFLAGGED $p_o = 735$ mm Hg

FIG. V.27 CORRELATION COEFFICIENT PROFILES

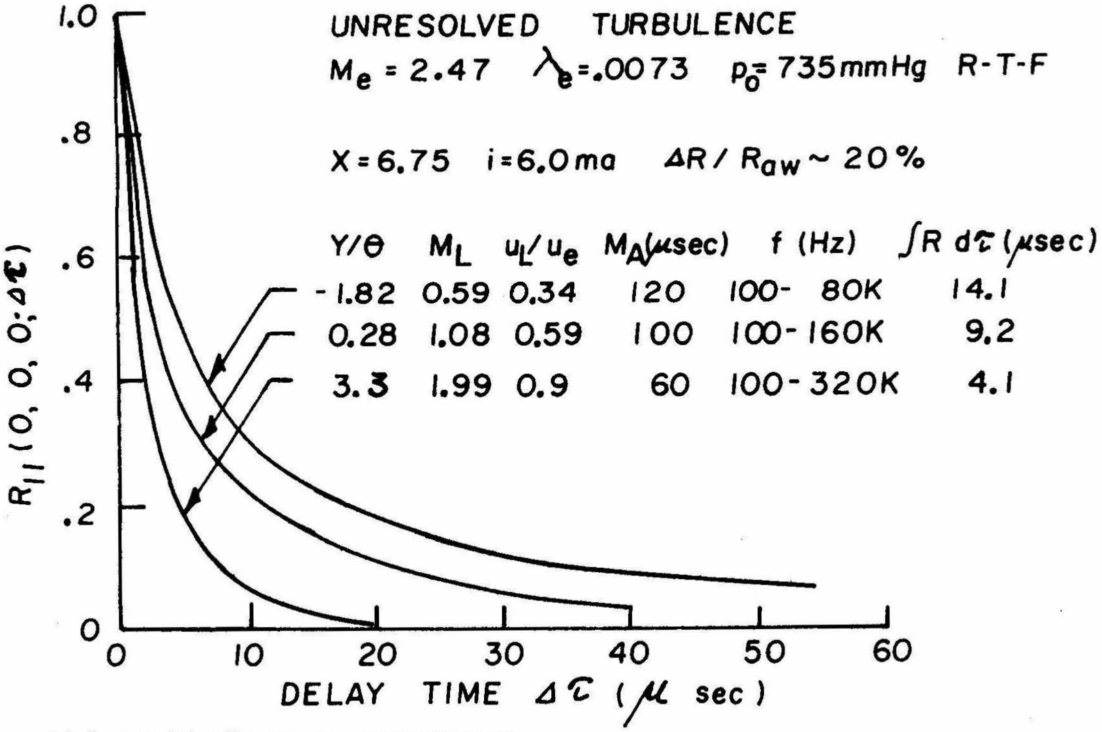

(b) VARIABLE Y-STATIONS

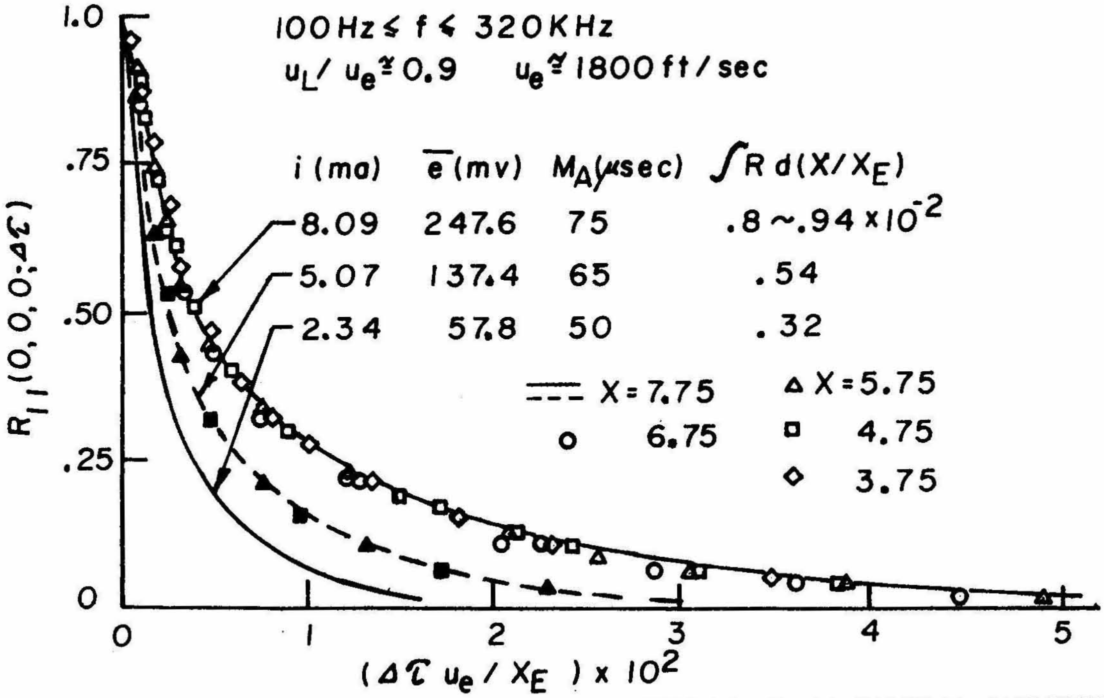

(a) SIMILAR AUTOCORRELATION FUNCTIONS - VARIABLE CURRENTS

FIG. V.28 COMPARISON OF AUTOCORRELATION FUNCTIONS

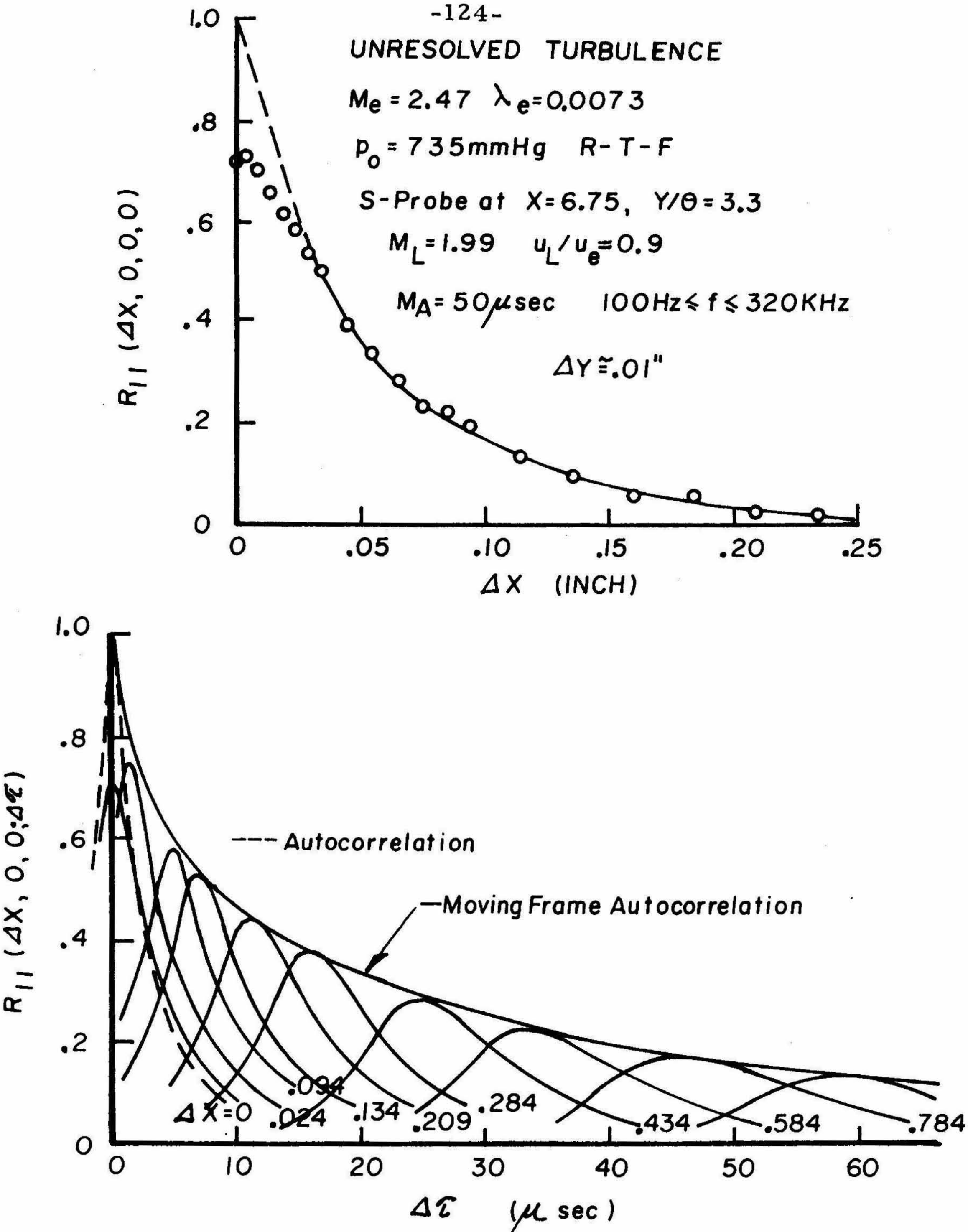

Streamwise Flow Component — Longitudinal Separation
Along Constant u_L/u_e

FIG. V.29 LONGITUDINAL SPACE-TIME CORRELATION FUNCTIONS OF STREAMWISE FLOW COMPONENT

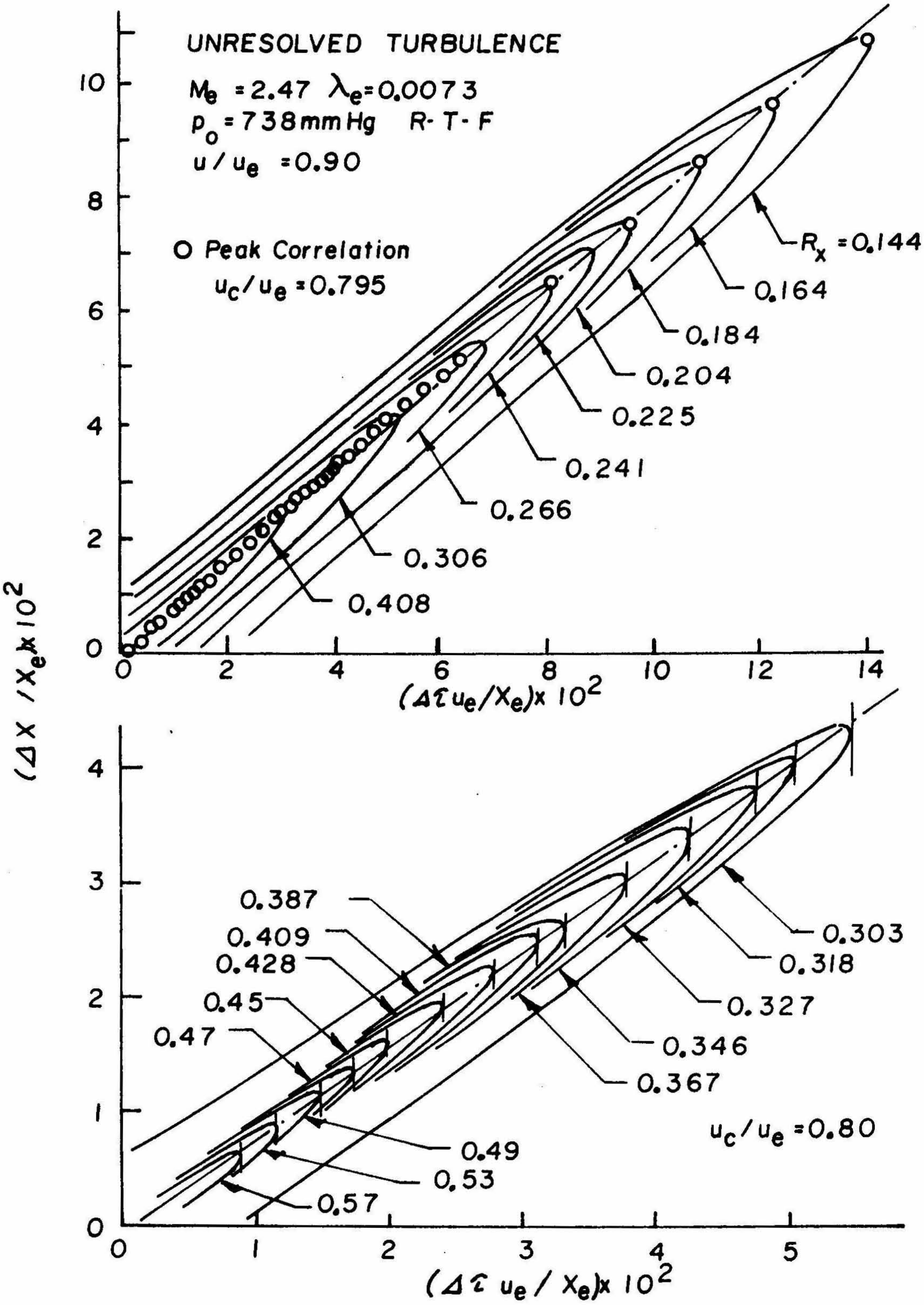

FIG. V. 30 TFML CONTOUR MAP -

SPACE TIME CORRELATION FUNCTIONS

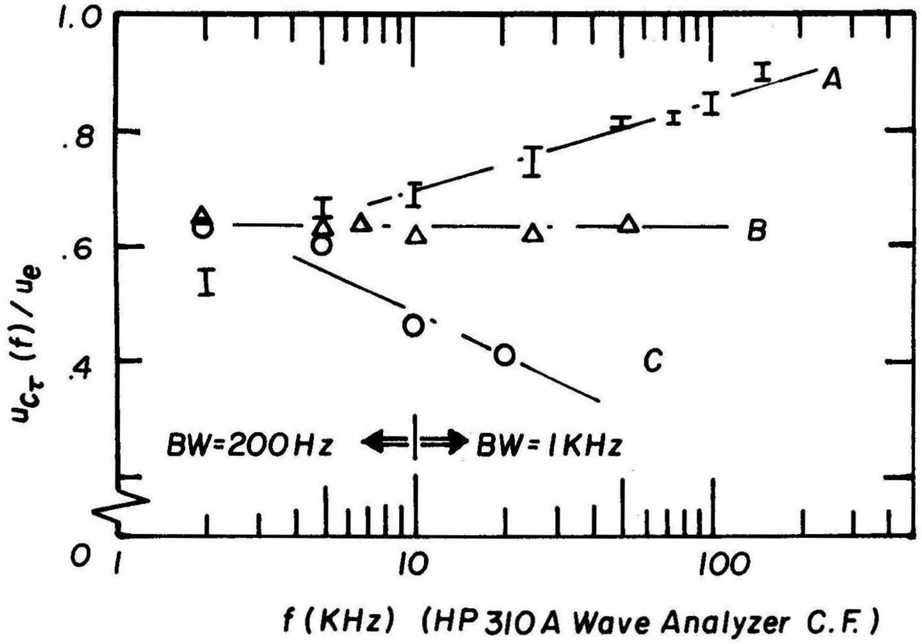

b) CONVECTION VELOCITY OF SELECTED FREQ. COMPONENTS

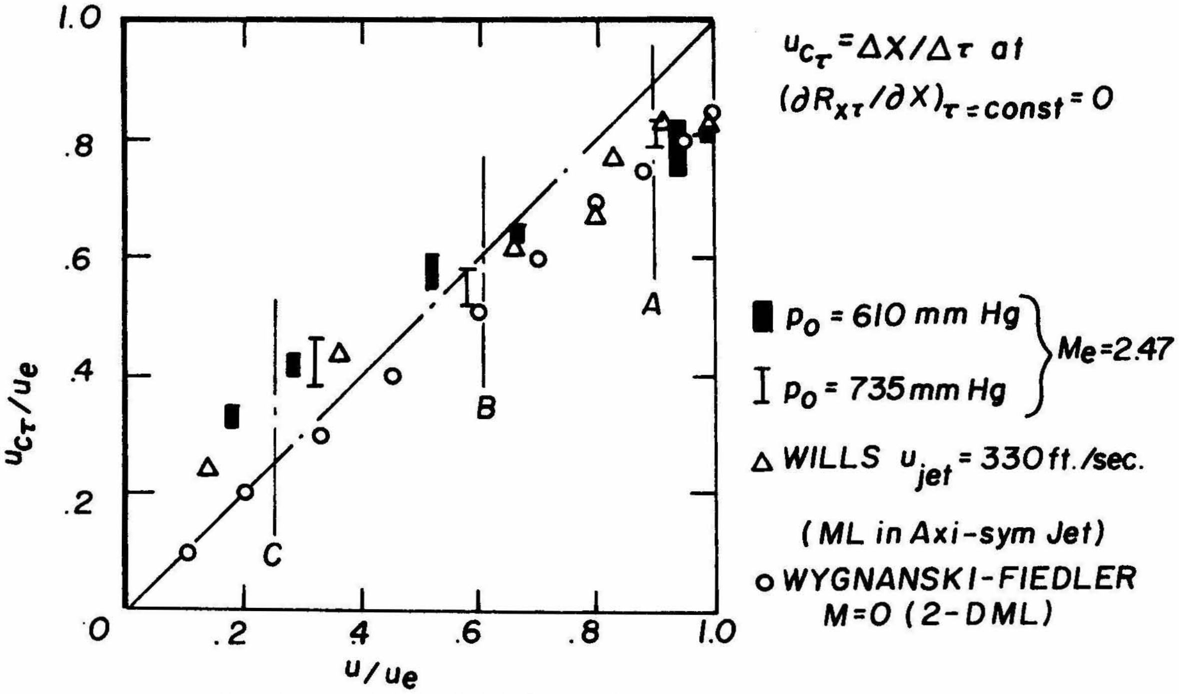

a) CONVECTION VELOCITY VS MEAN VELOCITY

FIG. V.31 TFML STREAMWISE TURBULENT

CONVECTION VELOCITIES

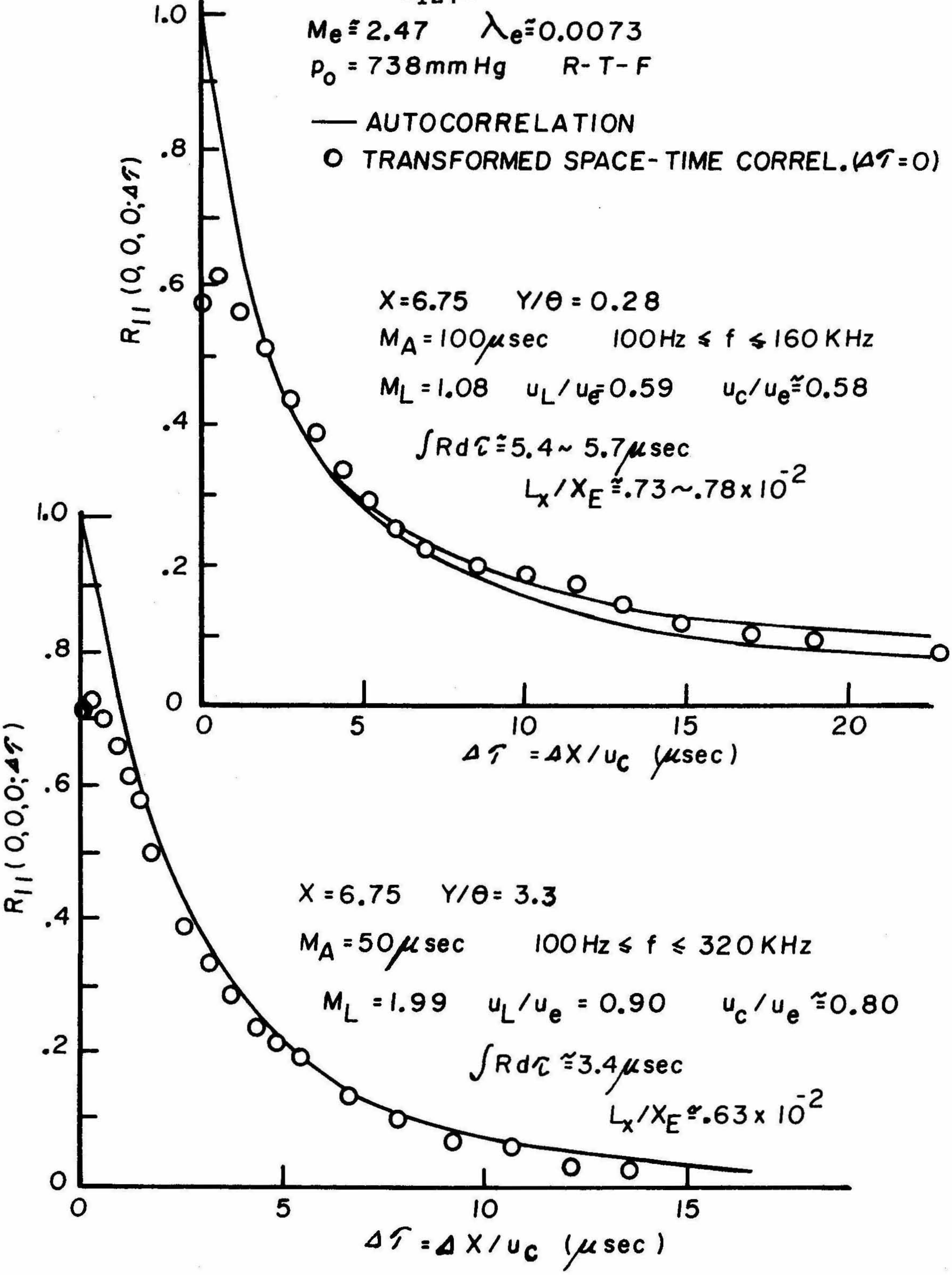

FIG. V.32 TFML-COMPARISON OF UNRESOLVED TURBULENT AUTO AND SPACE-TIME CORRELATION FUNCTIONS (TAYLOR'S HYPOTHESIS)

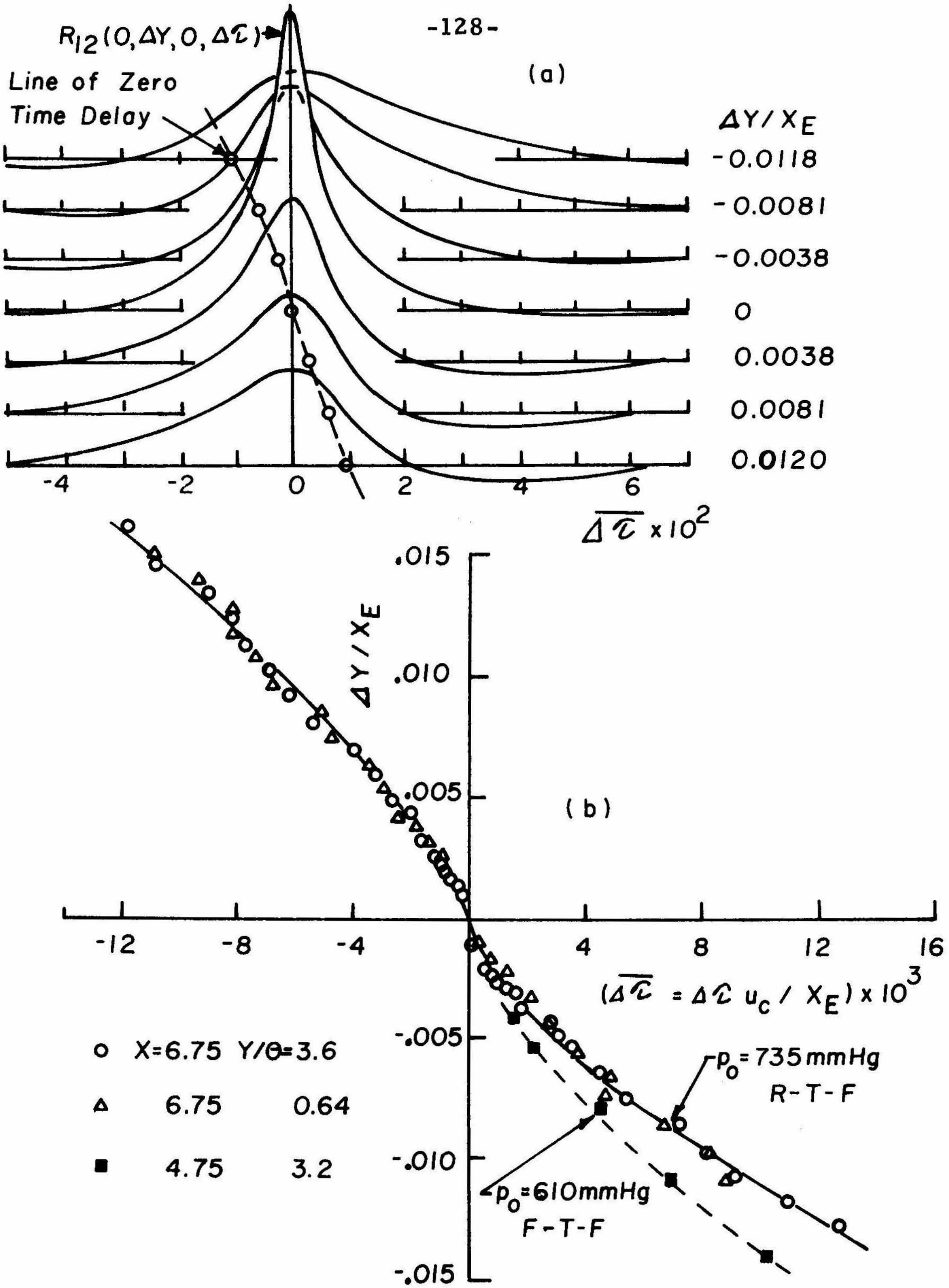

FIG. V.33 LATERAL SPACE-TIME CORRELATION FUNCTIONS AND ARRIVAL TIME OF MAXIMUM CROSSCORRELATION OF STREAMWISE FLOW COMPONENT

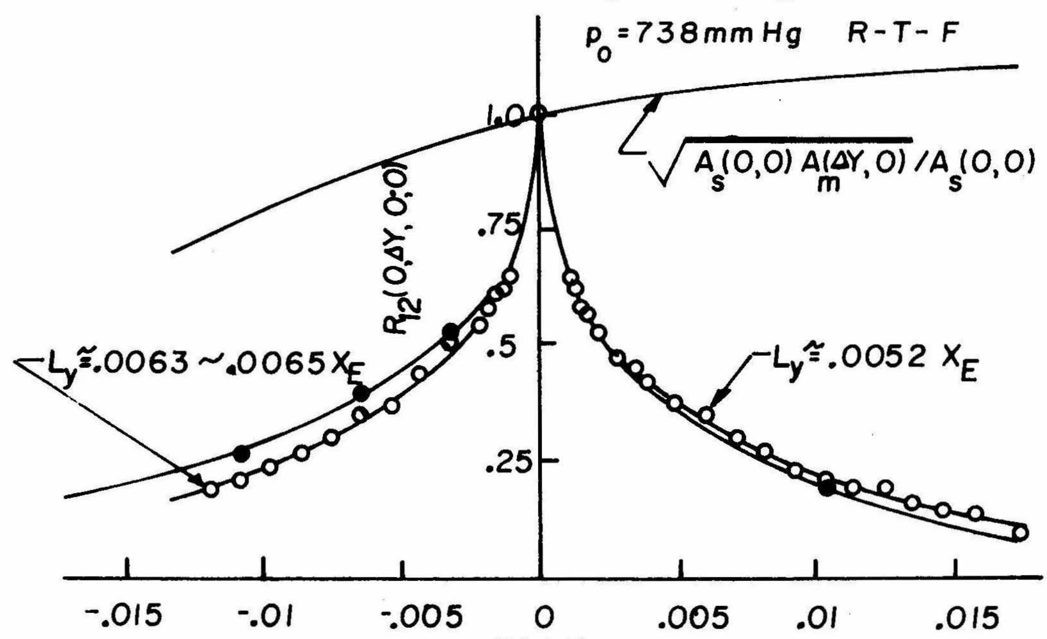

(a) S-Probe: $X = 6.75$

$Y/\theta = 0.64$ $i = 6.0$ ma $M_A = 50\,\mu$sec $100\,\text{Hz} \leq f \leq 320\,\text{KHz}$

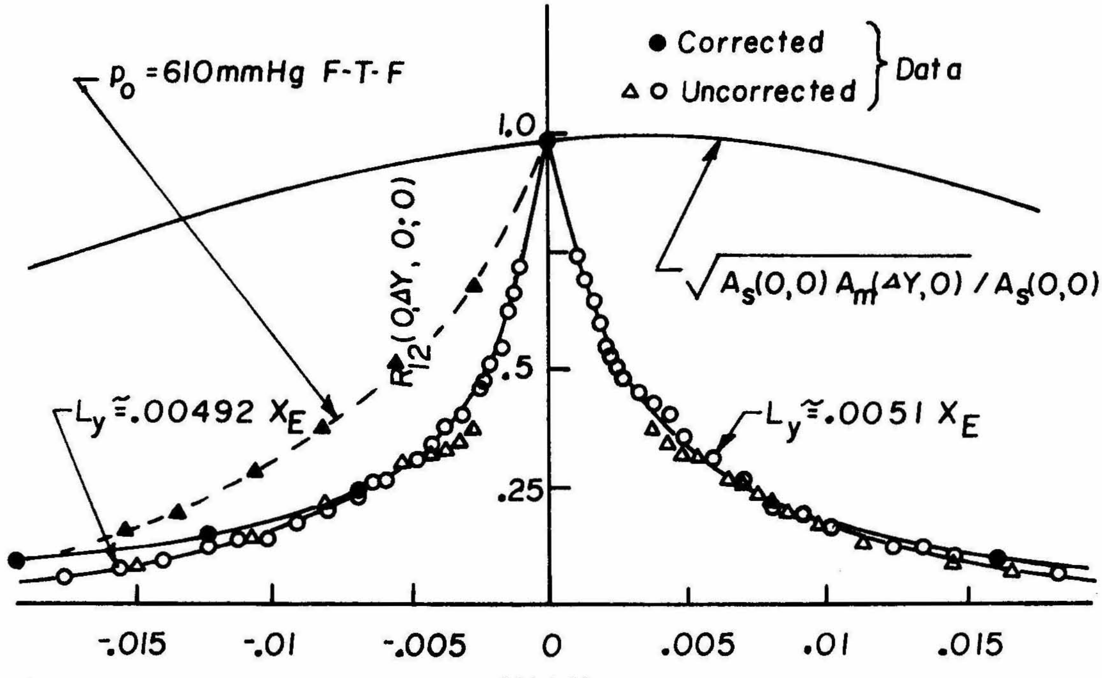

(b) S-Probe: $X = 6.75$

$Y/\theta = 3.6$ $i = 6.0$ ma $M_A = 50\,\mu$sec $100\,\text{Hz} \leq f \leq 320\,\text{KHz}$

FIG. V.34 LATERAL CORRELATION FUNCTIONS OF STREAMWISE FLOW COMPONENT

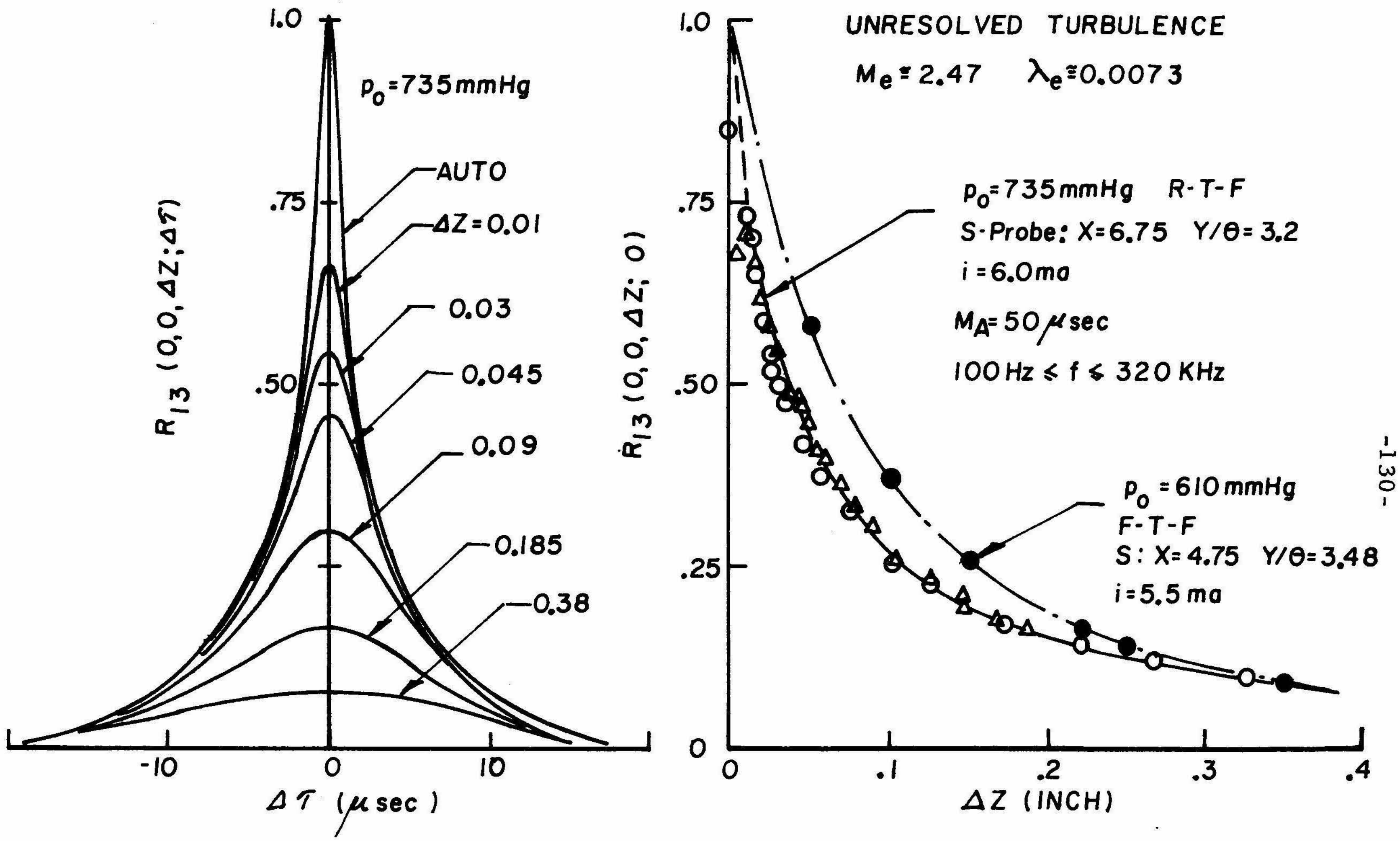

FIG.V.35 TFML-SPANWISE CROSS AND SPACE CORRELATION FUNCTIONS OF STREAMWISE FLOW COMPONENT

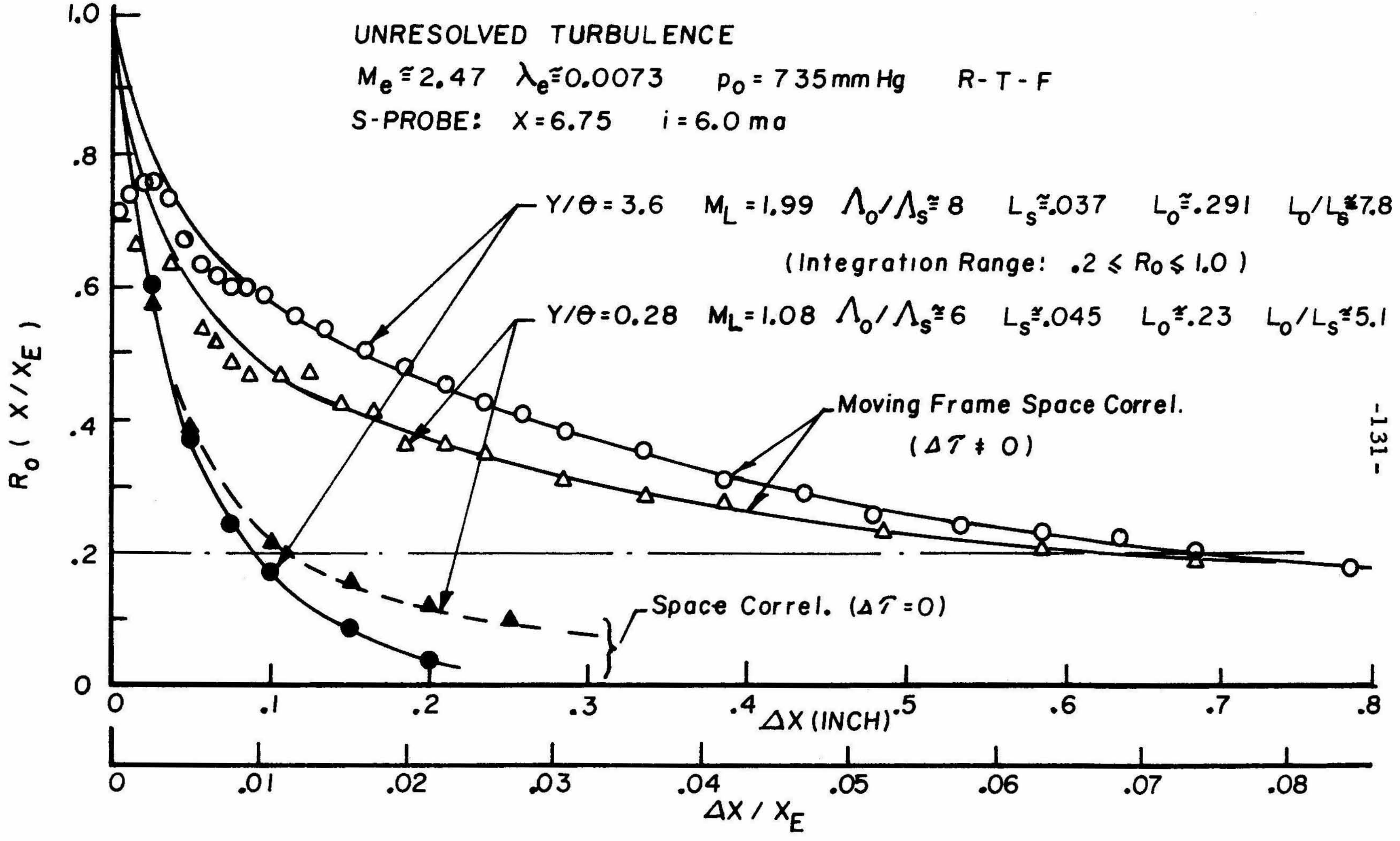

FIG. V.36 TFML-COMPARISON OF FIXED FRAME ($\Delta\tau = 0$) AND MOVING FRAME ($\Delta\tau \neq 0$) SPACE CORRELATION FUNCTIONS

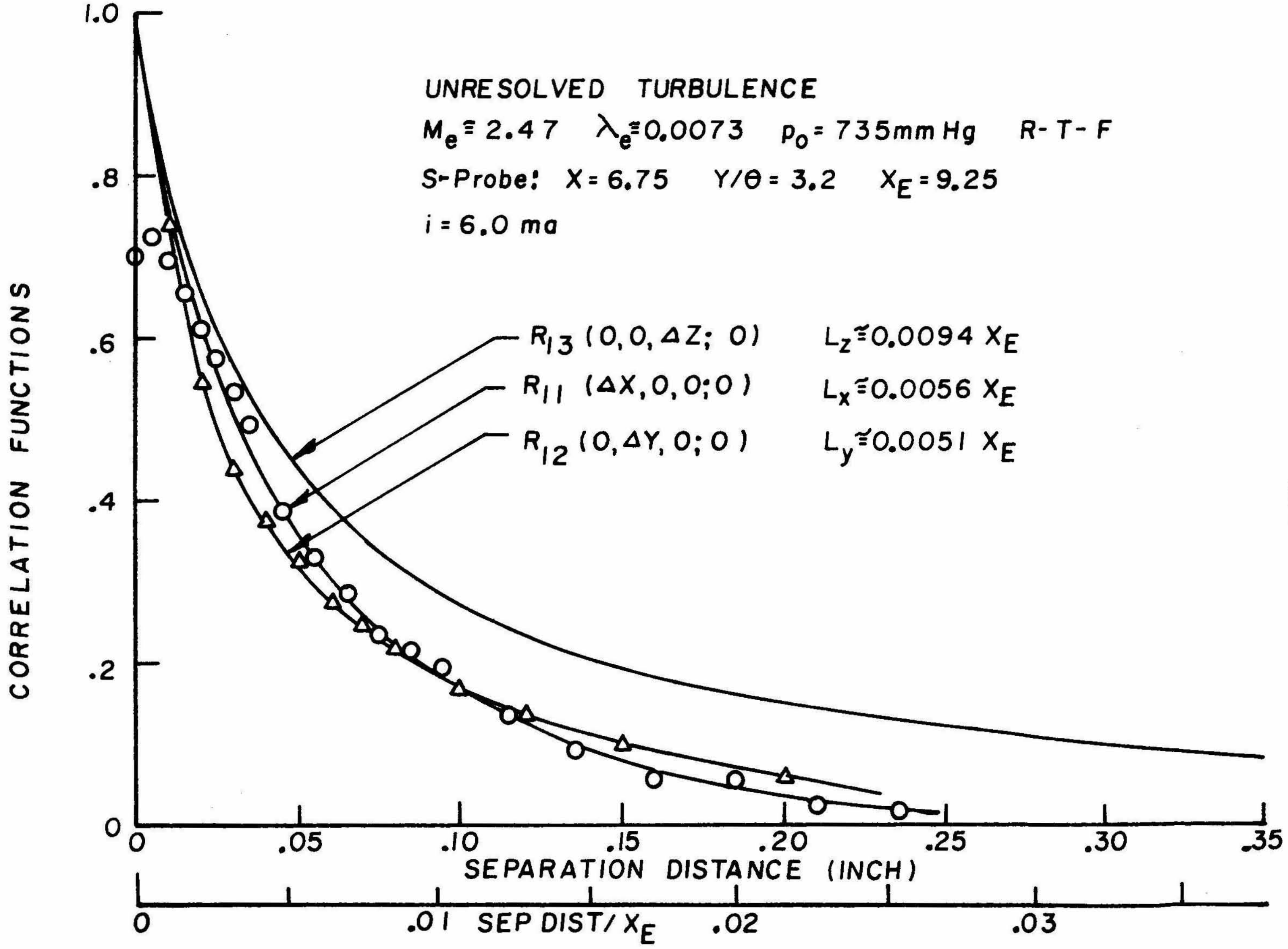

FIG. V.37 TFML-COMPARISON OF SPACE CORRELATION FUNCTIONS OF STREAMWISE FLOW COMPONENTS

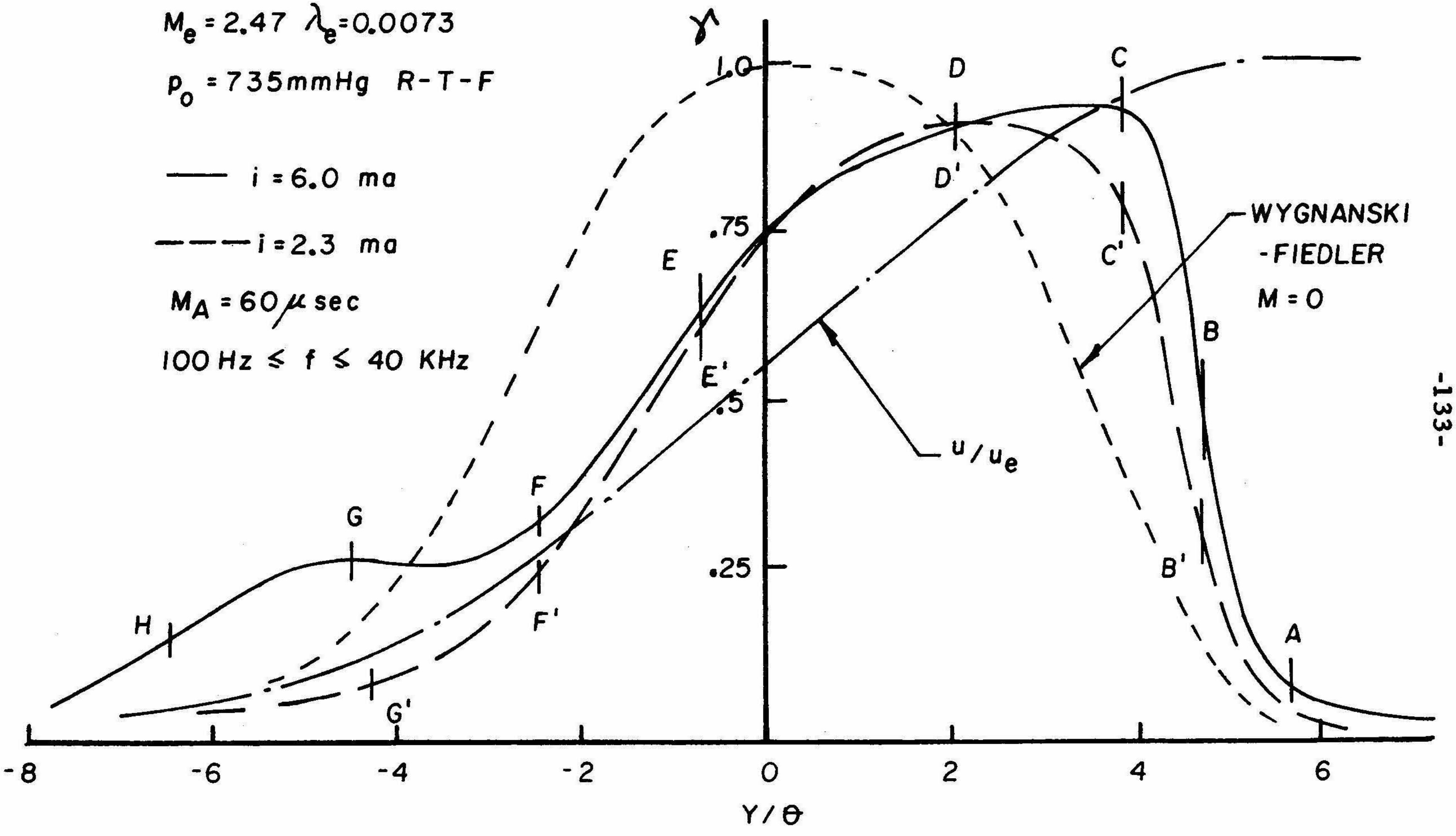

FIG. V.38 TFML INTERMITTENCY FACTOR PROFILES

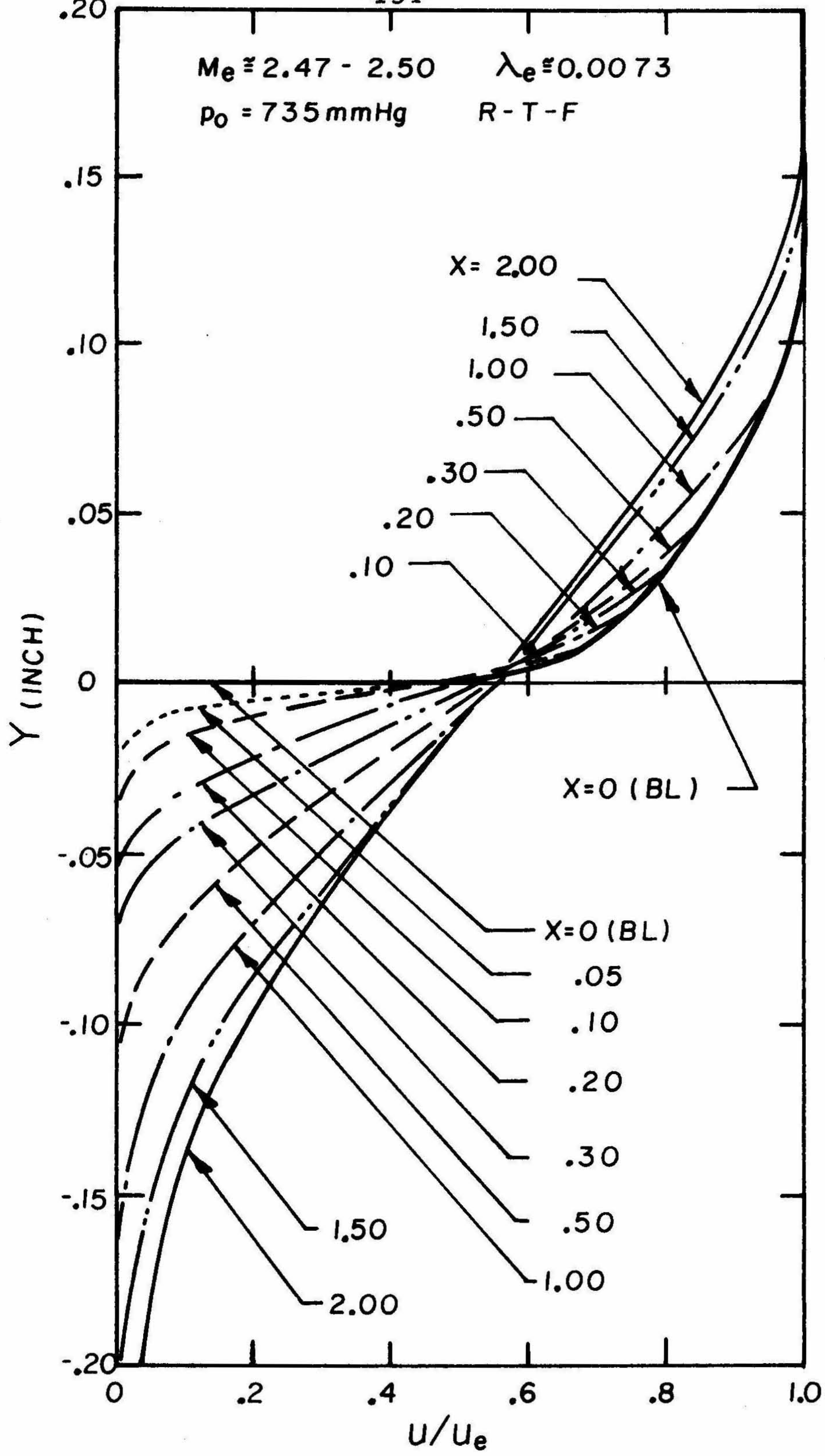

FIG.V.39 DEVELOPMENT OF INITIAL SUPERSONIC MIXING LAYER VELOCITY PROFILE

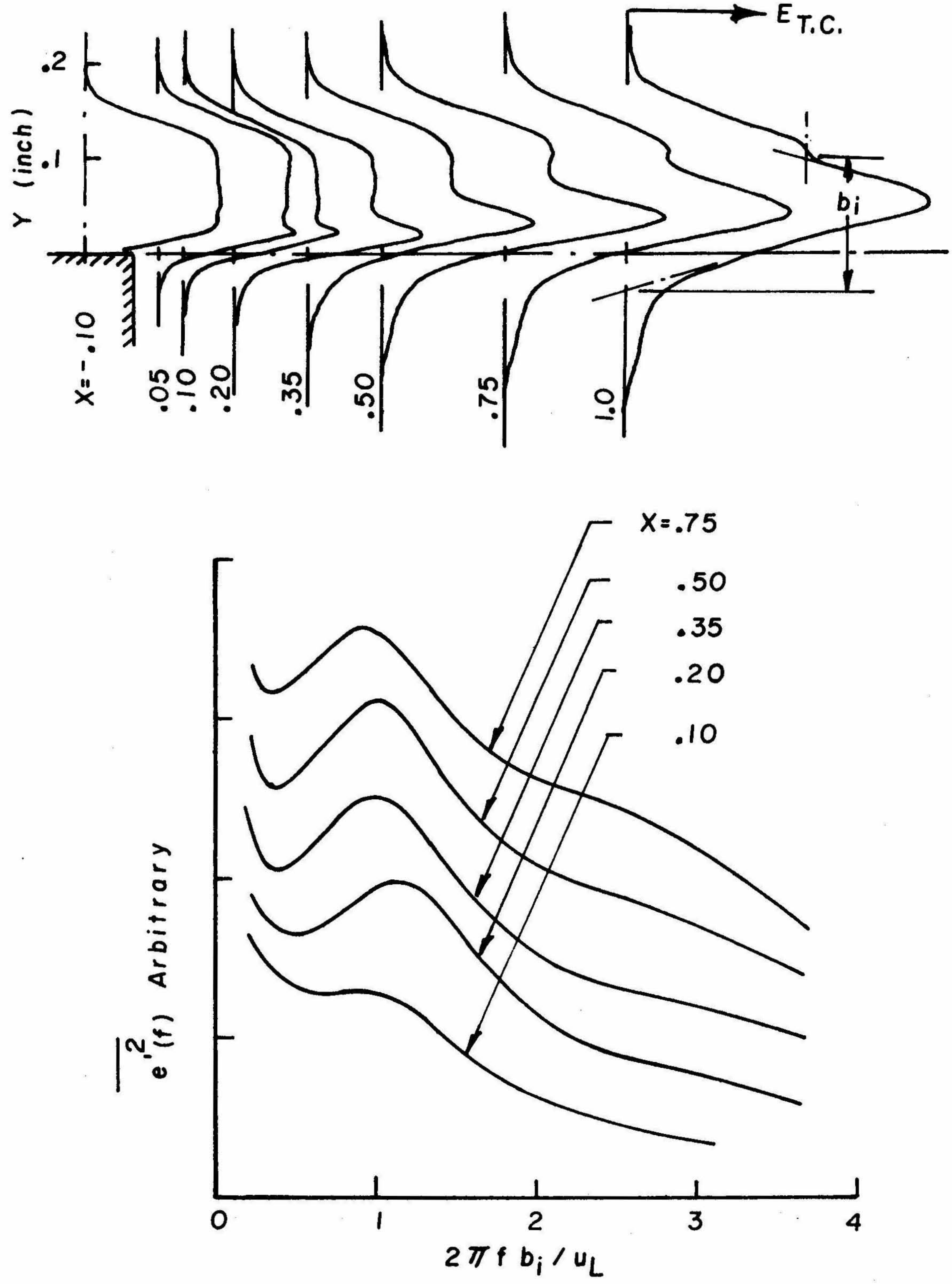

FIG. V. 40 STARTING TFML - E_{tc} PROFILES AND ENERGY SPECTRA AT PEAK E_{tc}

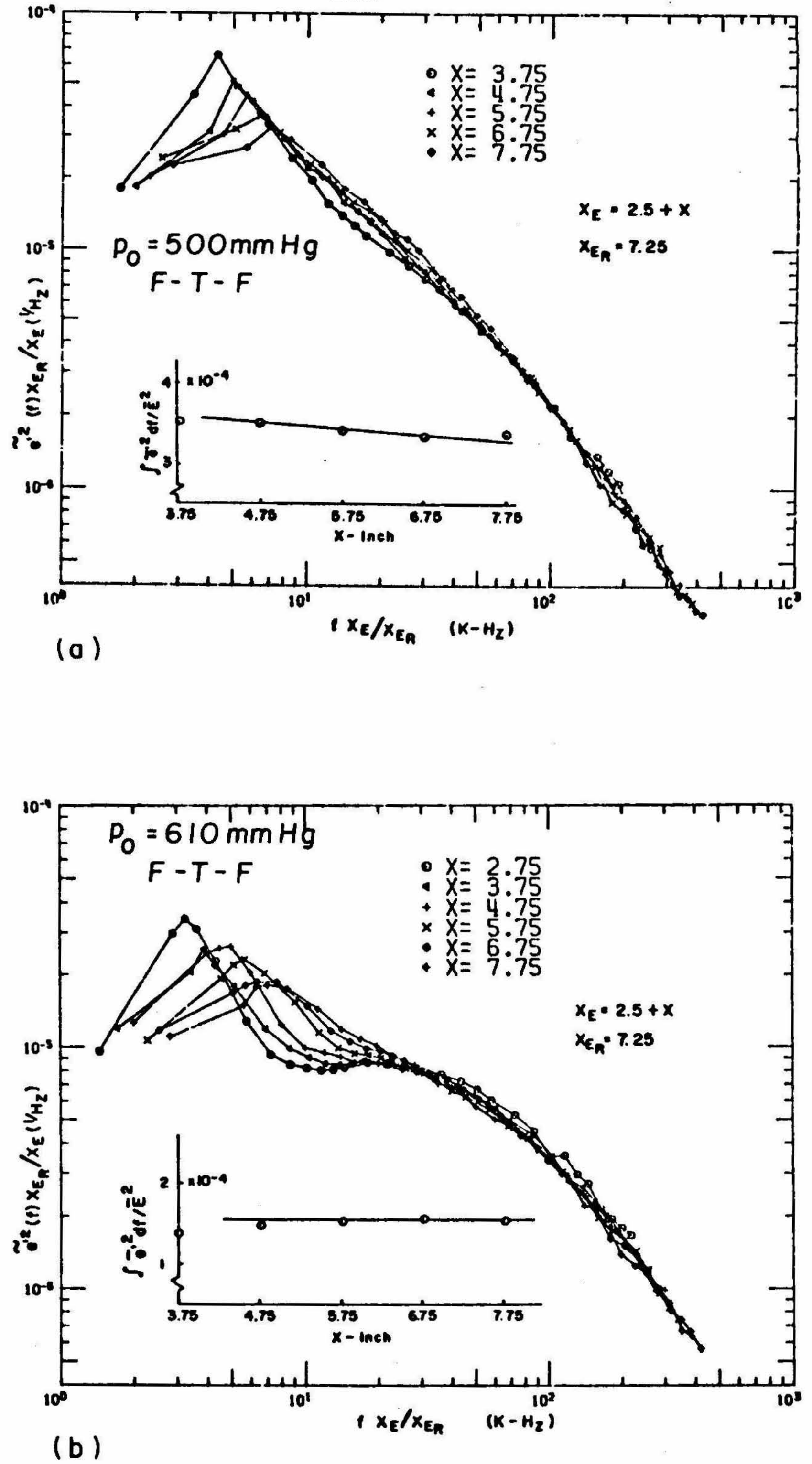

FIG. V.41 TML ENERGY SPECTRA WITH VARIABLE TOTAL PRESSURES

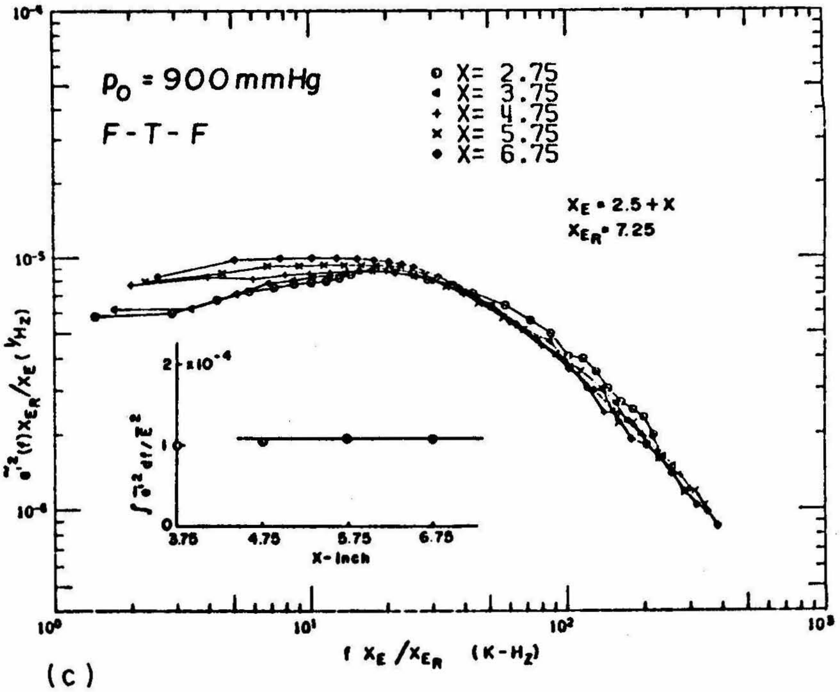

(c)

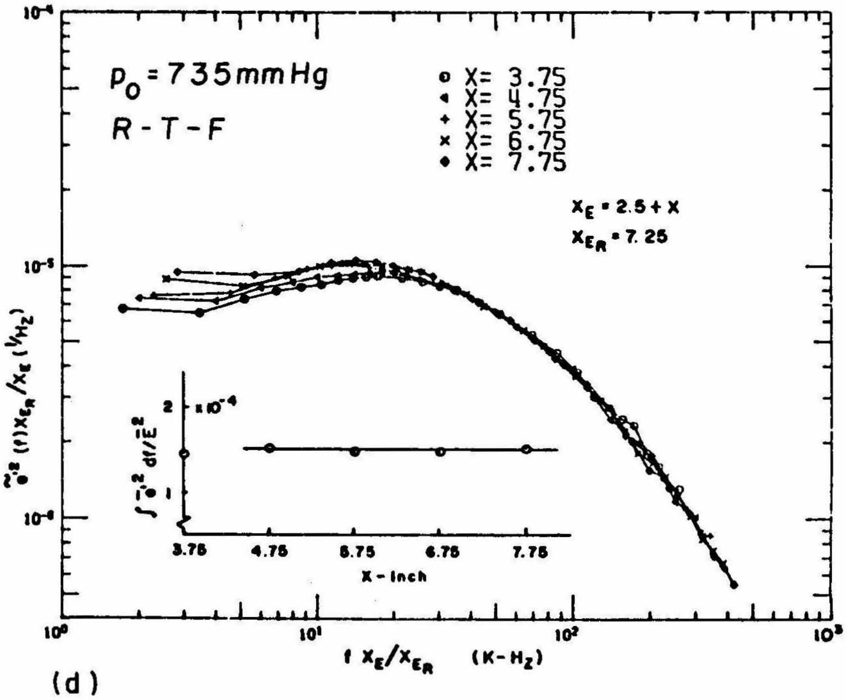

(d)

FIG. V.41 TML ENERGY SPECTRA WITH VARIABLE TOTAL PRESSURES

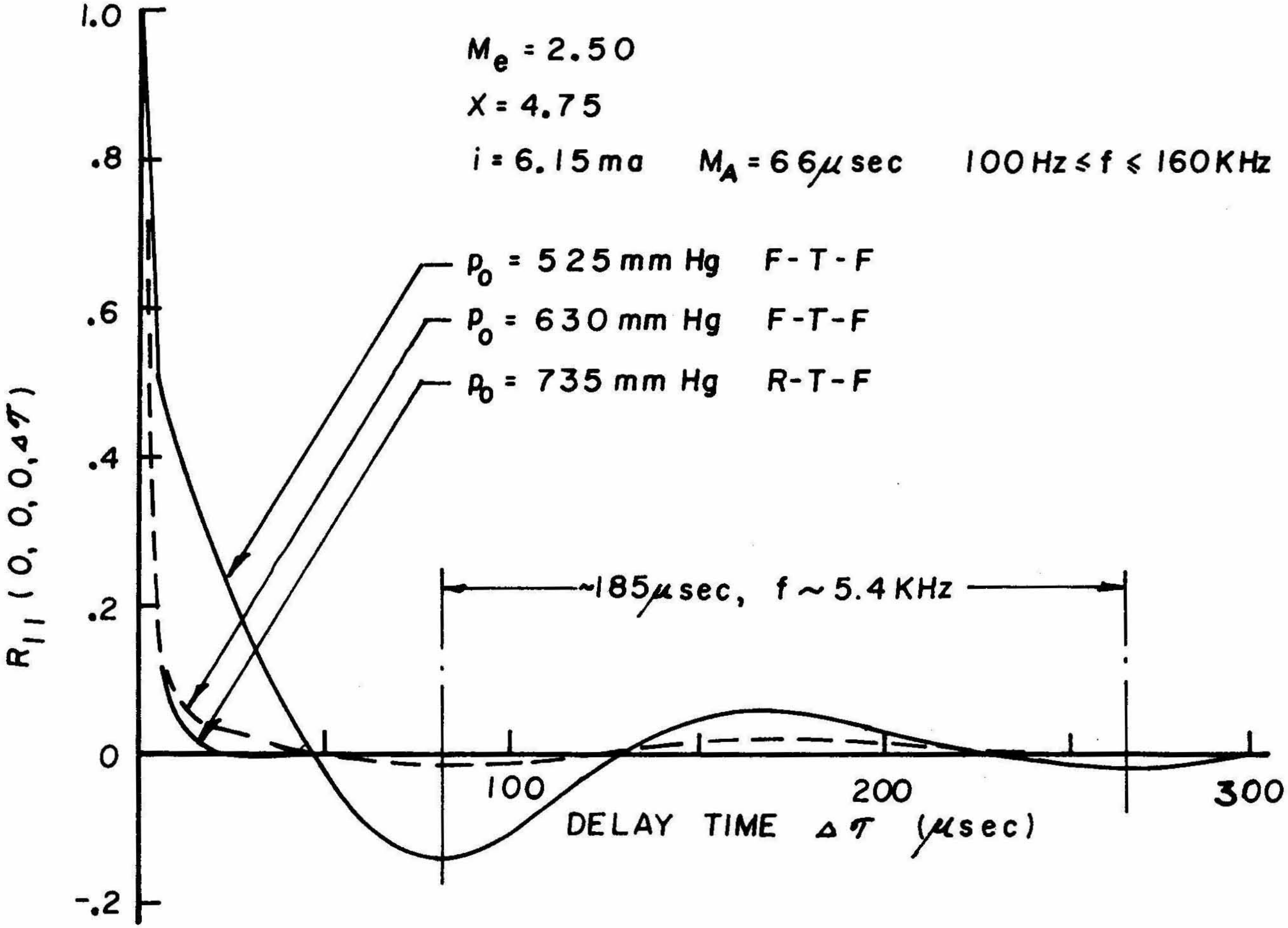

FIG. V.42 MIXING LAYER AUTOCORRELATION FUNCTIONS WRT VARIABLE STAGNATION PRESSURES

APPENDIX A

FLOWFIELD IMPROVEMENTS

A. 1. Porous Plate Characteristics

The unique setup of this experiment is the installation of the porous plate at the bottom wall behind a rearward facing step which permits an injection of fluid into the base region of separated flow. The stainless steel porous plate was supplied by Mott Metallurgical Corporation of Hartford, Connecticut. The overall dimension of 10-micron grain porosity plate is 0.25 inch thick, 2.0 inches wide and 8.0 inches long with 0.125 inch radii at the four corners. The original model of the present investigation was constructed with a single plenum chamber as Fernandez(22) has suggested. However, the check of blowing uniformity under the pressure level of actual testing condition revealed the non-uniform distribution of mass flow. A peak in mass flux distribution was detected in the vicinity where the inlet pipe was located in the plenum chamber. The observation implied that the mass flux distribution through the plate is dependent upon the flow condition inside the plenum chamber, which was also confirmed with the side port inlet nozzle. Rotation of the nozzle disclosed that the highest mass flux distribution was always noted in the region where the side port was directed.

In order to eliminate the undesirable effect, the model was modified to a double plenum chamber configuration. After several trials, the most effective flow damper was constructed in the following way. Uniformly patterned holes of 1/16 inch diameter were drilled on two sheets of aluminum. Another aluminum sheet with offset pattern of holes was sandwiched between the other two sheets and bolted together very tightly. In this way the flow must travel the gaps between three layers of aluminum sheets such that approximately 200 mm Hg pressure drop was obtained across the plate, creating a very uniform second plenum chamber. The longitudinal traces of hot-wire surveys taken along three spanwise stations (centerline and $Z = \pm 0.50$ inch) are shown in Figure A.1a. Local mass flux fluctuation of approximately 10% is observed, but the mean flow is relatively constant. The local fluctuations were damped at the height farther away from the plate.

The spanwise survey shows the interesting phenomenon produced by the effect of fences. Without fences, large peaks of jet-like mass flux appeared on both edges as shown in Fig. **A.1b.** First it was thought to be caused by the leakage between the porous plate and the model block. The edges were completely sealed with epoxy, and yet the same peaks appeared. Installation of fences, however, eliminated the peaks. This observation implies that very small pressure gradient created between the blowing and non-blowing regions is sufficient to alter the flow pattern such that jet-like flow is directed toward the low pressure sides.

Once the uniform blowing has been established, the mass flux versus plenum chamber pressure and pressure ratio across the plate were investigated. The mass flux through the particular plate appeared to become insensitive to the pressure ratio, p_{pl}/p_e, when the pressure ratio is approximately 6. Beyond this point, the mass flux is independent of external pressure distribution and dependent solely on the plenum chamber pressure (Fig. A. 2 a). The behavior of the plate appeared to be similar to the choked flow phenomenon in the sense that there is a sonic flow at the exit. However, Fernandez has estimated that the pressure ratio of an order of 200:1 is required to choke the type of porous plate used in the present experiment. Furthermore, the Mach number of the flow at the exit is quite low ($\lesssim 0.1$ which was confirmed by Pitot measurement) and hence the flow possesses negligible momentum compared to the freestream momentum. The maximum mass flux versus the plenum chamber pressure is shown in Fig. A. 2b, which appears to have approximately a parabolic relation which follows the argument made by Fernandez

$$\dot{m}_{plate} \sim p_{pl} \left[1 + (p_e / p_{pl})^2 + \cdots\right]$$

Since this represents the maximum mass flux for the given p_{pl}, the actual mass flux must be obtained by application of correction factor if $p_{pl}/p_e < 6.0$. However, the direct mass flux measurement taken from the flow meter is used during the test. The useful application of the foregoing information is to provide the conditions under which the spatial uniformity of the injection rate may be expected. Testing under the condition of $p_{pl}/p_e < 6.0$ implies the blowing rate over the plate will be non-uniform if the external pressure field is non-uniform. Therefore, it is desirable to conduct a test under the condition $p_{pl}/p_e > 6.0$.

A. 2. Simulated Streamline Block

The preliminary test revealed that the possible remedy for the undesirable pressure gradient produced by the termination of blowing is the tailoring of the downstream block to simulate an ideal streamline. Based on the self-similar flowfield obtained in the longitudinal region of $2.00 \le x \le 4.00$, the normalized streamline pattern was determined by integration of the continuity equation.

For a self-similar two-dimensional turbulent mixing layer, the stream function is given by

$$\psi_{eff} = \rho_e u_e x_{eff} f(\eta), \quad \eta = y_{eff}/x_{eff}$$

where x_{eff}, y_{eff} are measured from the effective origin. From the above expression for the stream function, we obtain

$$f'(\eta) = \frac{\rho u}{\rho_e u_e}$$

$$f(-\infty) = -(\lambda_e)_{eff}$$

Also from the momentum integral, we have

$$(\lambda_e)_{eff} = \frac{d\theta}{dx}$$

In the present experiment the effective origin was located at $x = -2.5$ inches and $y = 0.16$ inch, and hence

$$x_{eff} = x + 2.5 \text{ inches}, \quad y_{eff} = y - 0.16 \text{ inch}.$$

Also $(\lambda_e)_{eff}$ was 0.00706. Therefore, from the measurements of turbulent mixing layer in the self-similar region, we can determine the normalized stream function $f(\eta)$ (Fig. A. 3).

The following steps are used to reconstruct the streamline pattern with ψ = constant.

1) Choose the longitudinal station where the streamline block begins and determine $x_{eff_o} = x_{sta} + 2.50$.

2) Determine the effective stream function by $\psi_{eff_o} = -0.00706 \cdot x_{eff_o}$. The initial y_o coordinate can be determined by $y_o = -0.1 \cdot x_{eff_o} + 0.16$.

3) Subsequent coordinates of ψ_{eff} = constant can be determined by selecting an x_{eff} downstream of x_{eff_o}. Then $\psi_{eff_o} / x_{eff} = f(y_{eff}/x_{eff})$ gives the y_{eff}/x_{eff} from the normalized streamline curve.

The actual streamline block constructed for the downstream of porous plate ($x \geq 8.00$) is also shown in the same figure. Uniform pressure distribution obtained with the streamline block is also shown in Fig. III.1. The effectiveness of this modification is demonstrated in Section V.2.1.1.

A.3. Effect of Vertical Traverse Mechanism

The vertical traverse mechanism was originally installed in the aft portion of the test section. The forward tip of the probe holder support was at the x-station 8.00 when it was at the rearmost position so that the flow survey downstream of $x \cong 7.00$ was made impossible. In addition, the flow disturbance created by the relatively large struts fed into the large subsonic region associated with a TFML to produce an undesirable flow interference.

Major modification to relocate the vertical traverse out of the test section was, therefore, undertaken. At the same time, a motorized axial drive was designed and installed to increase the surveying capability up to 15 inches of axial traverse. The vertical traverse was relocated in the diffuser section, which eliminated the major flow interference from the traverse struts. The disturbance created by the probe holder and by the Pitot probe was unavoidable, but their contributions were negligibly small. After the modification the full sweep of vertical traverse produces a static pressure deviation of ± 0.5% at most.

A. 4. Effect of Finite Initial Turbulent Boundary Layer (TBL)

The presence of a finite TBL at the edge of the rearward facing step influences the subsequent development of TFML. The present experimental setup produces a TBL with thickness (δ) of approximately 0.12 ~ 0.14 inch and its momentum thickness (θ_o) of approximately 0.01 inch at the corner. $d\theta/dx \cong 0.007$ and the virtual origin at $x = -2.5$ have been determined from the preliminary TFML test. Based on these parameters, the momentum thickness of TFML is approximately 0.049 ~ 0.07 inch in the region 4.5 inches $\leq x \leq 7.5$ inches. Alber$^{(16)}$ suggested that $x/\sigma_\theta \theta_o > 10$ is required for the establishment of similar flow. $\sigma_\theta \cong 45$ is estimated for the present test from the correlation curves of σ_θ vs. M_e of Alber. Considering $\theta_o = 0.01$ inch, then the required distance is approximately 4.5 inches downstream of the step. Bradshaw$^{(51)}$ defined the criterion of 1000 θ_o whether the initial boundary layer is laminar or turbulent, which corresponds to 10 inches downstream of the step. Most of the current test program was carried out in the region 475 $\theta_o \leq x \leq 875\ \theta_o$

where the θ_o was momentum thickness of the turbulent boundary layer. The relaxation to the equilibrium turbulent flow was investigated in the fluctuation measurements and the length in the present experiment appears sufficient.

Another contribution of initial momentum thickness of the finite magnitude is an influence on establishing the actual dividing streamline position by mass balance. For a constant pressure assumption, the integrated momentum and continuity equations reduced to a form $\theta(x)-\theta_o = \int_{x_o}^{x} \frac{\rho_w v_w}{\rho_e u_e} dx = \int_{-\infty}^{y^*} \frac{\rho u}{\rho_e u_e} dy\Big|_x$, where $\theta(x)$ is a momentum thickness of mixing layer profile measured at x-station downstream of the step. Then the definition of y*, the lateral position of a dividing streamline determined by mass balance, is highly dependent on θ_o. However, in the region where the present test is conducted, the linear growth rate of momentum thickness agrees with the measured entrained mass ($d\theta/dx = \lambda_e = \frac{\rho_w u_w}{\rho_e u_e}$).

A. 5. Effect of Finite Length Fences

Although the flow field in the main test section over the entire injection region ($0 \le x \le 8.0$) appeared to be two-dimensional with the finite length fences extending 3.25 inches beyond the injection termination, the Pitot pressure surveys showed the presence of a secondary flow over the streamline block. The flow field deviation from the two-dimensionality was created by the low pressure produced in the base region of finite length fence by the flow expansion, which was sensed by the large subsonic region of the mixing layer flow.

The full length fences (L = 18.0 inches) covering the entire length of the test section replaced the finite length fences. The flow field in the region of interest ($0 \leq x \leq 9.75$) remained uniform and it appears the two-dimensional mixing layer was established.

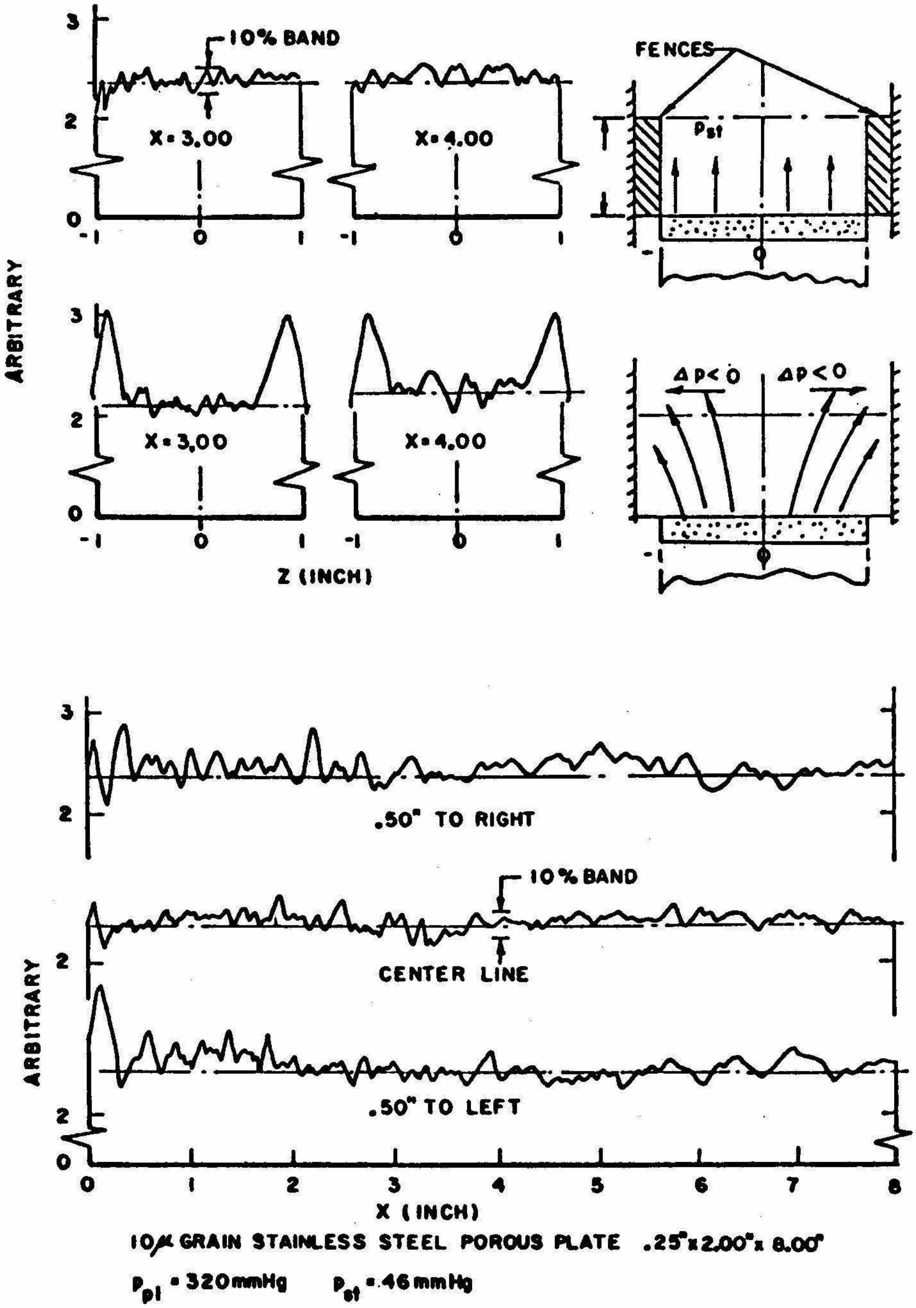

FIG. A.1 SPANWISE-LONGITUDINAL FLOW DISTRIBUTIONS THROUGH POROUS PLATE HOT-WIRE SURVEY 0.50" ABOVE SURFACE

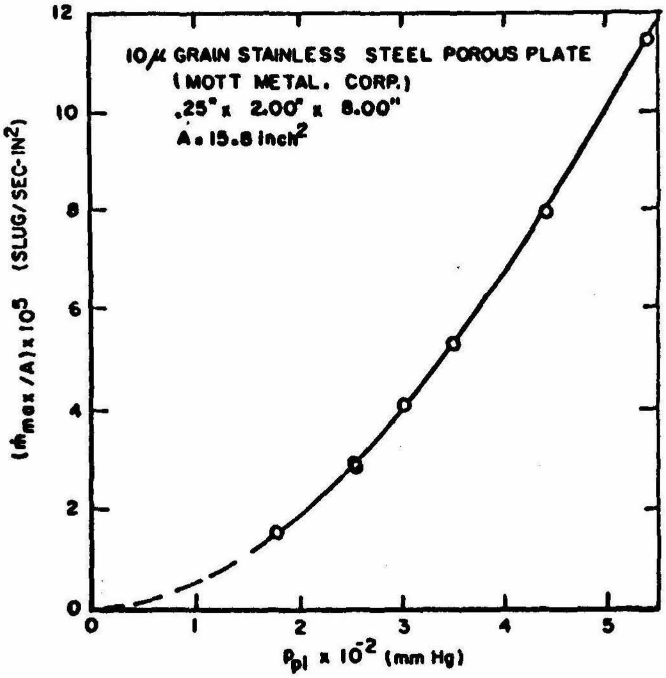

INJECTION PLATE - MAXIMUM MASS FLOW VS. PLENUM PRESSURE

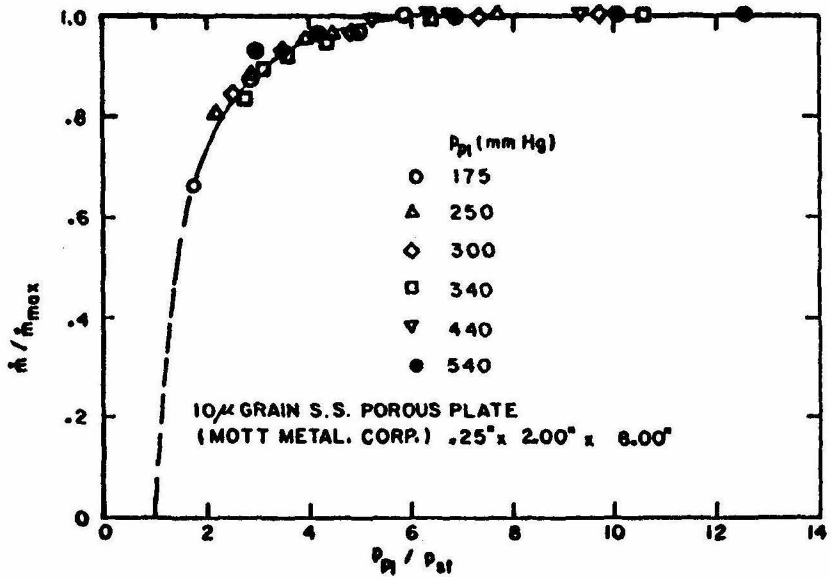

INJECTION PLATE - MASS FLOW CORRECTION

FIG. A. 2 CALIBRATIONS OF MASS FLOW THROUGH POROUS PLATE

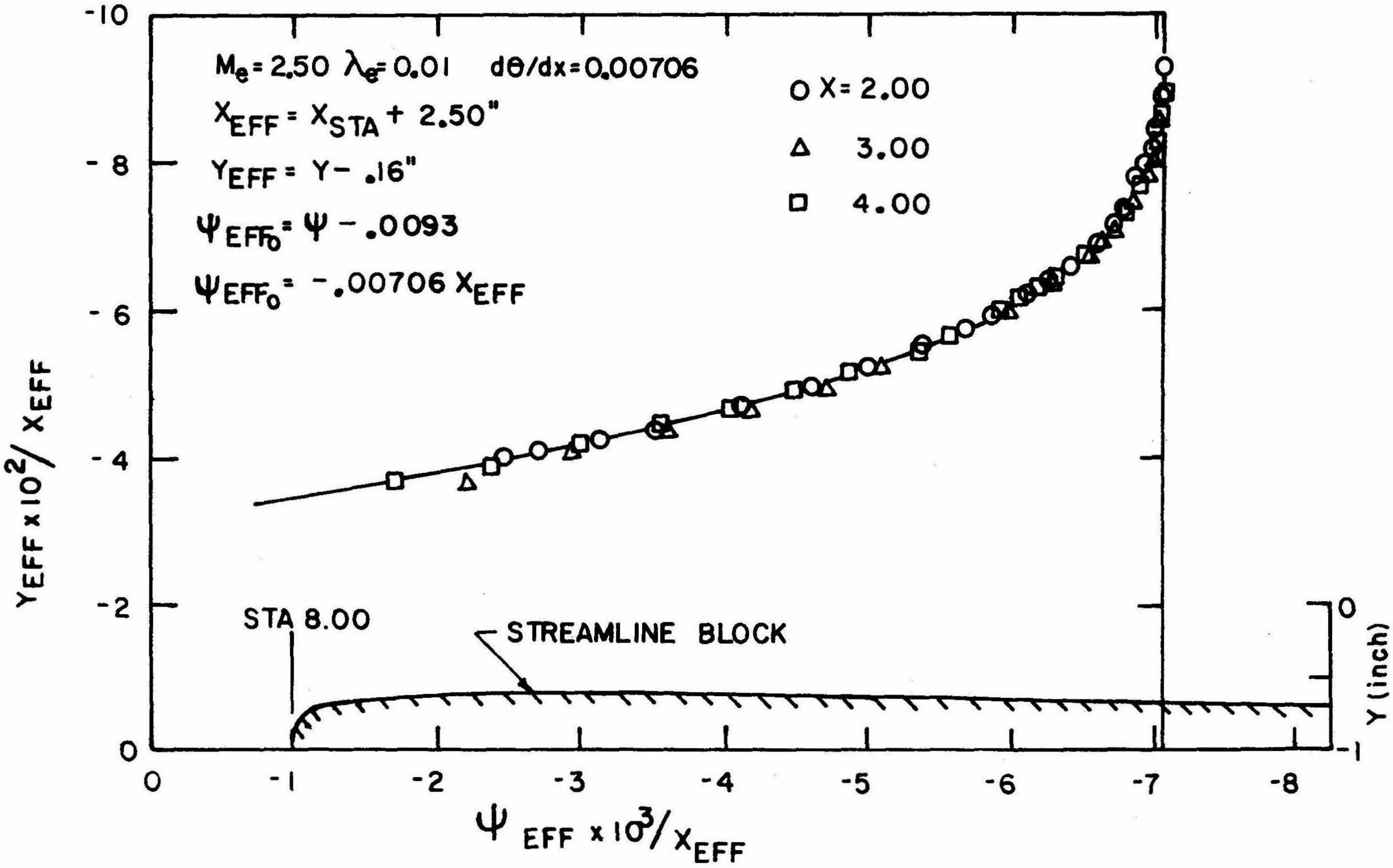

FIG. A. 3 NORMALIZED STREAM FUNCTION - $f(\eta)$

APPENDIX B

HOT-WIRE TECHNIQUE

Portions of a finite length hot-wire technique developed by Behrens(32) are summarized in this appendix. In addition, the approximations required to extend the application of its technique to the subsonic region of turbulent mixing layer are discussed.

B.1. Reduction of Mean Flow Quantities

The total temperature (T_o) and the Nusselt Number (Nu_o) based on the total temperature are required to compute the sensitivity coefficients and the thermal lag time constant (M_t) of wire when the fluctuation data are reduced. The iteration method used to account for the heat conduction loss to the end support is given by Ramaswamy.(27) The uncorrected adiabatic temperature (T_{awm}) of wire and Nusselt number (Nu_m) can be determined from the direct measurements by obtaining the mean resistance (R_w) or mean voltage outputs (E_w) corresponding to the several applied currents (i). A linear relation between R_w and i^2R_w was fitted by the least-square-error method. The value at $i = 0$ gives the adiabatic resistance of wire (R_{awm}) and the slope (k) determines the Nu_m. Gran(52) showed that it is more convenient to plot the data in $1/R_w$ versus i^2 for one reason that variation in R_w does not affect the value of abscissa as observed in the other method. Once again, R_{awm} is determined when $i = 0$ and slope (k) is determined by

$$k = \frac{R_{awm}}{i^2}\left(\frac{1}{R_{awm}} - \frac{1}{Rw}\right) \qquad (B.1)$$

The corrected adiabatic temperatures were determined from the following relations.

$$R_{awm} = R_r[1 + \alpha_r(T_{awm} - T_r)] \qquad \text{(B.2)}$$

$$\frac{T_{aw}}{T_{awm}} = \frac{\cosh\sqrt{\alpha_o} - T_{sup}/T_{awm}}{\cosh\sqrt{\alpha_o} - 1} \qquad \text{(B.3)}$$

where $\alpha_o = Nu_o/a; \quad Nu_o = Nu_m\,\psi_n; \quad a = k_w/[k_o(L/D)^2]$

$T_{aw} = \eta T_o$ = corrected adiabatic temperature of wire

ψ_n = End loss correction parameter found by iteration

k_o = Thermal conductivity of air at stagnation temperature

k_w = Thermal conductivity of wire

L/D = Aspect ratio of wire

η = Recovery factor

$Nu_m = R_r\,\alpha_r/(\pi DL\,k)$ = measured Nusselt number.

B.2. Thermal Lag Time Constant

The heat capacity of the hot-wire results in the response lag when the hot-wire is placed in fluctuating flow. The hot-wire set is equipped with a compensating amplifier whose response is the inverse of the response lag of hot-wire. Proper setting of amplifier time constant (M_A) requires a prior knowledge of wire time constant (M_t). M_t was computed by the following equation at different lateral positions.

$$M_t(y, i) = K\,\frac{1 - \tanh\sqrt{\alpha(y,i)}\,/\sqrt{\alpha(y,i)}}{Nu_o(y) - i^2 r_r\,\alpha_r/\pi k_o} \text{ (Function of applied current i)} \qquad \text{(B.4)}$$

where $K = \dfrac{\rho_w C_w D^2}{4\,k_o}$ is the property of wire and the thermal conductivity of air which is approximately constant (T_o distribution is ± 2%).

$$\alpha(y, i) = \frac{Nu_o(y)k_o}{k_w}\,(1 - i^2\,r_r\,\alpha_r/\pi\,Nu_o(y)k_o)\,(L/D)^2 .$$

$Nu_o(y)$ known from mean flow measurements.

Measurements of M_t with square wave technique quantitatively agree with the computed values of the above equation and the repeatability is found within ± 10% of mean values.

B. 3. Hot-wire Transfer Functions

Relationship between the fluctuation voltage response of real hot-wire to "ideal" or "massless" hot-wire is given as

$$\overline{e'^2_{f,m}} = \frac{\overline{e'^2_{f,i}}}{1 + (2\pi f M_t)^2} \qquad \text{(B.5)}$$

where $\overline{e'^2_{f,m}}$ = Measured mean square voltage fluctuation at frequency f.

$\overline{e'^2_{f,i}}$ = Ideal mean square voltage fluctuation at frequency f.

The relation between the input and output voltage of the amplifier is

$$\overline{e'^2_{f,A}}/\overline{e'^2_{f,m}} = [G_o\, G^*(f)]^2 \qquad \text{(B.6)}$$

where G_o = Zero frequency gain of the amplifier.

$G^*(f)$ = Frequency response of the amplifier.

The compensating amplifier response is

$$\overline{e'^2_{f,comp}}/\overline{e'^2_{f,A}} = \frac{1 + (2\pi f M_A)^2}{1 + (2\pi f M_A/\kappa)^2} \qquad \text{(B.7)}$$

where κ = floor to ceiling ratio (κ = 420 for the present set).

So the mean square voltage fluctuation sensed by the "ideal" hot-wire is

$$\overline{e'^2_{f,i}} = \frac{\overline{e'^2_{f,m}}}{[G_o G^*(f)]^2} \left\{\frac{1 + (2\pi f M_t)^2}{1 + (2\pi f M_A)^2}\right\} \left\{1 + \left(\frac{2\pi f M_A}{\kappa}\right)^2\right\} \qquad \text{(B.8)}$$

Power spectral density distribution is fully corrected for these amplifier responses. The power spectral measurements were taken with a Tektronix 1L5 Spectrum Analyzer whose resolution setting is taken equivalent to the bandwidth of the sampling instrument. The data,

$\sqrt{\overline{e'^2}(f)}$ versus frequency (f), were plotted on a Moseley X-Y plotter. The sweep rate of the spectrum analyzer was operated in manual mode, so that the response of amplitude of the signal was maximized. Therefore, additional correction required in the data reduction routine is the bandwidth of the instrument.

$$\overline{e'^2_{f,i}} = \frac{\overline{e'^2_{f,m}}}{BW[G_o G^*(f)]^2} \left\{ \frac{1 + (2\pi f M_t)^2}{1 + (2\pi f M_A)^2} \right\} \left\{ 1 + \left(\frac{2\pi f M_A}{\kappa} \right)^2 \right\}. \qquad \text{(B.9)}$$

The integrated mean square voltage fluctuation $(\overline{e'^2})$ is obtained by

$$\overline{e'^2} = \int_o^\infty \overline{e'^2_{f,i}}\, df = \frac{1}{BW\, G_o^2} \int_o^\infty \frac{\overline{e'^2_{f,m}}}{[G^*(f)]^2} \left\{ \frac{1+(2\pi f M_t)^2}{1+(2\pi f M_A)^2} \right\} \left\{ 1+\left(\frac{2\pi f M_A}{\kappa} \right)^2 \right\} df \qquad \text{(B.10)}$$

Hot-wire thermocouple output is correct only when

$$M_A = M_t\,,\ G^*(f) = 1.0 \text{ and } \left(\frac{2\pi f M_A}{\kappa} \right)^2 \ll 1\,.$$

Then $\overline{e'^2} = K_{tc}\, E_{tc}\ (\mathrm{mv}^2)$ (B. 11)

where K_{tc} = Calibration constant $(\mathrm{mv}^2/\mathrm{mv})$

E_{tc} = Thermocouple voltage output (mv) .

If the main contribution of total energy comes from the high frequency turbulent components where $(2\pi f M_t)^2 \gg 1$ and $(2\pi f M_A)^2 \gg 1$ were satisfied, the E_{tc} measurement can be interpreted properly by

$$\overline{e'^2} = \left(\frac{M_t}{M_A} \right) K_{tc}\, E_{tc} \qquad \text{(B.12)}$$

B.4. Sensitivity Coefficients

The fluctuating voltage of "ideal" hot-wire is expressed in terms of the sensitivity coefficients as the parameters

$$e'_{i,f} = -S_u u'_f - S_\rho \rho'_f + S_{T_o} T'_{o_f} \tag{B.13}$$

Sensitivity coefficients are defined as

$$\begin{aligned}
S_\rho &= C\{[B_1 \bar{\tau}_{wm} - B_2] + g[B_2 - B_1 \bar{\tau}_s]\} \, . \\
S_u &= C\{[(B_1 + B_3 a_1)\bar{\tau}_{wm} - (B_2 + B_4 a_1)] \\
&\qquad + g[B_2 + B_4 a_1 - (B_1 + B_3 a_1)\bar{\tau}_s]\} \, . \\
S_{T_o} &= C\Big\{[1 - m B_2 - \frac{a_1}{2} B_4 + (mB_1 + \frac{a_1}{2} B_3 - n)\bar{\tau}_{wm}] \\
&\qquad + g[m B_2 + \frac{a_1}{2} B_4 - 1 + (n - mB_1 - \frac{a_1}{2} B_3)\bar{\tau}_s]\Big\} \, .
\end{aligned} \tag{B.14}$$

where $C = \dfrac{4i\, R_r\, \alpha_r\, \eta\, T_o\, Nu_o\, k_o\, M_t}{\rho_w\, C_w\, D^2} \sqrt{1 + 1/(M_t \omega)^2}$

$$\left.\begin{aligned}
B_1 &= \partial \ln Nu_o / \partial \ln Re_o \\
B_2 &= \partial \ln \eta / \partial \ln Re_o \\
B_3 &= \partial \ln Nu_o / \partial \ln M \\
B_4 &= \partial \ln \eta / \partial \ln M
\end{aligned}\right\}$$

These values are determined by a function of local Mach number and Reynolds number and interpolated from the parametric curves given in Ref. 32.

$$\left.\begin{aligned}
n &= d \ln k_o / d \ln T_o \approx 0.885 \\
m &= d \ln \mu_o / d \ln T_o \approx 0.765
\end{aligned}\right\}$$

For air @ 300°K

$a_1 = 1 + \frac{\gamma-1}{2} M^2$

$g = \tanh\sqrt{\beta} / \sqrt{\beta}$ Function of current, i, and frequency, f. g vanishes as f → ∞ or/and $\alpha \to \infty$ (i.e., infinite hot-wire).

$\beta = \alpha\sqrt{1 + (\bar{\omega}/b)^2}$

$\bar{\omega}/b = 2\pi f K/(Nu_o - i^2 r_r \alpha_r/\pi k_o)$

$\omega = 2\pi f$.

The first square bracket terms in the sensitivity coefficients are independent of frequency response. The frequency response enters in the sensitivity coefficients through a function g. It was found that error contribution resulting from the neglect of g is less than 15% of RMS fluctuating quantities in the present investigation.

S_u and S_ρ are found to be related by $S_\rho = k_s S_u + k$ for all Mach number range where $k_s = B_1/(B_1 + B_3 a_1)$ and the contribution from k is negligible. The parallel relation between S_u and S_ρ, in fact, permits us to use the curve fitting technique of hot-wire mode separation (Appendix B-5).

B. 5. Extension of Curve Fitting Method - To Subsonic Flow

In order to separate the fluctuating flow properties, the fluctuation voltage can be expressed in terms of fluctuating flow quantities.

$$e' = -S_u u' - S_\rho \rho' + S_{T_o} T_o'$$

where u', ρ' and T_o' are non-dimensional fluctuations of velocity, density and total temperature, respectively. S_u, S_ρ and S_{T_o} are their respective sensitivity coefficients (Appendix B. 4). Mean square of the above equation after normalizing with respect to S_{T_o} becomes,

$$\frac{\overline{e'^2}}{S_{T_o}^2} = r_1^2 \overline{u'^2} + r_2^2 \overline{\rho'^2} + T_o'^2 - 2 r_1 \overline{u'T_o'} - 2 r_2 \overline{\rho' T_o'} + 2 r_1 r_2 \overline{\rho' u'}$$

$$r_1 = S_u / S_{T_o} \quad \text{and} \quad r_2 = S_\rho / S_{T_o} \qquad \text{(B. 15)}$$

In principle, all mean square and correlation quantities can be found by inversion of 6×6 matrix, if sufficient data were taken with six different overheat parameters. However, $S_u \cong S_\rho \cong S_{\dot{m}}$, in supersonic flow ($M \geq 2.0$) and it was found also that $S_\rho = k_s S_u + k$, (where k contribution is small and can be neglected) in all Mach number range; then the inversion is impossible because of the vanishing of the determinant. In this case the mean square voltage fluctuation can be rewritten as

$$e' = -S_u(u' + k_s \rho') + S_{T_o} T_o' \quad \text{or}$$

$$\tilde{e}'^2 = \frac{\overline{e'^2}}{S_{T_o}^2} = r^2 \overline{(u' + k_s \rho')^2} - 2 r \overline{(u' + k_s \rho') T_o'} + \overline{T_o'^2} \qquad \text{(B. 16)}$$

$$\text{where } r = S_u / S_{T_o}$$

and Morkovin's curve fitting technique to hyperbola in the mode diagram of $\tilde{e}'$ versus r can be extended in all Mach number range. The total temperature fluctuation will be most accurate among all of the fluctuation parameters to be computed, because it is determined by the zero intercept of ordinate. In this region error bound is much more easily defined. Mass flux fluctuation depends on the coefficient of r^2 which is highly dependent on the asymptotic slope of hyperbola. The correlation coefficient is described by the coefficient of r, (i.e., slope at small value of r) which means the position of vertex determines the degree of correlation coefficient, $R_{\overline{\dot{m}'T_o'}}$. Therefore, the mass flux fluctuation and correlation coefficient are more sensitive to the scatters of data. However, the effect of data scatters is reasonably averaged if sufficient numbers of data are collected as seen in the example fluctuation mode diagram (Fig. V.26).

In accordance with the approximation of Appendix B.4, the term which has been called mass flux is not exactly as it is meant to be but is modified by a correction parameter, k_s (i.e., $\dot{m}'/\dot{m} = u'/u + k_s\,\rho'/\rho$, where $S_\rho = k_s S_u$). The correction parameter k_s approaches 1, as the high supersonic flow is encountered with sufficiently high Reynolds number based on hot-wire diameter and can be less than 0.5 for low Mach number. Since no other suitable name is found, it will be called mass flux fluctuation in this writing. However, this definition is strictly true only in high supersonic flow where Mach number dependence of sensitivity coefficient vanishes and assumption of $S_{\dot{m}} \cong S_u \cong S_\rho$ is applicable.

B.6. Separation of Velocity, Pressure and Temperature Fluctuations

Separation of u' and ρ' requires the further assumptions. In supersonic freestream region where the flow is essentially inviscid, the vorticity mode is assumed absent. Laufer,(31) Kovasznay(28) and others showed that the freestream turbulence is most likely produced by the acoustic radiation from the turbulent boundary layer or mixing layer. Assuming isentropic process and considering a plane sound wave (Laufer(31)), the fluctuation voltage equation can be rewritten in terms of u' and p' (p' is normalized pressure fluctuation).

$$\frac{\overline{e'^2}}{S_{T_o}^{\,2}} = (\beta - r)^2\,\overline{u'^2} - \frac{2}{\gamma}(\beta - r)\left(\frac{\beta}{M^2} - r\right)\overline{u'p'} + \frac{1}{(\gamma M^2)^2}(\beta - M^2 r)\,\overline{p'^2} \qquad \text{(B.17)}$$

$$\alpha = \left(1 + \frac{\gamma - 1}{2}M^2\right)^{-1} \quad \text{and} \quad \beta = (\gamma - 1)M^2\alpha$$

At overheat operating at $r = \beta$, contribution from the velocity fluctuation vanishes and the mean square voltage fluctuation is proportional to the mean square pressure fluctuation. Similarly, velocity fluctuation is determined by the voltage fluctuation at $r = \beta/M^2$. Since the measurements were not taken exactly at $r = \beta$ or $r = \beta/M^2$, curve fitting of the data in the original form (Eq. B.16) was made to determine the $\sqrt{\overline{p'^2}}$ and $\sqrt{\overline{u'^2}}$. In reality, some residual turbulence associated with a wind tunnel characteristic such as a temperature spottiness produced by a compressor-dryer combination, the flow disturbance produced in the upstream plenum chamber, etc. exists in the freestream. However, these residual turbulences are much smaller in magnitude and uncorrelated with the acoustic radiation field in the well-designed wind tunnel. Freestream turbulence produced by the pure temperature spottiness can be detected if the linear mode diagram converges to $r = -\alpha$ as shown by Kovasznay.$^{(28)}$ The temperature spottiness in percent of total temperature can be found by $\widetilde{e}'$ at $r = 0$.

In the core of turbulent shear flow, the pressure fluctuation is assumed negligible compared with the velocity and the temperature fluctuations. Then the temperature and the density fluctuations are related by $T' = -\rho'$. Neglecting the second order fluctuation terms, the total temperature fluctuation can be expressed in terms of velocity and temperature fluctuations, $T_o' = \beta u' + \alpha T'$, where

$$\alpha = [1 + \tfrac{\gamma-1}{2} M^2(1 + \overline{q'^2})]^{-1}; \quad \beta = (\gamma-1)M^2\alpha \text{ and } \overline{q'^2} = (\overline{u'^2} + \overline{v'^2} + \overline{w'^2})/u^2$$

and can be neglected without introducing a serious error. The mass flux fluctuation term is as given before, $\dot{m}' = u' + k_s \rho'$. Inversion of mean square properties produces the velocity and temperature fluctuations explicitly in terms of mass flux and total temperature fluctuations.

$$\begin{pmatrix} \overline{u'^2} \\ \overline{T'^2} \\ \overline{u'T'} \end{pmatrix} = \frac{1}{(\alpha + k_s\beta)^2} \begin{pmatrix} \alpha^2 & k_s^2 & 2k_s\alpha \\ \beta^2 & 1 & -2\beta \\ -\alpha\beta & k_s & (\alpha - k_s\beta) \end{pmatrix} \begin{pmatrix} \overline{\dot{m}'^2} \\ \overline{T_o'^2} \\ \overline{\dot{m}'T_o'} \end{pmatrix} \tag{B.18}$$

Another approach is shown by Behrens(32) and Gran;(25) fluctuation voltage equation can be rewritten in terms of redefined sensitivity coefficients and new mode diagram can be constructed.

$$\frac{\overline{e'^2}}{S_T^2} = \overline{T'^2} + 2\,\mathbb{R}\,\overline{u'T'} + \mathbb{R}^2\,\overline{u'^2} \qquad (B.19)$$

where $S_T = \alpha S_{T_o} + S_\rho = \alpha S_{T_o} + k_s S_u$, sensitivity coefficient for temperature.

$$\mathbb{R} = (\beta S_{T_o} - S_u)/S_T$$

In the core of the mixing layer, both methods yield results within a few percent of each other.

B. 7 Correction of Crosscorrelation Functions

The crosscorrelation functions are obtained by the covariance of two signals divided by the square roots of variance of signal taken at surveying position. However, the variance of signal at different positions in the flow field were not always measured simultaneously with the crosscorrelation survey. In such cases, the data are corrected in the following manner. Recall that

$$C_{11}(\Delta x, 0) = K\, E_{tc}(\Delta x)$$

$$C_{12}(0, 0, 0; 0) = \{C_{11}(0, 0)\, C_{22}(0, 0)\}^{\frac{1}{2}} .$$

Then

$$\{C_{11}(0,0)\ C_{22}(\Delta x,\ 0)\}^{\frac{1}{2}} = C_{12}(0,\ 0,\ 0;0)\ \{C_{22}(\Delta x,\ 0)/C_{22}(0,0)\}^{\frac{1}{2}}$$

$$= C_{12}(0,\ 0,\ 0;0)\ \{E_{tc}(\Delta x)/E_{tc}(0)\}^{\frac{1}{2}}\ .$$

Finally

$$R_{12}(\Delta x,\ 0,\ 0;\Delta\tau) = \frac{C_{12}(\Delta x,\ 0,\ 0;\Delta\tau)}{C_{12}(0,\ 0,\ 0;0)\{E_{tc}(\Delta x)/E_{tc}(0)\}^{\frac{1}{2}}}\ . \qquad (B.20)$$

A technique for mode separation of crosscorrelation function is given by Demetriades.(47) Measurement of at least sixteen combined overheats of both wires will be required per sample point and a great deal of time is involved. In the present investigation, quantitative mode separation, therefore, has not been made.

APPENDIX C

FREESTREAM TURBULENCE

C.1. Qualitative Discussion

Because of the small cross-section (half height 1 inch and width 2.5 inches) but with relatively long longitudinal surveying dimension (8 inches) of test section, the complete elimination of wave interaction in freestream region is next to impossible. In addition, joints of nozzle blocks and downstream blocks, etc., create some infinitesimal mismatches which produce very weak interaction waves. These waves are expected to interact with turbulent boundary layer of opposite wall or turbulent mixing layer of test flow and in turn feed the complicated interaction patterns downstream. Although the weak interactions are expected to contribute little to the change in mean flow properties, the turbulent fluctuation level may be influenced appreciably. In order to assess qualitatively the natures of these interactions, hot-wire surveys were made in axial direction at approximately midpoint of freestream ($Y = 0.45$). The total fluctuation intensities obtained through thermo-couple output (E_{tc}), of Shapiro-Edward set are shown normalized with upstream boundary layer quantity (Fig. C.1.). Turbulent boundary layer was created by tripping the flow just upstream of the throat. Roughness of trip and operating total pressure influenced the nature of the boundary layer.

For a reference, a flat plate filler was installed behind the step with upper surface flushed with upstream block to extend the turbulent boundary layer all the way to X-station 10 inches. The rate of increase of fluctuation intensity under operating condition I ($d\overline{E}/dx \cong 0.14$/in.) remained constant up to X = 0.90 and higher rate ($d\overline{E}/dx \cong 0.6$/in.) downstream. The irregular pattern of intensity is probably caused by the wave interaction. The change in the rate of increase is obviously caused by the slight mismatch of the flat plate at X = 0 producing the weak wave and in turn amplifying the growth of turbulent boundary layer (effective tripping). Turbulent boundary layer fluctuation (E_{tc}) profile and boundary layer thickness determined by slope intercept method show the increase in turbulent boundary layer growing rate beyond X = 1.0. Observation complies with the suggestion of Liepmann(34) that the sound radiation from the turbulent boundary layer may be produced by the fluctuation of turbulent boundary layer displacement thickness. Laufer(53) also observed the similar phenomena.

In order to see the pattern of the interaction waves, the leading edge of flat plate filler was beveled such that expansion flow is initially created at X = 0 and recompressed to a little stronger shock wave. From the traces taken at two Y-stations, the initial and reflected shock patterns can be mapped. Schematic reconstruction of the major flow field confirmed the locations of wave interactions to occur. However, it was noted that amplitude of signal and growth rate were almost identical to the previous flat plate case, except where direct interaction of reflected wave occurred, indicating no further amplification of freestream turbulence by intensifying the shock waves.

Two other traces were taken with turbulent mixing layer downstream of X = 0 (Fig. C.1.). In general, the rate of increase is considerably higher, ($d\overline{E}/dx \cong 1.4$/in.), which is accompanied with initial offset of intensity, than the one with turbulent boundary layer. The irregular patterns are almost in phase with those of the turbulent boundary layer case, which indicated that there exists a fixed disturbance pattern in the test section whether it was boundary layer or mixing layer beyond X = 0. Case 2 was run with operating condition II. As will be discussed in Section V.4, the boundary layer upstream of X = 0 at this operating condition was not effectively tripped and the effect of laminar-turbulent transition was present and amplified in the mixing layer at f = 5 ~ 6 KHz. Although initial increase of growth rate differs from Case 3, it appears that final growth rates are identical. Case 3 was made with operating condition I. All spectral investigations have confirmed that fully developed turbulent flow in both upstream boundary layer and downstream mixing layer have been established. This has much sharper and shorter initial rise in turbulent intensity than Case 2.

There is a distinct difference in the growth rate of free stream turbulence between the flat-plate case and the mixing-layer cases. The intensity upstream of X = 0 increases very slowly with distance and independent of downstream conditions. The change in freestream turbulent intensity measured downstream of X = 0 depends on the type of flow that follows. The increase of growth rates of turbulence were detected by hot wire when the probe travelling axially at the middle of the test section was stationed approximately at X = 0.90 ~ 1.00 in. This is where the Mach wave ($\theta = 23^\circ$ for M = 2.47) emanating from the zero X-station intersects the probe path. This implies that the initial disturbance in the freestream is generated from the lower flow field and not from the opposite wall which sees no interference until further downstream.

The difference in the initial rise with mixing layer under two different operating conditions becomes apparent when the evolutions of the power spectral density with the distance are compared. In comparison with the higher frequency components, the initial rise of 5 KHz signal component takes much greater distance before it reaches the final growth rate (Fig. C. 2). The results shown in Fig. C. 1 are the energy of the flow fluctuation integrated over the entire spectral range. As will be seen later in the variation of spectral density distributions of freestream turbulence with respect to the operating Reynolds number (Appendix C. 3), under the operating condition II, the spectral components of 5 ~ 6 KHz contains the energy in order of magnitude higher than any other frequency components. Therefore, the shape of total energy profile is strongly dependent on the 5 ~ 6 KHz components. On the other hand, a broader power spectral distribution is observed in the fluctuation under the operating condition I. Thus the total integrated energy has more contribution from high frequency components, and hence its rise is more rapid than that for Case 2.

It has been noted that fluctuating field of relatively high frequency (~ 20 KHz) is observed in the freestream. Turbulent components of the free mixing layer fluctuating with the frequency greater than 20 KHz appears to be convecting with a velocity faster than $u_c(f)/u_e \sim 0.7$. Then the relative velocities between these components and the freestream become subsonic. Hence the acoustic radiation produced by the supersonic interaction of wavy wall model alone cannot explain the radiation energy measured by the high frequency components in the freestream.

Lighthill(54) also suggested that acoustic radiation may be generated by the supersonic quadrupole field in the shear flow. The average convection velocity of what seems to be a freestream turbulence field has been measured by space-time crosscorrelation with longitudinal separation of two probes. The convection velocity defined by $\Delta x/\Delta\tau$ gives approximately 80% of freestream mean velocity which is equivalent to the convection velocity of turbulent spot measured within the turbulent free mixing layer at the point of the maximum fluctuation. If it can be assumed that the supersonic quadrupole source is imbedded in the turbulent spot and radiating sound energy as convected downstream in the turbulent free mixing layer, Lighthill's hypothesis becomes valid argument. Then measured convection velocity inside and outside of turbulent free mixing layer can be synchronized. However, this portion of experimental evidence revealed the fact that the explanation of sound field generation, only by the argument of interaction of turbulent eddies and supersonic freestream, is insufficient.

C.2. Mode Diagrams and Power Spectral Density Distributions of Free Stream Fluctuation (R-T-F: p_o = 730 mm Hg)

Typical power spectral density distributions ($\overline{e'^2}$ vs f) of the freestream turbulence taken at three axial stations above the turbulent free mixing layer (X = 3.75, 4.75, 6.75) and one axial station over upstream boundary layer (X = -1.0) are presented in Fig. C. 3a and Fig. C. 3b for two overheat parameters (r = 0.075 and r = 0.45), respectively. The low overheat data set gives approximately the hot wire response to the total temperature fluctuation. The latter set corresponds to a combination of mass flux and total temperature fluctuations due to intermediate range of overheat used. To have a meaningful comparison of data, all of these measurements were taken under the same conditions.

The spectral distribution measured at X = -1.0 is significantly lower intensity than others, and shows broader energy distributions in higher frequency range (10 KHz ≤ f ≤ 75 KHz). The probe retracted downstream along the middle of the test section began to sense the freestream turbulence generated by the turbulent free mixing layer. Increases of turbulent signals have been observed in the entire frequency domain which indicates the strengthening of generating source of turbulent field, namely turbulent free mixing layer. Especially the contribution from the energy carrying large scale eddies shows astonishingly rapid development.

Since the starting of turbulent free mixing layer is discussed in detail in Section V. 3, the present observation will be made in the established flow regime. Although the measurements with both overheat parameters show the extensive growth of low frequency components, the data taken with higher overheat show more pronounced results.

The observation has established the certain qualitative trend of the turbulent field. The frequency of peak intensity measured by low overheat has remained nearly constant whereas the frequency of peak still shifts lower in higher overheat measurement as the flow moves downstream. This indicates the larger scale eddies of mass flux fluctuation are growing in turbulent free mixing layer and quickly adjust to the local condition, such that non-dimensionalized frequency ($f\delta/u$) of the peak remains constant. However, the total temperature fluctuation is somewhat slower in adjusting to the local condition.

Spectra of mass flux fluctuations ($\tilde{m}'(f)$) and total temperature fluctuations ($\tilde{T}_0'(f)$) measured at $X = 4.75$ and $X = 6.75$ along $Y = 0.40$ are shown in Fig. C. 4 a, $\tilde{m}'(f)$ of both axial stations are almost identical within the experimental scatter and largest intensity is contained in the lower frequency domain (3 KHz ~ 4 KHz). Total temperature fluctuation shows the increasing intensity as convected downstream and peaks in the frequency domain of 5 KHz to 6 KHz. Integrated quantities are given at the bottom of the figure. Note that the spectra collapsed to a single curve if the total temperature distributions are normalized by the integrated quantity. The same is true for the velocity fluctuation as can be observed in Fig. C. 4b. Assuming the acoustic field is a plane wave with adiabatic pressure-density relation, and assuming vorticity fluctuation is negligible in essentially inviscid freestream flow, pressure and velocity fluctuations can be reduced (see data reduction). The pressure fluctuations at the two stations appear identical and peak at 3 KHz range. The velocity fluctuations vary with X-station. If these freestream disturbances are generated by acoustic radiation from the selfsimilar turbulent free mixing layer, then the turbulence field of freestream is also similar and linearly dependent on the growth rate of turbulent free mixing layer. The collapse of spectral data to a single curve when properly normalized by the integrated quantity gives assurance to the above hypothesis.

Pressure fluctuations shown in Fig. C.4b are given in fractions of static pressure ($\overline{p}$). The integrated RMS pressure fluctuation of the two stations is approximately 1.6% of $\overline{p}$. For meaningful comparison of the pressure term with other fluctuation quantities, it is convenient to express the pressure fluctuation as percent of dynamic pressure ($\frac{1}{2}\gamma\, pM^2$) in which case it is 0.4%. However, Laufer(31) has shown that the disturbances in the freestream consist of additive contributions of acoustic energy from the turbulent boundary layer of four walls, then the turbulent intensities generated by the turbulent free mixing layer is less than the measured value even though turbulent free mixing layer contribution is greater than the turbulent boundary layer one.

Constant and relatively low level of pressure fluctuation with respect to the axial stations and also with lateral stations (shown later in this section) will contribute to the further simplification of separation of turbulent components in the core of turbulent free mixing layer. Kovasznay (28) hypothesized that the sound wave generated within the shear layer propagates freely through the outer boundary without appreciable reflection back into the layer. Then the intensity of sound wave outside of shear layer cannot be different from its intensity just inside the layer. The turbulent velocity fluctuation of turbulent free mixing layer is at least an order of magnitude greater than the pressure fluctuation measured outside (i. e., two orders of magnitude difference in mean square quantities). Therefore, neglect of pressure fluctuation from the equation of fluctuation voltage to reduce the turbulent velocity and temperature spottiness of highly turbulent shear layer is justifiable.

Mode diagrams of integrated spectra are constructed and the best curve fit of these data shows less than 1% of mass flux fluctuation ($0.6\% \leq \sqrt{\overline{\dot{m}'^2}}/\dot{m} \leq 0.8\%$) and less than 0.5% of total temperature fluctuation ($0.35\% \leq \sqrt{\overline{T_o'^2}}/T_o \leq 0.56\%$). Linearity of the curve implies the strong anticorrelation of mass flux fluctuation and total temperature fluctuation ($R_{\overline{\dot{m}\,T_o}}' = -1.0$) to exist. The mode diagram curves taken at X = 4.75 and 6.75 do not appear to converge at $r = \beta$ point, although the fluctuation of pressure spectra has shown the excellent agreement of these two stations. Because of low turbulence level of freestream, the signal-to-noise ratio of the amplifier response deteriorates and the confidence level of the absolute magnitudes of measurements are not high. Assuming the plane acoustic wave propagation, the foregoing results can be used to compute the streamwise velocity fluctuation ($\sqrt{\overline{u'^2}}/u_L$) and pressure fluctuation normalized with respect to freestream dynamics pressure ($\sqrt{\overline{p'^2}}/\frac{1}{2}\gamma pM^2$); which are approximately 0.5% and 0.4%, respectively. As will be shown in Appendix C.3, the streamwise velocity and pressure fluctuations induced by the upstream turbulent boundary layer with operating condition I are 0.2% and 0.1% respectively.

Very interesting results are observed in the next mode diagram (Fig. C. 5). These data were taken at fixed X-station (X = 4.75) by moving the probe in the lateral (Y) direction. Y = 0.5 is geometrically located in the middle of the freestream and Y = 0.25 is located approximately at the edge of turbulent free mixing layer where the turbulence is occasionally intermittent. The intensity of mean square voltage was obtained through the thermo-couple (E_{tc}). High pass and low pass filters were set so that signals outside of 100 Hz ~ 320 KHz were rejected. Time constant of amplifier (M_A) was set at 50 μ sec. Actual time constant (M_t) of wire response in the freestream with operating condition I is approximately 45 μ sec. Under these testing conditions, the mode diagrams of the freestream fluctuation taken at various lateral positions appear to converge at $r = \beta$ which indicates the pressure fluctuation remained almost constant with varying Y. Its level is approximately 0.4%. Velocity fluctuation ranges from 0.5% at midpoint to 0.75% at Y = 0.30, just outside of the turbulent free mixing layer. Increase of $\sqrt{\overline{u'^2}}/u_L$ is partially contributed from the infrequent passage of the turbulent edge.

C. 3. Effect of Laminar - Turbulent Boundary Layer Instability (Reynolds Number Dependence)

It will be mentioned in the spectral investigation of turbulent mixing layer (Section V. 2. 2. 2) that a peculiar peaking of spectral signal occurred near the frequency of 5 KHz when the test was conducted with p_o = 610 mm Hg and upstream tripping of the boundary layer with a strip of fine sand paper. These signals have been observed in free mixing layer and freestream. At first, the peculiarity of the signal was thought to be caused by strain-gauging of the hot-wire. However, these discrete signals appeared consistently for all different probes used and no appreciable shifts in frequency were noted. Previous experience has shown that the strain-gauging of the hot-wire occurs in relatively high frequency range and does not usually repeat in the same frequency, because no hot wire will be constructed exactly alike. Hence the strain-gauging has been discarded as the source of this consistent peaking. Mechanical vibration of the probe holder is below 100 Hz and most unlikely to influence the measurements. Therefore, it was suspected that the observed signal is inherent in the flow field.

The second speculation was that an oscillation of the entire mixing layer pivoted at the X = 0 station. A turbulent boundary layer of finite thickness is present at the starting point of the free mixing layer and the outer edge is expected to be fluctuating. This fluctuation causes the oscillation of weak shock wave emanating from the corner and in turn the turbulent free mixing layer itself may oscillate.

Another contribution to the suspected oscillation is from the possible unsteadiness of injected air.

Although these possibilities cannot be entirely ruled out, more positive clues to these peculiarities have been found when the testing condition was altered. Repeated experiments with different operating total pressures have revealed that the presence of intensity and the peak are dependent on Reynolds number. Possible cause of this phenomenon is the laminar-turbulent flow transition of the boundary layer as discussed below. If the argument of the foregoing paragraph of free mixing layer oscillations was true, then these disturbances should not propagate upstream in supersonic and hence should not be observable when the signals were sampled at upstream of the corner. Surprisingly, however, the same discrete signals have appeared in the measurements of upstream free stream and boundary layer! This finding confirmed that whatever the sources of disturbance may be, it must exist upstream of the test section.

Spectral density distribution were taken in the freestream at X = -1.0 station with wind tunnel stagnation pressure (p_o) varied, which changed the Reynolds number of the test section. Spectra of the mean square fluctuating voltage ($\overline{e'^2}$) taken at the same $S_{\dot{m}}/S_{T_o}$ are shown in Fig. C.6. Data at the total pressure settings of 420 mm Hg to 610 mm Hg were taken on the same day with the same probe and direct comparison of intensity level is possible. But the last data points (p_o = 735 mm Hg) were taken several days later and hence only the qualitative shape of the spectra, but not the level, may be compared with the other data.

At $p_o = 420$ mm Hg the energy spectra of hot-wire fluctuating voltage has been observed to be at very low level and flat in the frequency range of $500\text{Hz} \le f \le 30$ KHz. Integrated values of power spectral density distribution obtained by the hot-wire operated with several overheats yield the fluctuating mode diagram. The curve is perfectly linear and its intercept of ordinate is approximately 1×10^{-3} (or 0.1%). It intersects the abscissa approximately at $r = -\alpha$ where $r = S_{\dot{m}}/S_{T_o}$ (ratio of sensitivity coefficient of mass flux and total temperature) and $\alpha = (1 + \frac{\gamma-1}{2} M^2)^{-1}$. According to Kovasznay (see Data Reduction Section) this condition exists when the free stream fluctuation is caused by the entropy fluctuation (pure temperature spottiness of flow caused by the process of compression, after cooling, drying, etc.).* The shape of spectral distribution and the mode diagram imply that virtually no pressure fluctuation produced by the acoustic radiation is present in inviscid free stream and the boundary layer is laminar. Turbulence level is approximately 0.1% solely from temperature spottiness.

Approximately 10% increase in total pressure ($p_o = 470$ mm Hg) introduces the peaking of fluctuating voltage near 6 KHz and the peak intensity increases by a factor of 4 of laminar flow. The data taken with $p_o = 526$ mm Hg show the highest peak signal at almost 30 times higher than the laminar case. Slight decrease of the peak intensity is noted in $p_o = 610$ mm Hg data. Most of the integrated energy comes from the frequency band of 1 KHz to 15 KHz. The frequency

---

* It appears that the level of temperature spottiness may change with the condition of the dryer, which depends upon the heating and cooling cycle of the drying agents prior to the tunnel operation.

corresponding to the peak intensity appears to shift slightly lower as the Reynolds number increased. As mentioned in the section on data reduction, it is very reasonable to assume that temperature spottiness of flow is completely uncorrelated with velocity and pressure fluctuations in the freestream. Then turbulent velocity and pressure fluctuation intensity in freestream can be found if plane acoustic radiation field is assumed.

Several days after the foregoing test, one of the filters in the upstream settling-chamber was removed and the total pressure of the test section was increased to the atmospheric condition. Also, the boundary layer trip made of a strip of fine grain sandpaper (C-320) was replaced with coarse grain sandpaper (EC #30). During these alterations, the activated dryer was left cooled for a few extra days. It is possible that this condition might have changed the temperature fluctuation in the operating system.

The new testing condition definitely changes the pattern of turbulent intensity distribution. The discrete signal at 5 KHz vanished from the freestream (Fig. C.6) and boundary layer measurements, which is not shown. The spectra distribution is broader and extends into considerably higher frequency range (up to 100 KHz in the freestream). Although the level of intensity is the lowest in the low frequency range, it is higher in frequency above 15 KHz. However, as mentioned earlier, the temperature spottiness of the flow might have changed and the responses of different probes are not identical. Two sets of outputs made on different days may not be compared directly. However, spectra plotted in log-log scale is unaltered by multiplicative variation of intensity level, qualitative comparison of spectral distribution is valid.

Unfortunately, the level of integrated quantity was also different from the previous results. If it was assumed that temperature spottiness of the latter case was almost zero after the prolonged cooling of the dryer, resulting in very uniform temperature distribution throughout the dryer, then data obtained in two different days may be replotted in new fluctuation mode diagram. If it is assumed that temperature spottiness is completely uncorrelated from pressure and velocity fluctuations induced by turbulent boundary layer, then the mean square response equation of the hot-wire for freestream can be written as:

$$\frac{\overline{e'^2}}{S_{T_o}^2} = (\beta - r)^2 \frac{\overline{u'^2}}{\bar{u}^2} + \frac{2}{\gamma}(\beta - r)\left(\frac{\beta}{M^2} - r\right)\frac{\overline{u'p'}}{\bar{u}\,\bar{p}} + (\beta - r\,M^2)^2 \frac{\overline{p'^2}}{\gamma^2 M^4 \bar{p}^2} + \left(\frac{\alpha + r}{\alpha}\right)^2 \overline{\theta^2}$$

where $\bar{\theta} = T_s'$ temperature spottiness expressed in reference to total temperature

Laufer[31] shows that correlation coefficient, $R_{\overline{u'T'}}$, is -1.0 in freestream is reasonable when $R_{\overline{\dot{m}'T_o'}} = -1.0$. Thus we obtain

$$\sqrt{\frac{\overline{e'^2}}{S_{T_o}^2} - \left(\frac{\alpha + r}{\alpha}\right)^2 \overline{\theta^2}} = (\beta - r)\frac{\sqrt{\overline{u'^2}}}{\bar{u}} - (\beta - r\,M^2)\frac{\sqrt{\overline{p'^2}}}{\gamma M^2 \bar{p}}$$

Assume a pure laminar flow exists for the operating condition of $p_o = 420$ mm Hg, $\sqrt{\overline{\theta^2}} \cong .001$. Using this value, new mode diagrams are constructed and shown in Fig. C . 7. Highest intensity is observed with p_o = 526 mm Hg data and increasing-decreasing trend has been established. This indicates that the largest unstable eddies interacting with freestream (relative velocity may be supersonic) appears to be responsible for the freestream turbulence. Pressure and velocity fluctuations versus operating total pressure are shown in Fig. C. 8. Based on momentum thickness, the $R_{e_\theta} \cong 2400$ (for p_o = 735 mm Hg, M = 2.47) and associated pressure fluctuation is approximately 0.1% of dynamic pressure. Pressure fluctuation intensity measured in JPL supersonic tunnel at $M_e = 2.2$ and $R_{e_\theta} \cong 9000$ is shown to be approximately 0.2% of dynamic pressure (this value is obtained by 4 times Laufer's data taken for a single wall).

Appearance and disappearance of signal near the frequency of 5 KHz ~ 6 KHz with variation of Reynolds numbers and method of tripping definitely confirmed the idea of existence of laminar-turbulent instability. Below the certain operating condition, small disturbance created by fine grain size tripping was unable to effectively trip the supersonic flow to create the fully developed turbulent boundary layer. Combination of fine tripping and p_o = 900 mm Hg finally eliminated the discrete signal from mixing layer spectra as will be observed in Section V. 4.

Full turbulent boundary layer has been effectively developed when the combination of very coarse grain tripping and atmospheric operating condition was used as demonstrated. Qualitative agreement of the present investigation and extrapolation of Laufer's(43) experiment gives credence to the correctness of the present idea.

Contributory effect of the upstream flow instability to the subsequent free mixing layer behind the step will be discussed in Section V. 2.

C. 4. Freestream Autocorrelation (p_o = 610 mm Hg F-T-F)

Autocorrelation measurements of freestream turbulence along the middle of the test section (Y = 0. 45) at longitudinal locations ($-0.5 \le X \le 4.75$) are taken under the testing condition of p_o = 610 mm Hg with a fine trip (Fig. C. 9). Two important pieces of information have been gained from the measured data, which verifies the earlier conclusion from the power spectra distribution.

1) The magnitude of $A_{11}(0)$ distribution with respect to the X-stations shows that a noticeable abrupt change in freestream turbulent level occurred between X-station 0. 75 to 1. 75, which generating source can be traced back to the origin of the mixing layer at X = 0. This phenomenon was also verified in the hot-wire measurements taken with thermocouple output (E_{tc}).

2) Autocorrelation function $A_{11}(\tau)$ shows the existence of periodic oscillatory motion of flow which is nearly exponentially damped. Evaluation of the period of oscillation gives the frequency of approximately 5 KHz ~ 6 KHz. The discrete signal observed in the power spectral density distribution obtained at the same operating condition in fact coincides with this frequency (Appendix C-2).

To verify that the existence of oscillatory motions in the freestream flow is dependent upon the Reynolds number, the autocorrelation functions of freestream turbulence with various total pressure settings have been measured and shown in Fig. C. 10. Since the observed wave is a low frequency component, the band limited signal of 100 Hz to 40 KHz is sampled with a hot-wire operating with a moderate overheat (i = 6.4 ma). The total pressure setting of 418 mm Hg detects the presence of a very weak wave. The most intensified waviness has been detected with an operating pressure of 525 mm Hg and the frequency of periodic waves appears to be approximately 5 KHz. Further increase in total pressure has resulted in decreasing of intensity and frequency of waves. The autocorrelation measurements verified the observation of power spectral density distributions made in Appendix C. 3.

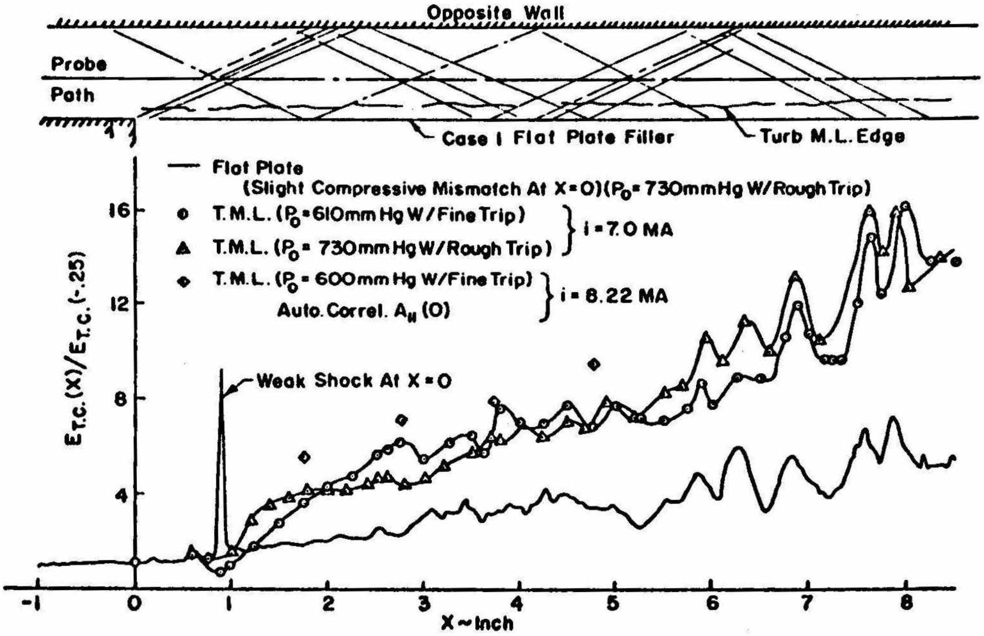

FIG. C.1 FREESTREAM TURBULENT INTENSITY DISTRIBUTIONS

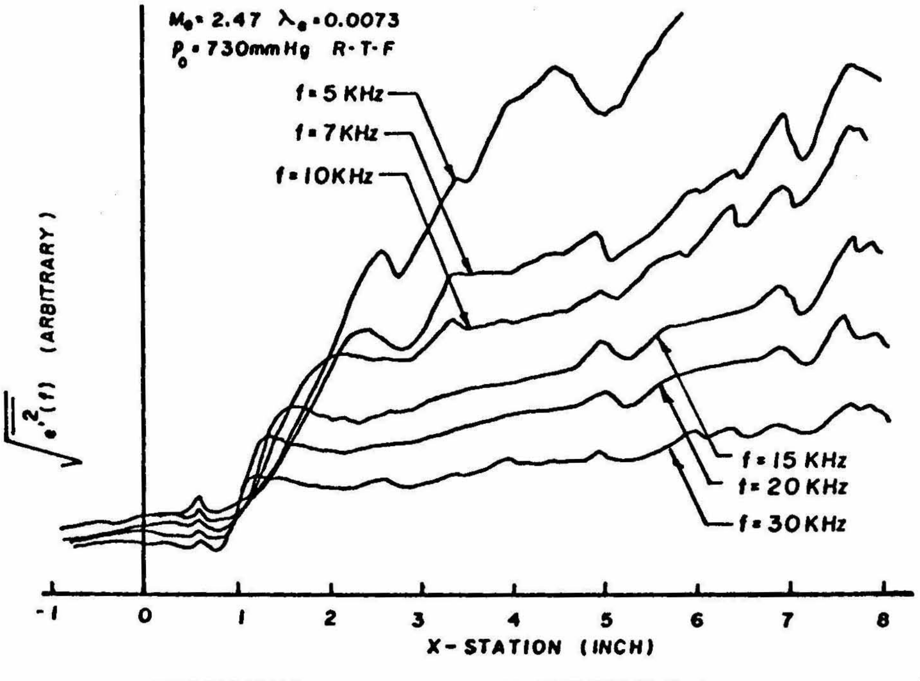

FIG. C.2 EVOLUTIONS OF POWER SPECTRAL DENSITY WITH THE DISTANCE

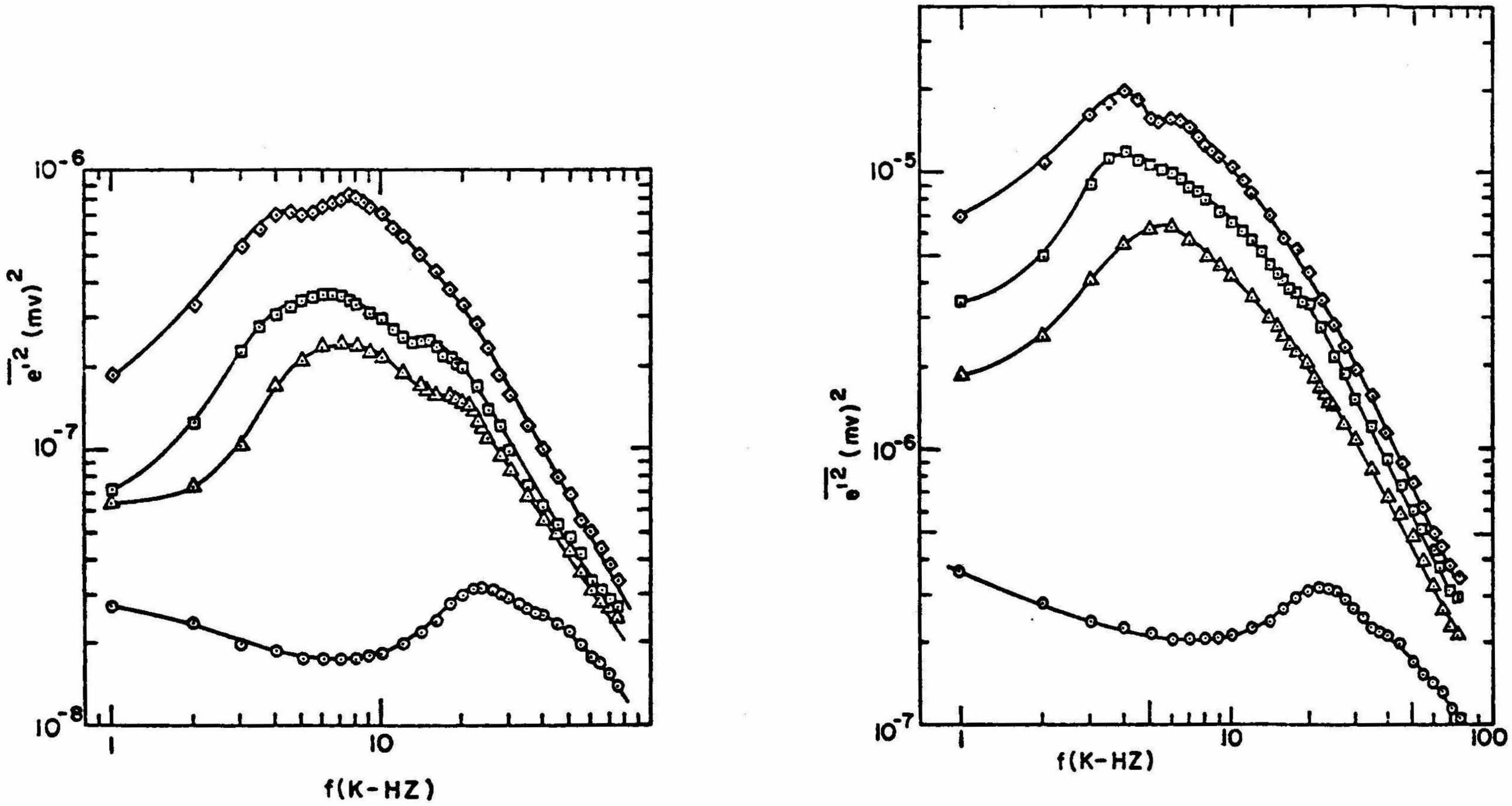

$S_{\dot{m}} / S_{T_0} = 0.075$

$S_{\dot{m}} / S_{T_0} = 0.45$

$M_e = 2.45$ $p_0 = 735$ mmHg R-T-F $Y = 0.45$

○ $X = -1.0$ △ $X = 3.75$ □ $X = 4.75$ ◇ $X = 6.75$

FIG. C.3 FREE STREAM ENERGY SPECTRA WITH VARIABLE X-STA.

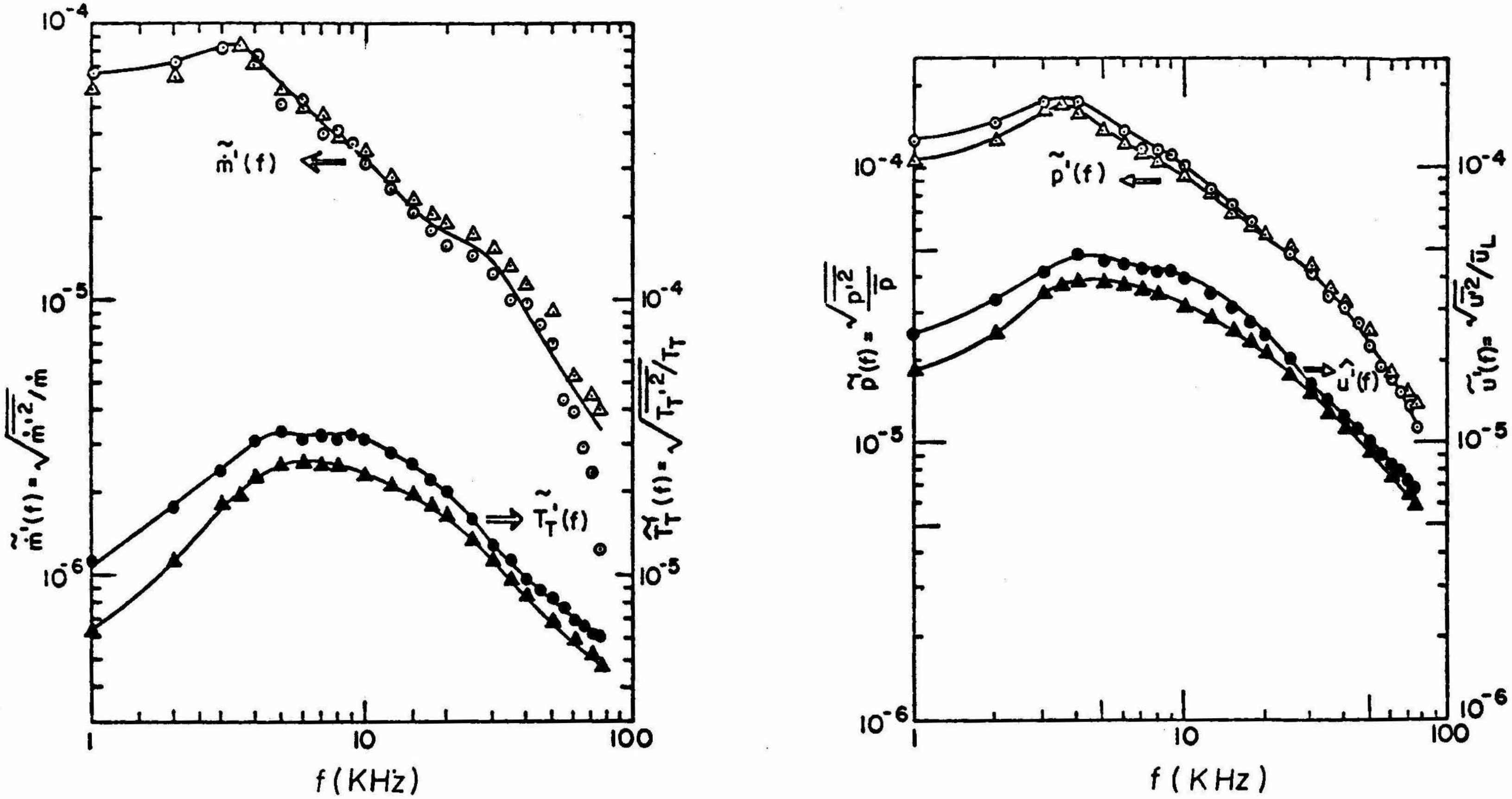

$M_e = 2.45$ $p_o = 735$ mm Hg R - T - F $Y = 0.40$ $\overline{u}_L = 1800$ ft/sec $\overline{p} = 46.5$ mmHg

○ $X = 6.75$ $\tilde{\dot{m}}' = .56 \sim .64 \times 10^{-2}$ $\tilde{T}' = .45 \times 10^{-2}$ $\tilde{p}' = 1.63 \sim 1.75 \times 10^{-2}$ $\tilde{u}' = .6 \times 10^{-2}$
△ $X = 4.75$ $.59 \sim .65 \times 10^{-2}$ $.35 \times 10^{-2}$ $1.53 \sim 1.61 \times 10^{-2}$ $.5 \times 10^{-2}$

FIG. C 4 FREESTREAM TURBULENT FLUCTUATION SPECTRA
(SOUND MODE)

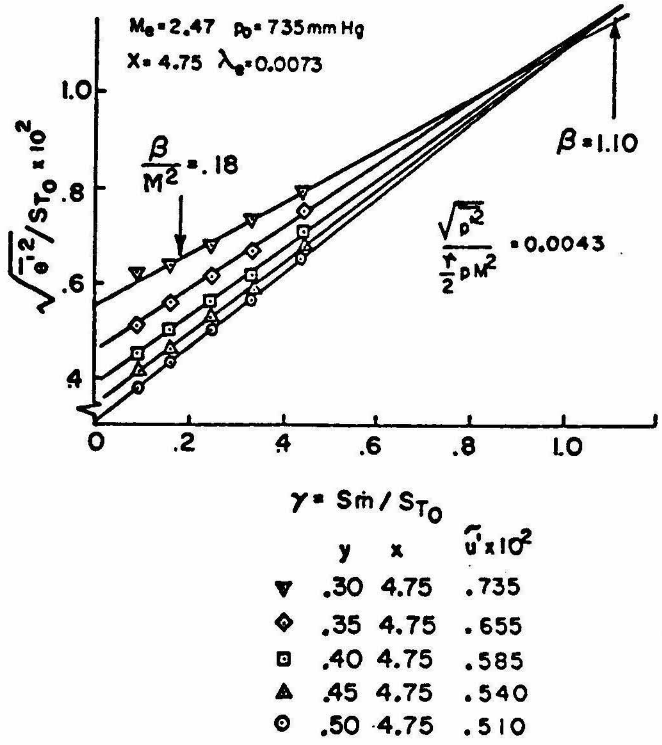

FIG. C.5 FREE STREAM FLUCTUATION MODE DIAGRAM Y-DISTRIBUTION

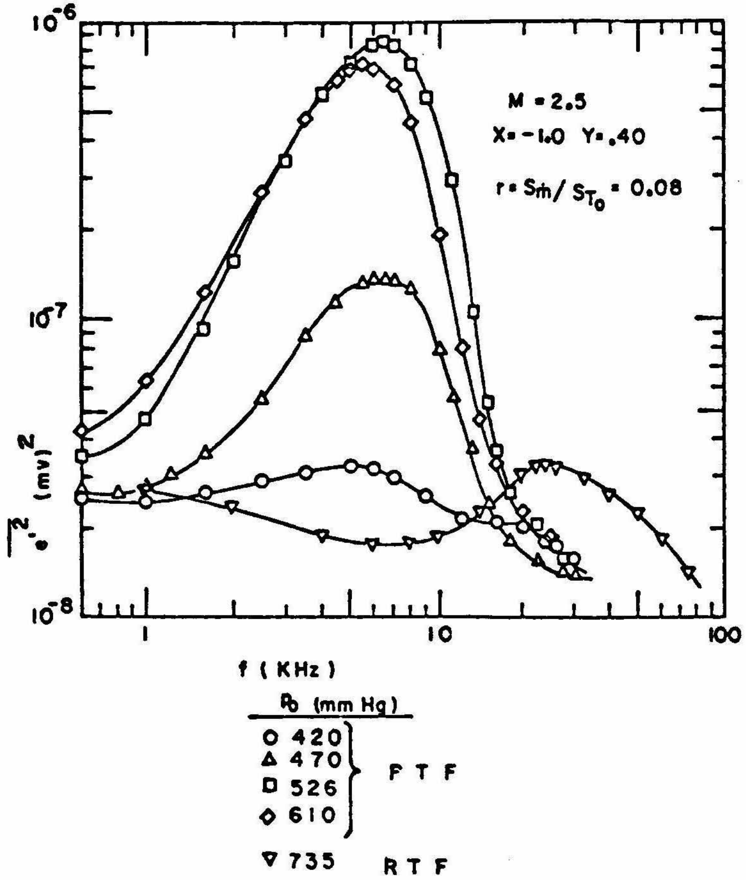

FIG. C.6 FREE STREAM ENERGY SPECTRA VARIABLE TOTAL PRESSURE

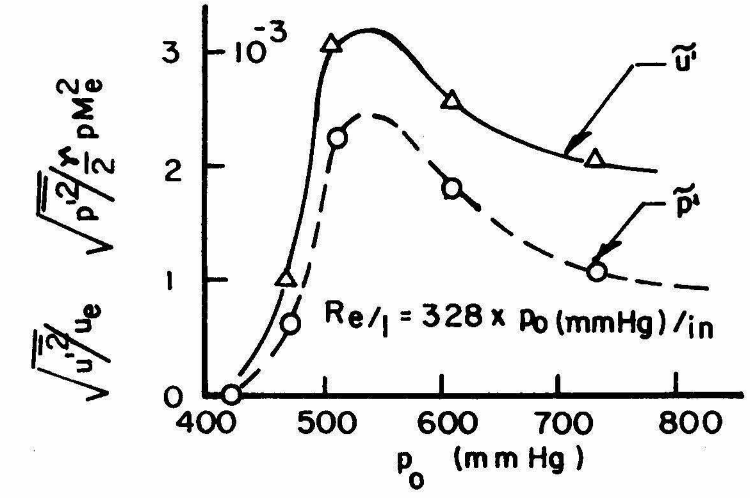

FIG. C. 8 FREE STREAM BOUNDARY LAYER INDUCED PRESSURE AND STREAMWISE VELOCITY FLUCTUATION

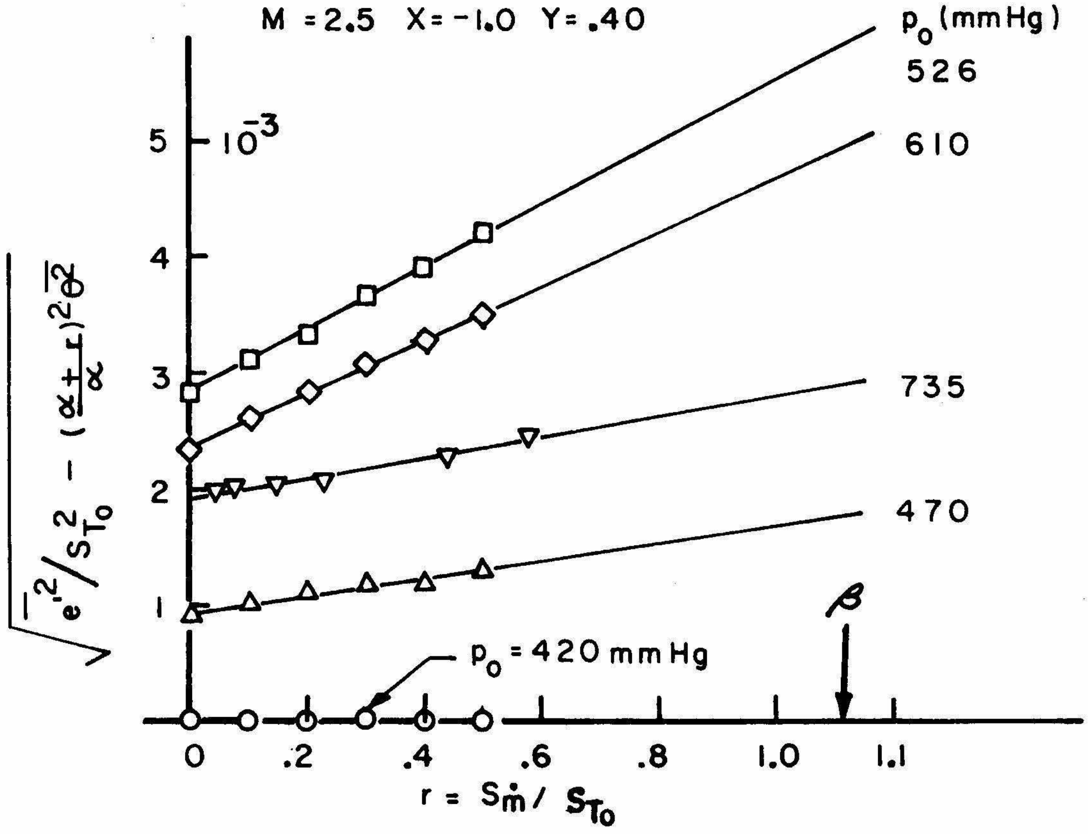

FIG. C. 7 FREE STREAM MODE DIAGRAM WITH VARIABLE TOTAL PRESSURE

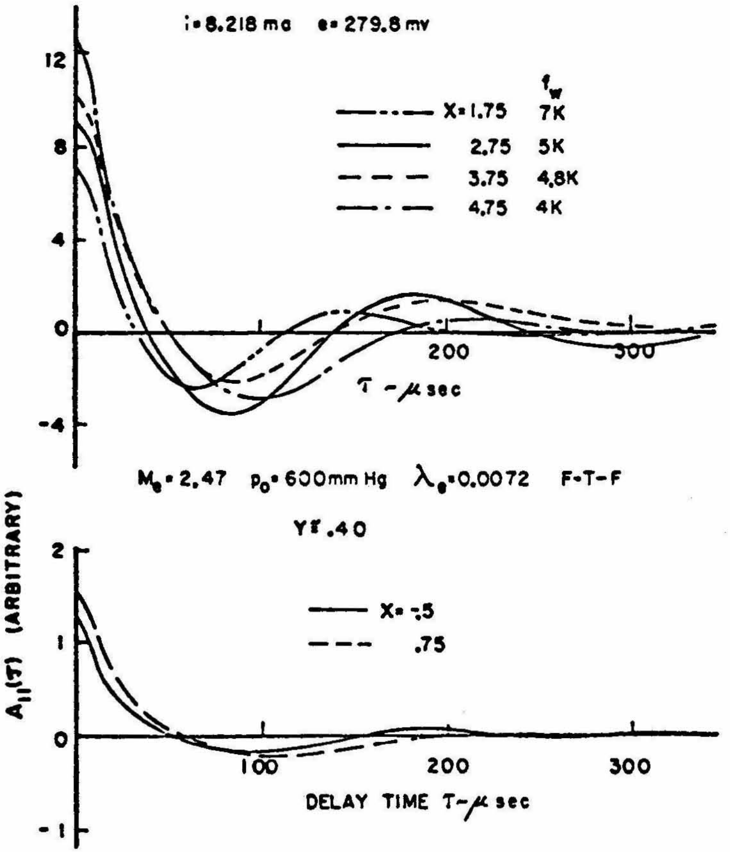

FIG. C.9 FREE STREAM TURBULENT AUTOCORRELATION

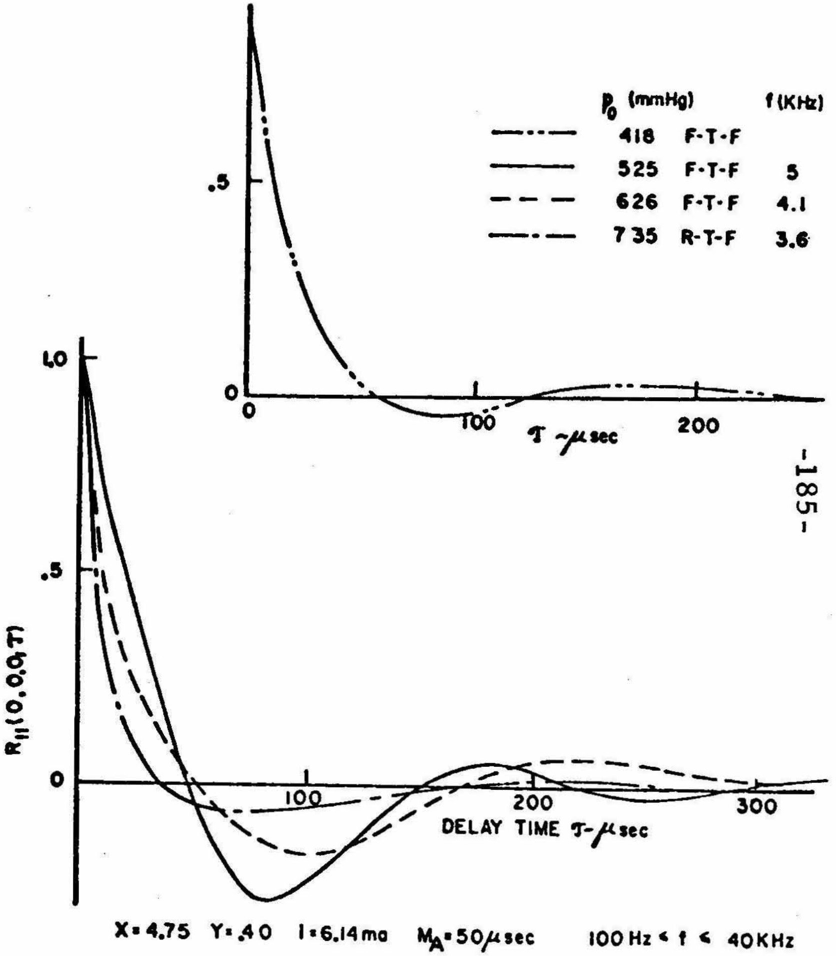

FIG. C.10 FREE STREAM TURBULENCE AUTOCORRELATIONS WRT VARIABLE STAGNATION PRESSURE

APPENDIX D

SUPPLEMENTAL DATA FOR SUPERSONIC TFML

D.1. Detailed Definition of Low Speed Tail of Pressure Profile

Very slight undershoot of Pitot pressure before recovering to the final value (Pitot p-prove senses static pressure as u → 0) at the low speed end of the Pitot pressure profile was noted in the direct measurement, which may have indicated the possible existence of reverse flow. The response of Pitot p-probe deviates from the true value as the local flow angle of attack exceeds the value approximately 15°. With a large flow angle, the Pitot p-probe senses the contribution from the cross-flow component. As a consequence the measured pressure is less than the true value.

To confirm that the observed undershoot is not the true indication of reverse flow, a 1 psig Statham differential pressure transducer was used to monitor the pressure difference between a forward facing Pitot p-probe, a rearward facing Pitot p-probe or a static p-probe and a fence tap distributed along Y = -0.5 inch. With a matched blowing rate, all probes registered the negative differential pressure in the low velocity regions. The crucial point is the comparison of the both Pitot pressures with a static pressure trace. Typical measurements are shown in Fig. D.1.a. Note, the pressure of the forward facing Pitot p-probe remains above the pressure trace of static p-probe and approaches it asymptotically without crossing the static pressure. On the other hand, the Pitot pressure distribution of the rearward facing probe remains below the static pressure indicating that it read the base pressure behind the Pitot p-probe. These data show that no reverse flow existed.

When the injection rate is decreased to create a recirculation zone, the pressures read on the rearward facing probe become greater than the static pressure indicating the existence of reverse flow with velocity approximately 8 to 10% of the free stream value as shown in Fig. D. 1. b.

The transducer showed approximately 0. 05 mm Hg of shift in pressure, which may have been partially created by the unsteadiness of the flow. The discrepancy of this magnitude corresponds to the uncertainty of measurements of approximately 0. 1% of static pressure. Therefore, with the combined effect of discrepanices caused by the flow angles with respect to probes and a transducer response, the uncertainty of the profile in very low speed region magnifies. The partial remedy was attempted with the use of a Pitot p-probe with smaller relative angle of attack but the improvement was minimal.

D. 2. Approximation of TFML Spreading rate with Density Ratio

The reason why the prediction of spreading rate of supersonic TFML with a density ratio appears to be valid is partially explained in the following discussion. The momentum balance across the dividing streamline of a mixing layer ($dp/dx = 0$) is

$$\int_{\eta^*}^{\infty} \frac{\rho u}{\rho_e u_e} \left(1 - \frac{u}{u_e}\right) d\eta = \int_{-\infty}^{\eta^*} \frac{\rho u^2}{\rho_e u_e^2} \, d\eta \qquad \text{(D-1)}$$

The universal velocity profile is assumed and the density profile is a function of Mach number. For $dp/dy = dT_o/dy = 0$:

$$\frac{\rho(\eta)}{\rho_e} = \frac{T_e}{T(\eta)} = \left\{1 + \frac{\gamma-1}{2} M_e^2 \left[1 - \left(\frac{u(\eta)}{u_e}\right)^2\right]\right\}^{-1} \qquad \text{(D-2)}$$

where $\eta = \frac{\sigma y}{x} = \frac{\sigma_i y_i}{x}$ and η^* is a location of the dividing streamline. Note that most of the density variation occurred in the supersonic side of the TFML above $u/u_e \sim .55$ (Fig. D. 2). Then the density below the dividing streamline is approximated by a constant value, namely, ρ_w/ρ_e.

With these assumptions, the momentum balance equation is reduced to

$$\int_{-\infty}^{\infty} \frac{\rho u}{\rho_e u_e} \left(1 - \frac{u}{u_e}\right) d\eta = \int_{-\infty}^{\eta^*} \frac{\rho u}{\rho_e u_e} d\eta \cong \frac{\rho_w}{\rho_e} \int_{-\infty}^{\eta^*} \frac{u}{u_e} d\eta$$

or

$$\sigma \theta \cong \sigma_i \frac{\rho_w}{\rho_e} \int_{-\infty}^{y_i^*} \frac{u}{u_e} dy_i = \sigma_i \frac{\rho_w}{\rho_e} \int_{o}^{X_E} \lambda_{e_i} dx \qquad \text{(D-3)}$$

$u(\eta^*)/u_e$ is approximately constant within the Mach number range of 1. 0 to 5. 0. Differentiating equation D. 3 with X, and letting $d\,\theta_i/dx = \lambda_{e_i}$,

$$\frac{d\theta}{dx} \cong \frac{\sigma_i}{\sigma} \frac{\rho_w}{\rho_e} \lambda_{e_i} = \frac{\sigma_i}{\sigma} \frac{\rho_w}{\rho_e} \frac{d\theta_i}{dx} \qquad \text{(D-4)}$$

The scaling parameter, σ_i/σ can be computed from the known experimental data. From the present investigation of $M_e = 2.47$ TFML, the measured quantities are

$d\theta/dx \cong 0.0073$ $\qquad$ $\rho_w/\rho_e \cong 0.45$

The incompressible value of Liepmann and Laufer(19) gives

$$d\theta_i/dx = 0.035$$

The computed scaling parameter is found very close to ρ_w/ρ_e

$$\sigma_i/\sigma \cong 0.465 \cong \rho_w/\rho_e$$

(σ_i/σ computed from the data of Maydew and Reed(1) and Sirieix and Solignac(11) is observed to be larger than ρ_w/ρ_e). Since the measurements of $d\theta/dx$ of the present investigation are more reliable than those of the previous investigators, it is assumed that the approximation of

$$\frac{\sigma_i}{\sigma} \cong \frac{\rho_w}{\rho_e} \tag{D-5}$$

is reasonable. (Note that incompressible binary mixing flow does not follow this rule).

Then the spreading of momentum thickness and width of supersonic TFML can be approximated from the incompressible values by density ratio relations.

$$\left.\begin{aligned} \frac{d\theta}{dx} &\cong \left(\frac{\rho_w}{\rho_e}\right)^2 \frac{d\theta_i}{dx} \\ \frac{dy}{dx} &\cong \left(\frac{\rho_w}{\rho_e}\right) \frac{dy_i}{dx} \end{aligned}\right\} \quad \text{Gives good approximations within 10\% of actual values} \tag{D-6}$$

D. 3. Mach Number Dependence of TFML

Maximum shear stress, momentum thickness growth rate and dividing streamline Mach number were shown to be varied with Mach number. To establish the trend, these quantities were computed from the available data. Experiments of Maydew and Reed(1) were carried out in the half jet region of axisymmetric jet exhausting into the quiescent air. Five Mach numbers of 0.70, 0.85, 0.95, 1.49 and 1.96 were investigated. Although questions of three-dimensional effects were raised, the mean flow quantities appeared to be reliable. Experiments of Sirieix and Solignac(11) were conducted in the wind tunnel equipped with a cavity and an adjustable end plate, and the flow in the cavity was very likely to be recirculating. Mach numbers of 3.0 and 4.0 were investigated. Schlieren photograph shows the existence of thick boundary layer on the half nozzle section and the regions investigated appear to be barely out of the influence of the initial boundary layer. However, the axisymmetricity and starting conditions observed by both experiments do not appreciably alter the mean velocity profiles, but may affect the spreading rates. The velocity profiles of both experiments agree reasonably well with the theoretical profile of Crane (35) with a proper choice of spreading parameter, σ. The foregoing statement, however, will not be true for the fluctuating field.

The computed results based on their experimental data are shown in Fig. V.13. Insufficient numbers of data were available below $u/u_e \doteq 0.10$ in some cases and in those cases data were extended according to Crane's curve in the low velocity region. Maximum shear stress ($\tau_{max}/\rho_e u_e^2$) starts with 0.012 of Liepmann and Laufer,(19) and remains relatively constant to M = 0.85 (Maydew and Reed data showed slightly higher values, $\tau_{max}/\rho_e u_e^2 = 0.0127$

and 0.0123 for M = 0.7 and 0.85, respectively). It decreases rapidly beyond M = 1.0 and the value of 0.0017 is attained with M = 4.0 data. Two points taken in the separated shear layer ahead of the forward facing step by Behrens(36) are also shown, which are higher than the trend established in the free mixing layer. Shear stress of the present investigation is 0.0028 and smoothly fills the gap between the two previous experiments. The shear stress measured by Brown and Roshko(20) for a two gas mixing experiment is considerably higher than the adiabatic supersonic TFML with density ratio ($\tau_{max}/\bar{\rho}(\Delta U)^2$ = 0.0106 for $u_1/u_2 = \sqrt{7}$ and $\rho_1/\rho_2 = 7$, $\bar{\rho} = \frac{1}{2}(\rho_1+\rho_2)$). Maximum shear stress normalized by the respective $d\theta/dx$ shows the slightly increasing trend with Mach number. The growth rate of momentum thickness ($d\theta/dx$) decreases with increasing Mach number similar to the behavior of shear stress with Mach number. Lowest $d\theta/dx = 0.004$ is obtained for M = 4.0.

Mach number at the dividing streamline is also shown. Although the existence of initial boundary layer was clearly evident in the experiments of Sirieix and Solignac, no boundary layer correction has been applied in momentum balance, i.e., θ_o of equation V.1 is set equal to zero. Predictions of the dividing streamline Mach numbers are made with an assumption that the linearly scaled velocity profile of the present investigation is invariant with Mach numbers. The upper curve represents the ideal self-similar flow case without influence of the initial momentum thickness, i.e., $\theta_o/\theta \ll 1$. Whereas the lower curve is predicted with an assumption that non-negligible θ_o based on the present investigation exists. The data points of the previous investigators computed without the effect of the inital momentum thickness match reasonably well with the upper curve.

The variation of linear scaling parameter, σ_m, is determined by the evaluation of momentum thickness with a universal velocity profile. The variation of σ_m is also shown in Fig. V.13. which is higher than ρ_w/ρ_e distribution.

D.4. Constant Turbulence Intensity of Self Similar TFML

The clue to the ever increasing trend of the measured turbulence energy was found to be the direct consequence of instrument response to high frequency turbulent components associated with the supersonic turbulent mixing layer.* It has been noted that substantial level of turbulent energy is carried by the high frequency components, say, 100 KHz and above. However, the amplifier response of the Shapiro-Edwards Model 50B hot-wire anemometer is flat up to 100 KHz and shows the degrading character as it was calibrated by Gran.[(25)] Also, the highest frequency cutoff of low-pass filter is 320 KHz. Therefore, the energy contribution resulting from the high frequency domain which extends beyond the filter cutoff point or in the degrading portion of the amplifier response affects the E_{tc} and the autocorrelation measurements due to the built-in characteristic of the amplifier.

Since the power spectral distribution of self similar turbulence shifts to a lower frequency range with the increasing longitudinal distance, the normalization of spectra with some characteristic dimension, such as mixing layer width, of TFML holds true. Then

---

* The author wishes to thank Professor A. Roshko for pointing out this fact.

E_{tc} or autocorrelation measurement taken near the beginning of fully developed TFML loses more energy contributions from the high frequency components than the one from farther downstream. Therefore, a false indication of continuously increasing trend of total energy level is observed with respect to longitudinal distance.

The spectra data have been corrected for the amplifier response and the proper compensation time constant so that the ideal response of wire to the high frequency turbulent field is simulated. Although ideal integration of spectra should be taken from zero to infinity in the physical frequency domain, this is not practical in the experiment due to the response characteristics of the instruments. The integration must be carried out within the consistent range of normalized frequency domain, especially when a comparison of integrated quantities obtained at the different positions of the flow field is desired. Once the integration of the spectra is carried out to the prescribed value of $f\theta/u_L$, a reasonably flat total energy distribution with respect to the longitudinal distance is obtained. However, the actual integrated energy is greater than the one computed due to the integration cutoff limit. Therefore, actual value should be taken from the result of the full range integration of the farthest downstream data. Nevertheless, it has demonstrated the existence of truly equilibrium flow. The results are presented in Sect. V.4.

D.5. Effect of Unmatched M_A and M_t

The E_{tc} data produce an error in the quantitatively reduced fluctuation intensity, if the time constant of compensating amplifier is set unequal to the time constant of wire response in the flow and the turbulence contribution of local flow is dominated by the low frequency spectrum components. Since the wire time constant, M_t, is directly dependent upon the overheat parameters, larger variations of M_t from the M_A setting will result for the wire operated at higher overheat than the one at low overheat. Therefore, the degree of overcorrection of data by M_t/M_A may become worse for the high overheat measurements. The typical mode diagram which shows the difference of data produced by the matched and unmatched time constant is illustrated in Fig. D. 3. The E_{tc} data with matched time constant ($M_A \cong M_t$) agree reasonably well with the integrated spectral measurements, in which case $\tilde{m}' = 0.05$ and 0.046, respectively. However, the E_{tc} measurements taken with $M_A < M_t$ overcorrect the data resulting in approximately 30% higher fluctuating voltage ($\sqrt{\overline{e'^2}}/S_{T_o}$) at $r = 1.2$. Curve fitting of these data points gives $\tilde{m}' \cong 0.074$, which is approximately 50% higher than the corrected value. The difference is less pronounced for the high frequency dominated turbulent field which is observed in the high speed side of the mixing layer.

D. 6. Development of Space-Time Correlation Function (Δx Separation)

Study of the spatial correlogram at three lateral positions (Fig. D. 4) reaffirms the same aspect of convection field discussed in Section V. 2. 2. 5. 2. For the clarity of data presentation, the time delay is shifted so the peak correlation points are aligned in a common axis. The line of zero time delay is also shown. The initially symmetric form of axial crosscorrelation function with respect to the negative and positive time delay ($\Delta\tau$) develops into the distorted pattern as the axial separation distance (Δx) increases. The M-probe positioned upstream of the S-probe has been delayed and thus a process in negative time delay represents the past occurence and in positive time delay as the future occurence with respect to the S-probe.

The definition of axial crosscorrelation is

$$C_{ms}(\Delta x, \Delta\tau) = \lim_{T \to \infty} \frac{1}{2T} \int_{-T}^{T} f_s(x, t) f_m(x-\Delta x, t-\Delta\tau) dt$$

The correlogram taken near the dividing streamline ($Y/\theta \sim 0.28$) shows the least development of distortion with x-separation which indicates a progagation of relatively uniform flow field along the dividing streamline. The turbulent flow fields above and below the dividing streamline (data taken near the maximum fluctuation, $Y/\theta \cong 3.2$, and subsonic region, $Y/\theta \cong -1.82$) distinctly show the asymmetric development of correlation functions with positive and negative delay time. A more pronounced and rapid development in the low-speed region may be attributed to the entrainment process of slow moving fluid at the lower boundary. The steeper slope of correlation function in the negative delayed time implies the arrival of sharper and distinctly patterned turbulent front. On the other hand, a relaxing of slope in positive delayed time implies the growing pattern of trailing tail of turbulence. The observation can be interpreted as the process of entrainment of mass at the turbulent front and the growth of turbulent scale as convected. The non-uniformity of propagating turbulent form also hints that the mean velocity and the convection velocity of a frozen turbulent spot may not necessarily be identical along the off-centered positions of turbulent mixing layer and the flow is highly intermittent near the edges. However, it cannot disclose the mechanism relating to the mean flow field and turbulent convection.

D. 7. Taylor's Hypothesis

Taylor's hypothesis assumes that "if the velocity of the flow field which carries the turbulent spot is much greater than the turbulent fluctuation velocity, then the sequence of changing u at the fixed point is simply due to the passage of an unchanging pattern of turbulent motion over the point." Thus he assumes $u = \phi(t) = \phi(x/u)$ and the correlation function $R_x = \dfrac{\overline{\phi(t)\ \phi(t + x/u)}}{\overline{u^2}}$.

Then he went on to prove that space correlation function and spectral function are Fourier transform pair.

$$R_x = \int_o^{\infty} F(f) \cos \frac{2\pi f x}{U}\, df$$

$$F(f) = \frac{4}{U} \int_o^{\infty} R_x \cos \frac{2\pi f x}{U}\, dx$$

where F(f) is the spectral function normalized to give

$$\int_o^{\infty} F(f) df = 1$$

This relation is found identical to the transform pair of autocorrelation and power spectra if the delay time, $\Delta\tau$, is replaced by $\Delta x/u$. Then the existence of the above transform pair is assured by Sect. V. 2. 2. 5. 1. provided $\Delta\tau = \Delta x/u$ exists. Therefore, validity of Taylor's hypothesis requires the finding of the existence of u, namely $u_c = \Delta x/\Delta\tau$.

D. 8. Interpretation of Space-Time Correlation (Δy Separation)

The lateral crosscorrelation measurements were taken with M-probe displaced above and below the S-probe on the same X-plane. S -probe was always delayed. The asymmetric form of correlation functions reversed the trend and the correlation peaks appear in the opposite side of zero time delay as M-probe crossed the positon of S-probe. Since the positioning of the delayed probe upstream of the undelayed probe depicts the future occurrence in positive delayed time with respect to undelayed probe, the shifting of delayed probe downstream will produce the mirror image pattern in negative delayed time. In positive Δy, the appearance of correlation in negative time delay indicates that the correlating signal passing over the M-probe is located downstream of the corresponding signal passing over the S-probe. For a negative Δy, the process is reversed and hence the correlation in the positive side of the time delay indicates the correlating flow passing over the M-probe is upstream of the S-probe.

D. 9. Fluctuation Signals and Probability Density Distributions

The raw fluctuation signals and corresponding response of intermittency meter outputs for the higher overheat taken at the marked positions are shown in Fig. D. 5. Corresponding probability density distributions for the two sampled overheat currents are shown in Fig. D. 6. The probability density distributions were obtained by using a SAICOR correlator and the signals were computed in a real time process as the experiments were conducted. As the turbulent mixing layer was penetrated by the hot-wire from the freestream side, noticeable positive fluctuating voltages began to appear, indicating the passage of an occasionally slower and hotter flow field ($\tilde{e}' = -r\dot{m}' + T_o'$) over the sensor. The one-sided fluctuation signal was most intense at location C and the positive skewness of the probability density distribution confirmed that the turbulent field which produced the positive fluctuation voltages dominates the flow. Recall that higher total temperature and lower convection velocity were measured in this region. At point D, the signals appeared to be extending evenly on both sides and a Gaussian-like probability density distribution was obtained. Up to this point, the qualitative probability distributions of both sampled currents were identical.

At point E just below the sonic point, negative spikiness began to predominate, indicating that the wire spent more time in a faster and colder fluctuation field. The skewness or probability distribution taken with the higher overheat reversed the distribution but the ones taken with a lower overheat remained relatively Gaussian in form, indicating the negative spikiness of the signal was produced primarily by the mass flux fluctuation. The Gaussian form of the probability distributions taken with the lower overheat within the mixing layer were not too surprising, because the mean total temperature profile is relatively constant. Kovasznay(28) observed similar phenomena in the supersonic turbulent boundary layer. Although Kovasznay was uncertain about whether the reversal of the skewness of probability distributions which occurred from the outer boundary layer edge to near the wall was caused by a real flow phenomenon or was an instrumentation phenomenon connected with operating a probe in the shear layer close to the sonic point, it is apparent that the observed phenomena do exist in the supersonic turbulent mixing layer of the present investigation.

Since the mean value of fluctuation must vanish ($\int e' \, dt = 0$), the skewness of probability density distributions taken near both edges of the mixing layer implies that the large excursions of fluctuation must exist for a shorter time and the small excursions in the opposite direction exist for a longer period. Fisher and Davies(48) have demonstrated in the incompressible mixing layer experiments that the convection velocity of turbulent field is strongly influenced by the large fluctuations in spite of the short ime for which they are present. In the region of almost zero skewness of probability density distributions, the two velocities are almost identical. Qualitatively, the measured convection velocity follows the trend of probability density distributions obtained with a high overheat as described above.

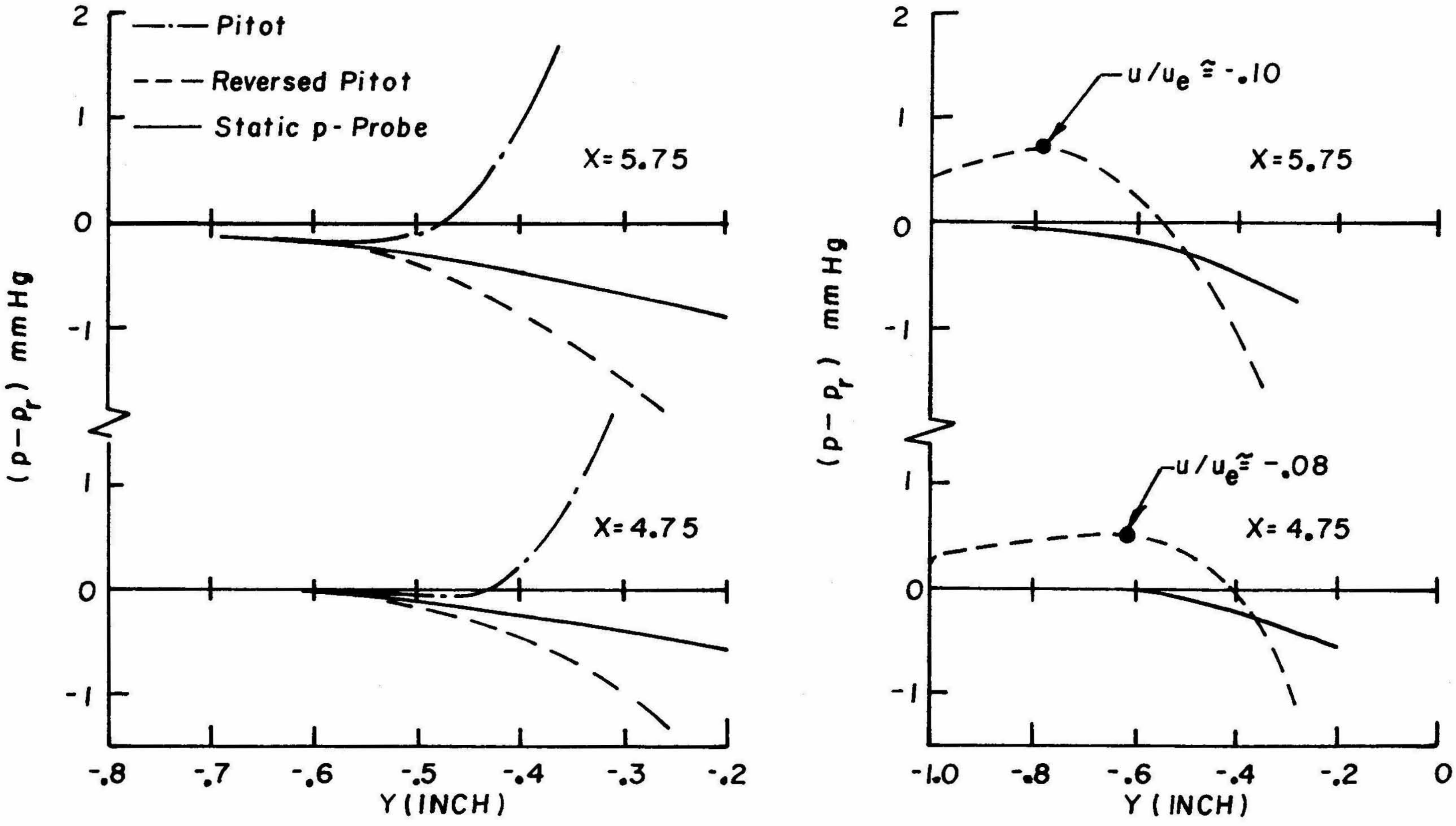

(a) Match-ed Injection $\lambda_e \cong 0.0072$

$M_e \cong 2.47$ $p_0 = 737$ mmHg $p_r = 45.5$ mmHg

(b) Under Injection (Reversed Flow) $\lambda_e \cong 0.0055$

$M_e \cong 2.55$ $p_0 = 737$ mmHg $p_r = 40.0$ mmHg

FIG. D.1. TFML-DIFFERENTIAL PRESSURE PROFILES OF MATCHED AND UNMATCHED INJECTION CONDITIONS

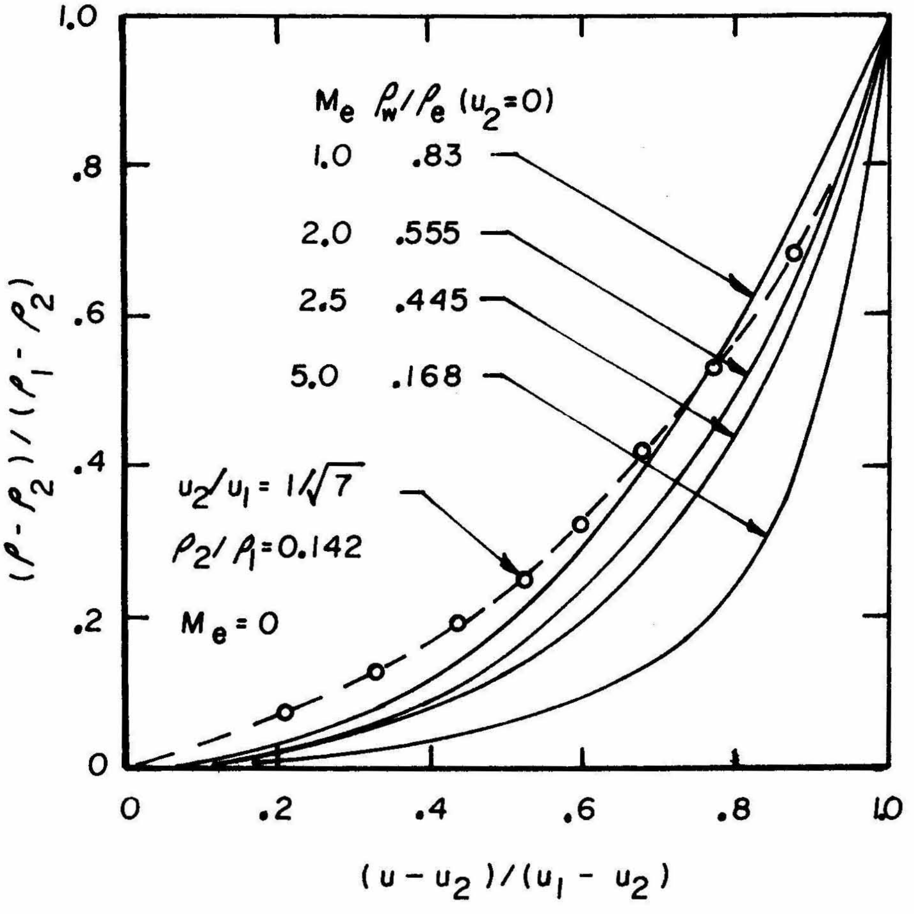

○ Density Ratio Equivalent to M = 5.5 Flow
(Ref. 20: BROWN & ROSHKO)

FIG. D. 2. TFML-DENSITY VS. VELOCITY DISTRIBUTIONS

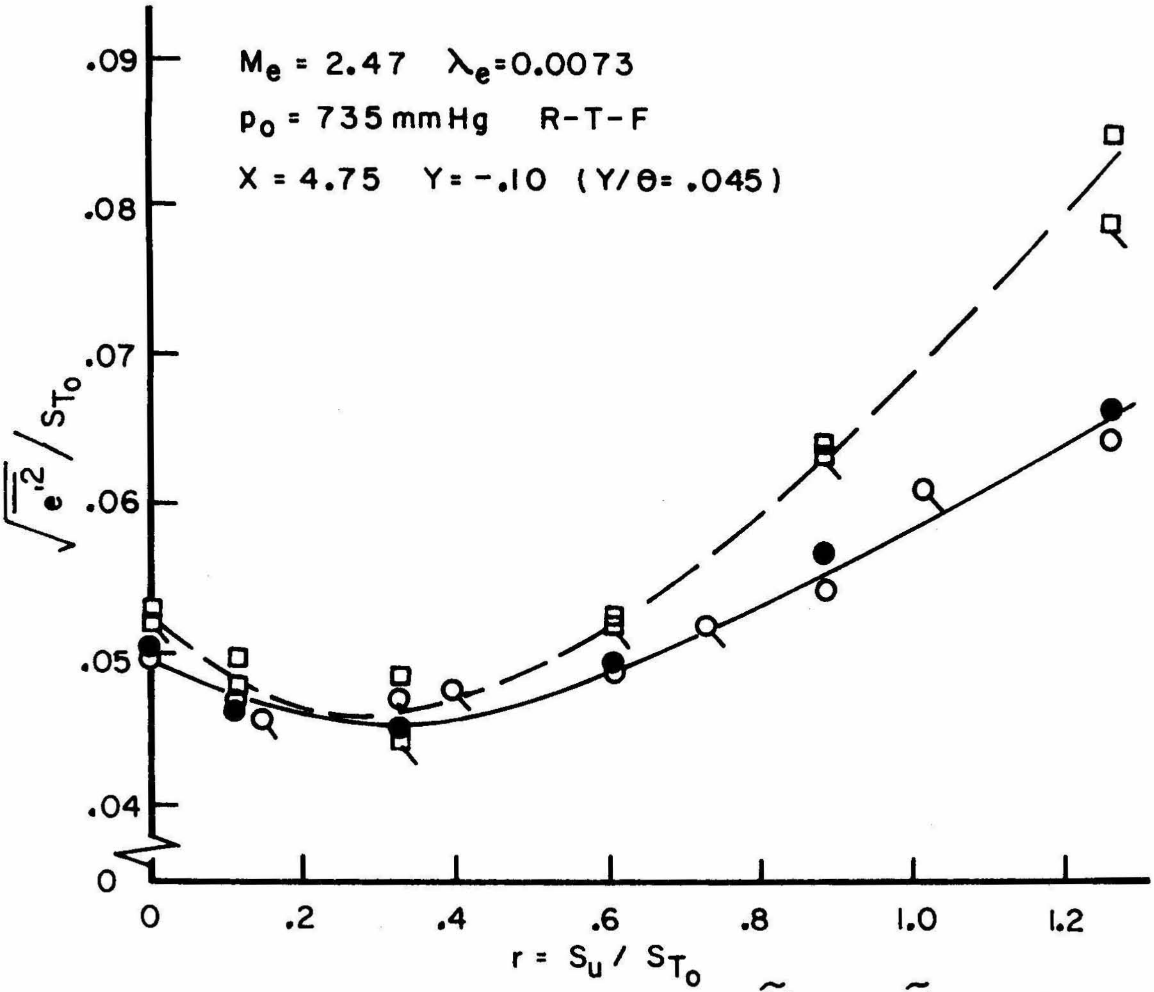

		$\widetilde{m}'$	$\widetilde{T}'_o$	$R_{\overline{m'T'_o}}$
●	SPECTRA (1KHz ≤ f ≤ 300KHz)	.046	.05	.29
○	E_{TC} $(M_A = M_t)$	.05	.05	.30
□	E_{TC} $(M_A < M_t)$	.074	.051	.44

FIG. D. 3. COMPARISON OF TFML FLUCTUATION MODE DIAGRAM E_{TC} VS INTEGRATED SPECTRA

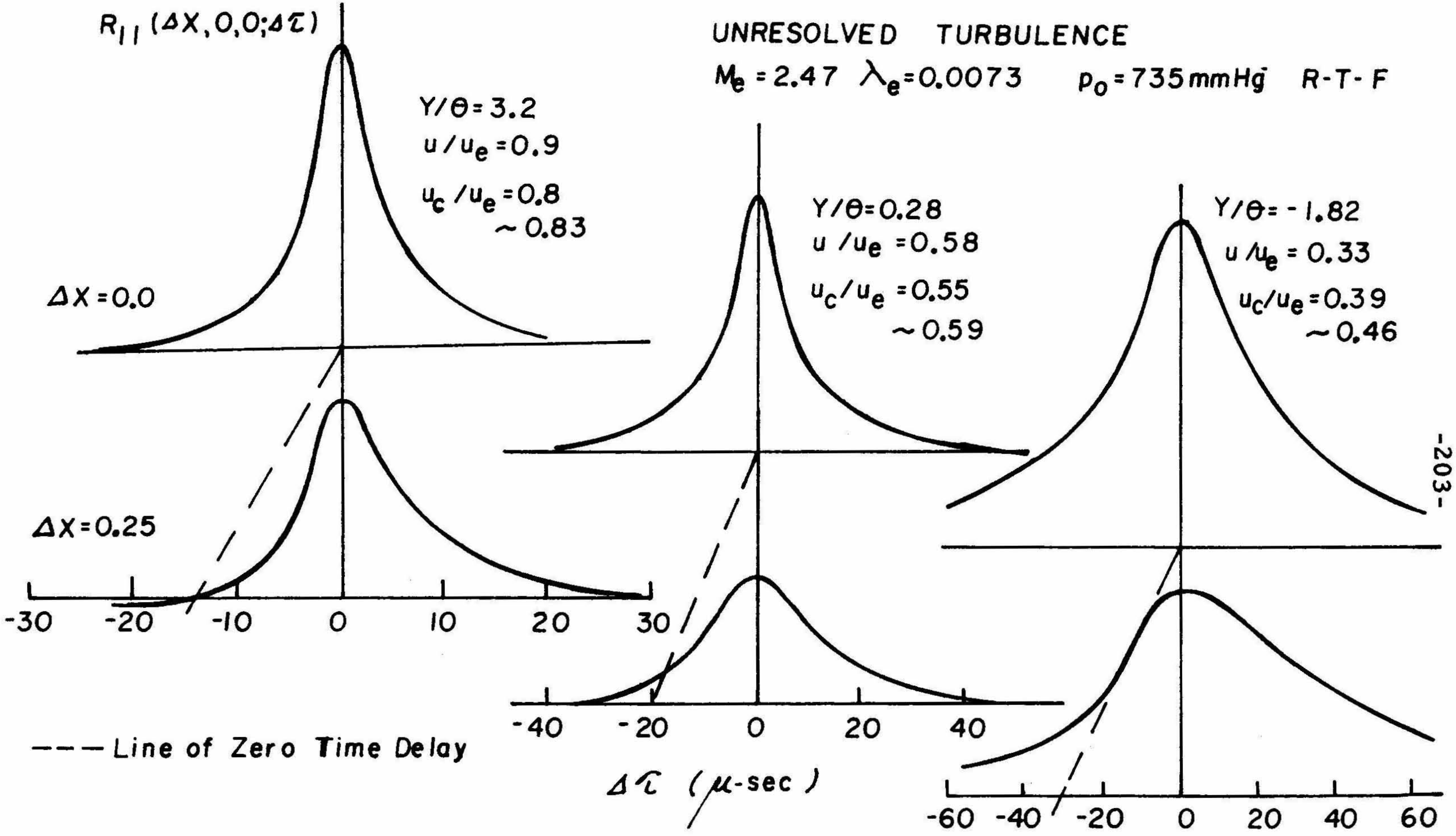

FIG. D.4 TFML LONGITUDINAL CROSSCORRELATION FUNCTIONS

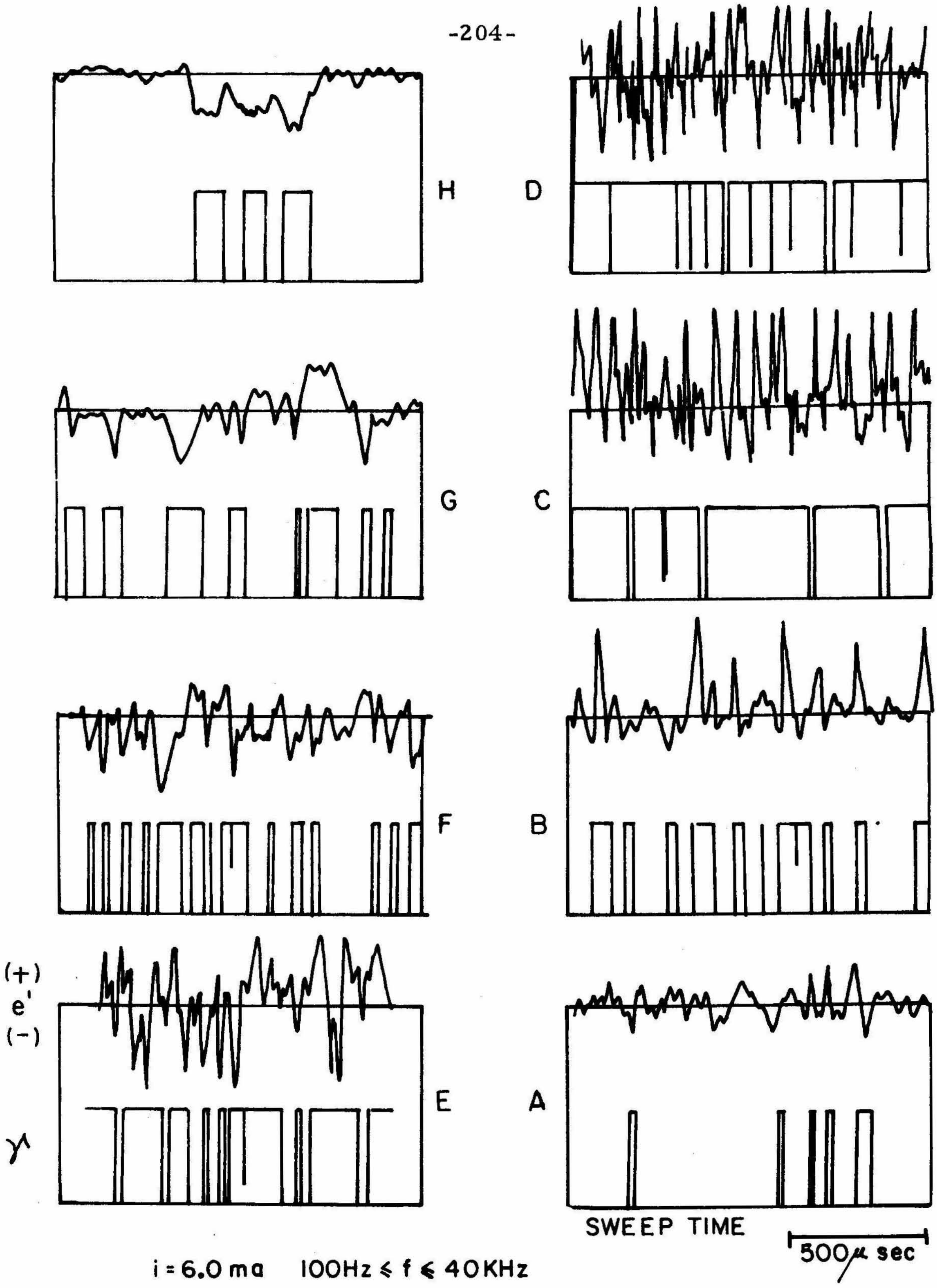

FIG. D. 5. TURBULENT FLUCTUATION SIGNALS AND INTERMITTENCY METER OUTPUTS

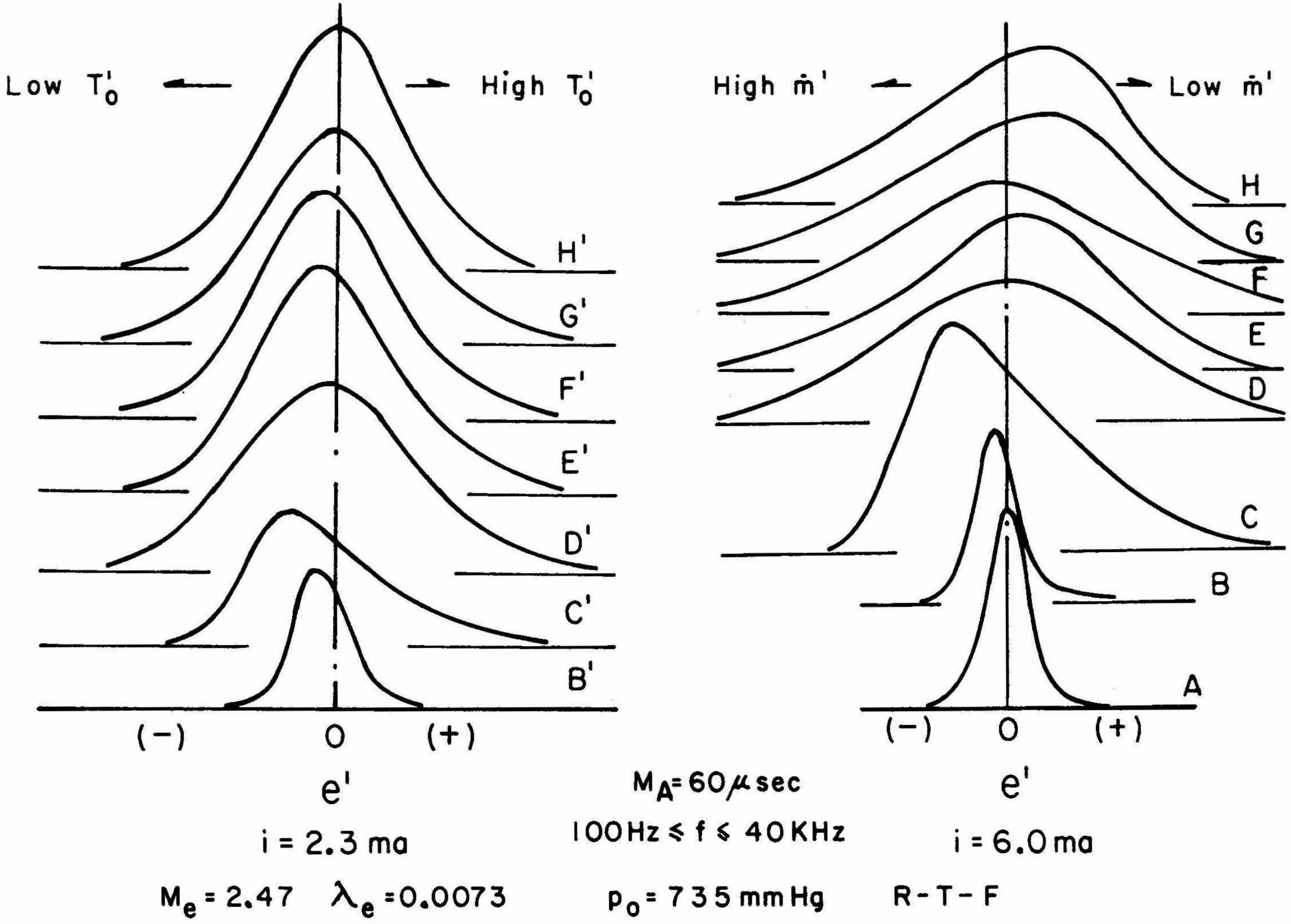

FIG. D.6. PROBABILITY DENSITY DISTRIBUTIONS

References

1. Maydew, R. C. and Reed, J. F., "Turbulent Mixing of Axisymmetric Compressible Jet (in the Half-Jet Region) with Quiescent Air," Sandia Corp., SC-4764 (RR), March 1963.

2. Johannesen, N. H., "The Mixing of Free Axially Symmetrical Jets of Mach Number 1.4," Aero. Res. Council 18967, FM 2490, January 1957.

3. Gooderum, P. B., Wood, G. P. and Brevoort, M. J., "Investigation with Turbulent Mixing of Free Supersonic Jet," NACA Report 963, 1950.

4. Bershader, D. and Pai, S. J., "On Turbulent Mixing in Two-Dimensional Flow," Journal of Applied Physics, Vol. 21, No. 6, p. 616, 1950.

5. Fuller, L. and Reid, J., "Experiments on Two-Dimensional Base Flow at M = 2.4," British RAE Report Aero 2569, 1956.

6. Charwat, A. F. and Yakura, J. K., "An Investigation of Two-Dimensional Supersonic Base Pressures," J. Aero. Science, Vol. 25, No. 2, pp. 122-128, February 1958.

7. Sirieix, P. M., "Base Pressure and Processes of Turbulent Mixing in Plane Supersonic Flow," La Recherche Aeronautique, Vol. 13, No. 78, pp. 13-20 (Translated by Irwin E. Alber).

8. Hama, F. R., "Experimental Investigations of Wedge Base Pressure and Lip Shock," NASA Tech. Report No. 32-1033, Jet Propulsion Lab., California Institute of Tech., Dec. 1, 1966.

9. Hill, J. A. F. and Nicholson, J. E., "Compressibility Effects on Fluid Entrainment by Turbulent Mixing Layer," NASA CR-131, Nov. 1964.

10. Roshko, A. and Thomke, G. L., "Results of Pilot Experiment on Supersonic Free Shear Layers," McDonnell Douglas Astronautics Company Report, DAL, Oct. 8, 1968.

11. Sirieix, P. M. and Solignac, J. L., "Contribution A L'Etude Experimentale De La Couch De Melange Turbulent Isobare D'un Ecoulement Supersonique," Office National D'Etudes Et De Recherches Aerospatiales, T.P. No. 327, 1966.

12. Chapman, A. J. and Korst, H. H., "Free Jet Boundary with Consideration of Initial Boundary Layer," Second U. S. National Congress of Applied Mechanics, June 1954, University of Michigan.

13. Channapragada, R. S., "Compressible Jet Spread Parameter for Mixing Zone Analysis," AIAA Journal, Vol. 1, p. 2188, 1963.

14. Nash, J. F., "An Analysis of Two-Dimensional Turbulent Base Flow, Including the Effects of Approach Boundary Layer," R and M 3344, 1963.

15. Korst, H. H. and Tripp, W., "The Pressure on a Blunt Trailing Edge Separating Two Supersonic Two-Dimensional Air Streams of Different Mach Number and Stagnation Pressure but Identical Stagnation Temperature," Proceedings of the Fifth Midwestern Conference on Fluid Mechanics, University of Michigan, Ann Arbor, pp. 187-199, April 1957.

16. Alber, I. E. and Lees, L., "Integral Theory for Supersonic Turbulent Base Flows," AIAA Journal, Vol. 6, pp. 1343-1351, 1968.

17. Gortler, H., "Berechnung von Aufgaben der freien Turbulenz auf Grund eines neuen Naherungsansatzes," ZAMM, 22, pp. 244-254, 1942.

18. Tollmien, W., "Berechnung der turbulenten Ausbreitungsvorgaenge," ZAMM, 6, pp. 468-478, 1926.

19. Liepmann, H. W. and Laufer, J., "Investigations of Free Turbulent Mixing," NACA TN 1257, 1947.

20. Brown, G. A. and Roshko, A., "The Effect of Density Difference on the Turbulent Mixing Layer," AGARD-CP-93, AGARD Conference Proceedings No. 93 on Turbulent Shear Flows, Sect. 23, pp. 1-23, 13-15 September 1971.

21. Fernandez, F. L. and Zukoski, E. E., "Experiments in Supersonic Turbulent Flow with Large Distributed Surface Injection," AIAA Journal, Vol. 7, pp. 1759-1769, 1969.

22. Fernandez, F. L., "Two-Dimensional Viscous Flows with Large Distributed Surface Injection," Parts I, II, and III. Ph. D. Thesis California Institute of Technology, 1969.

23. McQuaid, J., "Incompressible Turbulent Boundary Layers with Distributed Injection," Ph. D. Thesis, Engineering Department, Cambridge, Univ. (September 1966).

24. Oliver, R., "Operating Instructions -- Supersonic Wind Tunnel Compressor System," GALCIT Hypersonic Project Internal Memo #1, 1955.

25. Gran, R. L., "Step Induced Separation of a Turbulent Boundary Layer," Ph.D. Thesis, California Institute of Technology, 1970.

26. Behrens, W. H., "Flow Field and Stability of the Far Wake Behind Cylinders at Hypersonic Speed," Ph.D. Thesis, California Institute of Technology, 1966.

27. Ramaswamy, M. A., "Experimental Investigation of the Effect of Cooling on the Near Wake of a Circular Cylinder at Mach Number Six," Ph.D. Thesis, California Institute of Technology, 1971.

28. Kovasznay, L. S. G., "Turbulence in Supersonic Flow," J. of the Aeronautical Sciences, Vol. 20, pp. 657-674, October 1953.

29. Morkovin, M. V., "Fluctuations and Hot-Wire Anemometer in Compressible Flow," AGARDograph 24, 1956.

30. Kistler, A. L., "Fluctuation Measurements in a Supersonic Turbulent Boundary Layer," Physics of Fluids, Vol. 2, No. 3, pp. 290-296, May-June 1959.

31. Laufer, J., "Some Statistical Properties of the Pressure Field Radiated by a Turbulent Boundary Layer," Physics of Fluids, Vol. 7, No. 8, pp. 1191-1197, Aug. 1964.

32. Behrens, H. W., "Hot-Wire of Finite Length for Compressible Flow Fluctuation Measurements," (Forthcoming).

33. Behrens, W., "Total Temperature Thermocouple Probe Based on Recovery Temperature of a Circular Cylinder," Int. J. Heat and Mass Transf., Vol. 14, pp. 1621-1630, Pergamon Press, 1971.

34. Liepmann, H. W., "On the Acoustic Radiation from Boundary Layers and Jets," paper presented at the 23rd IAS Meeting, Jan. 24-28, 1955.

35. Crane, L. J., "The Laminar and Turbulent Mixing of Jets on Compressible Fluids - Part I," JFM Vol. 3, 1957.

36. Behrens, W., "Separation of a Supersonic Turbulent Boundary Layer by a Forward Facing Step," AIAA Paper No. 71-127, AIAA 9th Aerospace Sciences Meeting, New York, Jan. 25-27, 1971.

37. Hinze, J. O., "Turbulence - An Introduction to its Mechanism and Theory," McGraw-Hill, 1959, p. 268.

38. Spencer, B. W. and Jones, B. G., "Statistical Investigation of Pressure and Velocity Fields in the Turbulent Two Stream Mixing Layer," AIAA Paper No. 71-613, June 21-23, 1971.

39. Yule, A. J., "Two Dimensional Self Preserving Turbulent Mixing Layers at Different Freestream Velocity Ratios," A.R.C. R & M No. 3863, March 1971.

40. Batt, R. G., Kubota, T., and Laufer, J., "Experimental Investigation of the Effect of Shear-Flow Turbulence on a Chemical Reaction," AIAA Reacting Turbulent Flow Conference, June 17, 1970.

41. Bradshaw, P., Ferriss, D. H., and Johnson, R. F., "Turbulence in the Noise-Producing Region of a Circular Jet," JFM, Vol. 19, Part 4, pp. 591-624, 1964.

42. Wygnanski, I. and Fiedler, H. E., "The Two-Dimensional Mixing Region," JFM Vol. 41, p. 329, 1970.

43. Laufer, J. and Vrebalovich, T., "Stability and Transition of a Supersonic Laminar Boundary Layer on an Insulated Flat Plate," JFM Vol. 9, pp. 257-299, 1960.

44. Wills, J. A. B., "On Convection Velocities in Turbulent Shear Flows," JFM Vol. 20, part 3, pp. 417-432, 1964.

45. Wilmarth, W. W. and Wooldridge, C. E., "Measurements of the Fluctuating Pressure at the Wall Beneath a Thick Turbulent Boundary Layer," JFM Vol. 14, pp. 187-210, 1962.

46. Taylor, G. I., "The Spectrum of Turbulence," Proc. Royal Society of London, Series A, Vol. 164, Jan.-Feb. 1938.

47. Demetriades, A., "Theory of Hot-Wire Correlation Measurements in Compressible Flow with Applications to Wakes," Philco-Ford Corporation, January 1972.

48. Fisher, M. J. and P. O. A. L. Davies, "Correlation Measurements in a Non-Frozen Pattern of Turbulence," JFM Vol. 18, pp. 97-116, 1964.

49. Baum, E., "Initial Development of the Laminar Separated Shear Layer," AIAA J., Vol. 2, No. 1, January 1964.

50. Denison, M. R. and Baum, E., "Compressible Free Shear Layer with Finite Initial Thickness," AIAA J., Vol. 1, No. 2, February 1963.

51. Bradshaw, P., "The Effect of Initial Conditions on the Development of a Free Shear Layer," JFM Vol. 26, pp. 225-236, 1966.

52. Gran, R. L., Private Communication.

53. Laufer, J., "Aerodynamic Noise in Supersonic Wind Tunnels," JAS, pp. 685-692, Sept. 1961.

54. Lighthill, M. J., "On Sound Generated Aerodynamically. II. Turbulence as a Source of Sound," Proc. Royal Soc. A, Vol. 222, pp. 1-32, 1954.